# Microkelvin Nanoelectronics

Yurttagul, N.F.

**DOI**
10.4233/uuid:5a57df7e-682c-458a-8c28-45ae96c40d7b

**Publication date**
2020

**Document Version**
Final published version

**Citation (APA)**
Yurttagul, N. F. (2020). *Microkelvin Nanoelectronics*. [Dissertation (TU Delft), Delft University of Technology]. https://doi.org/10.4233/uuid:5a57df7e-682c-458a-8c28-45ae96c40d7b

**Important note**
To cite this publication, please use the final published version (if applicable).
Please check the document version above.

# MICROKELVIN NANOELECTRONICS

# MICROKELVIN NANOELECTRONICS

## Proefschrift

ter verkrijging van de graad van doctor
aan de Technische Universiteit Delft,
op gezag van de Rector Magnificus Prof. dr. ir. T.H.J.J. van der Hagen,
voorzitter van het College voor Promoties,
in het openbaar te verdedigen op vrijdag 17 juli 2020 om 12:30 uur

door

**Nikolai YURTTAGÜL**

Master of Science, Universität Kassel, Duitsland
geboren te Berlin, Duitsland

Dit proefschrift is goedgekeurd door de

promotor: prof. dr. ir. L.P. Kouwenhoven
copromotor: dr. A. Geresdi

Samenstelling promotiecommissie:

| | |
|---|---|
| Rector Magnificus, | voorzitter |
| Prof. dr. ir. L.P. Kouwenhoven, | Technische Universiteit Delft, promotor |
| Dr. A. Geresdi | Technische Universiteit Delft, copromotor |
| | |
| *Onafhankelijke leden:* | |
| Prof. dr. J.P. Pekola, | Aalto Yliopisto |
| Prof. dr. D. Zumbühl, | Universität Basel |
| Prof. dr. G. Steele, | Technische Universiteit Delft |
| dr. S. Conesa-Boj, | Technische Universiteit Delft |
| Prof. dr. Y.M. Blanter | Technische Universiteit Delft |

*Printed by:* Gildeprint, Enschede

*Front & Back:* Stylized artwork representing the electronic temperature between 500 μK and 20 mK. Lines are positioned evaluating the Fermi distribution, where a the chemical potential equals that of the charging energy of the CBT shown in Fig. 6.1.

Design by dr. Matthew Sarsby



Casimir PhD Series, Delft-Leiden 2020-17

ISBN 978.90.8593.444.8

An electronic version of this dissertation is available at
http://repository.tudelft.nl/.

*Ein jeder Mann muss seinen eigenen Weg in den Himmel finden.*

Friedrich der Große (1712-1786)

# SUMMARY

Of all parameters, determining the behaviour of a physical system in the laboratory, temperature is one of the most important, if not the most important. The study of solid matter at cryogenic temperatures revealed unexpected phenomena like superconductivity and was closely related to the verification of new and revolutionary concepts in solid-state physics in the last century. The nowadays pursued development of quantum effect devices is closely related to technologies of creating ultralow temperatures on the micro- and nanometerscale. Achievable electron temperatures in miniaturized electronic devices are currently limited to the millikelvin temperature regime, caused by the technical limits of $^3$He/$^4$He dilution refrigeration in combination with hot-electron effects, due to a strongly weakening electron-phonon coupling strength in miniaturized electronic conductors with lowering the temperature. New physical and technological concepts, like the use of topological materials for quantum information processing, created an interest in reaching lower electron temperatures in nanoelectronic devices than currently possible. For this purpose, a bridge to classical ultralow temperature research, where microkelvin cooling of bulk solids is achieved for several decades, has to be built.

This work is dedicated to the goal of enabling cooling of nanoelectronic devices to the yet unreached microkelvin regime. For enabling microkelvin refrigeration of nanodevices, methods for chipscale nuclear magnetic cooling are developed, in order to cool electrons on a chip to microkelvin temperatures by direct spin-spin thermalization with nuclear spins, bypassing the weak electron-phonon interaction. A decisive key for reaching a nuclear cooling power in miniaturized volumes, which is sufficient to refrigerate a nanoelectronic circuit to microkelvin temperatures, is the utilization of nonequidistant nuclear level splitting by nuclear quadrupole interaction in the nuclear refrigerant. The metal indium is proposed and utilized as nuclear refrigerant for this purpose, since it combines a strong quadrupolar interaction with a strong hyperfine interaction.

The ultilization of indium for magnetic cooling on the micro- and nanoscale is studied by integrating electrochemically deposited indium films onto a Coulomb blockade thermometer. Coulomb blockade thermometry is based on thermally activated single charge transport by tunneling between metallic islands and comprises an ideal and scalable solution for nuclear magnetic cooling and electronic thermometry on a combined, miniaturized platform. By combining indium microrefrigerators with an off-chip nuclear magnetic cooling stage, tailor made to couple the chip to an ultracold environment, cooling of a nanoelectronic device to microkelvin temperatures is demonstrated for the first time. With the cooling schemes for miniaturized electronic devices developed in this work, the foundation for quantum nanoelectronics at microkelvin temperatures is laid, opening the door to an experimentally unknown territory in physics.

# SAMENVATTING

Van alle parameters die het gedrag van een fysisch systeem in het laboratorium bepalen, is temperatuur wellicht de belangrijkste. Het onderzoek naar vaste materie op cryogene temperaturen heeft onverwachte fenomenen zoals supergeleiding onthuld en was nauw betrokken bij de verificatie van nieuwe, revolutionaire concepten in de vastestoffysica in de afgelopen eeuw. De hedendaags nagestreefde ontwikkeling van technologie gebaseerd op quantum mechanische effecten, is sterk verbonden aan de technologie om ultralage temperaturen te realiseren op de micro- en nanometer schaal. De elektron temperaturen die momenteel bereikt kunnen worden in chips op zulke schalen, worden beperkt door de technische limieten van $^3$He/$^4$He mengkoeling, in combinatie met warme elektron effecten veroorzaakt door een sterk afnemende elektron-fonon koppeling bij lage temperaturen. Nieuwe fysische en technologische concepten, zoals het gebruik van topologische materialen ten behoeve van berekeningen met quantum informatie, heeft de interesse gewerkt om lagere elektron temperaturen in nanoelektronische technologiën te realiseren dan op dit moment mogelijk is. Met dit als doel, moet een brug geslagen worden naar het klassieke ultralage temperaturen onderzoek, waar microkelvin koeling al enkele decennia geleden bereikt is.

Deze scriptie is gewijd aan de verwezenlijking van de koeling van nanoelektronische technologie tot het niet eerder bereikte microkelvin regime. Hiertoe worden methoden ontwikkeld om nucleaire magnetische koeling toe te passen op de schaal van de elektronische chips, door de elektronen tot microkelvin temperaturen af te koelen via directe spin-spin thermalisatie door nucleaire spins, waardoor de zwakke elektron-fonon interactie omzeild wordt. Het voornaamste postulaat van deze scriptie, is dat het gebruik van niet-equidistante nucleaire toestands splitsing door nucleaire quadrupool interactie in het koelmiddel, de beslissende factor is om een voldoende hoog nucleair koelvermogen te realiseren om geminiaturiseerde volumes tot microkelvin temperaturen af te koelen. Hiertoe wordt het metaal indium voorgesteld en gebruikt, omdat het een sterke quadrupool interactie combineert met een sterke hyperfijn interactie.

Het gebruik van indium voor magnetische koeling op de micro- en nanoschaal wordt bestudeerd door dunne lage indium door middel van elektrodepositie te plaatsen op een nanoelektronische Coulombblokkade thermometer. Coulombblokkade thermometrie is gebaseerd op het thermisch geactiveerde tunnelen van enkele elektronen tussen metallische eilanden en is ideale en schaalbare oplossing voor nucleaire magnetische koeling en elektronische thermometrie op een gecombineerd, geminiaturiseerd platform. Door indium microkoelers te combineren met een externe nucleaire koeltrap die speciaal ontworpen is om de chip aan een ultrakoude omgeving te koppelen, wordt de koeling van een nanoelektronische chip tot microkelvin temperaturen voor het eerst aangetoond. De koeltechniek ontwikkeld voor geminiaturiseerde elektronische technologie in deze scriptie, legt de basis voor quantum nanoelektronica op microkelvin temperaturen en opent de deur naar experimenteel onverkend gebied in de natuurkunde.

# ZUSAMMENFASSUNG

Von allen Parametern die das Verhalten eines physikalischen Systems im Labor bestimmen, ist die Temperatur zweifellos einer der wichtigsten, wenn nicht der wichtigste. Die Technologie der Erzeugung tiefer Temperaturen ermöglichte die Verifizierung einiger der wichtigsten Postulate der Quantenmechanik im letzten Jahrhundert und die heutige Entwicklung von auf Quanteneffekten basierenden Technologien ist eng verbunden mit der Entwicklung der Tieftemperaturphysik. Quantentechnologien wiederum wurden ermöglicht durch Entwicklungen in der Nanoelektronik und allgemein durch Methoden Materieeigenschaften wie die Temperatur auf der Mikro- und Nanometerskala zu kontrollieren. Die Entwicklung moderner Quantentechnologien, wie z.B. die Nutzung topologischer Materialien für die Quanteninformationsverarbeitung, hat nun ein wissenschaftliches Interesse an tieferen Elektronentemperaturen auf der miniaturisierten Größenskala, als bisher technisch erreichbar, erzeugt. Besonders Elektronentemperaturen unterhalb von 1 mK stellen hierbei in wichtiges, bisher unerreichtes Ziel dar.

Diese Arbeit ist dem Ziel gewidmet, den unerforschten Mikrokelvin Temperaturbereich für nanoelektronische Bauelemente nutzbar zu machen. Hierzu werden neue Methoden eingefürt, Materialien mit entsprechendem kernmagnetischen Eigenschaften mit Mikro- und Nanostrukturen zu integrieren und den einen kernmagnetischen Kühlungsprozess direkt auf dem Chip anzuwenden, welcher dann lokal auf Mikrokelvin Temperaturen gekühlt wird. Hierbei ist ein entscheidender Schlüssel zum Erreichen einer kernmagnetischen Kühlleistung, die ausreichend ist um eine nanoelektronische Schaltung für den Zeitraum von Tagen bis Wochen in den Mikrokelvin Bereich zu kühlen die Nutzbarmachung von nichtmagnetischen Wechselwirkung von Kernen mit dem Gitter, wie besonders der Kern-Quadrupol Wechselwirkung. In einigen Metallen tritt eine starke Kern-Quadrupol Wechselwirkung zusammen mit einer starken Hyperfeinwechselwirkung auf. Das Metall Indium hat hier die aussichtsreichsten Eigenschaften für die direkte Anwendung, wie in dieser Arbeit sowohl theoretisch als auch praktisch gezeigt wird.

Die Nutzung von Indium als Kern-Paramagnet für die magnetische Kühlung von Nanoelektronischen Schaltungen wird durch die Co-Integration von elektrochemisch abgeschiedenen Indium Shichten mit einem Coulomb-Blockade Thermometer realisiert. Mit einem Coulomb-Blockade Thermometer kann die Elektronentemperatur magnetfeldunabhängig, durch Messung von Tunnelströmen zwischen metallischen Inseln gemessen werden. Es stellt somit die ideale Plattform für die Erforschung von Kernkühlungsprozessen auf der miniaturisierten Skala dar. Durch eine Kombination von Indium Integration auf den Chip und Kühlung der elektrischen Zuleitungen mit einer makroskopischen Kernkühlungsstufe, wird in dieser Arbeit erstmals das Erreichen von Elektronentemperaturen unterhalb von 1 mK auf der Nanoskala demonstriert. Letzteres auf Zeitskalen von Tagen, und Leistungsdichten wie sie in Quantentransport Messungen auftreten.

# CONTENTS

# 1

# INTRODUCTION

*Experimenters reached the kelvin and the millikelvin temperature ranges only by overcoming substantial experimental difficulties. The problems presented by the microkelvin temperature range are at least as severe. It is therefore valid to ask whether we can really learn anything new about condensed matter at microkelvin temperatures, and if so, is that knowledge sufficiently valuable to justify investing the required manpower and financial resources?*

*The optimistic answer to these questions is that whenever we have entered a new temperature range, we have discovered new and important phenomena, widening our understanding of nature; there is no reason to suspect that this should be different for the microkelvin temperature range.*

*The pessimistic answer is that we have already learned so much at kelvin and millikelvin temperatures that little or nothing is left to make the "microkelvin effort" worthwhile. This is partly true, because condensed matter has been so thoroughly investigated in the kelvin and millikelvin temperature ranges that one can state with reasonable certainty that for some branches of condensed matter physics nothing new will happen at lower temperatures. However, there are branches for which one cannot make such a statement. And there are even branches for which one can state with reasonable certainty that new discoveries will be made.*

Frank Pobell, Solid-State Physics at Microkelvin Temperatures: Is Anything Left to Learn?

# 1

The ability of creating low temperatures in the laboratory is historically closely linked to decisive discoveries in physics, or experimental verification of new physical theories. Until the late 19th century, the development of cooling techniques (see Fig 1.1) was mainly performed to study the thermodynamic properties of gases and to refrigerate food for long journeys. This changed drastically in the 20th century, resulting in revolutionary developments which are still ongoing: The liquefication of $^4$He by the Dutch physicist Heike Kammerlingh Onnes in 1908 enabled the refrigeration of solid matter down to 4.2 K, and later even below 1 K by pumping the $^4$He vapor above a liquid $^4$He bath. Study of matter under these extreme conditions led to fully unexpected, groundbreaking new discoveries like superconductivity [1–3] and superfluidity [4]. Low-temperature physics then played a significant part in experimentally proving some the postulates of quantum mechanics by for example measuring the specific heat of solids at yet unaccessible temperatures [5]. A better understanding of solid matter with quantum physics enabled the significant technological revolution in the second half of the 20th century with semiconductor electronics and miniaturization of electronic devices. At about the same time, novel refrigeration techniques like adiabatic demagnetization of paramagnetic salts [6–8] and $^3$He/$^4$He dilution refrigeration [9–11] made the unexplored millikelvin temperature regime suddenly accessible. Once again new discoveries were made like for example the quantum Hall effect [12]. $^3$He/$^4$He dilution refrigeration became the workhorse of millikelvin refrigeration of miniaturized electronic devices and an essential (as well as commercial) factor for the development of quantum-effect devices, thus gaining importance far beyond the low-temperature physics community. The latter was already on the way to the microkelvin temperature regime with an unprecedented race towards absolute zero, lasting from about the 50s of the last century to the beginning of the 21st century [9]. Microkelvin temperatures were made accessible in the solid state with the development of adiabatic demagnetization of nuclear magnetic moments (nuclear magnetic cooling) [13, 14], which was already proposed in the early 20th century [15, 16] but could only be realized in combination with $^3$He/$^4$He dilution refrigeration. Nowadays, microkelvin refrigeration of metals by nuclear magnetic cooling has become an established technique [17–20] and under such extreme conditions, exotic states of solid matter like nuclear ferromagnets [21] or simple metal magnetic superconductors [22] were observed in bulk metals. A temperature of 100 pK, reached by nuclear demagnetization of the nuclear magnetic moments in Rh [23] is the lowest achieved temperature in the solid state up to now. Other than $^3$He/$^4$He dilution refrigerators, nuclear refrigerators are not commercially available and microkelvin refrigeration of bulk solids is currently performed only at few ultralow-temperature laboratories in the world [24].

While knowledge driven low-temperature research proceeds, some low-temperature techniques found their way into modern quantum device technologies, a field in turn driven by developments in micro- and nanoelectronics and semiconductor physics. Once electronic devices could be miniaturized so far that they reach the dimensions of the conduction electron wavelength, engineering of quantum systems on the miniaturized scale has become possible. The most challenging and fascinating opportunity here is the possibility of computing on the basis of quantum mechanical states [25]. Other than in a classical (digital) computer in which a bit as the elemental buidling block only appears

in one of two states (0 and 1), a quantum bit (qubit) can appear in an arbitrary linear combination of the two quantum states $|0\rangle$ and $|1\rangle$. This gives rise to a parallelism in information processing, holding the potential of solving computational problems of which classical computers are incapable of on realistic timescales [26–28]. Realizing a quantum computer is a significant technical challenge since quantum bits in the solid state require electronic I/O operations on a nanoelectronic device which is cooled down to cryogenic temperatures. Usually temperatures well below 1 K are necessary to prepare the system stable in its corresponding ground state and all operations have to be performed without destroying the fragile coherent phenomena used to store the quantum information. Strategies for making quantum information in usual quantum bit architectures [29–32] more robust are better shielding of the quantum hardware to avoid decoherence by coupling to the environment and/or using error-correction schemes. Promises to overcome the extreme fragility of quantum information on the hardware level are provided by novel ways of utilizing collective charge carrier excitations with non-Abelian exchange statistics (non-Abelian anyons) [33–36]. Non-Abelian anyons are expected to appear in low-dimensional structures and have non-commuting exchange operators, enabling quantum information processing by particle exchange, being intrinsically fault-tolerant and adiabatic. The adiabacity results from the fact that the exchanged particles are representing a highly degenerate ground state of the system which is protected by an energy gap (topological gap), and the computation scheme is thus called topological quantum computation. While signatures of states with non-Abelian exchange statistics could be found in low-dimensional semiconductors at temperatures in the millikelvin regime, lower electron temperatures in quantum devices would offer opportunities for accessing thermally fragile collective particle excitations in semiconductor nanostructures with non-Abelian exchange statistics or stabilize a topological quantum computer against intrinsic error sources. Alongside with other proposals in mesoscopic physics [24] and metrology, this creates a specific interest to proceed to lower electronic temperatures in nanoelectronic devices than achievable with $^3$He/$^4$He dilution refrigeration, and especially realizing the yet unreached microkelvin refrigeration on this size scale.

Refrigeration of nanoelectronic devices to submillikelvin temperatures imposes new technological challenges because miniaturization of electronic devices reduces their thermal coupling to the environment, while dissipation on the device heats the conduction electrons far above the temperature of the environment. By reaching electron temperatures down to about 5 mK, the established technique of $^3$He/$^4$He dilution refrigeration has reached its limits for cooling nanoelectronic devices. Even for reaching these low temperatures signficiant technical and financial effort is necessary, in order to achieve an effective transfer of the power dissipated in the electronic device via remaining lattice vibrations. This is illustrated in Fig. 1.1, where electron temperatures reached in bulk metals and miniaturized structures are compared. After about 40 years of technical improvement, nanoelectronic devices could be cooled about 2 mK close to the lowest achieved temperature in a $^3$He/$^4$He mixture of $\leq 2$ mK. The latter was already achieved in 1986 [50–52]. For a significant advancement to lower temperatures it is clear that once again nanoelectronics has to be brought together with one of the classical workhorses of ultralow temperature research, being the demagnetization of nuclear magnetic mo-

ments (ADR) this time. ADR, well proven in cooling solid matter to microkelvin temperatures, is a possible key to enable microkelvin temperatures for miniaturized devices. The working principle of this technique is the isothermal magnetization (at millikelvin temperatures) and adiabatic demagnetization of a metallic nuclear paramagnet, which can then cool far into the microkelvin temperature regime due to the weak magnetic moments of atomic nuclei. First attempts in using nuclear magnetic cooling for nanoelectronic devices consisted of just mounting a chip to a cold nuclear refrigerant, as cold as a few hundred microkelvin, and measuring the electronic temperature [44]. In all these experiments it could be demonstrated that the electron temperature stays far above the temperature of the nuclear refrigerant. This was not unexpected, since the weak thermal coupling of the electrons to the refrigerator by lattice vibrations, limiting effective electronic cooling on the miniaturized scale to millikelvin temperatures, was not resolved. In recent attempts the nuclear refrigerant was directly integrated onto the chip by film deposition techniques, in galvanic contact with the device, to overcome the electron-phonon obstacle. These attempts [45, 47] produced very low electron temperatures on a miniaturized device, close to the lowest electron temperature achieved with dilution refrigeration (see Fig. 1.1). A combination of cooling the device leads with a macroscopic stage [53, 54], while thermally isolated regions on the chip by thin-film nuclear refrigerant recently yielded the lowest ever measured electron temperature on a nanoelectronic device of 2.8 mK [47]. While this temperature surpassed everything achievable with $^3$He/$^4$He dilution refrigeration, it was not possible to keep it stable on timescales enabling a stable electronic base temperature for quantum transport experiments.

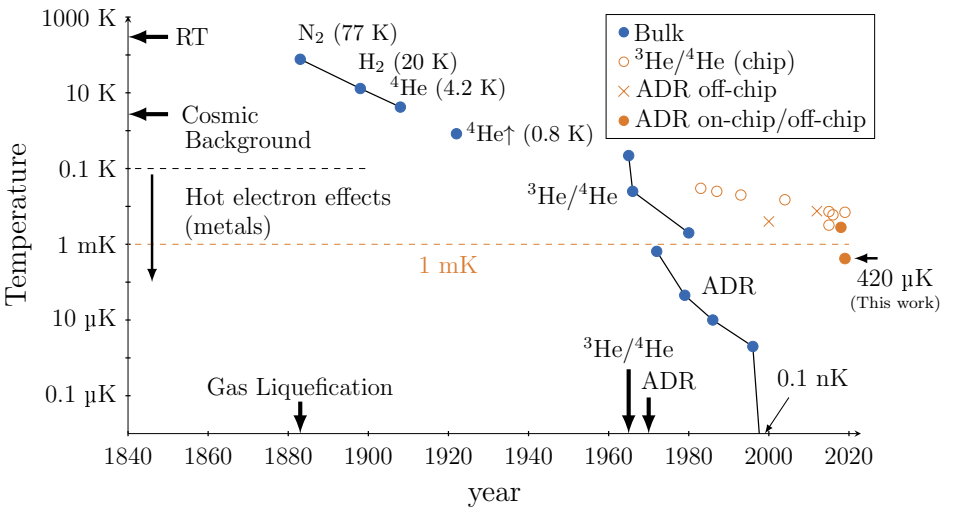


Figure 1.1: **Historical overview of the development of low-temperature techniques used for cooling solid-state materials** Temperatures reached in macroscopic solids are marked in blue, electron temperatures reached on miniaturized electronic devices are marked in orange. Abbreviations are ADR = adiabatic nuclear refrigeration (nuclear magnetic cooling), RT = room temperature. References: temperatures in bulk materials and cooling techniques [9, 37, 38], temperatures in miniaturized devices [39–49]. The marked electron temperature of 420 µK is the temperature which could be reached as a stable electron temperature in this work.

The experimental difficulties with on-chip integrated nuclear magnetic cooling have to be compared with the performance of bulk nuclear demagnetization stages, where temperatures of a few μK can be kept stable for several weeks [9, 20], provided by the enormous specific heat of nuclear moments at microkelvin temperatures. Based on a nuclear paramagnet generating cooling power out of its localized nuclear moments, the problem of implementing nuclear magnetic cooling on the chipscale can be formulated as miniaturizing the nuclear refrigerant in such a way that it can sustain a significant heat load and still provide a stable base temperature. This involves rethinking of conventional concepts, established in decades of applied nuclear magnetic cooling, in several ways.

Given that microkelvin refrigeration on a nanoelectronic device can be achieved, the next challenging problem comes up in the form of the question of how to measure the value of the electron temperature which is achieved. Since submillikelvin refrigeration of miniaturized electronics was never achieved, existing methods of nanoelectronic thermometry are also not characterized in terms of their applicability to the microkelvin regime. Many existing thermometry platforms based on mesoscopic devices loose their sensitivity at microkelvin temperatures because they work on the basis of electronic phenomena in solids which are deep in the ground state at microkelvin temperatures, as for example superconductivity in most of the materials which are commonly utilized for fabricating nanodevices. Fortunately, there was a significant development on this field during the last decades, resulting in the availability of several scalable solutions for electronic thermometry on the micro- and nanoscale [9, 55]. A technique which is well proven already in the low millikelvin temperature range [45–47] is Coulomb blockade thermometry [56, 57], which functional basis is the thermal suppression of charging in the single-electronics regime. Energy scales of charging in mesoscopic metallic structures can be tailored by device design, making Coulomb blockade thermometry the ideal candidate for exploring the microkelvin temperature range on the miniaturized scale.

In this work, the challenge of opening the microkelvin temperature regime for solid-state nanoelectronic devices is taken by realizing a nuclear magnetic cooling approach with integrated nanoelectronic thermometry. On-chip nuclear cooling is engineered to achieve a sufficient nuclear magnetic cooling power in miniaturized nuclear microrefrigerators, by enhancing the nuclear magnetization via the electric quadrupole moment of atomic nuclei instead of only the magnetic dipole moments, as in classical approaches. This novel scheme of quadrupole enhanced nuclear magnetic cooling is realized and evaluated by miniaturized In refrigerators, combined with Coulomb blockade thermometry based on $Al/AlO_x$ tunnel junction arrays. In this experimental implementation, the temperature of the conduction electrons, cooled by a nuclear spin system with defined volume integrated onto the device, is experimentally accessible. Off-chip nuclear cooling is adapted by utilizing, and further developing a novel parallel bulk stage cooling approach for cooling the device leads [47], providing a extremely low background heat leak into the electronic system of a nanodevice. Combining on- and off-chip nuclear magnetic cooling with self-calibrated Coulomb blockade thermometry, documented microkelvin refrigeration of a nanoelectronic device is achieved for the first time (see Fig. 1.1). In the following, a brief overview of the content of the work is given.

Chapter 2 provides a brief introduction of ultralow temperature cooling and thermometry of miniaturized electronic devices. The problem of thermalization of conduction electrons on the miniaturized scale is discussed and several techniques for cooling nanoelectronic devices and obtaining the electron temperature in these are introduced. The focus is put on nuclear magnetic cooling and thermally activated charging of tunnel junction arrays, being the functional basis of Coulomb blockade thermometers (CBTs).

Chapter 3 contains all methodologies developed and used for this work. These are fabrication and characterization of ULT CBTs, thick film device integration of In as nuclear refrigerant by electrochemical deposition, details of the cryogenic transport setup and construction and validation of the off-chip nuclear stage for cooling the device leads.

Chapter 4 summarizes experimental results obtained with direct nuclear demagnetization of metallic In microrefrigrators integrated onto the islands of a CBT. The experiments were performed in an otherwise unmodified, commercial dilution refrigerator.

Chapter 5 focuses on Coulomb blockade thermometry beyond the universal regime, in which junction arrays can be described with SET physics. Charging in the presence of random offset charge is studied with a Markov-chain Monte-Carlo (MCMC) algorithm, developed for this purpose. With the MCMC model it is shown that Coulomb blockade thermometry can significantly profit from the offset-charge stability of tunnel junction arrays, widening the temperature range of CBTs beyond currently postulated limits.

Chapter 6 presents results of on and off-chip nuclear cooling of a CBT with In, integrated as nuclear refrigerant onto the chip, as well as used to cool the device leads in a parallel stage configuration. With this cooling scheme, the first successful advancement into the microkelvin regime for a nanoelectronic device is achieved. Cooling of the islands of a CBT to a temperature as low as 421 μK, with temperature hold times of several days below 1 mK is demonstrated. Submillikelvin transport experiments are peformed by measuring finite bias CBT charging curves up to the Ohmic regime without observing self-heating. The latter is provided by the strong electron-nucleus coupling occuring in metallic In.

Chapter 7 gives a comprehensive study of the nuclear energy spectrum of polycrystalline In, integrated onto the islands of a CBT, with respect to the coupling of the electric quadrupole moment of In nuclei to the electric field gradient in tetragonal In. The quadrupolar coupling strength is determined by on-chip calorimetry and magnetic field cycling in the adiabatic regime and compared to previous studies. The results of this chapter implement scalable chipscale nuclear magnetic cooling and a novel scheme of quadrupole enhanced nuclear magnetic cooling of miniaturized electronic devices.

Chapter 8 finalizes the thesis by bringing the outcome of this work, a scalable microkelvin refrigeration technique with applicability to nanodevice technologies, in context with possible future implementations. Opportunities for topological quantum computation, brought by submillikelvin refrigeration, and several opportunities for mesoscopic physics in the microkelvin regime are discussed. Finally, a summary of the work is provided.

# 2

# THEORETICAL BACKGROUND

*Eine allgemeine Verknüpfung von Energie und Temperatur kann man wohl nur durch Wahrscheinlichkeitsbetrachtungen herstellen. Zwei Systeme sind in statistischem Gleichgewicht, wenn ein Transport von Energie die Wahrscheinlichkeit nicht vermehrt.*

Max Planck

## 2.1. THERMALIZATION OF CONDUCTION ELECTRONS ON THE MINIATURIZED SCALE



The challenge of cooling electronic devices with reduced dimensions to temperatures in the low millikelvin regime, and further, is marked by thermal decoupling of thermal degrees of freedom in a solid towards low temperatures. The historical view on the process of reducing the temperature of a body with defined geometry is, that reducing thermal degrees of freedom is related to reducing the amount of vibrations the atoms in this body perform around their equilibrium positions. While this picture works rather well at $T \gg 1$ K, it breaks down rather quickly towards subkelvin temperatures: The heat capacity of a metallic solid is generally expressed as $C = \gamma T + \alpha T^3$, where the linear term, $\gamma T$, covers the heat capacity of electrons and the cubic term, $\alpha T^3$, the contribution of lattice vibrations (phonons). The different temperature scalings in $C$ result from the different quantum statistics of electrons (fermions) and phonons (bosons). Localized magnetic moments, arising from particle spin, and oscillations of magnetic moments (magnons, neglected here for simplicity), also contribute to the specific heat of a solid. When the temperature is reduced far below 1 K, it is now clear that the classical means of "cooling by reducing the amount of lattice vibrations" becomes pointless, since at these temperatures the phonon contribution to the heat capacity of a solid becomes very small compared to the electronic heat capacity. This does not mean that a solid can not be cooled via lattice vibrations at cryogenic temperatures anymore; if the level of parasitic heating is low, a smaller thermal mass of phonons can still cool the electrons close to the phonon temperature, which is usually the case in macroscopic metals of the order of $V \geq \text{mm}^3$. In miniaturized electronic devices, where metallic or semiconductor volumes available for electron-phonon scattering are usually many orders of magnitude smaller, one can not assume *a priori* that phonons and electrons are at the same temperature. Nanoelectronic devices are subjected to relatively large external heat loads when driven with a bias and/or heated by parasitic heating sources on a small volume. The resulting overheating of electrons above the lattice temperature in the regime of weak electron-phonon coupling is called hot-electron effect [41].

The problem with cooling micro- and nanoelectronic devices to ultralow temperatures is that most established cooling techniques which are nowadays applied to cool these devices to millikelvin temperatures (some cooling techniques will be introduced in section 2.1) rely on cooling a non-metallic working substance, and are already operating far in the hot-electron regime. In thin-film devices, the volume can then be too small to excite a phonon state at a given temperature, and thermalization of electrons is only possible via substrate phonons extending into the thin film. The key to proceed to lower temperatures on the miniaturized scale is to find a way to couple conduction electrons better to a cold working substance, which can not only absorb the external heat load on the electron system, but can do this without warming up too quickly itself due to an insufficient heat capacity. The usual thermal situation of a thin-film nanoelectronic device is illustrated in Fig. 2.1. The electron gas in the thin-film structure is constantly heated by an external bias and by absorbing photons from the usually warmer electromagnetic environment. This heat load is transferred to the cold bath, being the substrate thermal-

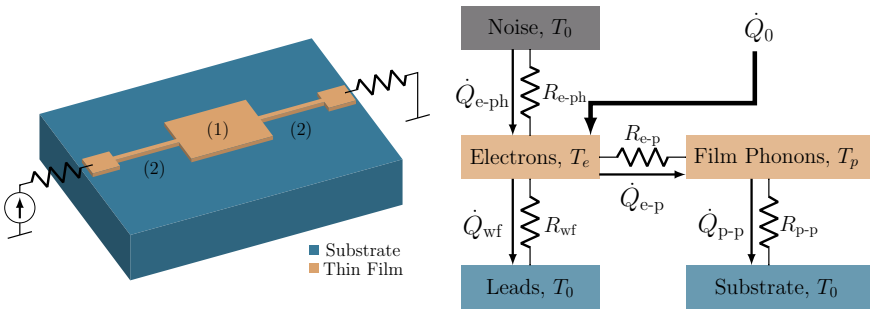


Figure 2.1: **Schematic overview of the available thermalization paths of conduction electrons in a thin-film device.** (1) Thin film device, (2) On-chip interconnects. The electron gas in the thin-film structure with reduced dimensions comes to thermal equilibrium with substrate phonons ($\dot{Q}_{\text{e-p}}$), film phonons ($\dot{Q}_{\text{p-p}}$), and with the electron temperature in the macroscopic leads ($\dot{Q}_{\text{wf}}$), while being constantly subjected to the heat load $\dot{Q}_0$.

ized with a phonon bath, by electron-phonon interaction, or via electronic heat transfer to the colder leads. Heat is carried by phonons and electrons with an additive effect on the total thermal conductivity. Thus, the thermal conductivity $\kappa$ of a conductor can be expressed by means of the electrical conductivity $\sigma$ with the Wiedemann-Franz law

$$\kappa/\sigma = L_0 T \tag{2.1}$$

with the temperature $T$ and the Lorenz number $L_0 = \pi^2 k_B^2/3e^2$. Heat relaxation via phonons becomes ineffective as more device size and temperature are reduced (see section 2.1.1). Cooling via the leads (Wiedemann-Franz cooling) is a favorable thermalization path towards low temperatures due to $\kappa \propto T$, but usually limited by finite electrical resistance (see Fig. 2.2). Significant electrical resistances of the order of $k\Omega$ can already occur at the interfaces between metallic thin films or metal-semiconductor interfaces. In the extreme limit of device miniaturization, discretization of energy states restricts the amount of available channels for heat transport. If electrical conduction is restricted to a single electronic state, the electrical conductance reaches a universal value of $2e^2/h$, setting the limit for the electronic conduction over a single electronic channel to $G_e = e^2/h$, as experimentally shown for a 1D electronic channel [58]. The Wiedemann-Franz law even holds for charge transport across a single quantum transport channel, independent of the heat carrier statistics [59–65], giving rise to the quantum of thermal conductance, $G_Q = \pi^2 k_B^2 T/3h$. This means that if an electron gas in a defined volume is thermally connected to the environment over one-dimensional interconnections, the heat flow over these interconnections is limited by the quantum of thermal conductance. Thus, in the limit extreme miniaturization, the thermal conductivity to the environment is determined by the number of quantum states, independent of their individual nature.

### 2.1.1. ABSORPTION AND EMISSION OF PHONONS

Electrons can exchange energy with the lattice by emitting or absorbing phonons. Since solids have Debye-temperatures $\Theta_D > 50$ K, optical phonons can be neglected, and assuming a linear dispersion for acoustic phonons at low temperatures is well justified. Since the speed of sound in metals is of the order of $c_s \sim$ km/s, the thermal wavelength

$\lambda_{th} = hc_s/k_B T$ can be of the order of the device size, depending on temperature. If $d \gg \lambda_p$, phonon wave packets with a characteristic frequecy dispersion, corresponding to the lattice, can be constructed inside the device and transport heat into the substrate. This means electrons relax thermal energy either by emitting phonons with wavelengths according to the thin-film lattice dispersion or the dispersion of the substrate lattice. In the first case, where the speed of sound changes over the film-substrate boundary, the refraction of phonons at the interface has to be taken into account giving rise to a finite thermal boundary resistance between electrons in the thin film and phonons in the substrate. Heat flow over the thin film-substrate interface then scales with [66, 67]

$$\dot{Q}_{\text{p-p}} = kA\left(T_p^4 - T_s^4\right), \tag{2.2}$$

$$\text{with} \quad k = \frac{\pi^2 k_B^4}{120\hbar^3} \frac{\left(c_{1L}^{-2} + 2c_{1T}^{-2}\right)\left(c_{2L}^{-2} + 2c_{2T}^{-2}\right)}{c_{1L}^{-2} + 2c_{1T}^{-2} + c_{2L}^{-2} + 2c_{2T}^{-2}} \tag{2.3}$$

where $A$ is the interface area, $T_s$ the substrate temperature and $c_{xL}$ and $c_{xT}$ the longitunal and transversal velocity of sound on either side of the film-substrate interface. If $t < \lambda_p$, the thermal resistance between the electron gas and substrate phonons is dominated by the ability of electrons to emit or absorb phonons, constructed according to the substrate phonon dispersion. In the limits of the free electron model, without dimensional discretization of the phonon density of states, the heat exchanged between phonons at temperature $T_p$ and electrons at temperature $T_e$ can be approximated as [41]

$$\dot{Q}_{\text{e-p}} = \Sigma V\left(T_e^5 - T_p^5\right) \tag{2.4}$$

$$\text{with} \quad \Sigma = \frac{8k_B^3\zeta(5)}{\pi^3\hbar^2}\left(\frac{k_F^2\gamma}{c_s^4}\right), \tag{2.5}$$

where $\zeta(x)$ is the Riemann zeta function, $\gamma = D(\varepsilon_F)\pi^2 k_B^3/3\rho$ is the Sommerfeld coefficient, $\varepsilon_F$ is the Fermi energy, $v_F$ the Fermi velocity, and $v_s$ the velocity of sound. The Sommerfeld coefficient is experimentally accessible by measuring the electronic contribution of the heat capacity $C_e = \gamma T$. Some calculated and measured values of $\Sigma$ are

Table 2.1: Collection of important material properties determining the electron-phonon coupling strength in some selected metals and calculated coupling constants $\Sigma$. The $k_F$ (calculated) are taken from [5]

| | $k_F$ ($10^{-6}$ eV s/m) | $c_s$ ($10^3$ m/s) | $\gamma$ ($10^{-3}$ J/kg K$^2$) | $\Sigma$ (Eq. 2.5) ($10^9$ W/m$^3$K$^5$) | $\Sigma$ (measured) ($10^9$ W/m$^3$K$^5$) |
|---|---|---|---|---|---|
| Al | 5.76 | 5.10 | 50.37 [68] | 0.73 | 0.2 [69],0.3 [42] |
| Cu | 4.46 | 3.57 | 10.84 [70] | 0.31 | 2.0 [42], 2.1 [67] |
| Ag | 3.94 | 2.60 | 5.98 [70] | 0.42 | 0.5 [71] |
| Au | 3.96 | 1.74 | 3.65 [70] | 1.26 | 2.4 [72] |
| In | 4.94 | 1.22 | 14.72 [73] | 41.22 | - |

collected in Tab 2.1. In general, Eq. 2.4 can not be applied if device dimensions are smaller than $\lambda_{\text{th}}$, but holds well for films extending in the substrate plane over several thermal phonon wavelengths [67]. There are models for treating electron-phonon coupling in restricted geometries [74], mainly introducing the effect of surface phonons and strain boundary conditions at the film-vacuum interface. With these models a low-temperature crossover from the $T^5$ temperature dependence in Eq. 2.4 to

$$T^5 \rightarrow -\Lambda\left(\frac{T^6}{T^*}\right)\ln\left(\frac{T}{T^*}\right) \tag{2.6}$$

is predicted. Here, $T^* = \hbar c_R / k_B d$ and $\Lambda$ (see [67] for details) are material and geometry dependent constants, with $d$ the film thickness and $c_R$ the acoustic surface phonon velocity. Experiments on low-dimensional phonon systems resulted in power laws of $T$ in $\dot{Q}_{\text{e-p}}$ with smaller exponents [75, 76]. Generally, Eq. 2.4 was successful in parameterizing the outcome of most experiments, with small deviations from the $T^5$ dependence.

### 2.1.2. ABSORPTION AND EMISSION OF PHOTONS

Thermal relaxation by emission of photons is equivalent to the emission of phonons, with the constraint that photons are not excitations of any kind of matter and can propagate through vacuum. The thermal wavelength of photons exceeds 1 cm already when passing below 1 K and thus will always exceed the dimensions of electronic micro- and nanostructures by many orders of magnitude. In order to describe the radiative coupling between an electron gas with other electronic systems, the electron gas width $d \ll \lambda$ is represented by an electrical resistance $R_e$ [62, 77]. The heat transfer between conduction electrons and the electromagnetic environment can then be represented as heat exchange between the real impedances $R_e$ and $R_u$ as thermal noise sources, at temperature $T_e$ and $T_u$ respectively. The heat $\dot{Q}_{\text{e-p}}$, exchanged between the noise sources is

$$\dot{Q}_{\text{e-ph}} = \frac{1}{2\pi}\frac{4R_eR_u}{(R_e+R_u)^2}\int_0^\infty \mathrm{d}\omega\, \hbar\omega\,[n_e(\omega) - n_u(\omega)] \tag{2.7}$$

with $n_i(\omega)$, the Bose-Einstein distribution of the reservoir $i$ with temperature $T_i$, $n_i = \left[\exp\left(\hbar\omega/k_B T_i\right) - 1\right]^{-1}$. Integration of Eq. 2.7 yields a closed form for $\dot{Q}_{\text{e-ph}}$, reading

$$\dot{Q}_{\text{e-ph}} = \frac{4R_eR_u}{(R_e+R_u)^2}\frac{\pi k_B^2}{12\hbar}\left(T_e^2 - T_u^2\right) \tag{2.8}$$

By comparing Eq. 2.8 with Eq. 2.4 one can see that for electron systems with small dimensions at $T \rightarrow 0$, heat transport via photons should dominate over heat transport via phonons, approximately scaling with $\dot{Q}_{\text{e-p}} \propto \Sigma V T_e^5$ (see Eq. 2.4). For perfect matching, $R_e = R_u$, the heat transferrred via photons is the heat conducted via one quantum of thermal conductance, $G_Q = \pi k_B^2/6\hbar$. One can define the crossover temperature [78]

$$T_{\text{Cr}} = \left(\frac{\pi^2 k_B^2}{15h\Sigma V}\right)^{1/3}, \tag{2.9}$$

below which energy exchange with the noise temperature $T_p$ becomes the dominating thermalization channel for electrons (in the absence of other degrees of freedom than phonons). For typical mesoscopic structures the crossover occurs at $T_c = 100 - 500$ mK.

### 2.1.3. THERMALIZATION VIA SPIN-SPIN INTERACTIONS

A spin mediated thermal relaxation channel for conduction electrons is the interaction with localized magnetic moments. Localized moments arise from paramagnetic ions, with a magnetic moment resulting from unpaired electrons, or from atomic nuclei, with a magnetic moment resulting from unpaired protons. Any spin Hamiltonian, with the spin operator $\mathbf{S} = [\mathbf{S}_x, \mathbf{S}_y, \mathbf{S}_z]^{\mathbf{T}}$ (For nuclear spins the spin operator is labeled as $\mathbf{I}$), has $2S+1$ discrete eigenvalues. The magnetic moment $\mu_\mathrm{B} = 57.8$ μeV/T of an electron spin is much larger than the magnetic moment of a nuclear spin with $\mu_\mathrm{n} = 31.5$ neV/T, but only nuclear spins are suited for conduction electron thermalization at millikelvin and submillikelvin temperatures, due to the large Curie temperatures (> 1 K) of metallic electronic paramagnets and quenching or delocalization of electronic magnetic moments of paramagnetic ions in host metals. Nuclear spins behave like localized magnetic moments down to extremely low temperatures (< 1 nK in most noble metals) and the nuclear spin basis always defines the direction of the magnetic moment. Thus, only nuclear spins are further discussed for electron thermalization by spin-spin scattering.

The distribution of spins onto discrete energy levels can be represented by a nuclear spin temperature $T_n$ in the framework of statistical physics. For calculating the distribution of $N$ nuclear spins onto the $2I+1$ discrete states, provided by a system with spin $I$, Boltzmann statistics can be applied and the spin temperature is defined by the partition sum

$$Z = \left[\sum_m \exp\left(-\frac{\varepsilon_m}{k_\mathrm{B} T_n}\right)\right]^N, \tag{2.10}$$

with $m$ the spin quantum number, and $\varepsilon_m$ the corresponding energy eigenvalue. The potential of the system to exchange heat is determined by its off-equilibrium state occupation, parameterized by the magnetization $M = k_\mathrm{B} T_n (\partial Z / \partial T_n)$. A finite magnetization is not necessarily caused by a magnetic field; According to the Wigner-Eckart theorem, different interaction channels, coupling to the magnetic and electric multipoles of the nucleus, are described in the same nuclear spin basis. Nevertheless, a magnetic field is still the most controllable way of experimentally altering a nuclear spin magnetization (see section 2.2.4). A nonzero magnetization gives rise to a nuclear heat capacity of

$$C_n = k_\mathrm{B} T_n \left(\frac{\partial^2 \log Z}{\partial T_n^2}\right) \tag{2.11}$$

The absolute amount of heat flowing between conduction electrons and nuclei, $\dot{Q}_\text{e-n}$, depends on the scattering rate enabled by the hyperfine interaction between electron spins and nuclear spins. The resulting decrease of the nuclear spin magnetization in time is usually expressed in form of a relaxation time approximation, given by

$$\frac{\mathrm{d}M}{\mathrm{d}t} = -\frac{M(t) - M_0}{\tau} \tag{2.12}$$

The relaxation time $\tau$ depends on the details of the spin eigenenergy spectrum and thus on the functional form of the magnetization $M$. In case of equidistant nuclear eigenenergies (Zeeman effect), the magnetization can be expressed by the Curie law $M \propto 1/T_n$,

for $k_B T_n \gg \varepsilon_m$. This allows to rewrite Eq. 2.12 in terms of the conduction electron temperature $T_e$ and the nuclear temperature $T_n$ as $\left(\dot{T}_n\right)^{-1} = (T_n^{-1} - T_e^{-1})/\tau$. The spin-lattice relaxation time $\tau$ is expressed (for $k_B T_n \gg \varepsilon_m$) by the Korringa relation $\tau = \kappa / T_e$ [79] with

$$\kappa^{-1} = \frac{256\pi^3}{9\hbar} \frac{\gamma_n^2}{\gamma_e^2} n^2 \left|\psi(0)\right|^4 \chi^2 k_B, \tag{2.13}$$



where $\gamma_n = \mu_n g_n$ and $\gamma_e = \mu_B g_e$ are the gyromagnetic ratios of nuclei and electrons, $\left|\psi(0)\right|^2$ the electron density at the position of the nucleus, and $\chi$ the free electron susceptibility. The spin temperature is evolving as $\dot{T}_n = (T_e T_n - T_n^2)/\kappa$, implying that electrons at temperature $T_e$ and nuclei at temperature $T_n$ exchange heat with the rate of $\dot{Q}_{\text{e-p}}$ with

$$\dot{Q}_{\text{e-n}} = C_n \left( \frac{T_e T_n - T_n^2}{\kappa} \right) \tag{2.14}$$

In case of non-equidistant nuclear level splitting, the linear dependence of the spin-lattice relaxation time with temperature, given by the Korringa-law, is not guaranteed anymore. In these cases the relaxation time is calculated with rate equations, assuming that the population of each spin level relaxes to thermal equilibrium, following a master equation $\dot{P}(k) = \sum_m W_{km} [P(k) - P(m)]$ [80], with $P(n)$ the probability that the level $\varepsilon_m$ is occupied, $P(k) - P(m)$, the deviation of the level populations from equilibrium values, and $W_{km}$ the transition probabilities. A signficant reduction of the spin-lattice relaxation time with non-magnetic level splitting could be observed for several metals [81]. For some other metals, a magnetic spin-lattice relaxation was also observed for systems with pure nonmagnetic level splitting. In, as an important material in this work, is an example of the latter group of metals. For In, measured rates of the dominating transitions $9/2 \rightarrow 7/2$ and $7/2 \rightarrow 5/2$ follow the Korringa-law very well in the limit of pure quadrupole splitting [82]. For most metals $\tau$ is only known in the fully magnetic limit.

By spin-lattice relaxation, conduction electrons transfer heat to magnetized nuclear magnetic moments with $\dot{Q}_{e-n} \propto T_e T_n$, to be compared to the phonon and photon thermalization channels, scaling with $\dot{Q}_{e-p} \propto T_e^5$ and $\dot{Q}_{e-ph} \propto T_e^2$. While electron-phonon scattering rates become clearly too long for efficient thermalization of miniaturized structures at submillikelvin temperatures, heat relaxation by emitting of photons has a beneficial temperature scaling with $T_e^2$, but is limited to a single quantum channel. For electron thermalization with nuclear spins there is a strong material dependence with $\kappa = 0.01 - 100$ Ks (see Tab. 2.2) for metals. Just given by the smallness of nuclear moments, the nuclear specific heat reaches values of the order of $C_n \sim$ J/mol K (see also Fig. 2.5) at temperatures well below 1 mK. For comparison, $\dot{Q}_{\text{e-p}}$ (Eq. 2.4), $\dot{Q}_{\text{e-ph}}$ (Eq. 2.8) and $\dot{Q}_{\text{e-n}}$ (Eq. 2.14) is calculated for a model system of a 100 µm × 100 µm × 0.1 µm Cu film and plotted in Fig. 2.2. The film is connected to macroscopic leads (perfectly thermalized with the substrate) via a non-ballistic contact with resistance $R_L$. The heat flow $\dot{Q}_{\text{wf}}$ over $R_L$ is calculated with the Wiedemann-Franz law (Eq. 2.1). For simplicity it is assumed that the electron gas is resistance matched to the electromagnetic environment ($R_e = R_u$) and the nuclear level splitting is adapted such that the nuclear heat capacity is maximized at a given bath temperature (see Fig. 2.5). A figure for comparing heating

and cooling powers to real systems is the parasitic heat load on the electron system, with lowest reported values into mesoscopic electron systems in well shielded structures is of the order of $10^{-18}$ W [47]. This parasitic heat load does not yet include the additional heat load due to bias. For bath temperatures ≤ 1 mK it is clear that electron-phonon, as well as electron-photon coupling is too weak to apply a sufficient cooling power to thermalize conduction electrons in a miniaturized structure. For a small electrical resistance of $R_L \leq 1\ \Omega$, connecting the electronic device to the leads, cooling powers of the order $10^{-16}$ WΩ are still reached at a bath temperature of 100 µK, making cooling over the leads

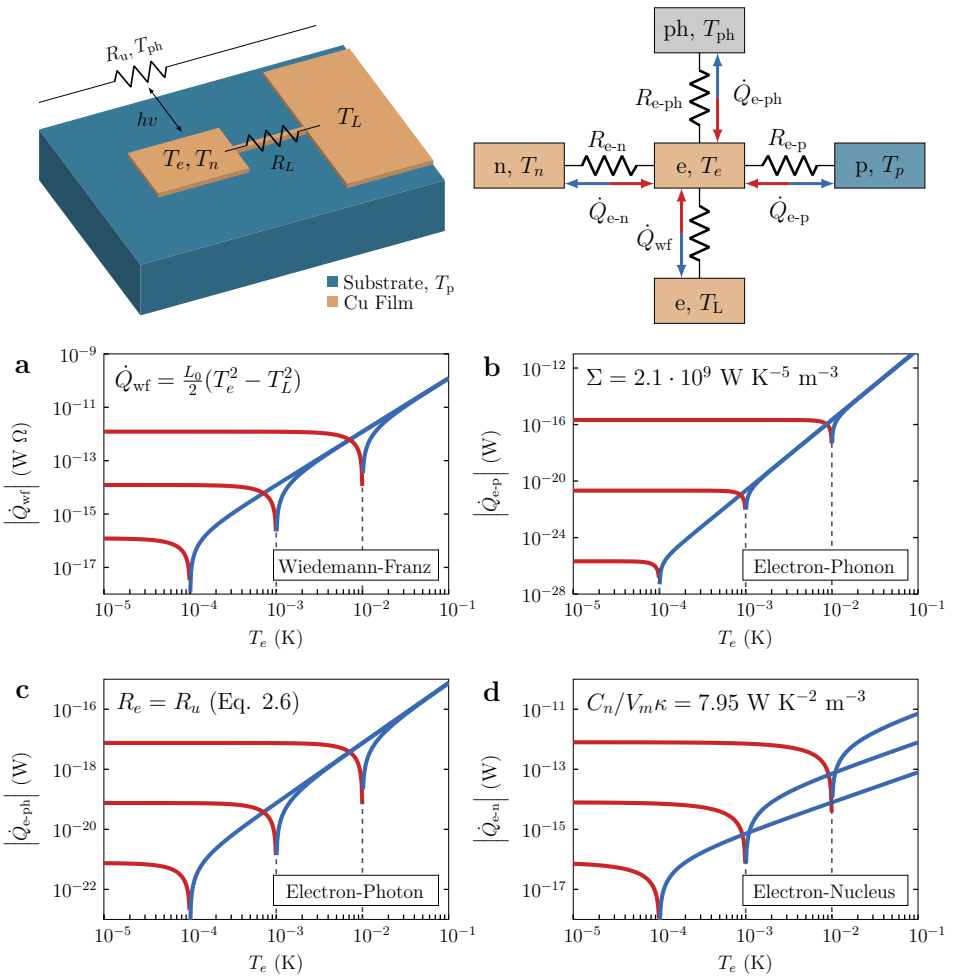


Figure 2.2: **Cooling and heating power, mediated by electron-phonon interaction, electron-photon interaction, spin-lattice relaxation, and cooling over an electrical resistance in a Cu film with defined volume.** The electron temperature is plotted against the absolute heat flow from/to phonons (**a**), photons (**b**), nuclear spins (**c**), and electrons at different bath temperatures (**d**). The bath temperatures are set to 100 µK, 1 mK and 10 mK and can be identified in all panels as those temperatures, where any cooling/heating power drops to zero.

a viable thermalization channel once $R_L$ can be sufficiently reduced. A significant submillikelvin thermalization efficiency is also found for electron-nucleus thermalization (see Fig. 2.2 d). Cu has a relatively long spin-lattice relaxation time with $\kappa = 1.2$ Ks (see Tab 2.2) and in materials with a smaller $\kappa$, conduction electrons will thermalize orders of magnitude faster with nuclear spins, increasing attainable $\dot{Q}_{\text{e-n}}$ by several orders of magnitude, enabling nuclear magnetic microkelvin refrigeration of nanoelectronics.



## 2.2. REFRIGERATION OF NANOELECTRONIC DEVICES

The lower temperature limit for cooling nanoelectronic devices with a refrigerator is usually not marked by the ability to cool a working substance to a specific temperature, but by diminishing thermal coupling between conduction electrons on the chip and the working substance (see Fig. 2.2). The finite heat conductivity between an electronic system and the refrigerator will lead to a higher electronic temperature in thermal equilibrium, once external heat input into the electron system exceeds the maximum amount of heat which can be transported from electrons to the refrigerator at the corresponding temperature. This can be overcome by finding a suitable refrigerator, characterized by a strong enough coupling to conduction electrons, which can also act as an intermediate between the main refrigerator with insufficient cooling power on the miniaturized system and the electron system itself. While the laws of thermodynamics require that any type of refrigerator runs in a cycle process, different types of cooling can be distinguished depending on the nature of this cycle process. **Continuous cooling** techniques provide a constant cooling power by mutual thermodynamic cycling and heat absorption. Examples are $^3$He/$^4$He dilution refrigerators (section 2.2.1) or thermoelectric coolers (section 2.2.2). For **Single-shot cooling**, heat absorption by the refrigerator is only possible in a specific part of the cycle process. These cooling techniques thus rely on a finite thermal budget, represented by a finite heat capacity and a time dependent cooling power. The distinction between single-shot techniques and continuous cooling techniques is not strict, meaning that any single-shot technique can in principle be turned into a continuous cooling technique. For some single-shot cooling techniques, this requires a significant technical effort. Nuclear refrigerators (section 2.2.4) for example are usually operated as single-shot refrigerators due to the large magnetic fields involved. The superconducting refrigerator introduced in section 2.2.3 operates on a very similar cycle process like a nuclear refrigerator, but can be implemented as continuous cooling technique just because the involved magnetic field can be much smaller. In the following, the most important known cooling techniques for cooling micro- and nanoelectronic devices are discussed in terms of their potential for reaching microkelvin temperatures.

### 2.2.1. $^3$HE/$^4$HE DILUTION REFRIGERATION

$^3$He/$^4$He dilution refrigeration relies on the finite solubility of $^3$He in $^4$He at zero temperature, given by the Fermi-gas property of the $^3$He isotope. By constantly admixing pure $^3$He into a diluted phase of $^3$He in $^4$He and removing it over a $^3$He concentration gradient, the positive mixing enthalpy of $^3$He and $^4$He in various concentration ranges results in cooling. Dilution refrigerators are implemented as gas networks for circulating gaseous $^3$He and condensing it before entering the liquid diluted phase, located in

the mixing chamber, while pumping the $^3$He at the end of the $^3$He concentration gradient. The cooling power obtained in the mixing chamber has to be partially spent on precooling the constantly supplied $^3$He, resulting in a continuous cooling power of [9]

$$\dot{Q}_{\mathrm{MC}} = \dot{n}\left(95\,T_{\mathrm{MX}}^2 - 11\,T_{\mathrm{EX}}^2\right), \tag{2.15}$$

in units of Watts. With the addition rate of $\dot{n}$ moles $^3$He into the diluted phase, the temperature of the $^3$He/$^4$He mixture $T_{\mathrm{MX}}$, and the temperature of $^3$He leaving the heat exchanger into the mixing chamber $T_{\mathrm{EX}}$. Towards larger $^3$He flow rates, the cooling power is limited by viscous heating, since $^3$He is not superfluid at operation conditions of a dilution refrigerator. Due to this, temperatures achieved by $^3$He, $^4$He dilution refrigerators are limited to the millikelvin regime. Usual operation temperatures are in the range of $5-500$ mK, the lowest temperatures ever reached with $^3$He/$^4$He dilution refrigeration are slightly below 2 mK [50–52]. Electron temperatures reachable on nanoelectronic devices, cooled by a dilution refrigerator, are limited by hot electron effects in the electron-phonon coupling regime (see section 2.1.1). The lowest achieved electron temperature on a nanoelectronic device with dilution refrigeration is 3.8 mK [46], at a base temperature of $\leq 2$ mK and was achieved by increasing the available volume for electron-phonon scattering on-chip by electrodeposition of thick metallic films and immersion of the chip into the $^3$He/$^4$He mixture. Due to hot-electron effects and $T_{\mathrm{MX}} > 1$ mK, dilution refrigeration is clearly inapplicable for reching the microkelvin temperature scale for thermally stable micro- and nanoelectronics. However as a continuous cooling technique at low millikelvin temperatures, dilution refrigeration can provide a low environmental temperature for a microkelvin refrigerator, e.g. a nuclear refrigerator (see section 2.2.4).

### 2.2.2. MICRO AND NANOSCALE THERMOELECTRIC COOLERS

While classical thermoelectric (Peltier) refrigeration based on semiconductor junctions is limited to temperatures far above 1 K [55], discretization and/or gapping of electronic energy spectra and charge quantization in nanodevices enabled the development of a novel various set of miniaturized thermoelectric coolers, reaching down to well below 100 mK [78] nowadays. Thermoelectric cooling in miniaturized structures is based on driving current over tunnel junctions into a reservoir with restricted density of states, such that the transport of highly energetic charge carriers is enhanced. This gives rise to a conversion of the work done by the current source, $P_{\mathrm{el}}$, to cooling power, $\dot{Q}_{\mathrm{el}}$, with efficiency $\eta = \dot{Q}_{\mathrm{el}}/P_{\mathrm{el}}$. A well studied example is cooling of a metal film over a biased metal-insulator-superconductor (NIS) junction [83, 84]. Tunneling into the gapped spectrum of the superconducting electrode cools the normal electrode, when the Fermi level in the normal electrode is shifted so far above the Fermi level in the superconductor, that tunneling from the normal electrode into the superconductor is mainly carried by states far above the Fermi-level in the normal electrode. The maximum cooling power, generated in the conduction electrons, at temperature $T_e$, of a NIS cooler is given by [55]

$$\dot{Q}_{\mathrm{el}} \approx 0.59\frac{\Delta^2}{e^2 R_t}\left(\frac{k_{\mathrm{B}}T_e}{\Delta}\right)^{\frac{3}{2}} - \frac{1}{2}\frac{\gamma_{\mathrm{D}}V_{\mathrm{opt}}^2}{R_t} \tag{2.16}$$

with the superconducting gap $\Delta$, the optimal voltage $eV_{\mathrm{opt}} \approx \Delta - 0.66k_{\mathrm{B}}T_e$, the Dynes parameter $\gamma_{\mathrm{D}}$, and the tunnel resistance $R_t$ (see Eq. 2.40). Instead of using a thin-insulator

film as tunnel barrier the Schottky barrier between a semiconductor and a metal can be used, giving rise to an S-Sm junction [85–87]. The lowest electron temperature reached with SIN coolers is 30 mK, at an environmental temperature of 150 mK [88]. Besides using superconductors with a material related gap, an asymmetry in the density of states of neighbouring metallic electrodes can also be introduced by a finite charging energy, giving rise to a Coulomb blockade refrigerator [89, 90]. Here, the effective gap is defined by the charging energy. Proposed schemes of Coulomb blockade refrigeration involve operating a SET at a bias $eV \gg k_B T_e$, with a theoretical maximum cooling power of [89]

$$\dot{Q}_{el} \approx 0.3 \frac{k_B^2 T_e^2}{e^2 R_t}, \tag{2.17}$$

when the gate charge is tuned to $n_g = \mp(k_B T_e/E_C + eV/4E_C) + 1/2$, giving rise to $\eta = k_B T_e/eV$. Other than SET cooling based on charge quantization, quantum dot cooling [91–93] relies on the restriction of electronic transport over a discrete electronic state. If an electron reservoir is connected to metallic electrodes via a quantum dot, the dot energies can be tuned such that only electrons above the Fermi level are transported out of the reservoir and electrons below the Fermi energy into the reservoir. All miniaturized scale thermoelectric cooling offer direct cooling of the electron gas by selective transport of hot electrons. However, these techniques also rely on partial conversion of an electric power into cooling power and thus require the operation at finite bias, with non-idealities like subgap currents having a severe impact on the cooling performance.

### 2.2.3. SOLID STATE REFRIGERATORS I - SUPERCONDUCTORS

Conduction electrons in several metals can be used for on-chip refrigeration due to the ability to enter the superconducting state. Upon switching, below the critical temperature $T_C$, the metal heat capacity drops from $C^N = \gamma T$ to $C^{(S)} \propto \gamma \cdot \exp(-\Delta/k_B T)$ (see also Tab. 2.1), with the supercoducting gap $\Delta$. The reduced specific heat in the superconducting state is established by the drop of the electronic entropy when states around the Fermi energy are gapped out over a distance of $2\Delta$. This allows to reduce the temperature of a superconductor from $T_i$ to $T_f = T_i^3/T_*^2$, when an adiabatic phase transition from the superconducting state to the normal state is performed. Here, $T_*^2 = \gamma_m/\beta$, and the heat capacity of phonons $\alpha T^3$. [94, 95]. The reduction of electron temperature upon entering the normal state adiabatically can be understood from the inability of the electrons to acquire an equilibrium Fermi-distribution by scattering. The cubic dependence of the final temperature on the initial temperature results from the transfer of the system from an effectively phononic heat capacity, when electron degrees of freedom are exponentially suppressed, to an electronic heat capacity, $\gamma T$, in the normal conducting state. Based on this property a superconductor can be used as working substance, cooling a metallic sample by a cycling process in which the working substance is switched between its superconducting and normal state with a magnetic field. The cycle consists of switching the working substance to superconducting whith heat flow from the metallic sample, followed by heat removal from the working substance to a wide bandgap superconductor in the second step [95]. Since it is necessary to transfer heat between two superconductors in the second step, the achievable cooling power is limited by phonon-phonon coupling, making miniaturization of a superconducting refrigerator difficult. When low enough

starting temperatures are accessible, the quasi-continuous cooling operation might be interesting to operate electronic devices at a few mK with this technique. The rather low magnetic fields necessary (compared to the magnetic cooling techniques discussed in the next section), allow the use of superconducting micromagnets, being another attractive feature of this potential cooling technique.



### 2.2.4. SOLID STATE REFRIGERATORS II - NUCLEAR COOLING

A very robust way of cooling solid matter to ultralow temperatures is magnetic cooling of its localized magnetic moments. In section 2.1.3 it was already discussed how a system of nuclear spins can effectively thermalize with conduction electrons via hyperfine coupling (electron spin magnetic moments in paramagnetic ions can be used for magnetic cooling as well, but these are disregarded here for the same reason as in section 2.1.3). Due to the weak dipolar-, and the absence of exchange coupling, the magnetization of an ensemble of nuclear spins can be manipulated with an external magnetic field down to very low temperatures, and is the only available way of refrigerating micro- and nanoelectronic devices to microkelvin temperatures in a technically feasible manner [9, 20].

A particle with only spin $I$ as degree of freedom has $2I+1$ discrete eigenergies $\varepsilon_m$, with the spin quantum number $m = -I, -I+1, ..., I$. The population of these eigenenergies for a mole of spins at a temperature $T$ is related to the molar partition function

$$Z = \left[\sum_m \exp\left(-\frac{\varepsilon_m}{k_B T_n}\right)\right]^{N_A} \tag{2.18}$$

with the Avogadro number $N_A$. The principle of magnetic cooling is that the magnetization, and thus the occupation probability, as well as the energy gapping of the energy spectrum, can be controlled with a magnetic field using the Zeeman-Effect, $\mathbf{H}_Z = -\mu_n g_n \mathbf{BI}$, with the magnetic field $\mathbf{B} = [B_x, B_y, B_z]^T$ and $\mathbf{I} = [\mathbf{I}_x, \mathbf{I}_y, \mathbf{I}_z]^T$. All thermodynamic state variables follow from $Z$ (see also Eq. 2.11). The nuclear spin entropy is

$$S = k_B \left[\frac{\partial(T_n \log Z)}{\partial T}\right]_B \tag{2.19}$$

It can be seen from 2.18 and 2.19 that in the high temperature limit $k_B T_n \gg \varepsilon_m$ and $Z \to I(I+1)$, 2.19 reduces to the Boltzmann formula $S = R\log(I(I+1))$, with the gas constant $R = k_B N_A$. Thus, either by reducing the temperature, or increasing the level splitting so far that $\partial Z/\partial T < 0$ or $\partial Z/\partial B < 0$, the spins will magnetize and reduce their entropy.

A nuclear cooling process is a thermodynamic cycle consisting of three working points and state transitions (see Fig. 2.3) of a nuclear paramagnet as the working substance (nuclear refrigerant). In step (1) a magnetic field is applied to the nuclear refrigerant, splitting the nuclear eigenenergies into $2I+1$ equidistant levels. By coupling the nuclear refrigerant to a refrigerator at temperature $T_i$, the working substance magnetizes according to $(B, T_i)$, as given by Eq. 2.18, reducing its entropy. In step (2), the nuclear working substance is thermally separated from the refrigerator at $T_i$ and the magnetic field is removed adiabatically. With this removal of the magnetic field performed isentropic, the

nuclear refrigerant can not return to its equilibrium magnetization at $B_f$ and will reduce $T_n$ accordingly to $T_f$. If the nuclear level splitting is equidistant and the demagnetization process is ideally adiabatic, the nuclear spin system will have reduced its temperature to $T_f = T_i B_f / B_i$ at $B_f$. After performing step (2), the working substance returns to its equilibrium magnetization by absorbing heat from the environment and warming up to $T_i$. Thus, cooling is limited by the finite nuclear heat capacity $C_n = T_n \partial S / \partial T_n$, making nuclear cooling a single-shot cooling technique, providing a maximum thermal budget of

$$Q_{\text{e-n}} = \int_{T_f}^{T_i} C_n \, \mathrm{d}T_n \tag{2.20}$$

The index for $Q_{\text{e-n}}$ is chosen because nuclear spins absorb heat via spin-lattice relaxation. Despite the historical notation of the term, the coupling of nuclear spins to the lattice is extremely weak and spin-lattice relaxation times observed in insulating nuclear paramagnets are of the order of weeks [9]. Spin-lattice relaxation times of the order of seconds and below are only reached in metals because the spin-lattice relaxation process is dominated by hyperfine interaction between nuclear spins and conduction electrons (see section 2.1.3), facilitating an electron-nucleus heat exchange $\dot{Q}_{\text{e-n}}$ given by Eq. 2.14.

The rather simple description of nuclear cooling with a constant $B/T$ ratio holds as long as the Zeeman interaction energy exceeds the energy scale of all nonmagnetic level splittings. With $T_n$ and $B$ surpassing specific limits, other interactions determine the nuclear heat capacity as well. Non-Zeeman coupling is caused by coupling of nuclei to each other and by coupling of nuclei to electric or magnetic fields via higher order multipole moments. Nucleus-nucleus coupling is enabled by direct magnetic dipole interactions

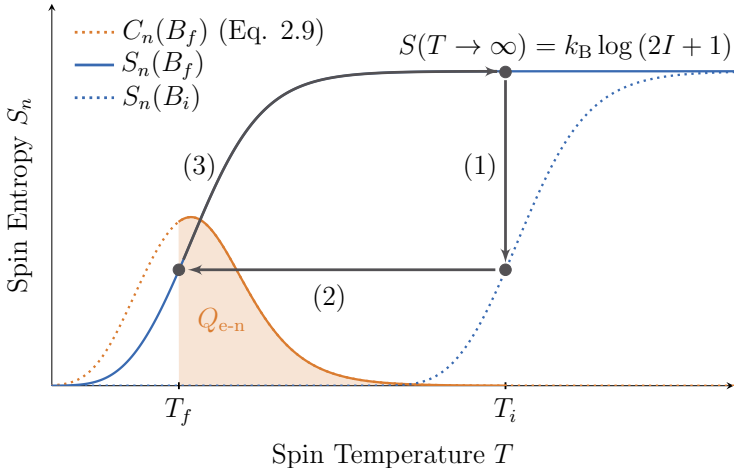


Figure 2.3: **Schematic overview of a nuclear magnetic cooling cycle.** **(1)** A nuclear spin system is magnetized in a magnetic field $B_i$, at temperature $T_i$. **(2)** The magnetic field strength is adiabatically reduced from $B_i$ to $B_f$. Ideally, the temperature drops to $T_f = T_i \cdot B_f / B_i$. **(3)** The system acquires a finite cooling power $\dot{Q}_{\text{e-n}}$ (Eq. 2.14) by returning to its equilibrium magnetization. The total amount of heat $Q_{\text{e-n}}$, which can be absorbed by the nuclear magnetic refrigerator, is obtained by integrating the nuclear heat capacity $C_n$ from $T_i$ to $T_f$.

which are extremely weak and become significant only at temperatures $T_n \ll 1\,\mu K$ [21]. Indirect coupling of nuclear spins via conduction electrons (Ruderman-Kittel interaction) is much stronger, leading to nuclear Curie temperatures of $\leq 100\,\mu K$ for metals with short spin-lattice relaxation times [21]. The only nonmagnetic contribution to the nuclear level splitting, caused by non-dipolar nuclear multipole interaction, significant in the temperature range of $\leq 1$ mK is the electric quadrupole interaction.

Nuclear quadrupole interaction occurs in nuclei with a non-isotropic charge distribution (only for $I > 1/2$), inducing a level splitting in combination with an electric field gradient. The latter occurs in solids with noncubic crystal structure, caused by an anisotropic charge distribution of valence electrons (see Fig. 2.4). The nuclear charge distribution is described by a traceless second rank tensor $\mathbf{Q}$ [96], with one symmetry axis, coinciding with the direction of the nuclear angular momentum (and magnetic dipole moment). If a basis for the nuclear magnetic dipole is defined, e.g. by an external magnetic field, this basis will automatically define the principal axes of $\mathbf{Q}$. The electric field gradient at the nucleus is described by the spatial derivatives of the electrostatic potential $V_{ij} = \partial^2 V/\partial x_i \partial x_j$. With the Laplace equation $\Delta V = 0$ and $V_{ij} = V_{ji}$, $\mathbf{V}$ can be identified as traceless and symmetric second rank tensor. The quadrupole interaction energy is classically given by the tensor scalar product of $\mathbf{Q}$ and $\mathbf{V}$ with

$$E_Q = \frac{1}{6}\sum_{ij} Q_{ij} V_{ij} \tag{2.21}$$

According to the Wigner-Eckart theorem, any nuclear state is fully described by its spin-coordinates. Consequently, there is a Hamiltonian $\mathbf{H}_Q$, proportional to $\mathbf{I} = [\mathbf{I}_x, \mathbf{I}_y, \mathbf{I}_z]^{\mathrm{T}}$ which represents the quadrupole interaction. This operator can be derived as [97]

$$\mathbf{H}_{\mathrm{Q}} = \frac{eV_{zz}Q}{4I(2I-1)}\left[3\mathbf{I}_z^2 + \eta\left(\mathbf{I}_x^2 - \mathbf{I}_{\mathbf{y}}^{\mathbf{2}}\right) - \mathbf{I}^2\right] \tag{2.22}$$

With the scalar nuclear quadrupole moment $eQ$, and $\eta$ parameterizing the anisotropy of the nuclear charge distribution in the plane normal to the principal z-axis of $\mathbf{V}$. $eV_{zz}Q/h$ is in the range of MHz to GHz for most metals (Tab. 2.2). A quadrupolar like level splitting, not caused by an electric field gradient and anisotropic nuclear charge, but by a hyperfine field, is found in nuclear paramagnets with van-Vleck paramagnetism [98]. This pseudoquadrupole interaction is equivalent to Eq. 2.22 with

$$\mathbf{H}_{\mathrm{PQ}} = \frac{A_0^2 \xi_{vv}}{2\mu_B^2 g_e^2}\left(3\mathbf{I}_z^2 - \mathbf{I}^2\right) \tag{2.23}$$

with the hyperfine energy $A_0$, and the van-Vleck susceptibility $\chi_{vv}$. The considerations regarding nonmagnetic nuclear level splitting allow to classify nuclear metallic paramagnets into several classes with respect to their nuclear magnetic properties important for nuclear cooling, and nuclear interactions with the electromagnetic environment. Pure Zeeman materials like Cu or Al have a rather long spin-lattice relaxation time in combination with either the absence of an electric field gradient (cubic crystal structure) or an isotropic nuclear charge distribution ($I = 1/2$). In these materials, the nuclear spin

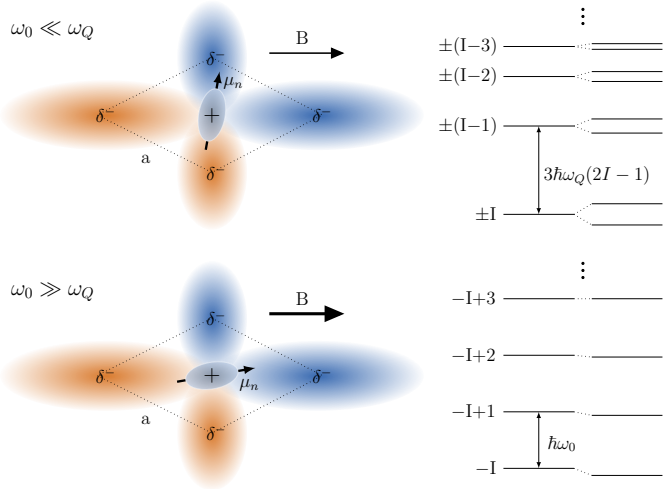


Figure 2.4: **Illustration of the mechanism leading to quadrupolar splitting of nuclear eigenenergies.** The magnetic field couples to the magnetic dipole of the nucleus, while the electric field gradient couples to its quadrupole moment. The electric field gradient $V_{zz}$ determines the nuclear spin basis in the absence of strong magnetic fields with $\omega_Q = eV_{zz}Q/\hbar$, inducing a non-equidistant nuclear level splitting. The magnetic field with strength $B$ determines the nuclear spin basis when Zeeman splitting $\hbar\omega_0 = \mu_n g_n B$ is much stronger than the quadrupole interaction energy. Thus, the level splitting is nearly equidistant in strong magnetic fields.

level spacing is equidistant down to very small fields and temperatures which allows to cool them to very low temperatures by nuclear magnetic cooling. Metals with nuclear quadrupole splitting like In, Sc, Sb, Re, Bi, or La have a large nuclear spin (large number of protons) and a non-cubic crystal symmetry, leading to a non-equidistant splitting of the nuclear eigenenergies at zero magnetic field and zero temperature. In these materials, nuclear cooling is limited to temperatures in which the population of the nuclear ground state is fully determined by the quadrupole caused energy gap between between ground state and first excited state. The nuclear specific heat of these materials at small magnetic fields and low temperatures is consequently fully determined by the quadrupole interaction energy scale. Significant van-Vleck paramagnetism occurs in intermetallics of Lanthanoids, as for example in the $Pr^{3+}$ ion (Tab. 2.2). Besides pseudo-quadrupolar level splitting, these materials show a strongly enhanced Zeeman splitting according to $\omega_0(1+K)$, with both effects caused by the admixture of electronic magnetic moments to the nuclear magnetic moments. This makes van-Vleck paramagnets extremely powerful nuclear refrigerants, since the nuclear spin entropy can be removed at much higher temperatures than for ordinary metallic nuclear refrigerants (Fig. 2.5 a).

The cooling performance of a nuclear refrigerant can be parameterized by calculating the nuclear entropy $S_n$ and the specific heat $C_n$ as a function of magnetic field and temperature (Fig. 2.5). Materials with pure Zeeman splitting loose their cooling power if the external magnetic field is completely removed upon nuclear demagnetization. Materials with nonmagnetic spin-splitting retain a finite cooling power at a temperature according

Table 2.2: **Material properties important for nuclear magnetic cooling of some selected materials.** Natural abundance in %, nuclear spin $I$, nuclear g-factor $g_n$, Korringa constant $\kappa$ (see Eq. 2.13), average nuclear quadrupole level splitting $\langle \hbar\omega_Q / k_B \rangle$, critical magnetic field $B_c$ for a superconducting phase transition. The magnetic field enhancement factors for the van-Vleck intermetallics are $K = 14.1$ ($PrNi_5$) and $K = 6.7$ ($PrIn_3$)

| | Ab. (%) | I | $g_n$ | $\kappa$ (Ks) | $\langle \hbar\omega_Q / k_B \rangle$ (mK) | $B_c$ (mT) |
|---|---|---|---|---|---|---|
| $^{27}$Al | 100.0 | 5/2 | 1.59 | 1.80 [9], 1.89 [99] | - | 10 |
| $^{45}$Sc | 100.0 | 7/2 | 1.36 | 0.090 [81], 0.014 [100] | 0.012-0.014 [101, 102] | - |
| $^{63}$Cu | 69.2 | 3/2 | 1.48 | 1.27 [9], 1.06 [99] | - | - |
| $^{65}$Cu | 30.8 | 3/2 | 1.59 | 1.09 [9] | - | - |
| $^{113}$In | 4.3 | 9/2 | 1.23 | 0.084 [80], 0.086 [82] | 0.22 [103] | 28 |
| $^{115}$In | 95.7 | 9/2 | 1.23 | 0.084 [80], 0.086 [82] | 0.22-0.23 [103, 104] | 28 |
| $^{121}$Sb | 57.2 | 5/2 | 1.35 | 1.60 [105] | 0.83[106] | - |
| $^{123}$Sb | 42.8 | 7/2 | 0.73 | 1.60 [105] | 0.67 [106] | - |
| $^{139}$La | 99.9 | 7/2 | 0.80 | 0.52 [107] | 0.024 [107] | - |
| $^{181}$Ta | 99.9 | 7/2 | 0.68 | 0.029 [108] | 2.6 [109] | 90 |
| $^{185}$Re | 37.4 | 5/2 | 1.28 | 0.03 [109], 0.38 [110] | 2.9 [109] | 20 |
| $^{187}$Re | 62.6 | 5/2 | 1.29 | 0.03 [109], 0.38 [110] | 2.7-2.8 [109, 111] | 20 |
| $^{207}$Bi | 100.0 | 9/2 | 0.91 | >100 [112] | 0.26 [113] | 90 |
| $AuIn_2$ | - | 9/2 | 1.23 | 0.11 [9] | - | 1.5 |
| $PrNi_5$ | - | 5/2 | 1.71 | 0.0003 [114] | 0.26 [98] | - |
| $PrIn_3$ | - | 5/2 | 1.71 | n.a. | 0.90 [115] | - |

to the energy scale of the nonmagnetic splitting when the field is removed. However, the operating temperature is also limited to this temperature range which is why materials with nuclear quadrupole interaction are usually not considered for nuclear cooling.

The latter is normally performed in nuclear refrigerators, consisting of a few moles of a metallic nuclear paramagnet, a superconducting magnet and a heat switch. For reaching temperatures sufficient for nuclear magnetization in the starting field $B_i$, the nuclear refrigerant is mounted as second cooling stage to a dilution refrigerator. Thermal contact to the dilution refrigerator is regulated with the heat switch, usually a superconductor which can be switched with a second solenoid. Detailed descriptions of nuclear refrigerators, reaching temperatures well below 100 µK in the working substance, can be found in the literature [116–122]. As refrigerant of choice, Cu is established for several decades due to the combination of large thermal conductivity, benefecial metallurgical properties, and a very low nuclear Curie temperature < 1 µK, enabled by a relatively long spin-lattice relaxation time. Some nuclear refrigerators contain a second $PrNi_5$ stage for precooling the main Cu stage to temperatures which would be beyond reach for a dilution refrigerator. With these systems, stable base temperatures of down to 1 µK in the Cu stage were obtained [9]. There has been some effort to use the microkelvin cooling capability, provided by nuclear refrigerators, for nanoelectronic devices. In first attempts, chips were just mounted on bulk nuclear cooling stages. In these experiments

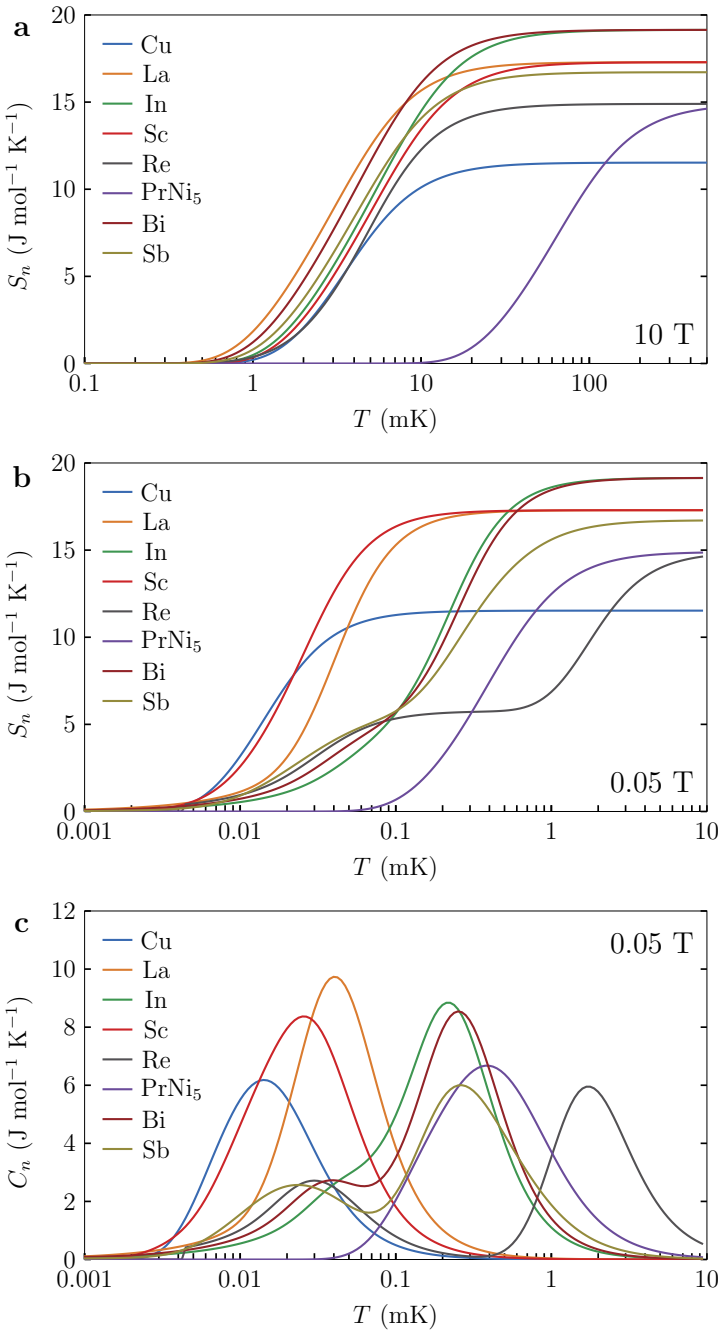


Figure 2.5: **Nuclear entropy $S_n$ and nuclear heat capacity $C_n$ of some metallic nuclear paramagnets.** **a** High field nuclear entropy (Eq. 2.19), in which the nuclear level splitting is fully determined by the Zeeman effect, with a very small nonmagnetic correction. **b** Low field nuclear entropy $S_n$ (Eq. 2.19), in which the nuclear level splitting is mostly affected by nuclear quadrupole splitting. **c** Low field nuclear heat capacity $C_n$ (Eq. 2.11), showing the optimal operation temperature in nuclear cooling as temperature where the specific heat peaks.

it was found that the electrons stay at a significantly higher temperature than the nuclear stage, as warm as ~10 mK, while the nuclear stage was cooled to well below 1 mK [44]. These results were not surprising, since the obstacle of weak electron-phonon interaction in miniaturized structures is not solved in such a way. In recent attempts, methods of miniaturization of the nuclear refrigerant and device integration as film material were employed [45, 47]. The principle of these techniques is the coupling of conduction electrons in the device effectively to the nuclear spin system by bringing both into galvanic contact. This way the electrons on the chip are directly cooled by the nuclei via spin-lattice relaxation (see Fig. 2.6 and section 2.1.3). Integrating Cu as nuclear refrigerant on-chip and performing the nuclear magnetic cooling process [45] allowed to cool conduction electrons on a nanoelectronic device well below the mixing chamber temperature, reaching 4.9 mK on a short timescale, limited by a large electronic heat leak which depleted the nuclear heat capacity before finishing the demagnetization. Nuclear magnetic cooling of the leads of the chip with individually heat switched Cu stages, additionally to integrating Cu nuclear refrigerant on chip (on- and off chip nuclear cooling), resulted in a reduction of the electronic heat leak to the order of aW, and a record electron temperature as low as 2.8 mK could be demonstrated, with $T_e < 3$ mK on the timescale of 1 h. [47]. The key to optimize the on-chip nuclear cooling efficiency, in terms of reaching long temperature hold times and low electron temperatures, is to maximize the on-chip integrated nuclear cooling power. By looking at Tab. 2.2 and Fig. 2.5 it is obvious that Cu with its small nuclear magnetic moment and long spin-lattice relaxation time is not the most appropriate choice for this purpose anymore. Furthermore, the absence of non-magnetic spin-splitting, being a benefit for reaching sub-100 µK temperatures in macroscopic stages, can turn into a severe drawback when only small amounts of nuclear refrigerant are available (as in thin film materials). At small magnetic fields, the magnetic nuclear heat capacity becomes very small to the diminishing Zeeman gaps between the nuclear eigenenergies. If an on-chip nuclear microrefrigerator is to be operated between 100 µK and 1 mK, In seems to be the most appropriate choice because its nuclear heat capacity is just forced to this temperature regime by electric nuclear quadrupole coupling. Furthermore, the Korringa constant is relatively short and the nuclear magnetic

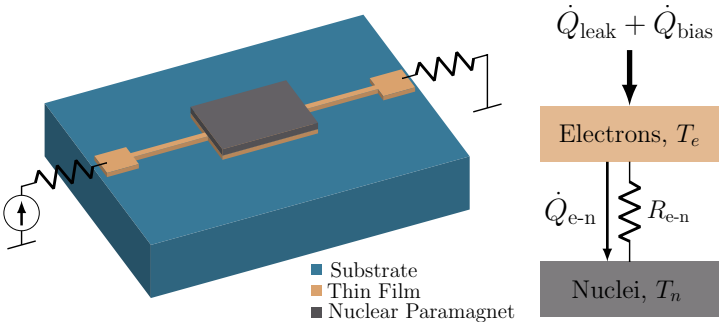


Figure 2.6: **Illustration of the principle of on-chip nuclear magnetic cooling.** A thin film consisting of a metallic nuclear magnetic material is in galvanic contact with the (thin film) device which is going to be cooled. The conduction electrons in the device can transfer heat into the nuclei of the refrigerant via spin-lattice relaxation.

moment is one of the largest of all elemental nuclear paramagnets. Other metals like Bi and Sb, as well as the intermetallic $PrNi_5$ fall into the same category. However, Bi and Sb have an even weaker electron nucleus coupling than Cu, while $PrNi_5$, despite the extremely short spin-lattice relaxation time would be extremely challenging to prepare as a thin-film material with sufficient quality. For reaching nanoelectronic temperatures even lower than 100 µK, materials like Sc or La become interesting.



## 2.3. ELECTRON THERMOMETRY ON THE MINIATURIZED SCALE

A wide variety of low-temperature thermometry techniques for the study of matter under extreme conditions was developed over the last centuries [9, 37, 38], with only few of these suited for measuring the electron temperature of nanodevices. In the latter, the coupling of electrons to other thermal degrees of freedom of the system can be so small that the electrons are thermally too well shielded from the thermometer. If for example a chip, containing a nanoelectronic device, is immersed into a liquid bath of $^3$He or $^4$He, there are many techniques to measure the He temperature down to extremely low temperatures, but the electron temperature on-chip can be completely different, due to the weak electron-phonon coupling towards ultralow temperatures. Thus, it becomes necessary to infer the electron temperature from an electronic transport feature which us as directly as possible related to the thermal distribution of electrons on energy states, described by Fermi-Dirac statistics (Eq. 2.37). The sensitivity of the temperature sensor needs to have an equivalent scaling towards ultralow temperatures and should not suffer from system parameters which are hard to control. This is best realized by primary thermometry techniques, in which temperature is related to one measurable quantity and natural constants otherwise [9]. Several primary nanoelectronic thermometry techniques are introduced in the following and discussed with respect to their applicability to nanoelectronic thermometry in the microkelvin temperature regime.

### 2.3.1. HYBRID JUNCTION THERMOMETRY

The usual implementation of hybrid junction thermometry is to connect a metal electrode over a tunnel junction with a material having a gapped energy spectrum (like a semiconductor or superconductor). If such a junction is biased with a voltage of the order of the gap, the measured current should have a well defined temperature dependence, only depending on the amount of occupied states above the Fermi-level in the metal. Due to smaller gaps, superconductors are usually better suited than semiconductors for hybrid junction thermometry at ultralow temperatures. The temperature dependent current over a NIS (see section 2.2.2) junction can be expressed by

$$I = \frac{1}{2eR_t}\int_{-\infty}^{\infty} \mathrm{d}E\, N_S(E)\left[f_N(E-eV) - f_N(E+eV)\right] \tag{2.24}$$

With the Fermi-distribution in the normal metal $f_N(E)$, given by Eq. 2.37, and the density of states in the superconductor, which can be approximated by $N_S(E) = E/\sqrt{E^2-\Delta^2}$, for $E \geq \Delta$ and $N_S(E) = 0$ otherwise. For $eV < \Delta$, Eq. 2.24 can be written in the form of [40]

$$I \approx I_0 \exp\left[\frac{-(\Delta - eV)}{k_\mathrm{B} T_N}\right] + \frac{\gamma_D V}{R_t\left(1-(eV/\Delta)^2\right)} \tag{2.25}$$

With the Dynes parameter $\gamma_D$. Thermometry based on measuring the current through a tunnel junction, separating a normal metal and a superconductor, was first realized by Rowell and Tsui [123], and more recently demonstrated to provide accurate electron thermometry down to 7 mK [40]. The temperature range of NIS thermometry is likely limited to temperatures > 1 mK, due to exponential suppression of quasiparticle current towards low temperatures, in combination with a sensitivity to non-idealities in the density of states inside the the gap. Hybrid junction thermometry with reduced self-heating can be realized by zero-bias operation in proximitized metal - superconductor junctions, in which a zero-bias anomaly was shown to have a defined temperature scaling [124].

### 2.3.2. QUANTUM DOT THERMOMETRY

If an electron reservoir is connected to a quantum dot, thermometry is enabled due to the possibility to restrict charge carrier transmission through the quantum dot to a single electronic state. If a voltage bias $eV$ is applied over a dot, connecting to electron reservoirs at temperature $T_S$ and $T_D$, the transmission coeffcient will ideally just depend on the probability to find a filled state in the source electrode and an empty state in the drain electrode, according to $f_S(E_0)(1-f_D(E_0))$, with $f(E)$ the Fermi-Dirac distribution (Eq. 2.37), and the dot level tuned to $E_0$. Idealized here means that the tunnel coupling of the dot to the reservoirs is weak enough that the energy uncertainty due to the limited lifetime of the dot state is much narrower than the thermal energy of the reservoirs. If this condition is met, a very elegant way of primary electron thermometry is enabled, because the voltage bias can be increased so far that the chemical potential difference of the reservoirs exceeds the thermal energy, $\mu_S - \mu_D = k_B T_S + k_B T_D$, and the transmission through the dot level enables mapping the Fermi-Dirac distributions of both reservoirs separately. The current through the dot can be written as [125]

$$I(V_G) = I_1 \left[ \exp\left( \frac{\mu_S - E_0}{k_B T} \right) \right] + I_0 \tag{2.26}$$

With the offset current $I_0$ and step height $I_1$ (see Fig. 2.7). To avoid self heating of the sensor, the drain can be replaced by a charge sensor, capacitively coupled to the dot. If the temperature of the reservoirs is approximately equal, $T_S \approx T_D$, the reservoir temperature is accessible by extracting the temperature due to thermal broadening of the conductance peak in the Coulomb resonance regime. In off-resonance, the tunnel conductance through the dot will be exponentially suppressed while on-resonance (isoenergetic tunneling) the dot has a linear I-V characteristics, with a conductance according to [126]

$$G = \frac{G_0}{\cosh^2 (E_0 - \mu_D)/2k_B T} \tag{2.27}$$

With $G_0 = Ae^2/h$, with $A$ depending on the transmission coefficient. By referencing the tunnel conductance to the large offset bias conductance $G_t$, and measuring the differential conductance in a small window around zero bias, reveals the temperature of the leads. Quantum dot thermometry was implemented by several groups in the temperature range $50-300$ mK [127–129] and used to determine electron temperatures down to 10 mK [125] and recently slightly below 7 mK [48]. A great aspect of this way of electron thermometry is that, as long as the level splitting in the dot is large enough, the sensor

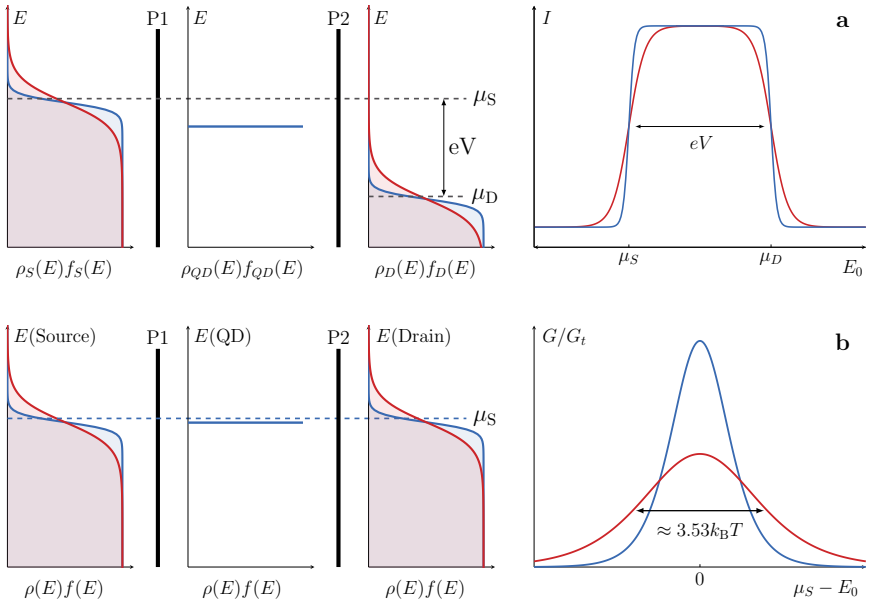


Figure 2.7: **Different implementations of quantum dot thermometry. a** Tunnel spectroscopy of the Fermi distribution in the leads by applying a voltage bias $eV > k_B T_e$ and sweeping the (sufficiently sharp) dot level with a gate, resulting in a measured current described by Eq. 2.26. **b** At $eV \ll k_B T_e$, the electron temperature can be deduced from the resonant tunneling conductance peak around zero bias, given by Eq. 2.27.

will be solely sensitive to the temperature of the leads. This in turn also imposes a sensitivity to voltage noise and charge noise on the system. By measuring the conductance peak thermometry below 1 mK electron temperature should be in principle possible.

### 2.3.3. SHOT NOISE OF COHERENT CONDUCTORS

The current noise of a quantum coherent conductor is a combination of Johnson-Nyquist noise and shot noise. While Johnson noise is usually hard to measure towards lower temperatures, shot noise offers an attractive thermometry method due to its temperature and frequency independence [130, 131]. For small bias voltage, noise is dominated by Johnson-noise, $S_I = 4k_B T/R$, while for $eV \gg k_B T$, the spectral density of the current noise should be linear in $V$ according to $S_I = 2eI$. The spectral density of the current fluctuations $S_I(V)$ for $n$ quantum channels, with conductance $1/R = 2e^2/h$ and transmission coefficient $T_n$, can be expressed as

$$S_I(V) = \frac{2e^2}{h} \sum_n T_n(1-T_n) \left[ eV \coth\left(\frac{eV}{2k_B T}\right) - 2k_B T \right] + S_I(0) \tag{2.28}$$

The accurate measurement of the noise spectral density requires a quite large amplification. By utilizing cryogenic amplification schemes, electron temperatures down to 6 mK could already be measured with high precision [131]. However, the rather severe requirements to the electronic setup make other comparable thermometry techniques, requiring less effort at similar or higher temperature accuracy, attractive.

### 2.3.4. THERMOMETRY WITH ARRAYS OF TUNNEL JUNCTIONS (COULOMB-BLOCKADE THERMOMETRY)

Other than for a single NIN junction, the current through a series of $n > 1$ tunnel junctions is expected to have a pronounced temperature dependence, due to the finite charging energy $E_C$ of the islands, enclosed by the junctions. $E_C$ corresponds to an energy scale which tunneling charge carriers have to overcome, either due to bias, or thermal energy. The attractiveness of such a thermometry technique is, that the capacitance of similar metallic islands is the only parameter setting the accessible temperature scale, if one operates in the limits of the orthodox theory (see section 2.4.1). In the validity limits of the latter, the thermal response of the device can be modeled in the well established and studied framework of computational single-electronics. Electron thermometry based on temperature dependent charging in single electronic circuits was first proposed and demonstrated by Pekola et al. in 1994 [56], and implemented various times.

The key feature of Coulomb blockade thermometry is the universal charging behaviour of tunnel junction arrays. If $k_B T$ stays above a defined fraction of $E_C$ [132], the temperature dependent conductance of a series array of $n$ tunnel junctions, biased with voltage $V_0$, behaves like a single electron transistor (SET), with an effective charging energy of $E_C = e^2/C_\Sigma \times (n-1)/n$ (see Eq. 5.5) and an applied bias of $V_0/n$ . This implies that the zero bias tunnel conductance as a function of $k_B T/E_C$ is invariant to $n$ in the universal regime. The universal behaviour of junction arrays allows to describe a series of $1 \times n$ tunnel junctions like a SET, for which the accessible system configurations are given by the number of excess charges on the island. The system can then be described in a simple way with a master equation, because $\mathbf{\Gamma}$ (Eq. 2.44) takes a block diagonal form with

$$\frac{\mathrm{d}P_k}{\mathrm{d}t} = -\Gamma_{k,(k-1)}P_{(k-1)} + \left(\Gamma_{(k-1),k} + \Gamma_{(k+1),k}\right)P_k - \Gamma_{k,(k+1)}P_{(k+1)} \tag{2.29}$$

where $\Gamma_{k,(k\pm1)}$ denotes the tunneling rate with which the system is evolving from the state of $k$ charges on the island to $k\pm1$ charges, and $P_k$ the probability to find the system with $k$ charges. The tunneling rates can be expressed by (see inset of Fig. 2.8 b for details)

$$\Gamma_{k,(k\pm1)} = \Gamma_1^{\pm}(k) + \Gamma_2^{\mp}(k), \qquad \Gamma_{(k\pm1),k} = \Gamma_1^{\mp}(k\pm1) + \Gamma_2^{\pm}(k\pm1) \tag{2.30}$$

The tunneling rates according to Eq. 2.30 are the tunneling rates defined with the orthodox theory (Eq. 2.41) with $\Delta F = e^2(k\pm1)^2/2C_\Sigma - e^2k^2/2C_\Sigma \pm eV_0/2$. The nonlinear increase of the electrostatic free energy $\Delta F$ with excess charge $k$ allows to introduce a cut-off charge number $N_{\max}$. The current through the array of tunnel junctions is then

$$I = e\sum_{k=0}^{N_{\max}} P(k)\left[\Gamma^+(k) - \Gamma^-(k)\right] \tag{2.31}$$

The probabilities $P(k)$, of finding the system at a specific excess charge, can be calculated by solving Eq. 2.29 for the tunneling rates in the steady state, when $\mathrm{d}P_k/\mathrm{d}t = 0$ (a single matrix operation for a SET). Numerical results for the differential tunnel conductance of a tunnel junction array with $n$ junctions in series are shown in Fig. 2.8, where the zero-bias tunnel conductance and the finite bias tunnel conductance of a tunnel junction

array with $n$ junctions is plotted at different electron temperatures. The lower temperature limit of the universal regime is defined as the temperature where $u = 2E_C/k_B$ (see Fig. 2.8) can not be mapped to a single conductance, when offset-charge on the device is taken into account [132]. Here, it is only possible to evaluate the system with a single offset charge, modelling single-electron tunneling between islands with different offset charges is beyond the capabilities of a master equation description (see chapter 5 for details).

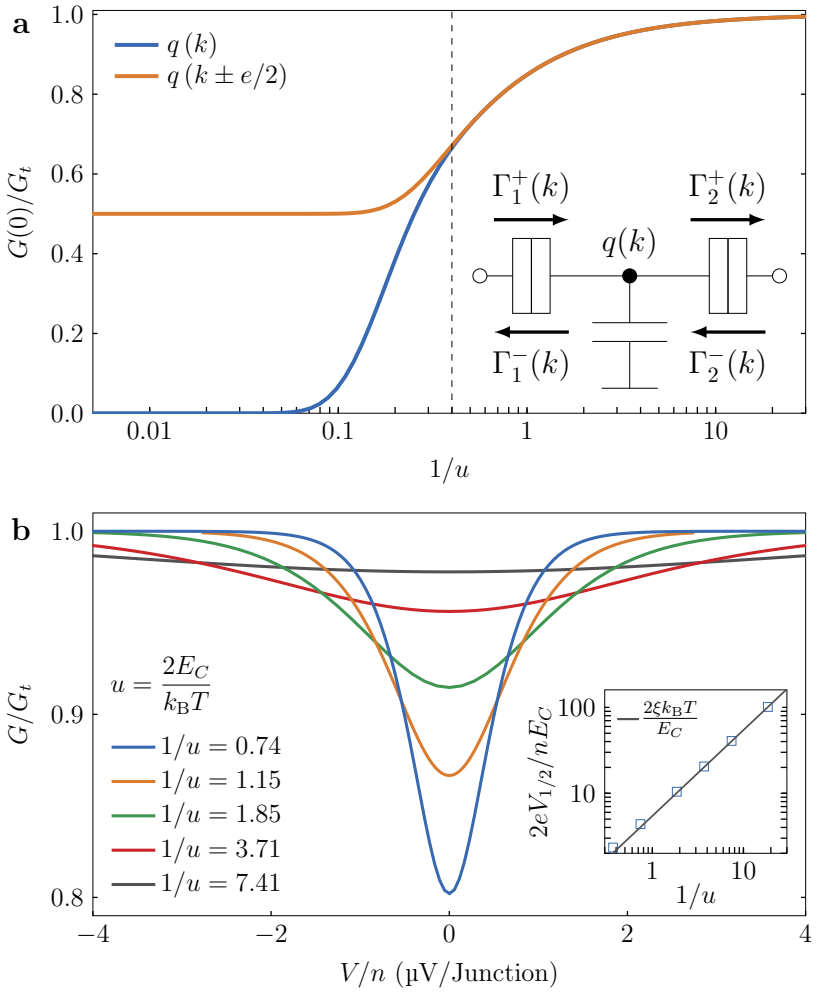


Figure 2.8: **Differential conductance of a CBT, calculated with the SET master equation tunneling model. a** Normalized zero bias tunnel conductance $G(0)/G_t$, plotted against the dimensionless temperature $1/u$, for zero offset charge, and $\pm e/2$ offset charge. The ohmic tunnel conductance is $G_t = 1/nR_t$. The inset schows a SET with the possible tunneling rates for charging the SET according to Eq. 2.30. **b** Full bias charging curves at different temperatures $1/u$, plotted against bias voltage $V/n$. Inset: full width at half maximum, scaled with the charging energy, $2eV_{1/2}/nE_C$, with $\xi \approx 5.44$, plotted against dimensionless temperature $1/u$.

The inset of Fig. 2.8 b shows another key feature of CBTs, being the linear scaling of the full width at half maximum $V_{1/2}$ in the temperature range $k_B T \geq E_C$. It can indeed be shown, by expanding the tunneling rates $\Gamma_i^{\pm}(k)$ in the high temperature limit [56], that here one obtains a primary thermometer in which $V_{1/2}$ scales only with the number of junctions in series $n$ and the electron temperature $T_e$, besides natural constants with

$$eV_{1/2} \approx 5.44 n k_B T \tag{2.32}$$

For $k_B T_e \leq E_C$, Eq. 2.32 is an overestimation of the electron temperature (see inset of Fig. 2.8 b). In this regime, thermometry is performed by calibrating the device with $E_C$, obtained from a series of charging curves. With known $E_C$, an equivalent high temperature approximation of the zero bias tunnel conductance $G(V)/G_t$ can be used, reading [56]

$$G(V)/G_t = 1 - \frac{E_C}{k_B T} g\left(\frac{eV}{n k_B T}\right) \tag{2.33}$$

with $g(x) = \left[x \sinh x - 4 \sinh^2(x/2)\right] / \left[8 \sinh^4(x/2)\right]$. Thus, CBTs are primary down to the limit of $k_B T \approx E_C$ and self-calibrated secondary thermomers at $k_B T_e < E_C$ (With small self-heating due to zero bias operation). This behaviour was confirmed in numerous experiments [42, 44–47, 57, 69, 132–137]. Conditions for CBTs, working in the universal regime, have to be met according to the assumptions made in the orthodox theory of tunneling. The eigenenergy spacing in the islands should be smaller than $k_B T$ and the tunnel resistance has to be set far above $R_Q$ (Eq. 2.42) to avoid cotunneling and electron delocalization. These conditions harmonize well with device considerations for making a CBT for the ultralow temperature range, since increasing the island volume goes along well with decreasing the charging energy. CBTs are much more stable against against noise sources due the large energy which charge carriers have to overcome, to tunnel across a long array of tunnel junctions. The islands are shielded from noise sources by the high impedance environment enabled by neighbouring tunnel junctions. The signal to noise ratio of the zero bias tunnel resistance increases towards lower temperatures due to a stronger charging effect, while narrowing of the charging peak towards further cooling can be counterbalanced by increasing $n$, which in turn brings the device further into the single electronics regime by suppressing cotunneling. These features make CBTs ideal thermometers for exploring the microkelvin regime for nanoelectronics.

CBTs might even be more versatile than predicted with the usually applied SET models. To current knowledge it is postulated that the universal regime is limited with the thermal energy surpassing $1/u \sim 0.4$ [132]. For smaller thermal energies it is expected that random offset-charges modulate the transmittance of the device in a way which does not allow a prediction with the SET master equation anymore (See Fig. 2.8). However, this limit was calculated using the SET master equation and a SET is well known to be very sensitive to random offset-charges. CBTs are usually realized by arrays of the order of $10-100$ junctions which should give the system a decent insensitivity to randomization of the tunnel current by varying offset charges on the islands. Thus, the usually postulated temperature range of two-decades might even be an underestimation of the real capabilities of those devices. To explore the limits of the universal regime, the SET master equation is not sufficient anymore but stochastic models, involving random offset charge on the islands, have to be utilized. This is done in chapter 5 of this work.

## 2.4. SINGLE ELECTRONIC CIRCUITS

In this section, a thermodynamic description of tunneling through a potential barrier is introduced, giving rise to the orthodox theory of tunneling [138, 139]. The orthodox tunneling theory defines the boundary conditions of the single-electronics regime and enables relatively simple stochastic (numerical) evaluation methods for single electroic circuits. The concepts in this section serve as a basis to understand the tunnel junction thermometry introduced in section 2.3.4, as well as a basis for the numerical description of single electronic circuits which are fabricated and characterized as part of this work.



### 2.4.1. ORTHODOX THEORY OF TUNNELING

Electron tunneling describes the coherent transport of an electron through a potential barrier, when the barrier height exceeds the kinetic energy of the electron. The basis of the orthodox tunneling theory is to derive tunneling rates of single charge tunneling events from the changes of the thermodynamic state variables like the electrostatic energy of the circuit [138]. The Helmholtz free energy of an such a system is given by

$$\mathrm{d}F = \mathrm{d}U - S\mathrm{d}T - \mathrm{d}W \tag{2.34}$$

With $U, S, W$ the internal energy, entropy, and work done by the voltage sources respectively. The free energy change $\Delta F - F_f - F_i$, accompanying the isothermal tunneling of a charge from energy $E_i$ to $E_j$, equals the change of the electrostatic energy with the total differential $\mathrm{d}F = \mathrm{d}U - \mathrm{d}W$. The tunneling rate is given by Fermi's golden rule as

$$\Gamma_{i\to j} = \frac{2\pi}{\hbar}\left|T_{ij}\right|^2 \partial(E_i - E_j - \Delta F) \tag{2.35}$$

$T_{ij}$ is the tunnel transmission coefficient from state $i$ to state $j$. The change of electrostatic energy $\Delta E = E_f - E_i$ compensates the change in free energy. Consequently, the total tunnel rate from filled states one side of the tunnel barrier to unoccupied states on the other side can be calculated by summing over all momenta $k_i$ and $k_f$

$$\Gamma = \frac{2\pi}{\hbar}\sum_i\sum_j \left|T_{ij}\right|^2 f(E_i)\left(1 - f(E_j)\right)\partial(E_i - E_j - \Delta F) \tag{2.36}$$

$f(E_i)$ is the probability of finding the state with $E_i$ occupied, while $1 - f(E_j)$ is the probability of finding the state with $E_j$ unoccupied. $f(E)$ is the Fermi-Dirac distribution

$$f(E) = \frac{1}{1 + \exp\left(\frac{E - E_F}{k_B T}\right)} \tag{2.37}$$

Neglecting the energy dependence of the transmission coefficient, $T_{ij} = T$, and introducing the density of states $D(E)$, the sums in Eq. 2.36 can be converted integrals with

$$\Gamma = \frac{2\pi}{\hbar}T^2 \int_{E_{c,i}}^{\infty} \mathrm{d}E_i \int_{E_{c,j}}^{\infty} \mathrm{d}E_j D_i(E_i) D_j(E_j) f(E_i)\left[1 - f(E_j)\right]\partial(E_j - E_i - \Delta F) \tag{2.38}$$

The product $f(E_i)\left[1 - f(E_j)\right]$ as a function of energy defines a narrow window around the Fermi-energy, becoming rectangular towards cryogenic temperatures (see Fig. 2.9).

When finite tunneling rates are only occuring in this narrow energy window, the densities of states $D_i$ and $D_j$ can be taken as constants too, given that the temperature is sufficiently low. The delta distribution eliminates one of the integrands, resulting in

$$\Gamma = \frac{2\pi}{\hbar} T^2 D_i D_f \int_{E_C}^{\infty} \mathrm{d}E f(E)\left[1 - f(E) - \Delta F\right] \tag{2.39}$$

With $E_C = \max(E_{c,i}, E_{c,j})$ being the higher of the conduction band minima $E_{c,i}$ and $E_{c,j}$. Without charging effects a tunnel junction between normal conducting electrodes behaves ohmic, which allows to introduce the phenomenological tunnel resistance

$$R_t = \frac{\hbar}{2\pi e^2 |T|^2 D_i D_f} \tag{2.40}$$

Working out the integral in Eq. 2.39 after inserting Eq. 2.40 in Eq. 2.39 leads to the main result of the orthodox single electron tunneling theory, enabling to calculate $\Gamma$ by

$$\Gamma(\Delta F) = \frac{1}{e^2 R_t} \frac{\Delta F}{\exp(\Delta F / k_\mathrm{B} T) - 1} \tag{2.41}$$

At this point it is useful to summarize the validity of Eq. 2.41. Since a continuous energy spectrum is assumed, the orthodox theory can only be applied when the energy quantization of the reservoirs from and to the electron tunnels is much smaller than the thermal energy $E_k \ll k_\mathrm{B} T$. The tunneling barrier shape must not be affected by image

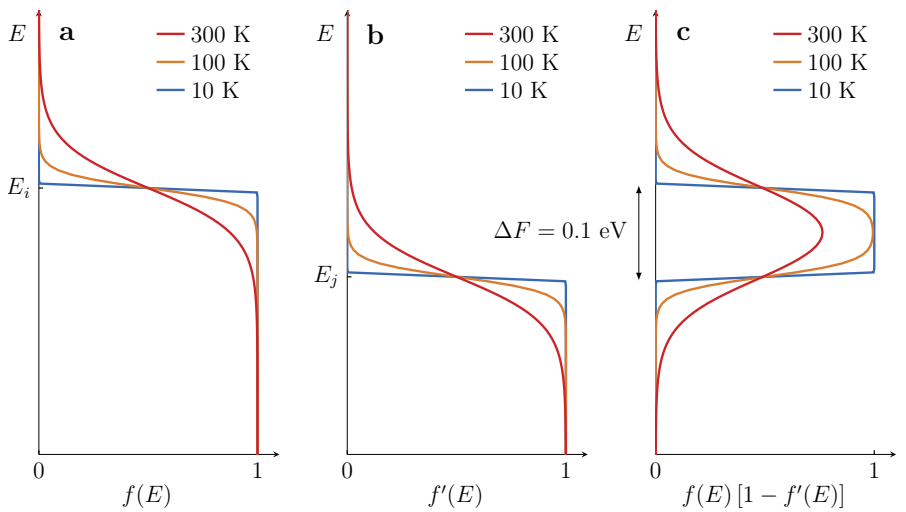


Figure 2.9: **Illustration of the dependence of the charge tunneling probability on the Fermi-distribution. a** For simplicity the energy of the initial state $E_i$ is chosen such that it aligns with the chemical potential in the initial state. **b** The energy of the final state $E_j$ is chosen at the chemical potential of the final state. The latter is shifted by -0.1 eV compared to the chemical potential in the initial state (This could be e.g. caused by a voltage drop over a junction). **c** At low temperatures, the probability that the starting state $E_i$ is filled and the end state $E_j$ is empty reduces the integral in to a well defined energy interval with width $\Delta F = E_j - E_i$.

charge effects, resulting from barrier traversal times exceeding any other time constant in the system. The charge number on an island has to result from an integer number of charges, which requires that electron states are sufficiently confined to the islands. In order to confine the electron to a certain volume, which it can enter or leave by tunneling over a potential barrier, the barriers and the volume (or island) have to be engineered in a way that the expecation value of the charge number $\langle N \rangle$ is not different from the number of electrons localized on the island. The enery gap is $\Delta E = e^2/C$ and $\Delta t \approx R_T C$. For the energy uncertainty to stay above $h$, the tunnel resistance has to exceed

$$R_t > \frac{h}{e^2} = R_Q = 25.813\ \mathrm{k\Omega} \tag{2.42}$$

In the limits of the orthodox theory, single-electron charging effects are observed, giving rise to single-electronic devices. The simplest single-electronic circuit is the single-electron box (Fig. 2.9), consisting of an island which is connected to a voltage source over a tunnel junction. As long as $V < e/C_\Sigma$, tunneling is prohibited due to the finite charging energy of $e^2/2C_\Sigma$ (Coulomb blockade). Here, $C_\Sigma = C_1 + C_2$ is the capacitance of the island. For pumping $n$ excess charges onto the island, inducing a charge of $q = ne$, the voltage source has to spend $q^2/2C_\Sigma$. In a real system, the charge state will also be affected by a finite temperature of the charge carriers and offset-charge. Charge transport is dominated by the charging energy as long as $E_C \gg k_B T$, whereas at $k_B T \geq E_C$ the average number of charges and on the island is additionaly determined by the temperature $T$. An offset-charge (induced by e.g. gates or the electrostatic environment of the island) on the electron box shifts the effective charging energy to $(q+q_0)^2/2C_\Sigma - q_0^2/2C_\Sigma$, with the possibility of even eliminating Coulomb blockade at $(q+q_0)^2 = q_0^2$.

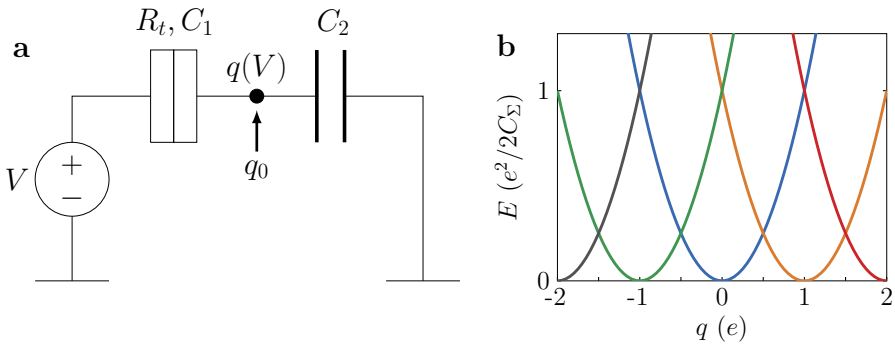


Figure 2.10: **Single electron box as the prototype circuit of single-electronics. a** Schematics of a single electron box, with tunnel barrier with resistance $R_t$, capacitance $C_1$ (of the barrier), and a capacitance $C_2$ to ground. At $T \ll E_C$, the number of integer charges on the island, $q = ne$, can be controlled with the bias voltage $V$. **b** Charging parabolas of the electron box, in dependency of the island offset-charge $q_0$. The curves are colored acccording to $q_0 = 0$ (——), $q_0 = -e$ (——), $q_0 = e$ (——), $q_0 = -2e$ (——), $q_0 = 2e$ (——).

If charges can be sufficiently localized by designing the system accordingly, charge transport in the circuit can be described by consecutive charging events, which are assumed to be discrete in time. Usually, the electrostatic potential difference across one or more nodes is known (e.g. from a grounded voltage source). One then starts with a certain

charge configuration on all nodes, and calculates all node potentials using the capacitance matrix $\mathbf{Q} = \mathbf{CV}$. Single charge tunneling events change the charge configuration, and knowledge about the series of tunneling events provides the knowledge about the charge state at any time. The current arising from a single tunneling event can be calculated with Eq. 2.41, according to $I = e\Gamma$. The discreteness of single charge tunneling events and the rather simple way of describing the system with thermodynamic state variables, single-electronic circuits can be rather well modelled with stochastic models.

### 2.4.2. COMPUTATIONAL SINGLE ELECTRONICS

A valid assumption according to the orthodox theory is that the tunnel rates of all possible single electron tunneling events, transforming the system from one charge state to another, only depend on the momentary state of the system and there is not correlation between charge states in time beyond these single charge transport events. This restriction enables to describe the tunneling events as a Markov chain, and the system can be described with a master equation. The system can exist in a set of states and the probability to find the system in the state $i$ is $P_i$. The probabilities evolve according to

$$\frac{\partial P_i(t)}{\partial t} = \sum_{i \neq j} \left[ \Gamma_{ij} P_j(t) - \Gamma_{ji} P_i(t) \right] \tag{2.43}$$

Here, $\Gamma_{ij}$ is the tunnel rate at which the system transitions from an initial state $i$ into another state $j$, and $P_i(t)$ is the probability of finding the system in state $i$. The next step in the main procedure of using the master equation is to find the set of relevant states in which $\mathbf{p} = [P_1, P_2, ..., P_n]^{\mathbf{T}}$ evolves according to $\dot{\mathbf{p}} = \Gamma \mathbf{p}$, with

$$\frac{\mathrm{d}}{\mathrm{d}t} \begin{bmatrix} P_1 \\ P_2 \\ \vdots \\ P_n \end{bmatrix} = \begin{pmatrix} \sum_{i \neq 1} \Gamma_{\mathrm{i1}} & -\Gamma_{12} & \dots & -\Gamma_{1\mathrm{n}} \\ -\Gamma_{21} & \sum_{i \neq 2} \Gamma_{\mathrm{i2}} & \dots & -\Gamma_{2\mathrm{n}} \\ & & \vdots & \\ -\Gamma_{\mathrm{i1}} & -\Gamma_{\mathrm{i2}} & \dots & \sum_{i \neq n} \Gamma_{\mathrm{in}} \end{pmatrix} \begin{bmatrix} P_1 \\ P_2 \\ \vdots \\ P_n \end{bmatrix} \tag{2.44}$$

The master equation approach is especially suited for single-electronic devices in which the nodes do not have many interconnections as it is the case for e.g. a short linear chain of tunnel junctions (see section 2.3.4). The simplest example is the single electron transistor (SET), for which the system only traverses between charge states which can be transformed into each other by additon or removal of single charges on a single node. In cases in which the relevant states are not easy to identify, a description of a single electronic circuit with the master equation can be very difficult. A suitable method here is to identify the relevant charge states by letting the system develop in a series randomly selected tunneling events, which are weighted with their transition rates (Markov-chain Monte-Carlo method, MCMC). The probability for a specific tunneling event to happen at a time $t$ is given by the Poisson distribution $P_0(t) = \mathrm{e}^{-\Gamma t}$. In a Monte-Carlo procedure all possible tunneling events are listed with their particular tunneling rate $\Gamma$, giving rise to a tunnel time according to the inverse of the Poisson distribution. The node charges are updated after a tunneling event and the procedure is repeated until it converges to a stable current. The most usual drawback of using MCMC methods are long runtimes.

# 3

# Device Fabrication and Cryogenic Measurements

*Labor omnia vincit improbus*

Vergil (70 B.C. - 19 B.C.)

## 3.1. FABRICATION OF AL-ALO$_X$ TUNNEL JUNCTION ARRAYS WITH INTEGRATED INDIUM NUCLEAR REFRIGERANT

For ultralow temperature electronic thermometry and integrated nuclear magnetic cooling, a fabrication scheme for Coulomb blockade thermometers (CBTs), based on arrays of Al-AlO$_x$ junctions in combination with patterned, thick In films as nuclear refrigerant, was developed. The CBTs are designed to operate in the temperature range of several hundred microkelvin, up to a few mK. In order to self-calibrate the CBTs for secondary mode operation (see sections 2.3.4, 3.4), charging effects should be still resolvable at elevated temperatures above 10 mK. If $1/u \sim 0.5$ (see Fig. 2.8) at $T \leq 1$ mK, the charging energy has to be set to $E_C \leq 50$ neV. This in turn requires a total island capacitance of the order of 1 pF, with the charging energy of $E_C = e^2/C_\Sigma \times (n-1)/n$ in the strong island coupling regime, $C_0 = C_\Sigma/2 \gg C_g$. In addition, the junction resistance $R_t$ has to be set well above $R_Q$ (see section 2.4) to operate in the single electronics regime. These conditions demand a larger flexibility than the one enabled by conventional shadow angle evaporation and oxidation techniques to fabricate tunnel junctions [140]. With shadow angle evaporation, the island capacitance is fully determined by the junction capacitance alone, thus scaling in an unfavorable way with the junction area regarding the junction resistance requirements enabled by the single electronics regime. Combining rather large island coupling capacitances with highly resistive, $< 1\ \mu m^2$ large tunnel junctions is enabled by fabricating the Al-AlO$_x$ junctions according to an *ex-situ* tunnel-via process scheme [141]. By employing tunnel vias, defined by etching of an interlayer dielectric, the *ex-situ* oxidation scheme allows to define $C_0$ separately from $R_t$.

*Ex-situ* fabricated tunnel junction arrays are combined with chipscale nuclear cooling functionality by a masked thick-film In electrodeposition scheme, developed for this purpose. The aim is to define the nuclear cooling power per CBT island by depositing a well defined molar amount of In per unit area, giving rise to a defined number of spins with the molar volume $V_m = 15.71\ \mu m^3/pmol$ of In. A nuclear spin heat capacity of several μJ/K is required for stable (timescale of days to weeks) microkelvin cooling in the presence of electronic heat leaks of the order of < 100 aW (see section 2.1.3). This requires integrated volumes of the order $10^5\ \mu m^3$, achieveable by electrochemical film deposition methods, providing thick metallic coatings with low intrinsic mechanical stress [142–145]. The latter would especially affect thick, vacuum-deposited coatings. The developement and detailed implementation of the corresponding device fabrication methods is described in the following. A summary of the tunnel junction process and detailed procedures are given in section 3.1.1. The procedure for electrochemical integration of thick, patterned indium films by pulsed electroplating is described in section 3.1.2.

### 3.1.1. FABRICATION OF AL-ALO$_X$ TUNNEL JUNCTION ARRAYS

Al-AlO$_x$ tunnel junction arrays are fabricated using an alternating film deposition/etching process, to generate metal electrodes in different layers of a multilayer stack, galvanically separated by a thick interlayer dielectric (ILD), and connected by through-via tunnel-junctions. The process is illustrated in Fig. 3.1. The fabrication process is summarized in the following, numbers leading the paragraphs relate to the panel numbers in Fig. 3.1

**(1)** The bottom electrode was deposited by DC magnetron sputtering (AJA ATC 1800-V, base pressure $8.7 \cdot 10^{-10}$ mbar on 4 inch substrate holder) of 180 nm Al (2 inch target, 99.9995% Al, Kurt J. Lesker) onto a Si/$SiO_2$ (thermal, 275 nm oxide thickness) wafer, with 0.19 W/cm$^2$ (DC-power 60 W, DC bias 336 V) at 4.7 µbar Ar chamber pressure. The substrate to target distance was about 10 cm (tilted 45°), with 20 rpm substrate rotation. The Al sputtering process is optimized with respect to step coverage (see step (6)). The resulting films are mirror reflective and form hillocks when heated to above 200 °C in air.



**(2)** After unloading the chip after step (1), 2.2 µm AZ-nLOF 2020 (Microchemicals GmbH) is spincoated (4000 rpm, softbake 110 °C on a hotplate) and patterned using electron beam lithography (RAITH Voyager, 50 kV acceleration voltage, 60 µm aperture, 2.1 nA beam current, dose 44 µC/µm$^2$). The pattern is aligned on rectangular ($10 \times 10$ µm$^2$), 100 nm thick W markers, sputter deposited and patterned by wet etching with KI/$I_2$ prior to step (1). The resist is developed in AZ-726 MIF (Microchemicals GmbH) after a crosslinking bake at 110 °C (hotplate). The Al bottom electrode was patterned by wet etching using a commercial etching mixture (Al etchant Type D, Transene INC.). The resist was removed afterwards in Technistrip NI555 (Microchemicals GmbH) at 60°C.

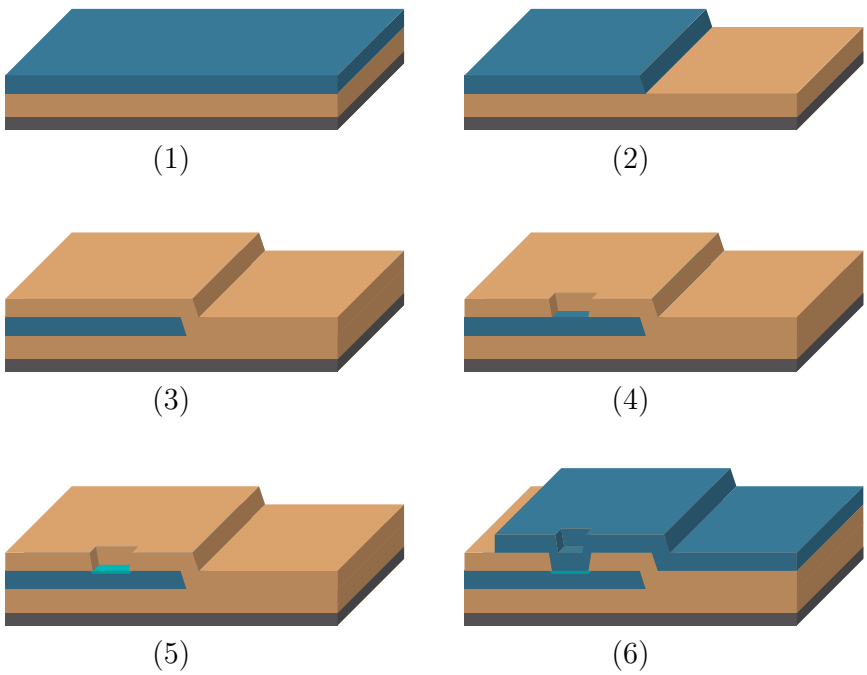


Figure 3.1: **Overview of the *ex-situ* tunnel jucntion fabrication process.** **(1)** Al base electrode deposition, **(2)** Base electrode etching, **(3)** $SiO_2$ interlayer dielectric deposition, **(4)** Ion etching of vias into the $SiO_2$ interlayer dielectric, **(5)** *Ex-situ* tunnel barrier formation by oxidation of the exposed bottom electrode, **(6)** Conformal deposition of the Al top electrode. The materials are colored according to: Si (■),$SiO_2$ (■),Al (■), $AlO_x$ (■).

**(3)** A 230 nm $SiO_2$ thick interlayer dielectric was deposited by RF-sputtering (Alliance AC450, base pressure $1.1{\cdot}10^{-7}$ mbar, 4 inch substrate holder, 4 inch target, 99.99% $SiO_2$, room temperature) with 0.39 W/cm$^2$ (RF-power 125 W, DC-Bias 141 V), at 8 µbar Ar pressure. The substrate to target distance was 8 cm, without tilt and rotation of the substrate.

**(4)** The vias were defined by spin coating 130 nm AR-P 6200.13 (Allresist GmbH, 4000 rpm, softbake at 150 °C on a hotplate) and patterned by electron beam lithography (RAITH Voyager, 50 kV acceleration voltage, 30 µm aperture, 0.1 nA beam current, dose 218 µC/µm$^2$). The resist is developed in AR-600-546 (Allresist GmbH). The pattern was then etched into $SiO_2$ interlayer dielectric by RIE (Oxford PlasmaPro 100 Estrelas) using 0.66 W/cm$^2$ (RF-power 120 W, DC bias -270 V) in pure $CHF_3$ (50 sccm), at a pressure of 6.7 µbar and 15° C, with 13 mbar He backing. The resist was removed in AR 300-76 (Allresist GmbH) at room temperature overnight. The RIE with pure $CHF_3$ results in a sloped edge, with the amount of slope defined by the used $CHF_3$ concentration and DC-bias.

**(5)** For tunnel junction formation, the chip was loaded into the AJA ATC 1800-V and the bottom Al electrode was depassivated by Ar plasma milling (15 min in 0.31 W/cm$^2$ RF-plasma (RF-power 100 W, -286 V DC-bias, at 4 µbar pure Ar). The main chamber was not equipped with an $O_2$ supply, which is why the oxidation had to be performed in the loadlock. The latter was connected to a $O_2$ bottle (99.999 % purity) via a mass flow controller for this purpose. For the oxidation procedure, the device was transferred in Ar flow into the loadlock (base pressure < $1{\cdot}10^{-7}$ mbar), where the $AlO_x$ tunnel barriers were formed by oxidation in pure $O_2$, at a pressure of 105 mbar, and room temperature for 140 min.

**(6)** Right after step (5) the chip was loaded into the main chamber *in vacuo*, followed by in-situ DC magnetron sputtering of 260 nm Al as top electrode. The deposition and patterning of the top electrode was performed in the same way as for the bottom electrode in step (1). After unloading the sample, 2.2 µm AZ-nLOF 2020 (Microchemicals GmbH) were spincoated (4000 rpm, softbake 110 °C on a hotplate) and patterned using electron beam lithography (RAITH Voyager, 50 kV acceleration voltage, 60 µm aperture, 2.1 nA beam current, 44 µC/µm$^2$). The resist was developed in AZ-726 MIF (Microchemicals GmbH) after a crosslinking bake at 110 °C (hotplate). The Al bottom electrode was then patterned by wet etching in a commercial etching mixture (Al etchant Type D, Transene). The resist was removed in Technistrip NI555 (Microchemicals GmbH) at 60 °C.

A schematic of an *ex-situ* tunnel junction is shown in Fig. 3.2. The use of electron beam lithography gives good control over the tunnel resistance $R_t$ (via the junction area), while the Al electrode overlap area $A_{\mathrm{el}}$ and the island area $A_{\mathrm{island}}$ extend over large dimensions. Modelling the electrode overlap junctions as plate capacitors, the island capacitance is

$$C_\Sigma = 2C_0 + C_g = 2\varepsilon_0\left(\frac{\varepsilon_{\mathrm{SiO_2}} A_{\mathrm{el}}}{d_{\mathrm{ILD}}} + C_T\right) + \varepsilon_0\left(\frac{\varepsilon_{\mathrm{Si}} A_{\mathrm{island}}}{d_{\mathrm{Si}}}\right) \tag{3.1}$$

with $C_0$ the mutual capacitance of the island, $C_g$ the capacitance to ground, $C_T$ the capacitance of the Al/$AlO_x$ tunnel junctions, $d_{\mathrm{ILD}}$ the thickness of the interlayer dielectric, $d_{\mathrm{Si}}$ the substrate thickness, and $\varepsilon_0, \varepsilon_{\mathrm{SiO_2}}, \varepsilon_{\mathrm{Si}}$ the vacuum permittivity, the static permittivity of the interlayer dielectric and the Si substrate respectively. For operating the device

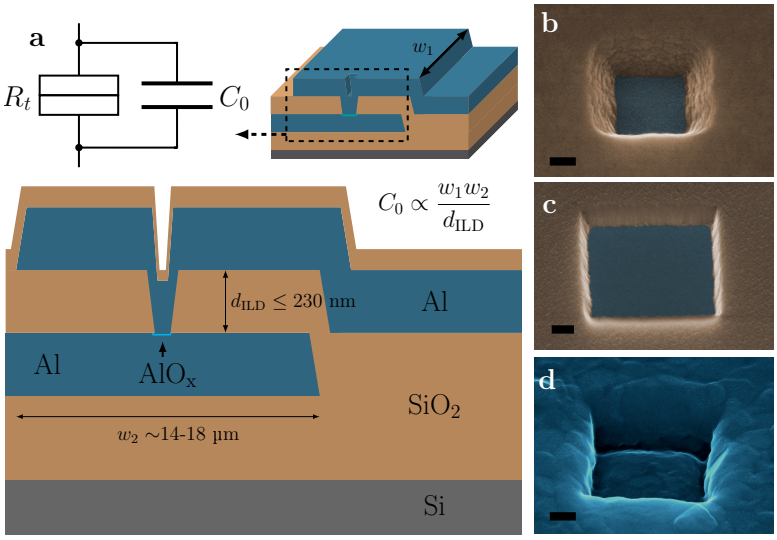


Figure 3.2: **Overview of Al-AlO$_x$ tunnel junctions, fabricated in an *ex-situ* oxidation process**. **a** Single tunnel junction and overlap junction of Al electrodes, inducing tunnel coupling and a mutual capacitance $C_0$ between islands. The tunnel resistance $R_t$ (Eq. 2.40) is defined by the junction area $A_t$ and the thickness $d_t$ of the $AlO_x$ tunnel barrier. $C_0 = \epsilon_0 \epsilon_{SiO_2} A_{el}/d_{ILD}$ (see Eq. 3.1) is defined by the island area $A_{el}$ and the $SiO_2$ interlayer dielectric thickness $d_{ILD}$. **b** SEM micrographs of a 250 nm×250 nm via, etched into the $SiO_2$ interlayer dielectric. **c** SEM micrographs of a 740 nm×740 nm via, etched into the $SiO_2$ interlayer dielectric. **d** Via in panel b, after oxidation and conformal coating with the top electrode. The scale bars in b-d correspond to 100 nm.

in the capacitive island coupling regime (see chapter 5), $d_{ILD} \ll d_{Si}$ ensures that the mutual capacitance of the islands exceeds their capacitance to ground ($C_0 \gg C_g$).

The *ex-situ* tunnel junction fabrication process is characterized by fabricating individually addressable junctions and measuring the current-voltage characteristics in a dilution refrigerator (Leiden Cryogenics CF1400, base temperature $T_{MC} \approx 10$ mK), as well as the tunnel junction resistance $R_t$ (Eq. 2.40) of single junctions at room temperature. At room temperature, a junction resistance of $R_t = 12.8 \pm 0.8$ kΩ µm$^2$ is obtained, with an increase in resistance of 30-35 % in towards cooling to base temperature of the dilution refrigerator. For tunnel junction thermometry in the single electronics regime, as described in section 3.4, a junction area of $0.55 \pm 0.1$ µm$^2$ was used. The junction quality can be estimated by measuring the SIS junction characteristics of single junctions, after reducing the electron temperature well below the critical temperature of Al, $T_c \approx 1$ K. The current-voltage characteristics of a single SIS junction, fabricated with the *ex-situ* tunnel junction process, is plotted in Fig. 3.3 a., showing a sharp current increase at $2\Delta = 360$ µV, in line with the expected gap value of $\Delta = 170$ µeV [5]. The subgap current is strongly suppressed in a $\Delta$ wide region around zero bias, while there is another region between $\pm\Delta$ and $\pm\Delta$ with a signficant tunnel current in the gap. This can be attributed to the *ex-situ* process scheme, with only one of the Al-AlO$_x$ interfaces is created *in-situ*. The bottom Al electrode is exposed to plasma etching and ion milling prior to oxidation. Since $AlF_3$ is

not volatile in the used RIE conditions, it can also be expected that the bottom electrode is enriched with fluorine and insufficiently removed by ion milling before Al oxidation. A significant improvement of the junction quality is expected when the oxidation is performed at elevated temperature [146–148]. The 250 nm thick Al electrodes are switched from the superconducting to normal conducting state at a field of 30 mT, indicating a slightly larger critical magnetic field than the bulk, where $B_c = 10$ mT [5]. With the critical field of bulk In at 28 mT [149], this is not expected to limit the achievable on-chip nuclear cooling efficiency. A fraction of the resistance increase towards ULT cooling of the tunnel junctions is caused by an unexpected magnetoresistance of 7-9 %, observed for junction arrays as decrease in normal state resistance $(n/m) \times R_t$ up to fields of about 3 T. This effect was found in all devices fabricated with the *ex-situ* scheme. The magnetoresistance is temperature independent up to about 100 mK (see Fig. 3.3 c,d) and shows no hysteresis when ramping the magnetic field in a cyclic manner.



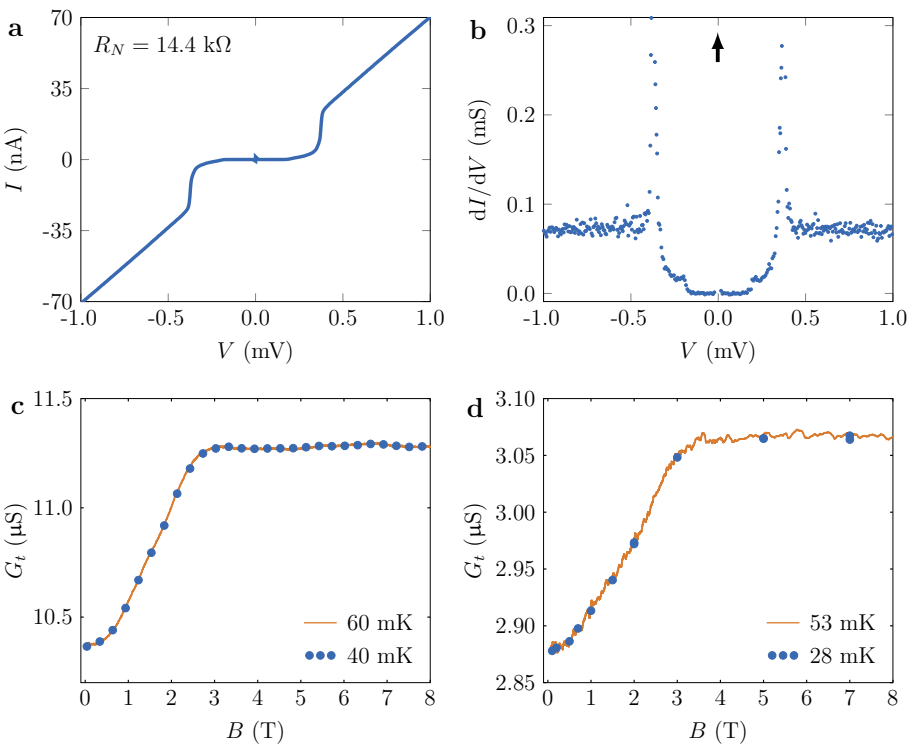


Figure 3.3: **Characterization of via based Al-$AlO_x$ tunnel junctions, fabricated with the *ex-situ* oxidation process**. **a** IV characteristics of a single Al-$AlO_x$ tunnel junction with junction area 1 μm$^2$, measured at zero magnetic field and a mixing chamber temperature of about 15 mK. **b** Differential conductance, obtained by numerical differentiation of the IV curve which is shown in panel a. The supercurrent conductance peak is out of scale **c** Conductance of a 36 × 15 tunnel junction array, measured against magnetic field at different mixing chamber temperatures. **d** Same as panel c, but for a tunnel junction array with $n = 36$ and $m = 5$ junctions.

### 3.1.2. INDIUM THICK FILM INTEGRATION

For integrating sufficient amounts of In onto the chip for chipscale nuclear magnetic cooling, a back end integration scheme based on electroplating thick, patterned In films onto the CBT islands was developed. The principle is shown in Fig. 3.4. In the first step, the device is coated with a hard, insulating capping layer in which deep trenches are etched. The whole device is then conformally covered with a metallic seed layer which comes into galvanic contact with the working electrode during electroplating (see also Fig. 3.5). The In metallization regions are defined by photolithography, using a thick positive resist (20-100 µm), passivating the surface partially. In order to not exceed an aspect ratio of 1, the maximum thickness of the electroplated film is marked by the depth of the trenches in the capping insulator + the smallest lateral dimension of the plated metal structures (given that the resist is thicker). In this work only thin (70 nm) capping layers were utilized to simplify the processing steps with respect to the etching depth.



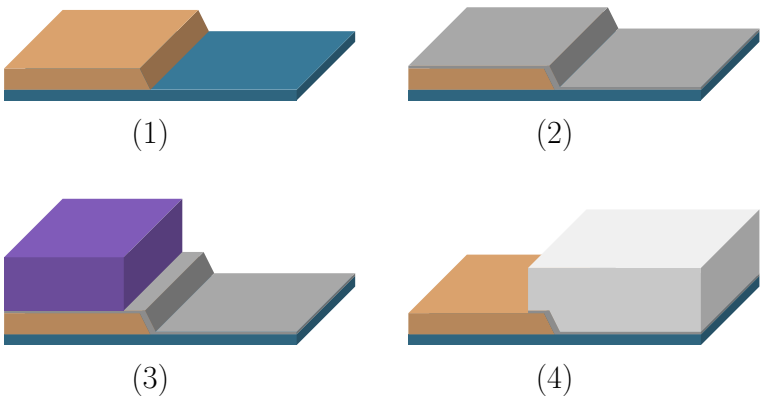


Figure 3.4: **Overview of the back-end masked electroplating process**. **(1)** Etching of trenches into a dielectric capping layer, **(2)** Conformal deposition of a metallic seed layer, **(3)** Defining the electrodeposition mask, **(4)** Electrochemical deposition of metal into the open regions and resist removal. The materials are colored according to: Base metal (■), interlayer dielectric (■), metal seed layer (■), resist mask (■), plated metal (■).

For the masked electrodeposition of In, a custom made plating bath is used with an unsealed borosilicate glass beaker as reaction container. The bath current is applied by a commercially available galvanostat module (PGSTAT204, Metrohm GmbH). The galvanostat can apply currents up to 400 mA in dynamic ranges with a bandwidth of 1 MHz, and has a built in waveform generator. For electrodeposition, a three-electrode setup is used in which the cell current flows between the counterelectrode and the working electrode, while the electrostatic potential drop over the working electrode is measured with an AgCl (in 4 mol/l KCl) reference electrode. As counterelectrode an 2×10 cm$^2$, 1 mm thick strip of pure In (99.999%) is used, gradually dissolving in the electrolyte. In Fig. 3.5 an overview of the setup is shown. The chip is galvanically connected to the working electrode by a custom made PTFE chip carrier, with the chip placed in a defined opening. Contact to the working electrode is made with a Cu frame, coated with In (Fig. 3.5 c), which is pressed onto the seed layer on a 2.5 mm wide, unpassivated area around the chip (Fig. 3.5 a). Only polyamide screws are used for parts submerged into the elec-

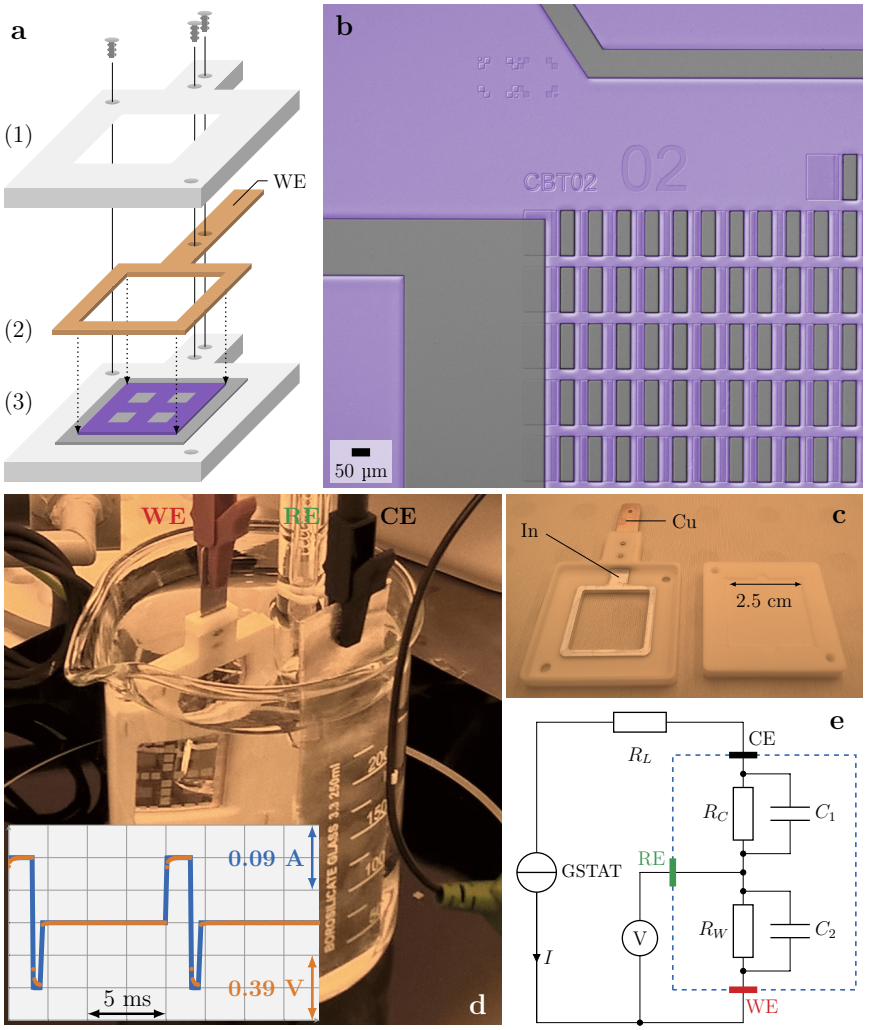


Figure 3.5: **Overview of the setup for electrochemical deposition of thick In films.** **a** PTFE chip carrier: (1) cap, facing the anode, (3) chip carrier, (2) Cu electrode frame, partially coated with In. **b** Microscope image of a device, coated with a Cu/Au seed layer and patterned plating resist. **c** Photograph of the PTFE chipcarrier. **d** Plating bath with working electrode (WE), counterelectrode (CE), and reference electrode (RE). Inset: two cycles of the waveform used for pulsed plating. **e** Circuit representing the used plating bath and galvanostat.

trolyte, in order to avoid bath contamination. The In films are gained by a cathodic reduction of trivalent In ions at the working electrode, according to the half reaction

$$In^{3+} + 3e^- \rightarrow In \qquad (-0.37\,V) \tag{3.2}$$

in a solution containing $In(SO_3NH_2)_3$ (105.36 g/l), $NaSO_3NH_2$ (150 g/l), $HSO_3NH_2$ (26.4 g/l), NaCl (45.84 g/l), Glucose (8.0 g/l) and Triethanolamine (2.29 g/l). The pH is kept in a range of 1.5-2 by adding $HSO_3NH_2$ to the electrolyte solution. The electrolyte is purified

to 3N with respect to metal contaminants, which is certified with an ICP mass spectrometry assay[1]. The negative standard potential of the reduction half-reaction of $In^{3+}$ results in a reduced cathode efficiency, due to $H_2$ formation at the cathode according to

$$2H_3O^+ + 2e^- \rightarrow H_2 + 2H_2O \qquad (0\ \mathrm{V}) \tag{3.3}$$

In films, plated with the setup shown in Fig. 3.5 using DC current, have a porous microstructure. This can be seen in Fig. 3.6, where the tetragonal crystal structure ($a$ = 0.453, $b$ = 0.723) of DC plated films is exposed as well. To avoid extensive crystallization and cathodic $H_2$ formation, an alternating current based deposition scheme was utilized. Here, the cell current is pulsed forward and reverse, removing material from the growing nuclei during the reverse phase and allowing $H_2$ to desorb. The electrical double layer (Helmholtz layer) at the cathode is newly formed in every cycle meaning that the flux of $In^{3+}$ ions to the cathode is not diffusion limited during the whole process. However, the net deposition rate is reduced because a part of the applied current is spent on recharging the Helmholtz layer with capacitance of the order of 10 - 100 µF [150]. The frequency is set to a range in which the forward pulse reaches full polarization.

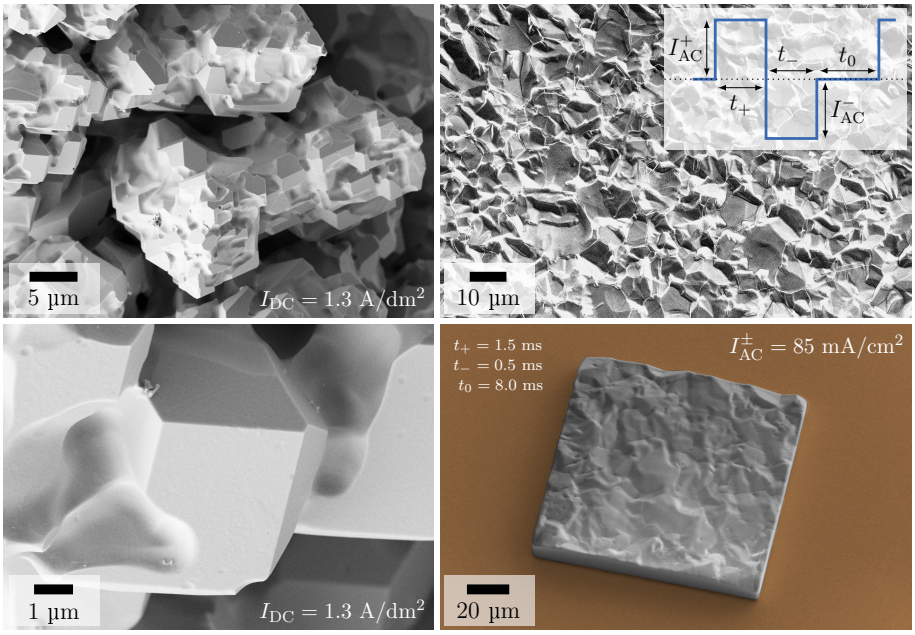


Figure 3.6: **Morphology of In films obtained DC electrodeposition and pulsed electrodeposition. left panels**: morphology of granular In films, with large tetragonal crystallites, obtained by DC electrodposition. **right panels**: morphology and patterning of dense In films obtained by AC electrodeposition into a photoresist mask (bottom), and bulk film (top). The inset of the top right panel illustrates the waveform used for pulsed plating.

[1] Lot number SD8181, order SN14481. Trace metal analysis provided by the supplier: 0.2 ppm Fe, <0.5 ppm Ni, <0.2 ppm Al, As, Ca, Cd, Cr, Cu, Hg, Li, Mg, Tl, V, Pb, Sb, Sn, 0.4 ppm Si

For integrating In nuclear cooling structures onto the islands of CBT tunnel junction arrays, fabricated as described in section 3.1.1 (from step (6) on), an In electrodeposition process resulting in the finest grain structure achieved in the performed electrochemical deposition experiments was utilized. The process is summarized in the following.

**(1)** The device was capped by RF-magnetron sputtering (Alliance AC450) of 70 nm $SiO_2$ with 0.39 W/cm$^2$ (RF-power 125 W, DC-Bias 141 V) at 8 µbar Ar pressure. The substrate to target distance was 8 cm without tilt and substrate rotation. 2.7 µm AZ ECI 3027 (Microchemicals GmbH) was spin coated (4000 rpm, softbake 100 °C, hotplate), followed by patterning with h-line exposure (MicroWriter ML2, Durham Magneto Optics Ltd, 405 nm exposure wavelength, dose 210 mJ/cm$^2$) and RIE (Oxford ICP100, process gases $SF_6$, $Cl_2$, $CHF_3$, HBr) using 0.15 W/cm$^2$ (RF-power 50 W, DC bias -235 V) in pure $SF_6$ (30 sccm), at a pressure of 8 µbar and room temperature with 13 mbar He backing. The Si carrier wafer was coated with 500 nm Cr. The resist is removed in AZ 100 (Microchemicals GmbH). To avoid loss of material due to ion milling of the Al films during the RIE of the capping layer, the lithography and etching process is performed alternating on the top electrode (etch depth 70 nm $SiO_2$) and bottom electrode (etch depth 300 nm $SiO_2$).

**(2)** The exposed Al top electrode (see step (6) in section 3.1.1) was depassivated by ion-beam milling (250 eV ion energy, 80 nA ion current in 0.7 µbar Ar) and a seed layer of 270 nm Cu (0.5 nm/s, ±20° substrate to source orientation, 99.99 % Cu source) and 30 nm Au (0.1 nm/s, ±20° substrate to source orientation, 99.99 % Au source) was deposited by electron beam evaporation (Alliance EVA 450, base pressure $8.3{\cdot}10^{-8}$ mbar, 7.4 kV emission voltage) on a water cooled substrate holder. The substrate to source orientation was continuously varied between −20° and +20° to provide a sufficient step coverage (sputtering targets were not available). All materials were evaporated from a W crucible.

**(3)** As masking layer for the plating process, 35 µm AZ 40 XT (Microchemicals GmbH) was spin coated (2000 rpm, linear soft-bake ramp for 7 min from 60 °C to 125 °C). The mask was patterned by UV lithography (1 µm resolution, 375 nm exposure wavelength, dose 800 mJ/cm$^2$) and developed in AZ 726 MIF (Microchemicals GmbH), after a post exposure bake (linear soft bake ramp for 2 min from 60 °C to 105 °C). Prior to electroplating, the seed layer was cleaned by 30 s immersion in 2.5% TMAH (aq) and 1 min $O_2$ plasma clean (200 W, 200 sccm $O_2$ without substrate bias) to avoid skip plating in step (4).

**(4)** The electroplating process was performed at room temperature in a stirred aqueous solution of 0.26 M $In(SO_3NH_2)_3$ (Indium Corporation) using 99.999% pure In as the counterelectrode. Details of the electrochemical setup for In deposition and the electrical contact of the CBT chip to the working electrode can be taken from Fig. 3.5 and the corresponding text. The cell current duty cycle was 1.5 ms, 85 mA/cm$^2$ (0.39 V, forward), 0.5 ms, -85 mA/cm$^2$ (-0.39 V, reverse) and 8 ms off. The measured cell current and voltage is plotted for 2 cycles in in the inset of Fig. 3.5 d. The In film was deposited with a total amount of $10^5$ cycles. The mask is removed in DMSO at room temperature, followed by the removal of the Cu/Au seed layer in $I_2$/KI (10 g KI and 2.5 g $I_2$ in 100 ml DI $H_2O$).

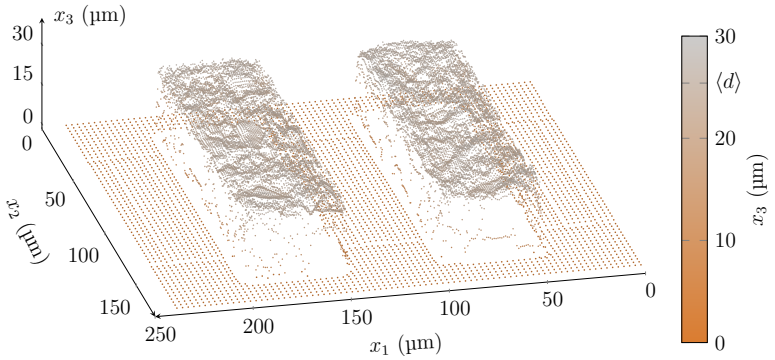


Figure 3.7: **In nuclear magnetic cooling bars on two CBT islands mapped with interference microscopy.** The average thickness $\langle d \rangle$ of the In cooling structures is marked on the scale of the colorbar. The pixel density in the Cr coated regions around the In nuclear cooling bars is reduced for better illustration purposes.

A SEM micrograph of several islands of a fully fabricated array of tunnel junctions, with an indium volume of $50 \times 140 \times 24.5\ \mu m^3$, integrated onto each island is shown in Fig. 3.8. The deposited In volume is characterized by mapping the surface of a fully fabricated device by interference microscopy (see Fig. 3.7), after sputtering a thin (25 nm) Cr film onto the whole chip. The obtained average In thickness 25.4 µm, giving rise to a net deposition rate of 0.04 nm per cycle with the process described in step (4). With the obtained In thickness, the total amount of In integrated per island is 11.4 nmol. As can be seen in Fig. 3.8, the film surface is much more smooth on the sides of the film than on the top surface. Thus, the patterning resolution of the In films plated into a resist mask allows a denser integration than expected from the surface morphology of the In films.

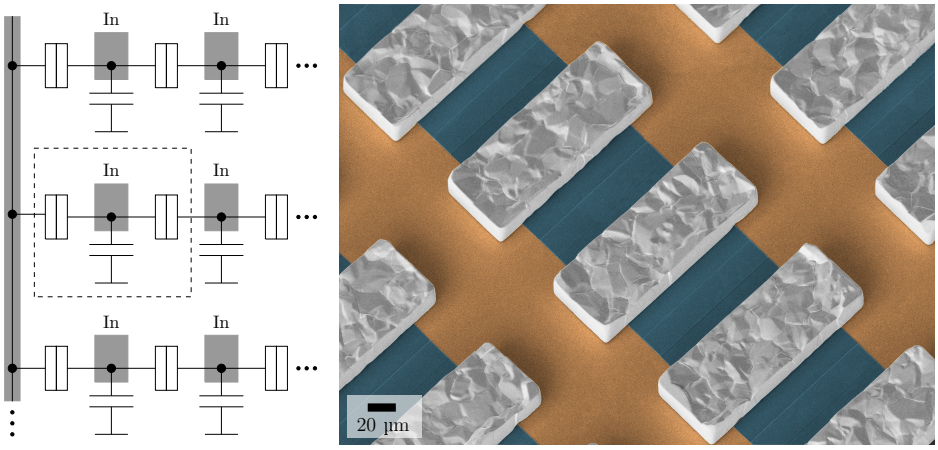


Figure 3.8: **Overview of a fully fabricated CBT device with electrodeposited In islands.** **a** Schematics of a tunnel junction array with the electroplated In structures integrated onto the leads and the islands. **b** SEM micrograph of several islands in a device with a total of 36 tunnel junctions in series ×15 in parallel.

## 3.2. Cryogenic Transport Measurements

Transport measurements were performed in a commercial dilution refrigerator (Leiden Cryogenics, MK126-700), with a cooling power of about 600 µW at 120 mK (outside of the mixing chamber), and a base temperature of 5-7 mK. The mixing chamber temperature was monitored with a paramagnetic salt thermometer made of $Ce_2Mg_3(NO_3)_{12}{\cdot}24H_2O$ (CMN) and regulated with a resistive heater. The dilution unit resides in a stainless steel insert (12.6 cm), in a dewar containing 143 L $^4$He, hanging on a steel frame. Mechanical decoupling of the latter is provided by a pneumatic isolation. The device is mounted on a Cu coldfinger residing in a RF-shield (see Fig. 3.9), with the whole assembly screwed into the mixing chamber plate. Further metallic RF shields are thermally anchored at the 50 mK plate and the still (see Fig. 3.9). Electrical contact to the room temperature electronics, driving the experiment, is made by Cu wires, thermally anchored to each plate and filtered on the Cu coldfinger stage by a lossy transmission line (Cu powder epoxy) filter and a series RC-filter. A magnetic field is provided by a coaxial superconducting electro-

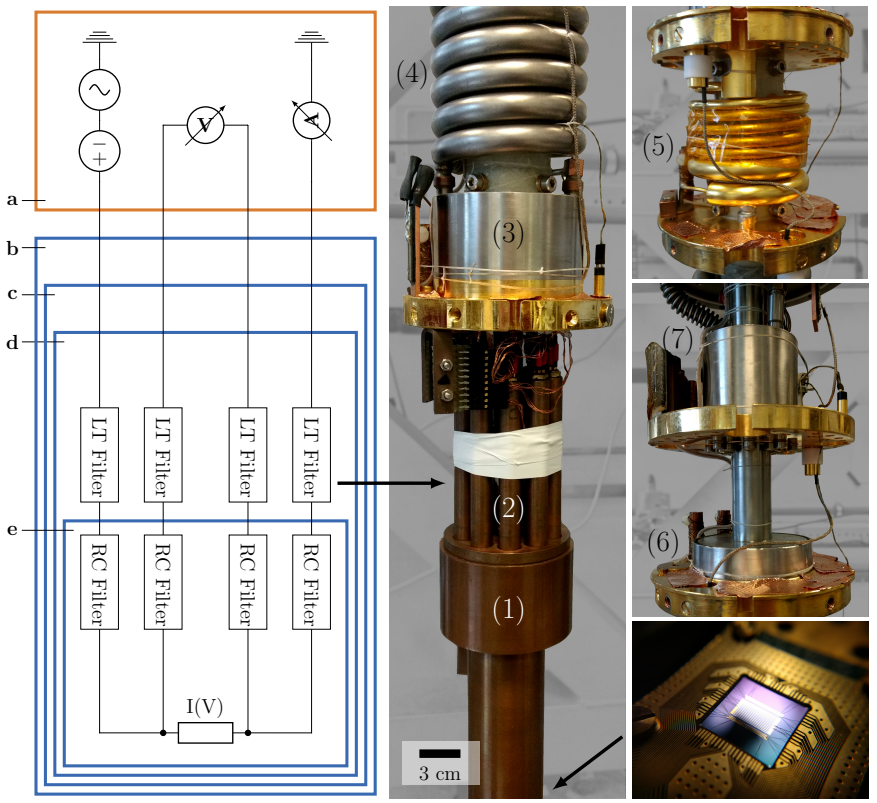


Figure 3.9: **Overview of the low-temperature electrical measurement setup**. **a** room temperature electronics **b** IVC shield (steel), **c** still plate RF shield (steel), **d** 50 mK plate RF shield (steel), **e** device RF-shield (Cu), (1) on the main panel. Wet dilution unit with 1 K pot (7), still (6), 50 mK plate (below (5)), upper heat exchangers (5), silver sinter heat exchangers (4), mixing chamber (3), Cu powder lossy transmission line (LT) filter (2).

magnet (American Magnetics Inc.) with magnetic field strength up to 13 T. The magnet is powered with a four quadrant power supply (American Magnetics, 4Q06125PS), driven by a AMI model 430 PS programmer. The magnet can be run in persistent mode using a thermal switch. The device under test is glued with silver-epoxy on the Cu coldfinger in the magnetic field centre and connected to the driver electronics via a printed circuit board, connected to the Cu wire loom via a plug connector. Bias is applied to the device via 16 digital to analog converters, supplying voltages from -4 V to 4 V with a bit depth of 16 bit. Outcoming signals are fed into differential amplifiers or IV converters. Voltage and current is measured with digital multimeters (Keithley 2000 DWM) after amplification. Interfaces with the I/O measurement rack, containing the DAC and amplifier modules, are solely realized via non-galvanic connections.



### 3.2.1. DIFFERENTIAL CONDUCTANCE MEASUREMENT

The differential resistance of the device under test is measured by standard low-frequency lock-in techniques, using a combination of two digital lock-in amplifiers (Stanford Research Systems, SR830). Herefore, a small AC voltage $V = V_{\mathrm{AC}} \sin(\omega_0 t)$, with $\omega_0 = 18.31$ Hz is applied by one of the lock-in amplifiers to the isolated input of the measurement rack, resulting in an output voltage of $V_{\mathrm{in}} = V_{\mathrm{DC}} + V_{\mathrm{AC}} \sin(\omega_0 t)$. The voltage and current over the device after all voltage drifts and adding of noise to the signal is the Fourier sum

$$V_{\mathrm{d}}(t) = V_0 + \sum_{i=1}^{\infty} \left( V_k \sin \omega_k t + \varphi_k \right), \qquad I_{\mathrm{d}}(t) = I_0 + \sum_{i=1}^{\infty} \left( I_k \sin \omega_k t + \varphi_k \right) \tag{3.4}$$

Prior to be fed into the lock-in input ports over the isolated output of the measurement rack, $I_d$ is converted into a voltage $V_{\mathrm{in,I}} = I_{\mathrm{d}}(t) G_{\mathrm{IV}}$ by a transimpedance amplifier, with the current gain $G_I$. The output voltage is amplified according to $V_{\mathrm{in,V}} = V_{\mathrm{d}}(t) G_{\mathrm{VV}}$. The I-V conversion yields the gain $G_{\mathrm{IV}}$ in units of V/A and the differential V-V amplification yields the gain $G_{\mathrm{VV}}$ in units of V/V. In both lock-ins, the signal is multiplied with the reference voltage and low-pass filtered. The result of the fully digital operations in the lock-in amplifiers is the phase sensitive conversion of the input signals into the Fourier component of the reference frequency. The lock-in amplifiers return the output voltage

$$V_{\mathrm{res,i}} = \int_T \mathrm{d}t \; V_{\mathrm{in,i}}(t) \sin(\omega_0 t + \varphi) \tag{3.5}$$

with $i = 1, 2$. The lock-in amplifiers are synchronized with respect to the reference frequency, $\omega_0$, by applying the reference voltage of one lock-in to the other via a transistor-transistor logic (TTL serial) interface. The differential conductance is calculated from the resulting Fourier components $V_{\mathrm{res,1}} = I_0 G_{\mathrm{IV}}$ and $V_{\mathrm{res,2}} = V_0 G_{\mathrm{VV}}$, resulting in

$$G = \left( \frac{\mathrm{d}I}{\mathrm{d}V} \right)_{V_0} \approx \frac{I_0}{V_0} \left( \frac{G_{\mathrm{IV}}}{G_{\mathrm{VV}}} \right) \tag{3.6}$$

Here, $V_0 = V_{\mathrm{DC}} \pm V_{\mathrm{offset}}$ has to be corrected for the offset voltage $V_{\mathrm{offset}}$, in order to obtain the differential conductance at the output voltage $V_{\mathrm{DC}}$. For the CBTs with a symmetric nonlinear response in $G(V)$, due to charging effects, a digital drift compensation depending on the shape of $G(V)$ is employed (see for example Fig. 4.4 or Fig. 6.4), which requires to measure $G$ over a small voltage range. An overview of the electrical measurement setup, regarding the differential conductance measurement is shown in Fig. 3.10.

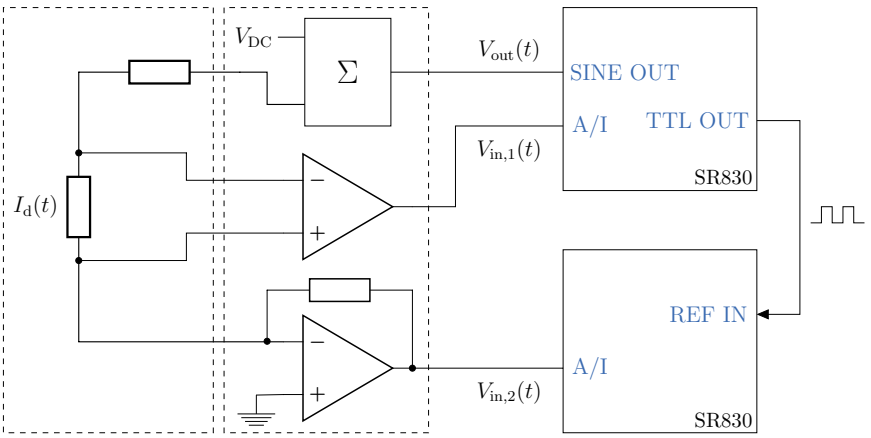


Figure 3.10: **Overview of the two lock-in amplifier setup for low-noise differential resistance measurements**. One lock-in provides a small AC bias to the isolated input of the IVVI power supply and a reference clock to lock-in 2 via a serial interface. The measured voltage and current over the device is then fed into the lock-in amplifiers, in which the Fourier component of current and voltage is determined by the lock-in technique.

### 3.2.2. MODIFICATIONS TO REDUCE EDDY CURRENTS

For performing the nuclear cooling cycle, the strength of the external magnetic field has to be swept over wide ranges. Variable magnetic fields $\dot{B}$ (by varying field strength or mechanical oscillations in static field) induce Eddy-current heating in electrical conductors according to $\dot{Q}_B \propto V\dot{B}^2/\rho$ with the volume $V$ of the conductor, and its specific electrical resistance $\rho$ [9]. To reduce Eddy-currents, conducting loops and large volumes of good conductors are reduced to a minimum. For this, the Cu device RF-shield (e in Fig. 3.9) is sliced on one side and the resulting gap is filled with stycast epoxy. Grooves are milled into the Cu coldfinger to reduce Eddy-current heating close to the chip. The described modifications lead to a measurable reduction in heat leak on-chip (Fig. 4.6 and Fig. 4.8).

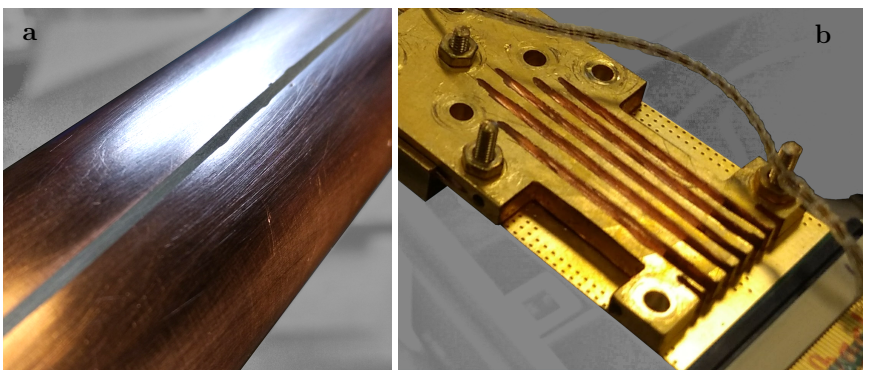


Figure 3.11: **Modifications to reduce Eddy currents in variable magnetic fields. a** Slotted RF shield (see Fig. 3.9 **e**). The slots are filled with Cu powder epoxy. **b** Grooves milled into the back of the Cu coldfinger.

## 3.3. ON AND OFF CHIP NUCLEAR MAGNETIC COOLING STAGE

For on- and off-chip nuclear magnetic cooling experiments, a custom nuclear stage is constructed, tailored to nuclear magnetic cooling of the leads of an electronic chip, and providing an ultracold environment for the chip stage. Such an approach is proven to reduce heat leaks into single CBT islands to values of < 100 aW [44, 47]. The concept on which basis the stage is constructed and an overview of the finalized stage is shown in Fig. 3.12. The assembly comprises a bulk stage made of Cu, which can be thermally decoupled from the $^3$He/$^4$He dilution refrigerator (MK126-700, see section 3.2), used as precooling stage, by a single Al heat switch. A secondary set of parallel In stages, made of In wire connections to the chip, refrigerates the device leads. A last stage of nuclear microrefrigerators, integrated onto the chip, cools thermally isolated regions on the chip. The parallel In stages have to be galvanically separated from the bulk Cu stage, but need to deposit a sufficient heat of magnetization during precooling into the dilution unit. In order to achieve this, the In stages are thermally anchored to the bulk Cu stage via insulating, thin epoxy resin films (see (7) in Fig. 3.12). The epoxy-resin films transfer heat to the mixing chamber according to $\dot{Q}_{\mathrm{th}} \propto AT^4$ (see section 3.3.3). The polymer film thermalization junctions transfer the heat of magnetization of the In stages to the dilution unit at millikelvin temperatures and thermally close when In stages and the bulk Cu stage are demagnetized after closing the main Al heat switch. When both stages cool to < 1 mK, heat transport over the epoxy films will drop by a factor of about $10^8$, providing further thermal isolation of the In stages. In total, a set of $N$ parallel In nuclear cooling stages can be magnetized and demagnetized by switching a single heat switch. The magnetic field required for magnetic cooling was applied by a coaxial superconducting solenoid with a rated field of 13 T (see section 3.2). The stage is constructed such, that the chip resides in the field center, in order to provide the maximum nuclear cooling power for the miniaturized nuclear refrigeration structures, having the smallest amount of nuclear working substance in the system. Electrical connections passing through higher stages are heaviliy filtered to attenuate high frequency electromagnetic noise. The lower stage filters are thermalized by utilizing meandering PCB lossy transmission line filters, thermally anchored to the Cu stage via epoxy films between the Cu tracks and the Cu stage. This, in addition, increases the area available for thermalization of the In stages.

### 3.3.1. STAGE CONSTRUCTION

The bulk Cu stage (1.7 mol, see (2) in Fig. 3.12) is milled out of 99.9995 % pure Cu and not annealed in order to reduce Eddy-currents, scaling with the specific resistance (see section 3.2.2). The In stages are made from 99.9999 % pure In (2 mm In wire, MaTeck GmbH), rolled out with a small nonferrous metal rolling pin, to flatten it onto a thin epoxy resin membrane on the Cu stage. Into these, 99.99 % pure In wires (1 mm In wire, MaTeck GmbH) are cold welded to ensure good low temperature interconnects, and routed down to the chip leads. For electrical connections to the chip, 99.99 % pure In wires (0.7 mm In wire, MaTeck GmbH) are cold welded to the 1 mm In wires on one side, and cold welded by pressing onto the electrodeposited In bonding pads on the chip (see Fig. 3.13). The In stages are annealed for 48 h at room temperature, using a turbo molecular pump before cooling the experiment down. Electrical connections from the upper In stages pass through the slotted lossy transmission line filter and connect to the

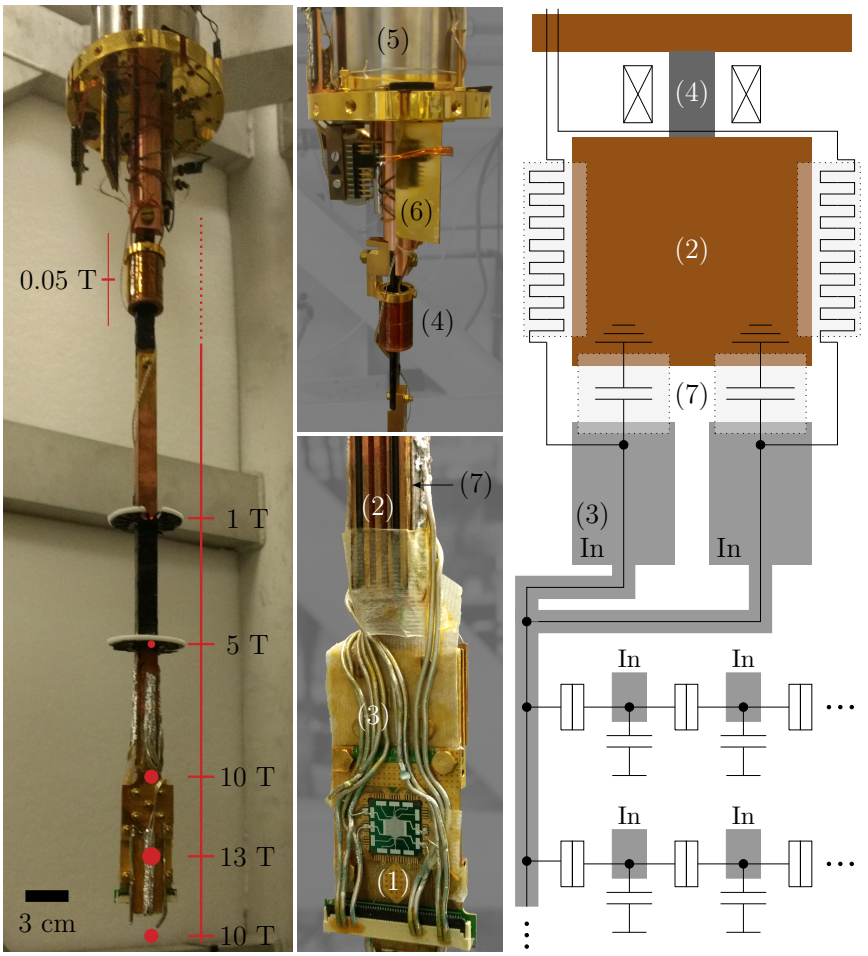


Figure 3.12: **Overview of the demagnetization stage used for on and off chip nuclear magnetic cooling.** (1) Chip mounted into a PCB motherboard which is screwed into a Cu coldfinger. (2) Slotted Cu stage which can be thermally decoupled from the mixing chamber (5) with a single Al heat switch (4). PCB lossy transmission line filters are glued into the slots of the Cu bulk stage (2) with Cu powder epoxy. Another filtering stage (6), consisting of a lossy transmission line and a 5th order RC filter in series (see Fig. 3.14 a), is thermally anchored to the mixing chamber plate. A parallel set of In nuclear stages (3) is cooling the device leads by magnetic cooling. The In stages are precooled via 30 µm thick thin epoxy resin films (7), providing galvanic decoupling but sufficient thermal coupling to the Cu stage. The right panel shows the schematic of the stage with a CBT mounted as device (see also Fig. 6.1). Patterned In thick films are used for on-chip nuclear magnetic cooling.

RC filter stage (see (6) in Fig. 3.12) via NbTi wires, with the Cu matrix removed in $HNO_3$ (1:25 aq). The Al heat switch is made by spot welding Al foils with Cu foils at the end [151] and was obtained from Leiden Cryogenics B.C. The connection to the heat switch is a single M4 bolt, with both mating surfaces Au plated. The heat switch resides in a field compensated region of the main magnet. In order to provide mechanical stability, the switch is fully encapsulated in epoxy, laced with Cu powder, for stiffness and noise

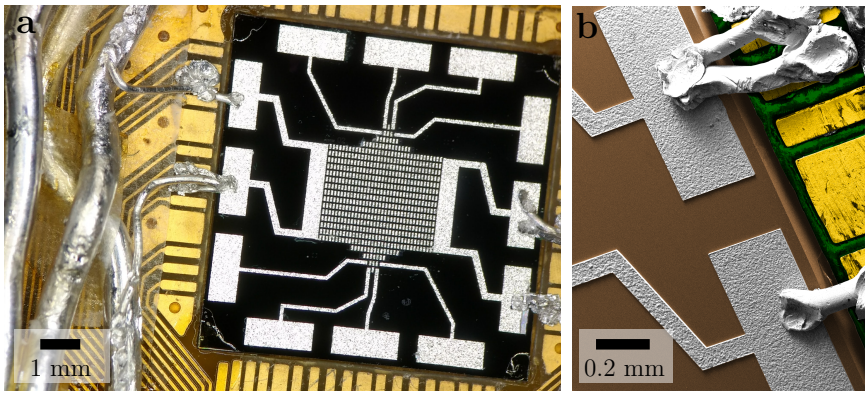


Figure 3.13: **Thermal contact of the In stages for cooling the leads to the plated In interconnects on the chip**. **a** In-In cold welding contacts between the parallel In stages and the chip (containing a CBT, see also section 6.2). **b** SEM micrograph of In-In welds made at room temperature, providing cryogenic metal-metal joints.



filtering. A small superconducting solenoid is used to control the heat switch. The heat switch shows closing behaviour with an applied current of ±90 mA through the solenoid. To be confident of a closed switch in a large magnetic field, a working current of 140 mA is used to close the switch. The superconducting electrical connections to the switch quenches when operated above 300 mA. The heat switch current is sourced from a constant current TTi EL3001R power supply unit (PSU). When the PSU is attached, the galvanic isolation from the measurement electronics is broken, thus, the leads to the PSU are physically unplugged when performing nuclear cooling cycles.

### 3.3.2. FILTERING OF ELECTROMAGNETIC NOISE

Both electronic filtering and microwave shielding is applied to provide a low thermal noise [152] environment for submilllikevin experiments. Electrical lines are filtered by custom made copper-powder filters [153] at each stage of the dilution refrigerator. The Cu powder-epoxy mixture is 1:3 by mass of copper to epoxy, matching the thermal expansion of pure copper. Voids in the epoxy casting were removed in a vacuum chamber. Loctite Stycast 2850FT, with catalyst CAT 24LV, was used as epoxy resin. The copper powder was supplied by ALDRICH Chemistry, and specified as copper powder (spheroidal), $20 \pm 10\,\mu$m, with 99% purity. The same mixture was used for all Cu powder filters. RF absorbing materials are installed in the volumes between plates to reduce the resonant quality factor of the spaces between the plates, and inner surfaces were covered with an infrared absorbing paint. A combined RC and copper powder filter is anchored to the mixing chamber plate of the dilution refrigerator (see (6) in Fig. 3.12 and Fig. 3.15 a). The RC filter component provides a sharp cutoff at 50 kHz. The entire board is covered by copper powder epoxy to prevent microwave leakage. The board accommodates 12 lines in arranged in 6 pairs. The lowest filtering stage are PCB lossy transmission line filters (see (2) in Fig. 3.12 and Fig. 3.15 c), mounted inside the slots of the copper nuclear cooled stage. These are made from printed circuit boards with a long meandering trace, resulting in an effective continuous element filter. The line resistance is $R = 4.6\,\Omega$. The

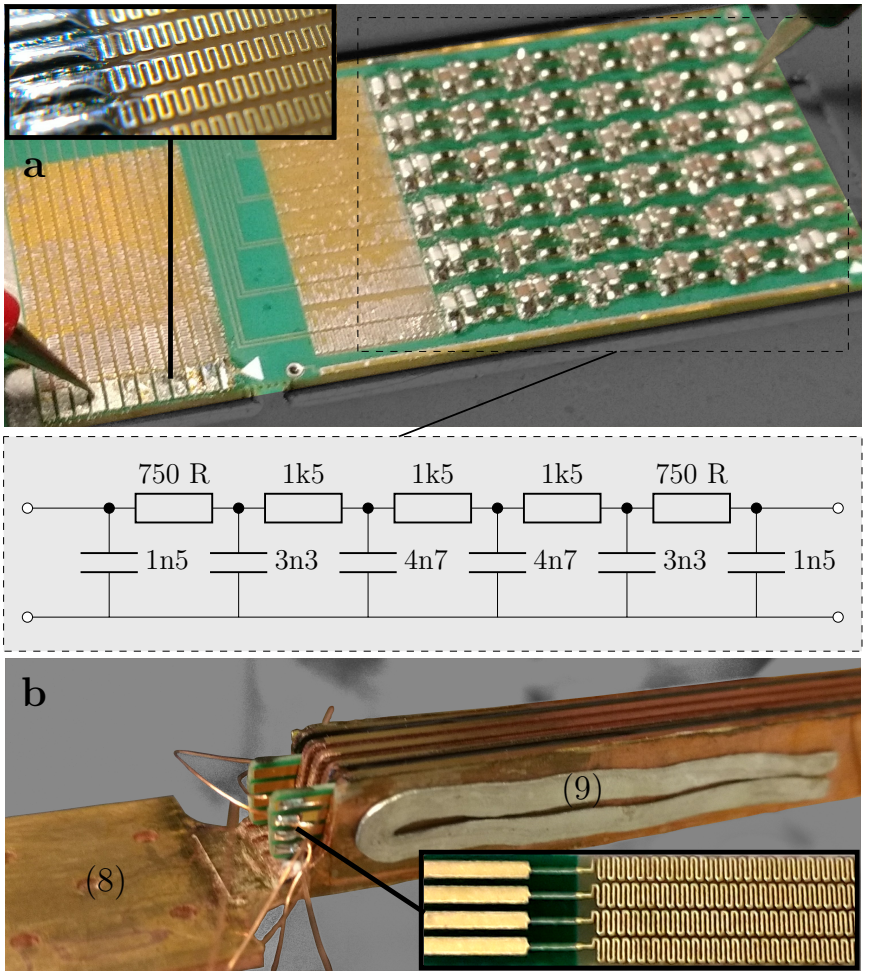


Figure 3.14: **Overview of the filters used in the on- and off-chip nuclear cooling stage. a** Image of the upper filter (see (6) in Fig. 3.12) consisting of a 11 component RC filter in series with a lossy transmission line. The PCB is later on covered with a mixture of Cu powder and Stycast (figure shows the bare board). **b** Image of the lower filter (see (2) in Fig. 3.12), consisting of long meandering Cu tracks on a PCB which is glued into the slots of the Cu stage with Cu powder-epoxy. Cu coldfinger (1) without the PCB chipcarrier and rolled out In wire (2).

PCBs have four meandering Cu traces on each side. The dual Cu layers and the 0.8 mm board thickness slot into 1 mm spaces in the copper stage. The gaps are then filled with Cu powder epoxy, giving rise to a capacitance of ~ 250 pF to ground.

### 3.3.3. THIN FILM THERMALIZATION

Thermalization over an epoxy resin layer is characterized by measuring the thermal conductivity of two 1 cm × 1.6 cm × 1 mm Cu pieces, pressed together with a 30 µm epoxy resin film in between. A calibrated $RuO_2$ resistance thermometer and a resistive heater

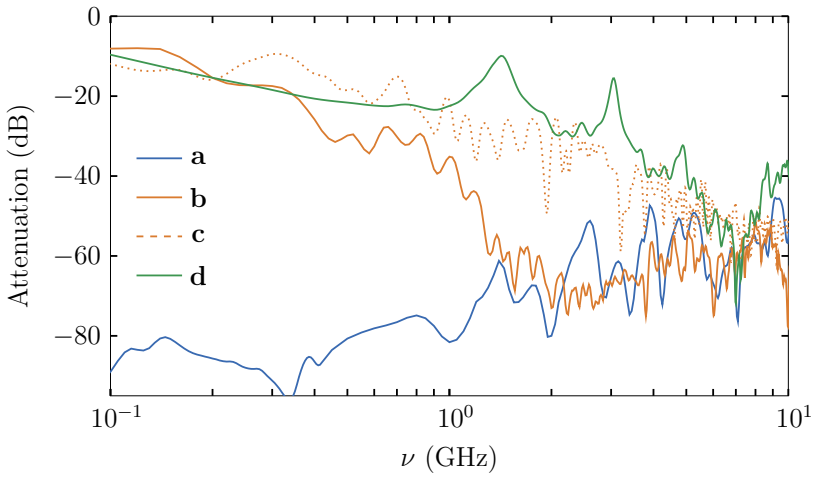


Figure 3.15: **Frequency dependent attenuation of the filters shown in Fig. 3.14, and the thermalizer shown in Fig. 3.16, measured with a network analyzer. a** Upper filter (see (6) in Fig. 3.12 and Fig. 3.14 a), **b** Lower filter, glued into the slots of the Cu stage (see (2) in Fig. 3.12 and Fig. 3.14 c) **c** Bare PCB of the lower filter. **d** Epoxy thermalizer which is shown in Fig. 3.16, attenuating high frequency signals via its capacitance to ground.

are glued onto the backside. The temperature $T_2$ on the backside of the thermalizer is measured at different mixing chamber temperatures $T_{\mathrm{MC}}$, set by the mixing chamber heater, and different heating levels provided by the heater on the backside of the stack. The results are fitted to $\dot{Q}_{\mathrm{th}} = kA(T^a - T^a_{\mathrm{MC}})$, parameterizing the heat transport over the epoxy film with the constants $k$ and $a$ and the contact area $A$. Measured data are shown in Fig. 3.16 The fitting procedure results in $a = 3.95$ and $k = 1.27 \cdot 10^{-4}\,\mathrm{W\,K^{-3.95}\,m^{-2}}$. The results obtained are close to parameters obtained in a similar experiment [154].

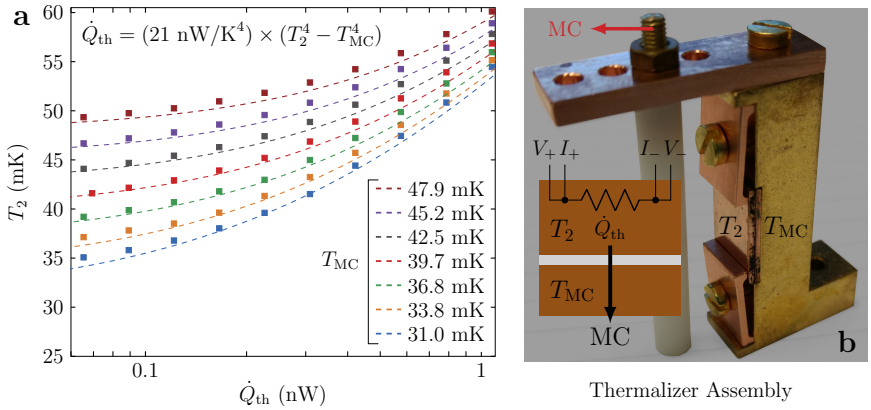


Figure 3.16: **Experimental characterization of a Cu-Epoxy-Cu thermalizer. a** Heat flow $\dot{Q}_{\mathrm{th}}$ through the epoxy resin layer, measured against the thermalizer temperature $T_2$ at different mixing chamber temperatures (given in the legend). **b** Image of the thermalizer characterization assembly without heater and thermometer.

## 3.4. COULOMB BLOCKADE THERMOMETRY

Coulomb blockade thermometry is implemented to track the electron temperature while performing ultralow temperature nuclear magnetic cooling experiments on-chip. In this section, application aspects of Coulomb blockade thermometry, as realized in this work, are introduced. Coulomb blockade thermometry (see also section 2.3.4) is realized based on tunnel junction arrays (in the following: tunnel junction array = CBT), fabricated according to the *ex-situ* scheme, described in section 3.1.1, combined with the indium integration scheme described in section 3.1.2. The tunnel via area and the island overlap area determine the island capacitance $C_\Sigma = 2C_0$, setting the range of the thermometer, according to Eq. 3.1. The on-chip integrated indium has an important double impact on the thermometer performance by enabling a nuclear cooling power and determining the volume available for electron-phonon coupling per island. For performing primary electron thermometry, the differential conductance $G$ (see section 3.2.1, Eq. 3.6) of the CBT is measured and normalized to the ohmic tunnel conductance $G_t = R_t \times m/n$ of a $n \times m$ tunnel junction array, reached at high bias. The full charging curve is fitted to the master equation tunneling model of a SET (Eq. 2.30 and Eq. 2.31) with $N_{\max} = 330$. A full charging curve can be fitted for the electron temperature $T_e$ and the charging energy $E_C = e^2/C_\Sigma \times (n-1)/n$, at given number of junctions in series $n$. This self-calibration procedure is performed as follows: The mixing chamber temperature is set to a range of different temperatures using a resistive heater. After a sufficiently long (10 - 30 min) thermal relaxation time, where all parts of the dilution refrigerator come to thermal equilibrium, $G/G_t$ is measured over a defined voltage bias window. The set of isothermal charging curves (see Fig. 3.18 a and b) is fitted to the master equation tunneling model for a common $C_0$. For all devices fabricated with the *ex-situ* tunnel junction process the uncertainty in $C_0$ was always < 5 % within a set of isothermal charging curves.

Some devices show a non-isothermal behaviour at low-temperatures, in a way that the tunnel current is enhanced at finite voltage bias due to insufficient electron-photon thermalization (Fig. 3.17 a). When the CBT is cooled by dilution refrigeration, the parasitic heat flow into the conduction electrons on the islands, due to Joule-heating and thermal noise sources, has to be balanced by heat removal via phonon emission. Due to the diminishing electron phonon coupling strength towards ultralow temperatures (Eq. 2.4), the heat input due to dissipation of bias current can lead to a finite bias self-heating of the sensor above the equilibrium temperature at zero bias, making a charging curve at constant mixing chamber temperature non-isothermal. Bias dependent overheating is usually corrected by a non-isothermal expansion to the master equation tunneling model, in which the self-heating of the CBT is analytically captured [42, 69]. The thermal balance, taking into account heat flow between a single island $k$ and the environment, as well as between neighbouring islands $k \pm 1$ is modelled as (see also Eq. 7.8 and Eq. 7.9)

$$\dot{Q}_{\text{island}} = \frac{V_k^2}{R_t} + \sum_{\pm} \frac{L_0}{2R_t}\left(T_{k\pm1}^2 - T_k^2\right) - \Sigma V\left(T_k^5 - T_p^5\right) + \dot{Q}_{\text{res}} \tag{3.7}$$

with the Lorenz number $L_0$, the junction voltage $V_k = V/n$, and the residual heat leak $Q_{\text{res}}$. The island temperature $T_k$ is the electron temperature on the island. The enhancement of the electron temperature above the substrate temperature $T_k > T_p$ is a com-

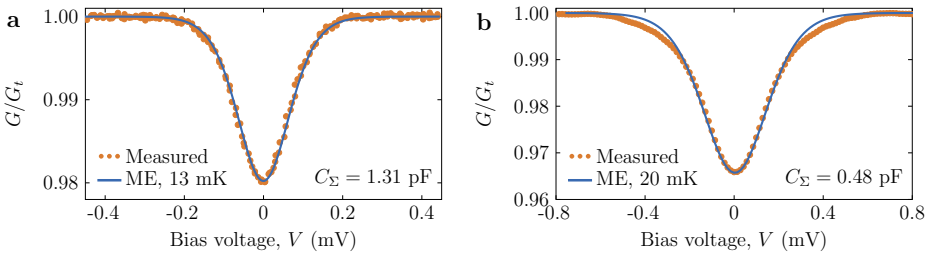


Figure 3.17: **Comparison of isothermal charging curves regarding self-heating**. **a** ULT charging curve a CBT with $n = 26$, $C_0 = 1.31$ pF and an In volume of $280 \times 400 \times 25.4$ µm$^3$ per island. **b** ULT charging curve of a CBT with $n = 36$ and $C_0 = 0.48$ pF and an In volume of $50 \times 140 \times 25.4$ µm$^3$ per island, showing finite-bias self-heating. The curves are fitted to a the master equation (ME) tunneling model described in section 2.3.4.



bination of insufficient thermalization through electron-phonon scattering and thermalization over the tunnel junctions. The latter can be usually neglected, leading to $\dot{Q}_{\text{island}} = V_k^2/R_t - \dot{Q}_{\text{e-p}} + \dot{Q}_{\text{res}}$. At a given heat leak, self-heating of the CBTs fabricated in this work should predominantly depend on the volume of the electroplated In bars on the islands. The correct scaling of finite bias overheating behaviour of different CBT devices can be experimentally shown to scale also in the expected way with the In island volume as can be seen in Fig. 3.17.

The functionality and scalability of the CBTs fabricated in this work is evaluated by comparing isothermal charging curves of the devices to the mixing chamber temperature and then comparing the charging behaviour of different devices at the same electron temperature. In Fig. 3.17 a and b, isothermal charging curves of two different CBTs, at different mixing chamber temperatures, are plotted for comparison. Besides self-heating, the dependency of the lowest achievable electron temperature on the In island volume can be clearly demonstrated: the CBT in panel b is well thermalized with the mixing chamber temperature down to about 10 mK, while a CBT without integrated In is overheated already at >20 mK. As can be seen in Fig. 3.18 c, the CBTs with different island overlap area, but identical interlayer dielectric thickness, behave as expected with the island capacitance $C_0$ scaling in a linear way with the the Al electrode overlap area $A_{\text{el}}$, as described by Eq. 3.1. This establishes the correct behaviour of the CBTs as well as a good scalability of the *ex-situ* tunnel junction process.

Once the charging energy $E_C = e^2/C_\Sigma \times (n-1)/n$ is obtained by the self calibration procedure, the CBT is operated in secondary mode in which the temperature is obtained by the zero bias tunnel conductance $G(0)/G_t$ with analytical approximation of Eq. 2.33 (see e.g. 5.20). Operating the CBT is secondary mode avoids self-heating of the sensor at finite bias. Due to the magnetoresistance of the junction arrays (see section 3.1.1, Fig. 3.3), $G_t$ is measured as a function of magnetic field and used as a field dependent calibration parameter. The offset-bias is compensated by a dynamic tracking procedure in which a bias compensation according to the differential of the differential conductance is applied (see 3.2.1). The width of the bias window in which the differential is obtained is varied as a function of peak curvature to avoid averaging (see for example Fig. 6.4).

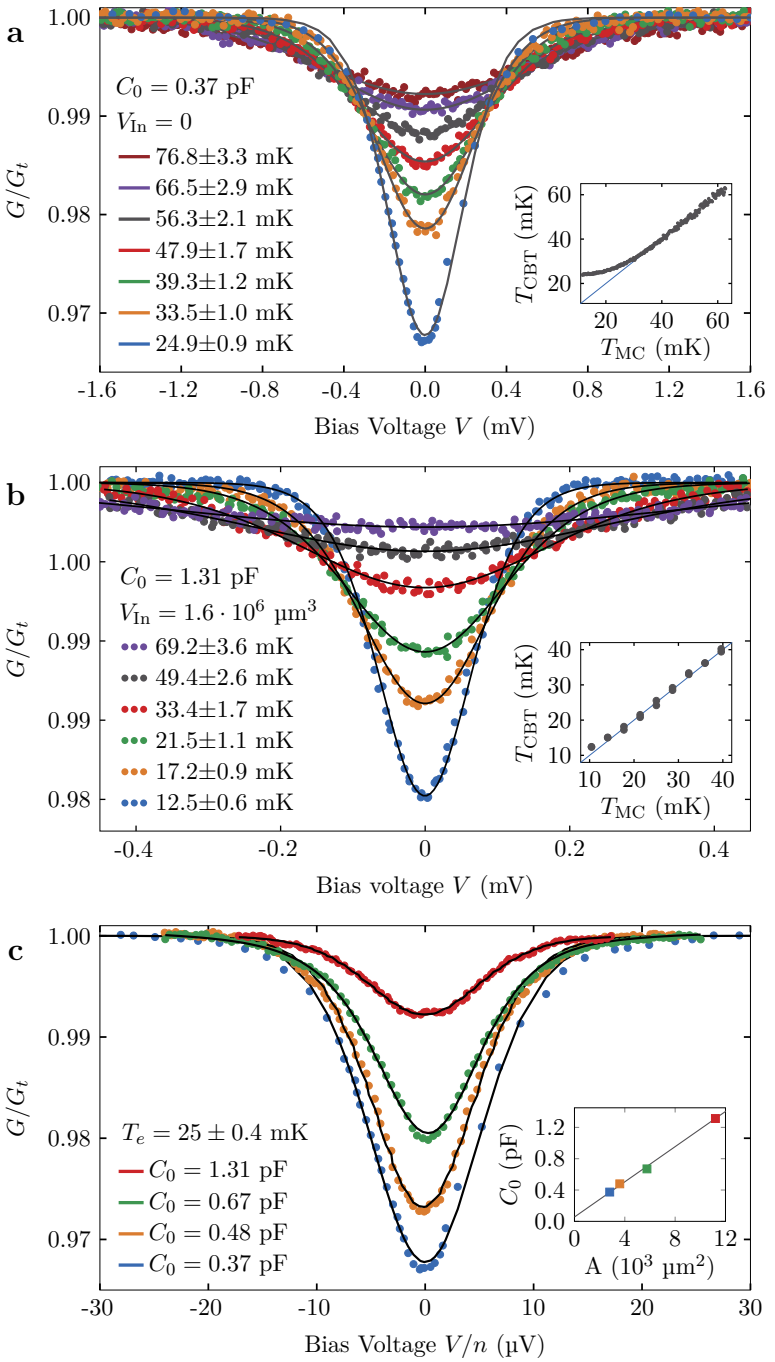


Figure 3.18: **Overview of the thermal response of the fabricated CBTs with respect to device geometry. a** Isothermal charging curves of an 36×15 junction array without In on the islands. **b** Isothermal charging curves of an 26×7 junction array with 280 × 400 × 25.4 µm$^3$ large In islands integrated onto the islands. **c** Isothermal charging curves of CBTs with different island capacitance $C_\Sigma$ at the same temperature. Inset: the electrode overlap area is plotted against the coupling capacitance $C_0 = C_\Sigma/2$, obtained with the master equation.

# 4

# On-Chip Nuclear Magnetic Cooling with Indium

*There is plenty of room at the bottom.*

Richard Feynman (1918-1988)

This chapter is based on N. Yurttagül, M. Sarsby, A. Geresdi, *Indium as a High-Cooling-Power Nuclear Refrigerant for Quantum Nanoelectronics*, Physical Review Applied **12**, 011005 (2019)

## 4.1. INTRODUCTION

Quantum electronics relies on the precise control of electronic states in nanostructures, which is possible if the energy separation of a quantized spectrum is much higher than the thermal energy $k_B T$. Thus, efficient cooling of electrons is vital for solid state nanoelectronics and is an important design consideration for existing scalable quantum technologies. Access to novel states of matter such as electron-nuclear ferromagnets [155–157], non-Abelian anyons in fractional quantum Hall states [34, 35], topological insulators [158] or exotic superconductivity [159–161] requires further progress in cooling of nanoelectronics, approaching the microkelvin regime (see also sections 8.2, 8.3).



Electron temperatures of the order of 10 mK are accessible in semiconductor and metallic nanostructures by mounting the chip, containing the devices, on an insulating substrate, cooled by a dilution refrigerator. The lowest achievable electron temperature is limited by the heat transferred from the electrons at a temperature of $T_e$ to cold phonons at a temperature of $T_p$ (Eq. 2.4), while the electron gas is constantly heated by the dissipation of electrical signals and electrical noise. In the electron-phonon coupling limit (see section 2.1.1), a residual electronic heat leak of 10 aW to a well-shielded nanostructure [162] with $V = 1\,\mu m^3$ already yields $T_e \approx 25$ mK even as $T_p$ approaches zero. Increasing the coupling volume $V$ by electrodeposition of thick metal films [46], and by improving thermalization, utilizing liquid $^4$He immersion cells, led to steady state values of $T_e \approx 4$ mK [43, 46, 163] in specially built dilution refrigerators. The key to reduce the electron temperature further involves coupling the electron system to a cold bath without the necessity of heat transport via phonons. This can be achieved by chipscale nuclear magnetic cooling (see sections 2.1.3, 2.2.4), [45, 47]. In the limit of small Zeeman splitting compared to $k_B T_n$, the magnetization of the nuclear spin system is $M \propto B/T_n$ at a magnetic field of $B$ and a temperature of $T_n$. $T_n$ can be reduced by adiabatically lowering the magnetic field from $B_i$ to $B_f$. In the absence of an external heat load and nonmagnetic level splitting, $M$ stays constant and consequently $T_{n,f} = T_{n,i} \times B_f/B_i$ [13, 16, 20]. This technique has become the workhorse of ultralow-temperature physics, with the lowest attainable temperature of $T_n \sim 100$ pK [164]. On-chip nuclear magnetic cooling utilizes the spin-lattice relaxation to cool conduction electrons close to the temperature of a cold nuclear spin system which is co-integrated with the electronic device. The direct cooling power of the nuclear spins on the electron gas $\dot{Q}_{\text{e-n}}$ is given by (section 2.1.3), [9, 165]:

$$\dot{Q}_{\text{e-n}} = \tau_1^{-1} n C_n \left(T_n - T_n^2/T_e\right), \tag{4.1}$$

where $C_n$ (Eq. 2.11) is the nuclear heat capacity, $n$ the number nuclei in moles and the spin-lattice relaxation time $\tau_1 = \kappa/T_e$ (see section 2.1.3). If the magnetization is weak, $C_n$ can be approximated by the Schottky law $C_n = \alpha B^2/T_n^2$. Here, $\alpha = N_A I(I+1)\mu_n^2 g_n^2/3k_B$ with the Avogadro constant $N_A$. Then, Eq. 4.1 reads $\dot{Q}_{\text{e-n}} = \alpha n \kappa^{-1} B^2 (T_e/T_n - 1)$. The choice of the nuclear refrigerant is based on finding a material with a large $C_n$, while keeping $\kappa$ small to have efficient coupling to the electrons. The material-dependent figure of merit $\alpha/\kappa$ allows to compare different materials. In addition, the experimental implementation should allow for a large $n$ and $B_i^2/T_{n,i}^2$ ratio for efficient cooling and long cold time, while the reachable base temperature of a nuclear refrigerator is on the other hand determined by details of the nuclear spin level spectrum (see section 2.2.4).

Thus far, Cu was the sole material used for chipscale nuclear cooling [45, 47, 53]. Naturally occuring Cu nuclei have a spin of $I = 3/2$ and a large g-factor of $g_n = 1.5 - 1.6$ (see Tab. 2.2), yielding a molar Curie constant of $\alpha_{\mathrm{Cu}} = 3.22\,\mu\mathrm{J\,K\,T^{-2}\,mol^{-1}}$ [9]. Bulk Cu nuclear demagnetization stages benefit from an extremely low nuclear ordering temperature [166], which allows to magnetically cool Cu nuclei to $T_n < 1\,\mu\mathrm{K}$ [167]. However, the weak electron-nucleus coupling given by $\kappa = 1.1 - 1.3\,\mathrm{Ks}$ (Tab. 2.2) is a limitation for electron cooling in Cu. Furthermore, the absence of a strong Ruderman-Kittel interaction and the absence of nuclear quadrupole coupling (due to the cubic crystal symmetry of Cu), leads to a strong decrease of the effective nuclear heat capacity towards small magnetic fields. Since $C_n$ is extensive, the latter can be compensated for by scaling up the amount of refrigerant which is simple in bulk stages but extremely complicated if thin-film materials are used. To overcome this limit, In is introduced as an on-chip nuclear refrigerant in this work. In features a shorter spin-lattice relaxation time with $\kappa_{\mathrm{In}} = 0.08 - 0.09\,\mathrm{Ks}$ (Tab. 2.2), and a large nuclear spin of $I = 9/2$, with $\alpha_{\mathrm{In}} = 13.8\,\mu\mathrm{J\,K\,T^{-2}\,mol^{-1}}$, enhancing the molar nuclear magnetic cooling power by a factor of $\frac{\alpha_{\mathrm{In}}}{\kappa_{\mathrm{In}}} / \frac{\alpha_{\mathrm{Cu}}}{\kappa_{\mathrm{Cu}}} = 60$ compared to Cu. The splitting of nuclear spin eigenenergies due to interaction of the nuclear quadrupole with the electric field gradient in tetragonal In crystals of about 0.23 mK (Tab. 2.2) stabilizes the cooling power towards small magnetic fields, where the system attains a fully nuclear quadrupole heat capacity while the magnetic heat capacity vanishes. Quadrupolar coupling limits the lowest attainable $T_n$ with In to about 100 µK (see Fig. 2.5). In addition, the magnetic field has to be kept above $B_c = 28\,\mathrm{mT}$ to avoid the thermal decoupling of electrons by the superconducting phase transition [168].



To demonstrate the applicability of In as a nuclear refrigerant for nanoelectronics, the electron temperature $T_e$ on a nanoelectronic device, co-integrated with In as nuclear refrigerant on-chip, is directly measured while ramping $B$ to perform the nuclear demagnetization. While primary electron thermometry in the millikelvin regime has been realized in several ways [40, 55, 130, 131], Coulomb blockade thermometry (sections 2.3.4, 3.4) is utilized due to its lack of sensitivity to magnetic field [134]. CBTs rely on the universal temperature dependence of single charge localization in mesoscopic metallic islands [56] and have been proposed to provide the reference scale for millikelvin range thermometry [133]. Coulomb blockade thermometry is furthermore not constrained by material properties regarding the thermometer range which makes it an ideal candidate for extending mesoscopic electron thermometry into the microkelvin temperature regime.

## 4.2. EXPERIMENTAL SETUP

A Coulomb blockade thermometer with In cooling blocks, integrated onto the islands, is fabcricated according to section 3.1. Fig 4.1 shows an overview of the device and how it is thermally anchored to the fridge, as well as the geometrical and electrical parameters of the thermometer. The islands are formed within $n = 36$ tunnel junctions, each with a total capacitance $C_\Sigma = 2C_0 + C_g$, determining its charging energy $E_C = e^2/C_\Sigma \times (n-1)/n$. The zero bias conductance of the device, $G(0)$, decreases by $\Delta G = G_t - G(0) \sim G_t E_C / k_{\mathrm{B}} T_e$ in the limit of $E_C \ll k_{\mathrm{B}} T_e$ [56] and retains its universal behavior down to $1/u \approx 0.4$, with higher order corrections if the universal regime of charging is defined by the charge stability of a SET [132], (see also chapter 5 for details). The charging energy $E_C$ is set by

the overlap area between adjacent islands (see Eq. 3.1), which is independent of the tunnel junction area determining the junction resistance $R_t$ (Eq. 2.40). This flexibility in design is enabled by creating the Al-$AlO_x$-Al tunnel junctions *ex-situ* in vias, through the interlayer dielectric (section 3.1), [141]. The junction area is $0.55 \pm 0.1$ µm$^2$ with a $R_t = 12.8 \pm 0.8$ kΩ µm$^2$ at room temperature, close to previously reported values [141], yielding a device resistance $1/G_t = 55.8$ kΩ in an array of $n \times m = 36 \times 15$ junctions. The device resistance is temperature-dependent and saturates at 89 kΩ below $T = 1$ K, owing

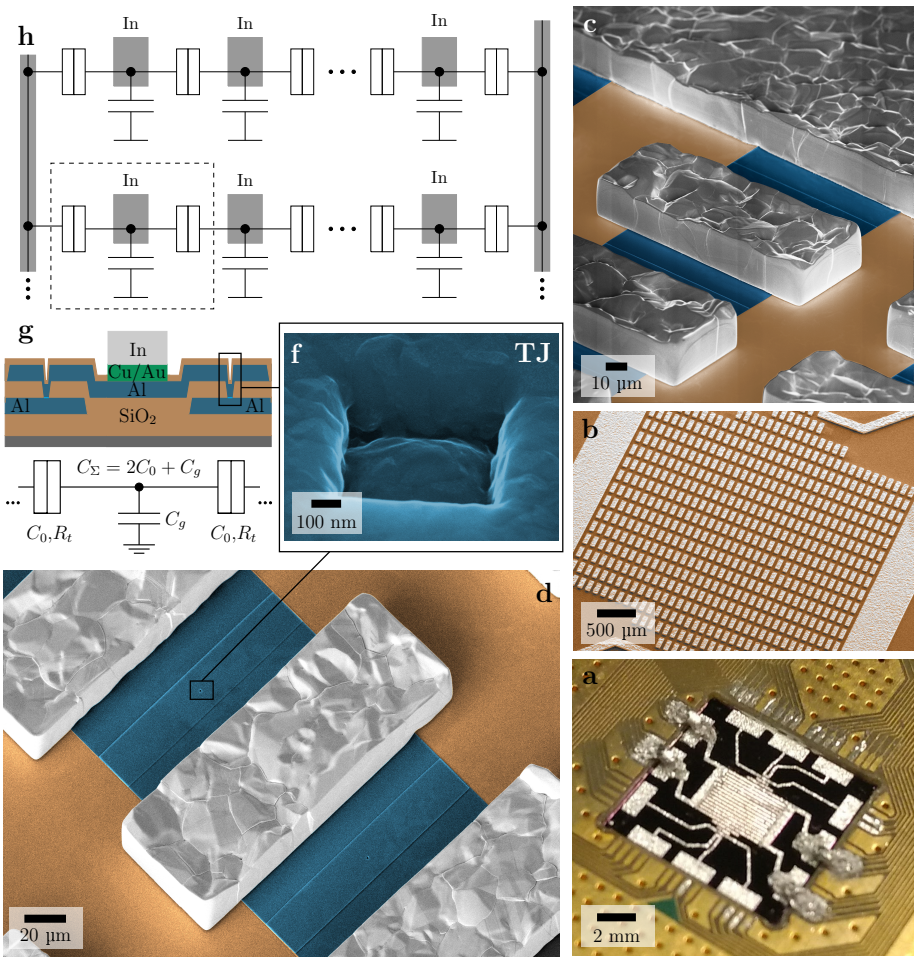


Figure 4.1: **Overview of the cryogenic experimental setup and the CBT device used for on-chip nuclear magnetic cooling and thermometry.** The CBT is made of an array of 36 × 15 tunnel junctions with electrodeposited In cooling bars (140 × 50 × 25.4 µm$^3$) for local nuclear magnetic cooling of each island. **a** Overview of the chip, containing the CBT, bonded to a PCB by In-In cold welding. **b** Low magnification SEM micrograph of the device shown in a. **c** SEM micrograph of a single island, connected to the electrodeposited In leads. **d** SEM micrograph of a CBT island. **g** Cross section of a single CBT island with schematics: $C_0$ is defined by the overlap area of the Al electrodes and the $SiO_2$ film thickness **f** Tunnel junction (TJ). **h** Schematic overview of the CBT.

to the height of the $AlO_x$ tunnel barrier [169]. The nuclear magnetic cooling functionality is integrated by electroplating In blocks with defined volume onto each island (see section 3.2). With the used 25.4 µm thick films, an In integration density of 1.6 pmol/µm$^2$ is achieved, determining the nuclear cooling power $\dot{Q}_{\text{e-n}}$ (see Eq. 4.1), per unit area.

The device is mounted onto a Cu carrier block inside an RF-tight enclosure, cooled by an unmodified commercial wet dilution refrigerator. The mixing chamber temperature is measured by a calibrated CMN thermometer and reaches 5 mK. (see section 3.2 for further details regarding the cryogenic setup). The CBT is attached by In-In room temperature welding (Fig. 4.1) in a four wire geometry. Twisted pairs of the electrical wiring pass through a Cu powder [170] and a discrete component 3rd order RC low-pass filter with cutoff frequency 50 kHz to reduce the thermal noise into the device. The CBT device was designed with an island overlap area of $w_1 \times w_2 = 18 \times 100\,\mu\text{m}^2$ (Fig. 3.2) and an $SiO_2$ interlayer dielectric with an initial thickness of $d_{\text{ILD}} = 230\,\text{nm}$ (thinned down further by Ar milling). With $\varepsilon_r = 3.5 - 4.2$ for sputtered $SiO_2$ [171], this gives rise to an expected capacitance of $C_0 = 260 - 580\,\text{fF}$ (Eq. 3.1, assuming thinning of the ILD by not more than 100 nm). The charging energy $E_C$ is determined by simultaneously fitting a set of $G(V)$ curves against a master equation single-electronics model [56], (see sections 3.2.1, 3.3) at different $T_{\text{CMN}}$ values, set by heating the mixing chamber. The differential conductance $G(V)$ of the CBT is measured using standard low frequency (18.31 Hz) lock-in techniques as a function of the DC voltage bias, $V$ (see sections 2.3.4). Some of the obtained isothermal charging curves are plotted in Fig. 4.2. The fit results in $C_0 = 479 \pm 1.9$ fF ($E_C = 0.15$ µeV). This corresponds to the CBT working as primary thermometer between 1.5 mK and 250 mK. This range is limited by offset charges on the low side [132] and instrumental resolution on the high side. The measured electron temperature $T_{\text{CBT}}$ agrees well with $T_{\text{MC}}$ for temperatures above 30 mK, but decouples and saturates at about 20 mK,

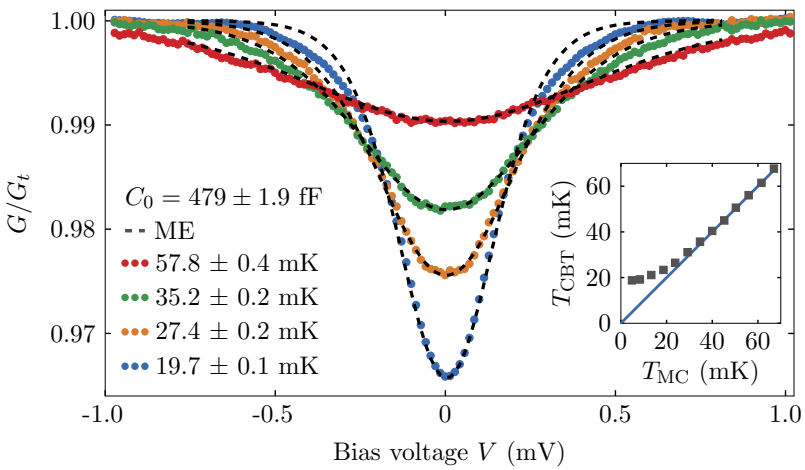


Figure 4.2: **Isothermal charging curves of the CBT used for on-chip nuclear cooling experiments.** the tunnel conductance $G$ is normalized with the asymptotic tunnel conductance $G_t$ and fitted to a master equation model (dashed). Inset: $T_{\text{CBT}}$, measured against the mixing chamber temperature (set with resistive heater).

demonstrating the inefficiency of phonon cooling. After about a week after cooldown the temperature of the CBT at base temperature decreases to 15 mK. This effect was seen in all studied CBTs and is probably caused by time dependent heat leaks [9].

## 4.3. HIGH FIELD NUCLEAR MAGNETIZATION EFFICIENCY

As described in section 2.2.4, a nuclear magnetic cooling cycle consists of an isothermal magnetization step, followed by gradually removing the field to reduce the nuclear spin temperature. Since the metallic nuclear refrigerant is heated in a variable magnetic field $\dot{B}$, the magnetization step usually does not result as an isothermal process. In the present case the nuclear spin magnetization involves removal of heat of magnetization via electron-phonon interaction. Field dependend heat leaks are dominated by Eddy-current heating, occuring in a rectangular electrical conductor, exposed to a changing magnetic field according to $\dot{Q}_e = \Theta V \dot{B}^2/\rho$ [9]. Here, $V$ is the specimen volume, $\rho$ the specific resistivity, $\Theta = d^2k^2/16(1+k^2)$ a geometry factor with $k = w/d$, where $d$ and $w$ is the thickness and width of the specimen respectively. For the In cooling bars with $V \approx 1 \cdot 10^{-13}$ m$^3$, $\rho \approx 8 \cdot 10^{-8}$ Ω m, and $\dot{B}$ up to 100 mT/s (which would correspond to a rather severe movement of the chip in the field), heating due to Eddy-currents in a single island will be of the order of $10^{-20}$ W, negligible compared to other heating sources.

Fig. 4.3 shows CBT temperature, measured during different precooling runs at fields of 12 – 13 T. Precooling the CBT, a typical $T_{CBT} \approx 20$ mK is found after 24 h and $T_{CBT} \approx 16$ mK after 72 h of precooling at $B_i = 12.8$ T. After a long time the CBT reaches about the same temperature as in small fields (see section 4.2). This is expected due to the absence of any further thermal impedance to the mixing chamber as e.g. a heat switch.

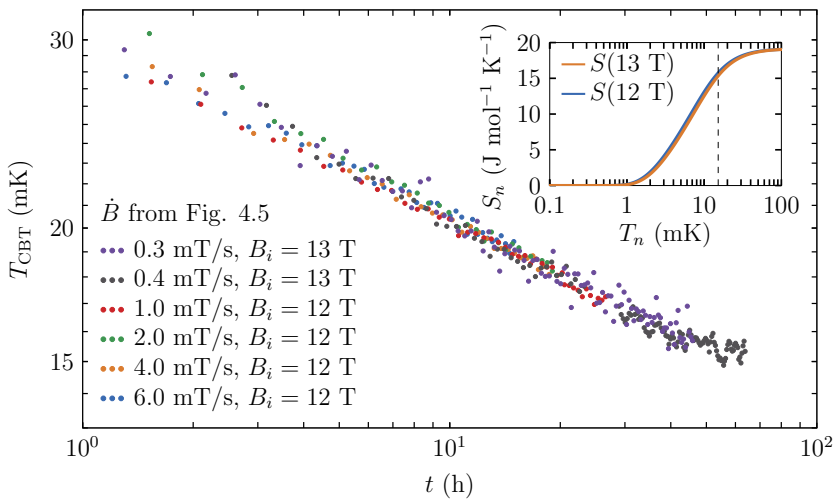


Figure 4.3: **Nuclear magnetization performance of the In on-chip refrigerant at 12 T - 13 T.** The different magnetization attempts are labeled according to the field ramp rate in the demagnetization step performed afterwards (see 4.5). In high field, the equilibrium temperature of $T \sim 15$ mK is reached after 3-4 days. Inset: the obtained $T_{CBT}$ and the single island nuclear entropy (Eq. 2.19) reveal an entropy removal of about 17%.

## 4.4. ON-CHIP NUCLEAR DEMAGNETIZATION WITH CONTINUOUS COULOMB BLOCKADE THERMOMETRY

To perform the nuclear demagnetization, the device is precooled at $B_i$ (see section 4.3), and the field strength is reduced to $B_f$ (see also section 2.3.4), with a constant rate $\dot{B}$, while measuring the normalized zero bias tunnel conductance, $G(0)/G_t$, of the CBT. For the present experiments, the starting field is chosen as $B_i = 12-13$ T and the final field is $B_f = 40$ mT. The differential conductance minimum is continuously tracked in a dynamic bias window in order to compensate for voltage bias drifts over the several hours timescale of the nuclear cooling experiments. The voltage bias window is continuously updated following the zero bias point, determined by the measurement software based on the nonlinear $G(V)$ curve. The differential conductance, measured during a demagnetization step with 0.4 mT/s in a dynamical bias window, is shown in Fig. 4.4 a (see also Fig. 4.5). Towards reducing the magnetic field, the differential conductance drops and the curvature of the charging peak becomes larger, narrowing the used bias window.



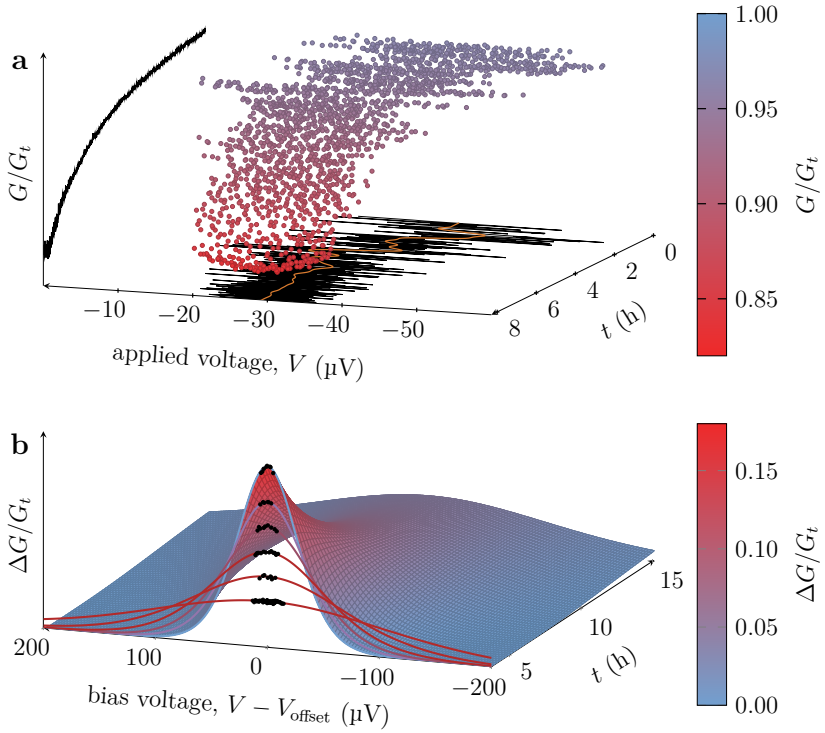


Figure 4.4: **Overview of the dynamic offset-bias compensation and thermometry procedure. a** Normalized CBT zero bias conductance $G/G_t$, measured with offset-bias compensation according to the measured slope in $\Delta V/\Delta I$, plotted against the demagnetization time $t$, at constant field ramp rate of $\dot{B} = 0.4$ mT/s, and $t = 0$, at $B = B_i$. A better localization of the peak with reducing the field (and thus also temperature) can be clearly seen in terms of a reduced bias window and stable offset bias. **b** The measured tunnel conductance around zero bias is compared to a SET master equation model of single electron tunneling (see. section 2.3.4).

The differential conducance, measured over a small bias window, is compared to the master equation model (see section 2.3.4), with respect to the curvature of the peak around zero bias. For this, the differential conductance is calculated in a large bias window, with the zero bias region of the measured conductance fitted to a temperature $T_e$. The results are illustrated in Fig. 4.4 b. For a better visibility, $\Delta G/G_t = 1 - G/G_t$ is plotted instead of $G/G_t$. It can be seen that the peak curvature is in excellent agreement with the model calculations and thus the temperature calibration according to the measured zero-bias conductance. This analysis confirms the functionality of the CBT throughout the entire temperature range of the experiment, and thus enables continuous thermometry during on-chip nuclear demagnetization. The measured electron temperature for a set of demagnetization attempts with varying magnetic field ramp rate, and starting temperature between 16 – 20 mK, is summarized in Fig. 4.5. For all attempts, the strong electron-nucleus coupling results in a drop of the electron temperature $T_{\mathrm{CBT}}$ from its initial value, while $T_{\mathrm{MC}} \approx 5$ mK remains essentially constant (see Fig. 4.6 for details). From the results shown in Fig. 4.5 and 4.6, the lowest electron temperature of $T_e = 3.2 \pm 0.1$ mK is obtained for the lowest starting temperature of 15.5 mK and a field ramp rate of 0.4 mT/s. This temperature surpasses reported values for on-chip nuclear magnetic cooling, reaching $T_e = 4.7$ mK by utilizing Cu as nuclear refrigerant [45], and demonstrates superior performance compared to phonon-cooled devices, where steady values above $T_e = 3.9$ mK were measured in a custom-built dilution refrigerator [46].

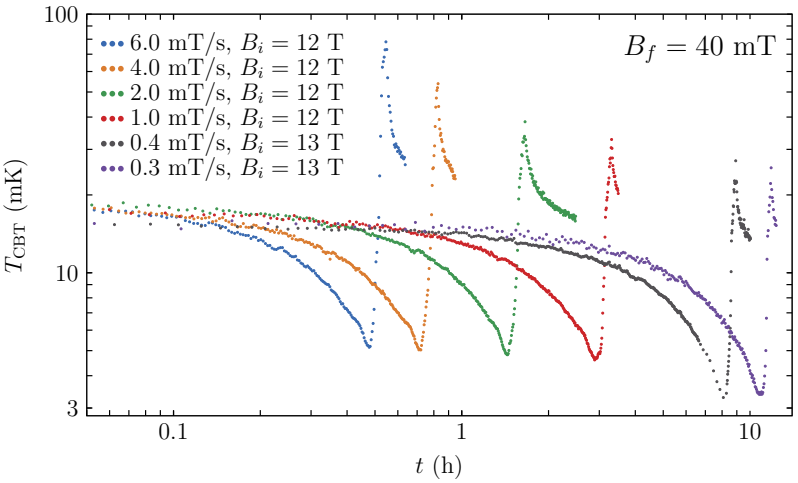


Figure 4.5: **On-chip nuclear magnetic cooling runs with varying field ramp rate.** The electron temperature measured with the CBT is plotted against the demagnetization time for a given ramp rate $\dot{B}$ with $t = 0$ at $B = B_i$.

In each run, upon reaching the lowest temperature at $B \approx 2$ T, the stage warms up quickly, and thermally relaxes to the starting temperature after the field ramp stops at $B_f = 40$ mT. This behaviour indicates that the nuclear heat capacity depletes by parasitic heat leaks before the field ramp is finished. All data exhibit a similar behaviour, with a minimum temperature well below $T_{\mathrm{CMN}} \approx 5$ mK. This behaviour is consistent with the results ob-

tained in [45] with on-chip integrated Cu islands. Remarkably, the fraction of starting temperature to end temperature seems to be invariant to the field ramp rate. The runs with 0.4 mT/s and 0.5mT/s reach a lower end temperature due to a higher starting temperature and a higher starting field (13 T vs. 12 T), compared to the other runs.

## 4.5. MODELLING THE NUCLEAR COOLING PROCESS

In order to determine the heat input by parasitic heating for each demagnetiation run (see Fig. 4.5), the time evolution of $T_n$ and $T_e$ on a single island is numerically calculated. For this purpose, the weak thermal coupling to phonons (Eq. 2.4) is neglected and it is assumed that the heat flow between the electrons and nuclei is described by Eq. 2.14

The treatment is complicated by the presence of nuclear quadrupole interaction (see section 2.3.4). Since cooling can not be kept for fields $B < 1$ T, where the Zeeman splitting should still dominate, the nuclear heat capacity is calculated by taking the quadrupolar interaction in the high field limit, assuming an axially symmetric nuclear charge distribution ($\eta = 0$, Eq. 2.22). Given that the polar angles $\phi$ and $\theta$ parameterize the orientation of the principal $x_3$ axis of the electric field gradient tensor (see section 2.3.4 and [97]), the quadrupole Hamiltonian (Eq. 2.22) is transformed into the basis of the Zeeman-Hamiltonian, where the total nuclear energy spectrum is [172]

$$\mathbf{H} = \mathbf{H}_Z + \mathbf{H}_Q = -g_n\mu_n B\mathbf{I}_z + \frac{3}{2}\frac{eQV_{zz}}{4I(2I-1)}\left(\cos^2\theta - 1\right)\left(3{\mathbf{I_z}}^2 - \mathbf{I}^2\right) \tag{4.2}$$

$$+\frac{3}{2}\sin\theta\cos\theta\left[(\mathbf{I}_z\mathbf{I}_+ + \mathbf{I}_+\mathbf{I}_z]\,\mathrm{e}^{-\mathrm{i}\phi} + (\mathbf{I}_z\mathbf{I}_- + \mathbf{I}_-\mathbf{I_z})\,\mathrm{e}^{\mathrm{i}\phi}\right] + \frac{3}{4}\sin^2\theta\left(\mathbf{I}_+^2\,\mathrm{e}^{-2\mathrm{i}\phi} + \mathbf{I}_-^2\,\mathrm{e}^{2\mathrm{i}\phi}\right), \tag{4.3}$$

With the commutation relations of angular momentum operators, $[\mathbf{I}_z, \mathbf{I}_\pm] = \pm\mathbf{I}_\pm$, it can be seen that the terms depending on $\phi$ are not diagonal in the eigenbasis of the Zeeman-Hamiltonian. Assuming $g_n\mu_n B > eQV_{zz}$ is well satisfied at $B \geq 1$ T (see Tab. 2.2) for all $m_z$. Off-diagonal terms are thus taken as perturbation and

$$\mathbf{H} = -g_n\mu_n B\mathbf{I}_z + \frac{eQV_{zz}}{4I(2I-1)}\frac{3\cos^2\theta - 1}{2}\left(3\mathbf{I}_z^2 - \mathbf{I}^2\right). \tag{4.4}$$

The eigenvalues $\varepsilon_m$ of Eq. 4.4 are averaged over $\theta$ and the nuclear heat capacity (Eq. 2.11) is calculated from the nuclear entropy (Eq. 2.19) with the partition sum

$$Z = \left[\sum_m \exp\left(-\frac{\varepsilon_m}{k_B T_n}\right)\right]^N, \tag{4.5}$$

with the number of nuclear spins given by $N = nN_A$, where $n = 11.4$ nmol is the amount of In integrated per CBT island. With known entropy, the parasitic heat load on the electron system ,$\dot{Q}_0$, can be calculated in dependency of $T_e$ and $B$. For this, the nuclear entropy $S_n = k_\mathrm{B}(\partial \log Z/\partial T)$ and the nuclear spin specific heat $C_n = T(\partial S/\partial T)$ are numerically calculated from the partition sum, at a given magnetic field and $T_n, T_e$. With the given magnetic field profile $B(t)$, the temperature change $\partial T_n/\partial B$ is then calculated under adiabatic conditions ($\partial S/\partial B = 0$), in small field increments. For each magnetic field increment, the heat exchange between nuclei and electrons is calculated by solving

a coupled set of differential equations, parameterizing the temperature of the nuclei and electrons respectively. The nuclar spins cool with reduction of the field and warm up by interacting with the electrons at temperature $T_e$ (see also Eq. 2.14), according to

$$\frac{dT_n}{dt} = \frac{T_e T_n - T_n^2}{\kappa} + \frac{\partial T_n}{\partial B}\frac{\partial B}{\partial t} \tag{4.6}$$

Neglecting the effect of phonons, the parasitic heating $\dot{Q}_0$ on the electron system is fully applied to the nuclear spins. The electrons transfer the heat via spin-lattice relaxation to the nuclear spins, giving rise to the heat balance $\dot{Q}_\mathrm{e} = -\dot{Q}_\mathrm{n}$ where $\dot{Q}_i = nC_i \mathrm{d}T_i/\mathrm{d}t$. With the heat capacity of the electron system as $C_e = \gamma T_e$ (see Tab. for the corresponding value for In), and a parasitic heat leak $\dot{Q}_0$, the electron temperature $T_e$ evolves as

$$\frac{dT_e}{dt} = -\frac{C_n}{\gamma}\left(\frac{T_n - T_n^2/T_e}{\kappa}\right) + \frac{\dot{Q}_0}{n\gamma T_e}. \tag{4.7}$$

In order to obtain $\dot{Q}_0$ for the whole demagnetization process, the electron temperature, obtained from an adiabatic process, is fitted to a $\dot{Q}_0$, resulting in the measured electron temperature for each field increment. For all evaluated datasets, the model resulted in a $T_n$ which is so close to $T_e$, even for the largest heat leaks, that electron overheating can be neglected. This results from the short spin-lattice relaxation time of In and allows to simplify the following analysis by only evaluating the electron temperatue $T_e \approx T_n$.

The resulting simulated electron temperatures are plotted in Fig. 4.6, together with measured CBT temperatures for all performed on-chip nuclear demagnetization runs with different field ramp rates (see Fig. 4.5). The results are summarized in Fig. 4.6, by plotting $T/T_0$ and $B/B_0$, where $B$ is the actual field, $B_i$ the precooling field, and $T_e = T(B)$ is the measured temperature as a function of field, referenced with the temperature $T_i$ at the end of the precool. An ideal adiabatic nuclear magnetic cooling process, applied to a nuclear spin system with pure Zeeman splitting of the nuclear eigenenergies, is characterized by $T/T_i = B/B_i$ (see section 2.3.4). It can be seen in Fig. 4.6 b that all demagnetization runs have about the same efficiency down to about $0.3B_i$. This implies that the heat leak into the electron system is fully independent of the ramp rate over a wide field range. Accordingly, the fitted heat leak shows a very clear linear dependence, $\dot{Q}_0 = a|\dot{B}| + \dot{Q}_\mathrm{res}$, with $a = 18\,\mathrm{fW/(mT\,s^{-1})}$, and $\dot{Q}_\mathrm{res} = 0.18\,\mathrm{fW}$ per island. Notably, the largest measured heat leak per island is 108 fW, similar to earlier reported values in similar experiments [45], but much higher than figures for combined on- and off-chip refrigeration [47, 173]. The linear $\dot{Q}_0(\dot{B})$ is in striking contrast with observations on macroscopically large nuclear cooling stages, where Eddy-currents in the bulk refrigerant lead to a $\dot{Q}_0 \propto \dot{B}^2$ [9]. It is also inconsistent with a dominating static heat leak, yielding a constant $\dot{Q}_0$, or with an environmental coupling of $\dot{Q}_0 \propto T_e^n - T_\mathrm{env}^n$, where the heat capacity of the environment, $C_\mathrm{env}$, is exceeding the heat capacity of the nuclei with $C_\mathrm{env} \gg C_n$. On one hand, this proves that neglecting the electron-phonon interaction was justified, because a significant heat exchange with the mixing chamber, having by far the largest heat capacity in the system, would give rise to a heat leak increasing towards longer demagnetization times. That the latter does not occur, confirms that the metallic islands of the CBT

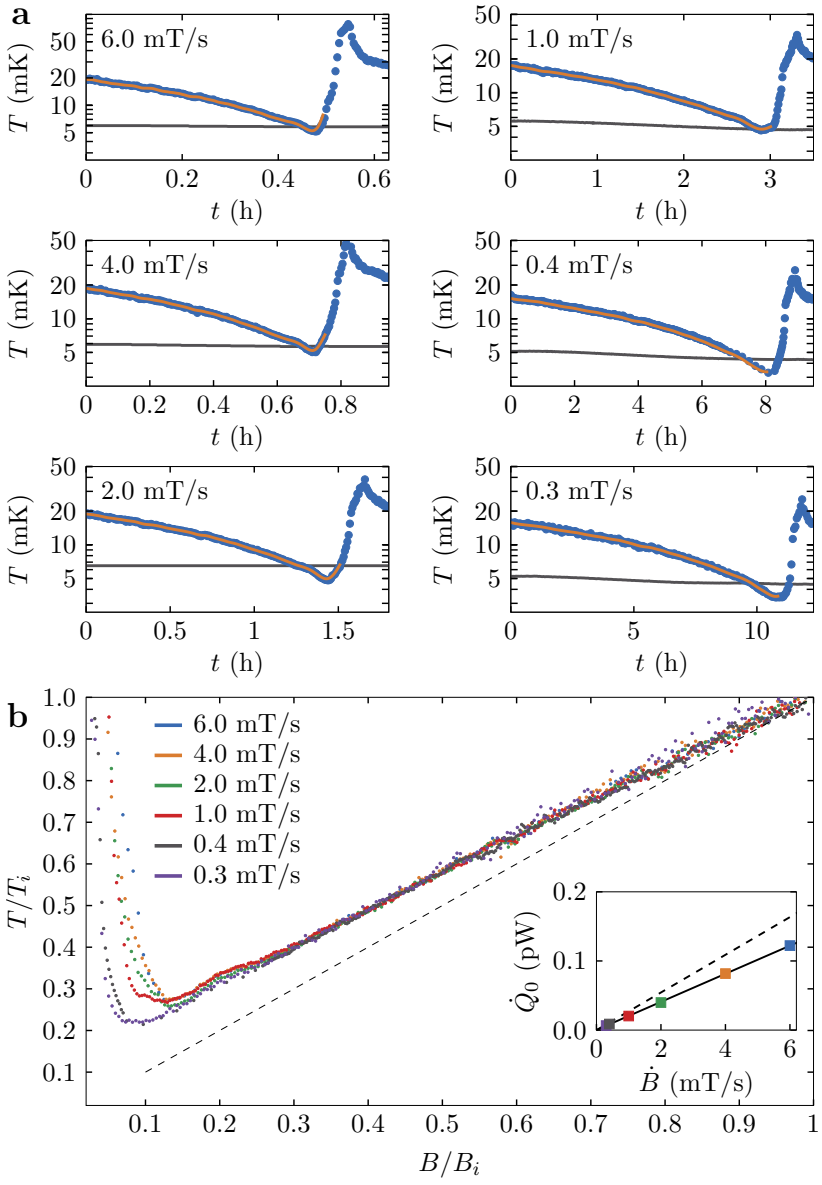


Figure 4.6: **Comparison of on-chip demagnetization attempts with different magnetic field ramp rates and varying starting conditions.** The CBT temperature (blue dots), modelled electron temperature (orange solid line, calculated with Eq. 4.6 and Eq. 4.7) and the mixing chamber temperature (black solid lines) are plotted against the demagnetization time. **b** All runs from panel a, normalized to the starting field $B_i$ and the starting temperature $T_i$. **Inset of b** Heat leak into a single island from the calculated electron temperature in a. The dashed line is the same result without stage modifications to reduce Eddy currents (see Fig. 4.8).

are thermally well decoupled from the environment. However, the rate-independent $Q_0$ suggests the presence of a well-coupled thermal mass, consuming the In nuclear heat capacity over the timescale of the experiment, and having a heat capacity of the order of $C_n(B)$. The source of the heat leak could be at least partially attributed to Eddy-current heating off-chip, as can be seen in the inset of the main panel of Fig. 4.6. Without the modifications on the coldfinger to reduce the cross-section area in field (see section 3.2.2), the heat leak is significantly larger (see also Fig. 4.8). Only taking data shown in the lower panel insets of Fig. 4.6 and Fig. 4.8, the heat leak could be explained by a thermal mass which is heated by Eddy-currents and thermally well coupled to the chip, while thermally only weakly coupled to the mixing chamber (such as the electrical wires connecting to the chip). The data can be also explained by an overestimation of the nuclear heat capacity, or an internal parasitic heat capacity on-chip, which both can be ruled out by calorimetric analysis performed at a later stage (see section 7.5), making the device leads a likely source of parasitic heating.



Since temperatures were only measured on-chip and on the mixing chamber plate, the exact source of the heat leak remains unclear. Measuring the temperature of the leads and the temperature of the Cu coldfinger, which should agree with the chip substrate temperature during a demagnetization process, could give more insight regarding the heat leak origin(s). Recent experiments using an on and off chip nuclear cooling approach with Cu [47] have revealed a significant reduction of residual heat leaks to the order of a few tens of aW per CBT island by cooling the leads with a parallel set of macroscopic nuclear demagnetization stages. This, in combination with the results obtained in this work points to the device leads as the unwanted parasitic heating source.

## 4.6. ON-CHIP NUCLEAR COOLING POWER OF IN AND CU

The implementation of In as on-chip nuclear refrigerant can be benchmarked by comparing the obtained results with a similar experiment using Cu [45]. The measured electron temperature of the on-chip demagnetization run with 0.4 mT/s (see Fig. 4.5) and measured electron temperature in [45], with calculated $T_n$ for both, are plotted in Fig. 4.7 The calculations based on Eq. 4.6 and Eq. 4.7 confirm that the In nuclei are strongly coupled to the electron system, implying $T_n = T_e$ throughout the entire experiment with $\dot{B} = -0.4\,\mathrm{mT/s}$, resulting in $\dot{Q}_0 = 7.85$ fW/island. In contrast, the weaker hyperfine coupling, resulting in a longer spin-lattice relaxation time, of Cu results in a deviation between $T_n$ and $T_e$, despite a similar heat leak $\dot{Q}_0 = 6.3$ fW/island [45], demonstrating the limitations of Cu as an on-chip refrigerant. An evaluation considering the nuclear cooling power integrated on-chip can be made by comparing the nuclear heat capacity integrated per unit area, $\alpha' = \alpha n/A$ and $\alpha'/\kappa$, as a figure of merit containing both the material parameters and the device geometry. Using the Schottky approximation of the heat capacity as here, enables to compare the nuclear cooling properties without taking into account quadrupolar couling here. The device used in this work features $\alpha'/\kappa_{\mathrm{In}} = 250\,\mu\mathrm{W}/(\mathrm{m^2KT^2})$, which is a factor of 3300 increase compared to 0.076 $\mu\mathrm{W}/(\mathrm{m^2KT^2})$, implemented in [47] by an evaporated Cu film. The obtained results can also be compared with [45], where 2.33 $\mu\mathrm{W}/(\mathrm{m^2KT^2})$ was achieved using electroplated copper, further demonstrating the importance of the film thickness of a nuclear microre-

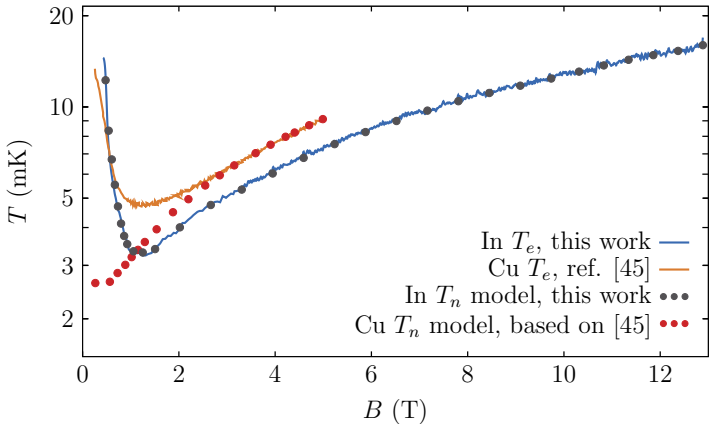


Figure 4.7: **Comparison of a typical on-chip demagnetization attempt of this work with on-chip nuclear cooling with Cu.** The measured electron temperature, $T_e$, obtained during the field ramp is plotted as a function of field for both experiments, the calculated temperature of the nuclei, $T_n$, is plotted as dots.

frigerator. Without taking nuclear quadrupole enhancement of the nuclear spin specific heat into account, the short-spin lattice relaxation time of In compared to Cu, allows to integrate an order of magnitude larger nuclear cooling power per area onto the chip.

## 4.7. CONCLUSIONS

It was demonstrated that electron temperatures of $3.2 \pm 0.1$ mK can be reached by nuclear magnetic cooling on-chip, using electroplated In as nuclear refrigerant. This result is the coldest measured electron temperature without additional off-chip nuclear demagnetization cooling. On-chip cooling of nanoelectronics with In is viable, despite a large molar heat leak of 0.8 μW/mol, to be compared to typical heat leaks of well isolated macroscopic demagnetization stages, generally falling in the range of 0.1 nW/mol to 1 nW/mol [20]. Using electrochemical film deposition methods, 1.6 pmol/μm$^2$ of In could be integrated onto the chip. This, considering the material parameters as well, gives rise to orders of magnitude increase in the on-chip integrated cooling power per surface area compared to state-of-the-art devices, utilizing Cu thin films. Furthermore, In is the preferred material of cryogenic interconnects [30], which provides the possibility to integrate In refrigerant in scalable quantum bit architectures. It can be therefore concluded that on-chip integrated nuclear refrigeration with In is a versatile means to decrease the electron temperature of nanoscale devices. Demagnetization with varying field ramp rate reveals signatures of a good thermal decoupling from the mixing chamber at ultralow temperatures, which is a required feature of nuclear demagnetization in general. However, parasitic heating hinders progress to lower temperatures by using an on-chip approach. The large nuclear cooling power, achieved by integrating In as on-chip nuclear refrigerant, combined with an on-and off chip nuclear magnetic cooling approach, reducing the nuclear heat leak to values obtained in [47], could make on-chip integration of In films a possible path towards microkelvin cooling of nanoelectronics.

## 4.8. ADDITIONAL DATASETS

Fig. 4.8 shows on-chip nuclear demagnetization experiments performed with the same device as in Fig. 4.6, but without the modifications described in section 3.2.2 to reduce Eddy-current heating. The heat leak obtained by a numerical procedure (section 4.5) results in the same linear behaviour as in the inset of Fig. 4.6 b, but the amount of parasitic heating is reduced. This implies that parasitic heating had an indirect impact on the heat leak seen by the electrons on chip, most probably by heating up the attached mass, which was leading to the rate independent heat leak, by Eddy-current heating.



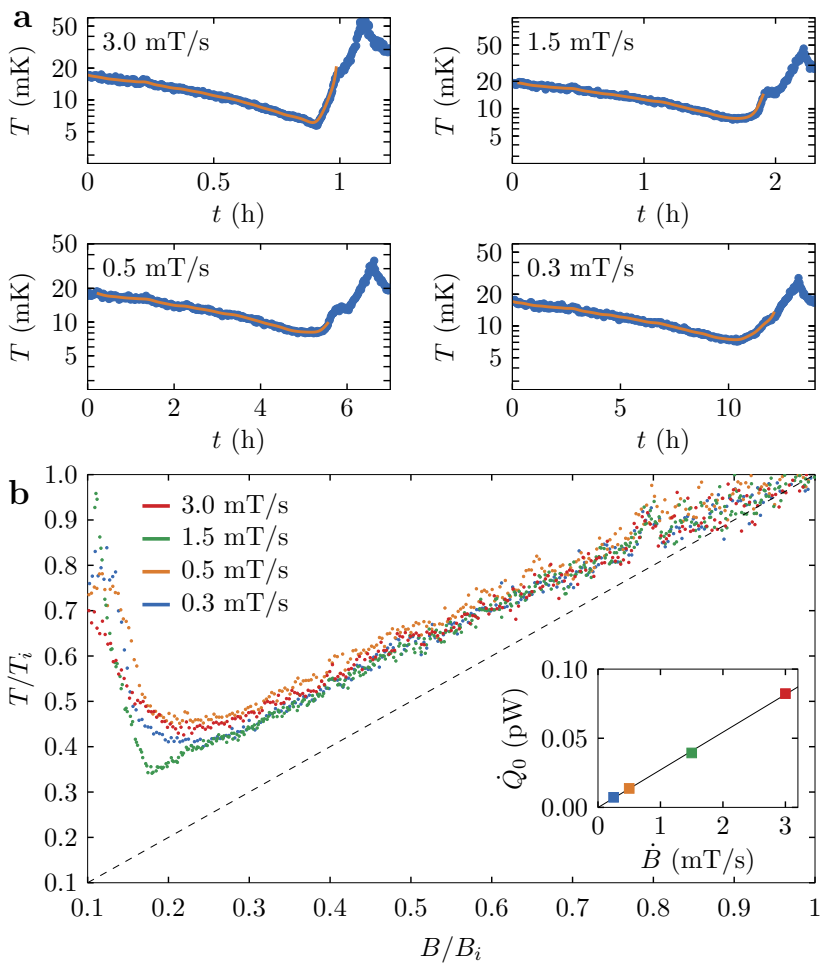


Figure 4.8: **Comparison of on-chip demagnetization attempts with different magnetic field ramp rates and varying starting conditions.** The CBT temperature (blue dots), modelled electron temperature (orange solid line, calculated with Eq. 4.6 and Eq. 4.7) plotted against the demagnetization time. **b** Runs from panel a, normalized to the starting conditions. **Inset of b** Heat leak an island from the electron temperature in a.

Fig. 4.9 shows on-chip nuclear magnetic cooling attempts for a CBT with a larger In volume plated onto the islands. The island volume is $280 \times 400 \times 25.4\ \mu m^3$ instead of $50 \times 140 \times 25.4\ \mu m^3$, which was implemented for the device described in section 4.2, implying a nearly 12 times larger nuclear specific heat at the same conditions. The low temperature calibration of the CBT is shown in Fig. 3.18. The larger island volume leads to a lower equilibrium temperature with the mixing chamber: the nuclear magnetization can be performed to a temperature as low as 10 mK. However, the nuclear heat leaks are so large that the demagnetization efficiency is smaller than for the previous devices.

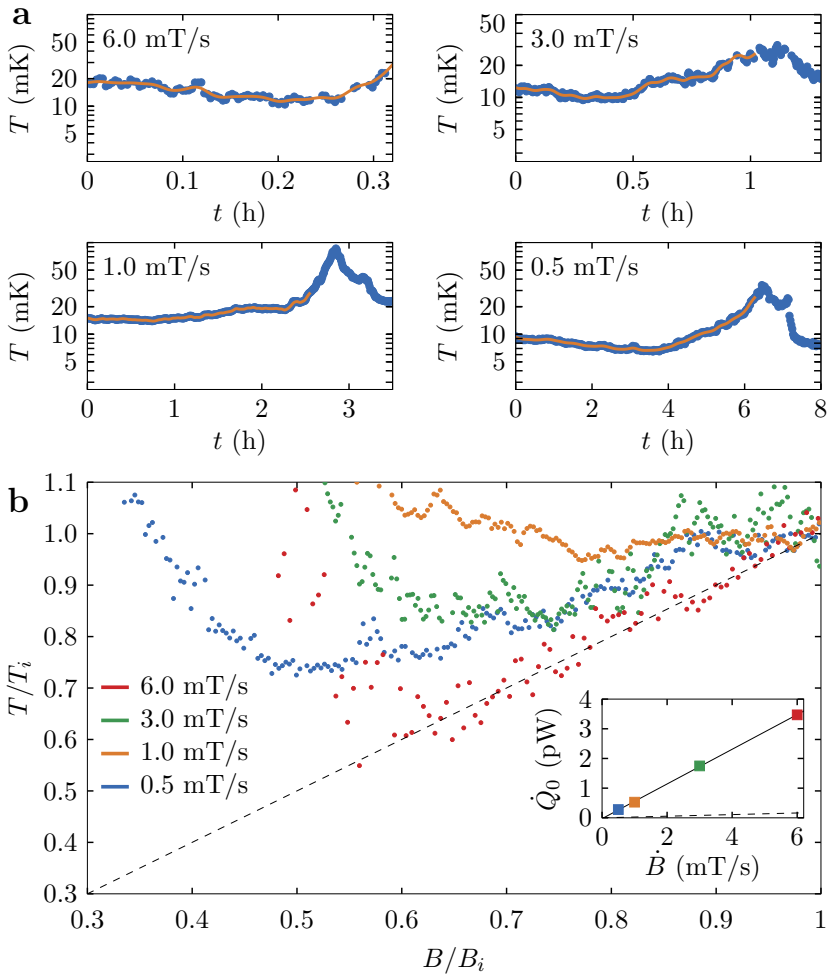


Figure 4.9: **Comparison of on-chip demagnetization attempts with different magnetic field ramp rates and varying starting conditions.** The CBT temperature (blue dots), modelled electron temperature (orange solid line, calculated with Eq. 4.6 and Eq. 4.7) plotted against the demagnetization time. **b** Runs from panel a, normalized to the starting conditions. **Inset** Heat leak into an island from the electron temperature in a.

# 5

# Coulomb Blockade Thermometry Beyond the SET Regime

*... dass dies praktisch gleichbedeutend ist mit niemals, erkennt man, wenn man bedenkt, dass in diesem Zeitraume gemäß den Wahrscheinlichkeitsgesetzen viele Jahre enthalten sein müssten, in welchen durch bloßen Zufall an demselben Tage alle Bewohner einer großen Stadt Selbstmord begingen, oder in allen Gebäuden derselben ein Brand entstünde, während doch die Versicherungsgesellschaften sich in guter Übereinstimmung mit den Tatsachen befinden, wenn sie solche Fälle nicht in Betracht ziehen.*

Ludwig Boltzmann, 1898

## 5.1. INTRODUCTION

While charging effects in single electronic circuits were (and are) considered for many technological applications, it turns out that they offer opportunities for versatile and reliable nanoelectronic thermometry (see section 2.3.4). Pekola et al. have demonstrated in 1994 [56] that single electron tunneling in a linear (in series) array of $n$ tunnel junctions, enclosing islands with a classical charging energy $E_C$, follows a universal behaviour in the way that the zero bias tunnel conductance suppression as a function of $k_B T_e/E_C$ is invariant to the number of junctions in series $n$, with the electron temperature $T_e$. The universal charging behaviour enables electronic thermometry, rather simple to realize by established methods of micro- and nanoprocess technologies. Another aspect in terms of applied single-electronics is, that due to the universal behaviour the computational problem of a large junction array can be reduced to a SET ($n = 2$) which can be modelled using a master equation approach (see sections, 2.3.4, 2.4.2). The simple computational effort depends on the applicability of the orthodox theory (Eq. 2.41) of electron tunneling, requiring single charge tunneling between energies on a continuous spectrum. This can be achieved by long arrays of metallic islands, connected by tunnel junctions. For an array of $n$ tunnel junctions in series, cotunneling of $N$ charge carriers is suppressed with $(R_t/R_Q)^{N-1}$ [139]. Here $R_t$ (Eq. 2.40) is the junction resistance and $R_Q = h/e^2$ is the quantum unit of resistance. In the range of $k_B T_e \simeq E_C$, the universal charging behaviour gives rise to a well proven, wide range, and self-calibrating primary thermometer for the electron temperature, denoted as Coulomb blockade thermometer.



The limits of Coulomb blockade thermometry with respect to the accessible temperature scale are reached at high temperatures, when the tunnel conductance suppression by charging becomes unmeasurably weak at $k_B T \gg E_C$, and at low temperatures when random offset charges affect the electrostatic potential of the islands in such a way that they randomly alter the device conductance. To current knowledge the lower temperature range limit is reached at $k_B T/E_C \sim 0.4$ [132]. This value was obtained by solving the master equation of single electron tunneling in dependency of the background charge $q_0$ on the island of a SET, in the limiting cases of $q_0 = 0$, representing full Coulomb blockade, and $q_0 = e/2$, as the extreme case of no blockade. The limit of the universal regime is then defined as the temperature where the two limiting cases acquire distinguishable zero bias tunnel conductance values, implying that the measured tunnel conductance can not be mapped back to a single temperature anymore without exact knowledge of $q_0$. While the universal regime of charging allows the description of an array of $n$ junctions with a SET, exploring the limits of the universal regime of an array of many tunnel junctions with a SET model can not *a priori* be assumed to give a correct result for any $n$. Moreover, it is well known that SETs are extremely sensitive to random offset-charges towards the full Coulomb blockade regime. Coulomb blockade thermometry is on the other hand implemented by, and profits from, a large number of tunnel junctions in series, having an extraordinary resistance to randomization by offset-charges [138, 174, 175]. The offset charge stability of tunnel junction systems in the regime $T > 0$ and $k_B T/E_C \ll 1$ was never investigated. A suitable model for probing the limits of the universal regime has to provide the correct charging energy of the system, depending on the exact charge distribution on the array in the few-electron regime. Furthermore, it

has to capture the effect of random offset charges on each island. This is not possible with a master equation approach due to an enormous configuration space, but a natural operation area for a Markov-chain Monte Carlo (MCMC) algorithm. Starting from an initial charge configuration, a MCMC model predicts the probabilistic evolution of charge states by tunneling events whose probabilities are calculated in the framework of statistical thermodynamics and stochastically selected. Historically, MCMC models were seldom used because they usually require a large number of iterations to converge and thus the corresponding computational resources. The main field of application in terms of tunnel junction arrays was the study of charge solitons at $T = 0$ K [176, 177], where single electronic MCMC algorithms converge rather quickly. Charging in CBTs at finite temperature was to best knowledge never studied by applying MCMC methods.

Consequently, this work implements a MCMC model to 1) predict the limits of the universal regime of Coulomb blockade thermometry in dependency of the array length $n$ and 2) calculate the temperature dependent tunnel conductance of an array of $n \times m$ tunnel junctions in the presence of random background charge on the islands. The main question for both problems is how the effect of many charging nodes, manifests itself in terms of the width of the conductance distribution at a given temperature.



## 5.2. BASIC CONSIDERATIONS

Basic understanding of the boundary conditions of charging in tunnel junction arrays can be obtained analytically. The type of circuit considered is the typical implementation of a CBT, comprising an $n \times m$ array of junctions. An overview is shown in Fig. 5.1. The device is symmetrically biased by two grounded voltage sources, fixing the electrostatic potential in the most left and right node at $\varphi_L$ and $\varphi_R$ respectively and providing the constant voltage bias $V_0 = \varphi_L + \varphi_R$ which drops over the array. The electrostatic potential $\boldsymbol{\varphi} = [\varphi_1, \varphi_2, ..., \varphi_{n-1}]^{\mathrm{T}}$ on the island nodes, at a given charge state $\mathbf{q} = [q_1, q_2, ..., q_{n-1}]^{\mathrm{T}}$, is obtained with the capacitance matrix $\mathbf{C}$. The mutual capacitance of the islands $C_i$ couples neighbouring islands, giving the capacitance matrix a block diagonal form. Island capacitance to ground $C_{gi}$ only contributes to the diagonal elements of $\boldsymbol{\varphi}$, giving rise to

$$-C_i\varphi_{i-1} + \left(C_i + C_{i+1} + C_{gi}\right)\varphi_i - C_{i+1}\varphi_{i+1} = q_i \tag{5.1}$$

The junction voltages are given by the island potentials as $V_i = \varphi_i - \varphi_{i-1}$, leading to $V_i C_i - V_{i+1}C_{i+1} + V_{gi}C_{gi} = q_i$. The total island charge $q_i = n_i e + q_{0i}$ is the sum of the charge $n_i e$, induced on the island $i$ by excess charge carriers as well as the gate charge and background charge $q_{0i}$. The total electrostatic energy of the system is given by

$$F = \frac{1}{2}\sum_{i-1}^{n} C_i\left(\varphi_i - \varphi_{i-1}\right)^2 + \frac{1}{2}\sum_{i=1}^{n-1} C_{gi}V_{gi}^2 \tag{5.2}$$

For now it shall be assumed that $C_i \gg C_{gi}$ and $C_i = C_0$, well satisfied in an implementation as described in section 3.1.1. In this limit, the islands are strongly coupled (local charging limit). If for example a single charge tunnels onto the first island of an array of $n$ tunnel junctions in series, each with $q_{0i} = 0$, the charging energy is larger than the single island (SET) charging energy because, apart from shifting the voltages of the first two

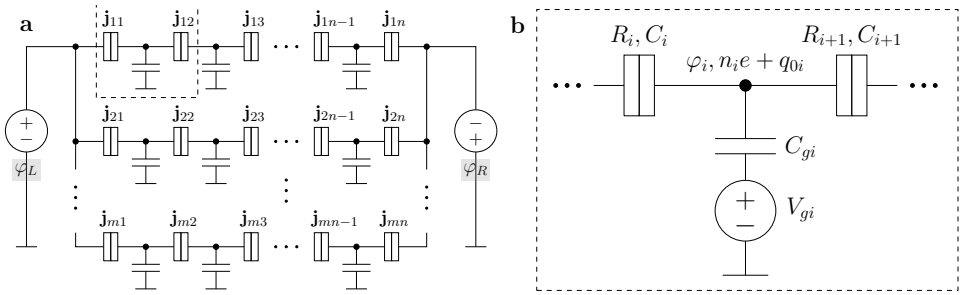


Figure 5.1: **Schematics of a tunnel junction array of $n$ junctions in series times $m$ representing the single electronic circuit which is investigated in this chapter.** **a** Overview of the full device with voltage sources. The junctions are labeled with $j$. **b** The nodes (islands) are characterized with their total charge and the island potential $\varphi_i$. The excess charge can be varied in discrete units of $e$ by tunneling and continuously by $q_{0i}$.

junctions according to $V_1 - V_2 = e/C_0$, the voltage over the remaining $n-2$ junctions will be raised to $V_2$ as well. In the general case of the $k$th island being occupied with a single integer charge, the junction voltages change according to the simultaneous boundary conditions $e(V_{k-1} - V_k) = e/C_0$ and $\sum_{i=1}^{k-1} V_i = -\sum_{i=k}^{n} V_i$. Both conditions can only be fullfilled if the junctions 1 to $k-1$ acquire a potential drop of $eV_1 = e^2/C_0 \times (n-k)/n$ while the junctions $k$ to $n$ acquire $eV_2 = e^2/C_0 \times k/n$. The charging energy is given by

$$E_C(k) = \frac{C_0}{2}\left[kV_1^2 + (n-k)V_2^2\right] \tag{5.3}$$

Here the single charge carrier charging energy was defined as $E_C = \Delta F$ (see section 2.4.1) with $F_i = 0$. In the limit of $C_0 \gg C_g$, the total island capacitance is defined by $C_\Sigma = 2C_0$. The charging energy of the array for charging the $k$th island with a single charge is then

$$E_C(k) = \frac{e^2}{C_\Sigma}\left[\frac{k(n-k)^2}{n^2} + \frac{k^2(n-k)}{n^2}\right] = \left[\frac{kn-k^2}{n}\right]\frac{e^2}{C_\Sigma} \tag{5.4}$$

For $k = 1$ one obtains the form of $E_C$ which determines the behaviour of a series of $n$ tunnel junctions in the universal regime (see section 2.3.4) , given by the expression

$$E_{C0} = \left(\frac{n-1}{n}\right)\frac{e^2}{C_\Sigma} \tag{5.5}$$

One can also arrive at Eq. 5.4 and Eq. 5.5 by considering the general form of the charging energy $E_C(k) = e^2/2C_{\text{eff}}(k)$, where $C_{\text{eff}} = C_0\left[k^{-1} + (n-k)^{-1}\right]$ is the capacitance of the $k$th island, connected to the leads via $k$ times the capacitance $C_0$ and $n-k$ times $C_0$ in series. According to Eq. 5.4, the effective charging energy of an array of $n$ junctions depends on the exact island which is charged. Transporting a charge from source to drain, over $n$ junctions in series, requires to overcome an energy barrier of $n/2-1$ times the effective charging energy of charging the first island, given by 5.5. This implies that a long array ($n \gg 2$) should have a much stronger conductance suppression towards lowering the temperature beyond the SET regime, if the offset charge on each island is close to zero.

Turning to the effect of offset charge $q_{0i}$ on the islands, it is immediately clear that a treatment of random offset charges is beyond reach for an analytic discussion. What can be considered is the most extreme case of offset charge in which the charge configuration is such, that tunneling of a single excess charge leaves the free energy of the array unchanged ($\Delta F = 0$). For a SET this state is reached when the offset charge on the island equals $q_0 = \pm e/2$ so that $\Delta F = (q_0 \pm e)^2/2C_\Sigma - q_0^2/2C_\Sigma$ becomes zero. For $n > 2$ the same is often assumed [174]. However this can not be correct since tunneling inside an array modifies all junction voltages, and a tunneling event which is isoenergetic for $n = 2$ has to cost energy for $n > 2$. If all islands of a junction array with $n$ are charged by the same $q_{0i} = \pm q_0$, the junction voltages are linear in junction number with $C_0 V_i - C_0 V_{i+1} = \pm q_0$, while the voltage over the whole array has to vanish with $V = \sum V_i = 0$. This requires

$$V_1 = \pm \frac{(n-1)}{2} \frac{q_0}{C_0}, \qquad V_n = \mp \frac{(n-1)}{2} \frac{q_0}{C_0}, \qquad V_{i+1} = V_i - \frac{q_0}{C_0} \tag{5.6}$$

If an electron tunnels onto island $k$, all voltages are modified from $V_i$ to $V_i'$. One is now looking for a uniform $\pm q_0$ minimizing the change in free energy of the system such that

$$\Delta F = \frac{C_0}{2} \left( \sum_i V_i'^2 - \sum_i V_i^2 \right) = 0 \tag{5.7}$$

Since $V_i - V_{i+1}$ is constant except for $i = k$ there is a trivial solution. The charge $\pm q_0 \pm e$ on island $k$ forces $V_k - V_{k+1}$ to acquire the value $(\pm q_0 - e)/C_0$ and $\Delta F$ can be zeroed by index shifting all $V_i'$ with respect to $V_i$ such that $V_1', ..., V_k' = V_{n-k}, ..., V_n$ and $V_{k+1}', ..., V_n' = V_1, ..., V_k$. Thus, only for a specific value $q_0$ the voltages will be aligned with $V_k' = V_n$, $V_{k+1}' = V_1$ (For $-q_0$ equivalently $V_k' = V_1$, $V_{k+1}' = V_n$), which allows to calculate $q_0$ as

$$V_k - V_{k+1} = \frac{q_0 - e}{C_0} = \pm \frac{(n-1)}{2} \frac{q_0}{C_0} - \left[ \mp \frac{(n-1)}{2} \frac{q_0}{C_0} \right] \tag{5.8}$$

By solving for $q_0$ one then finds the offset charge which has to be placed on each island to enable charge tunneling without change in free energy $\Delta F = 0$. This occurs if

$$q_0 = \pm \frac{e}{n} \tag{5.9}$$

This has important consequences to the charging behaviour of junction arrays in the limit $C_0 \gg C_g$. While a single island has a charge degeneracy at $q_0 = \pm e/2$, an array of $n$ tunnel junctions has a charge degeneracy at $q_0 = \pm e/n$. In Fig. 5.2 the numerically calculated electrostatic energy for $n = 2$ and $n = 40$ junctions is plotted for three different charge states, being no charge on the array, a positive single charge on the array, and a negative single charge on the array. The electrostatic energy of the array is calculated with Eq. 5.2 in the limit of $C_0 \gg C_g$. For the single island the interpretation is straightforward and equivalent to SET physics: For $q_0 = 0$ the tunneling process has to overcome the Coulomb gap $e^2/2C_\Sigma$ to charge the island. Increasing the offset charge from 0 to e/2 closes the gap, until charge states are degenerate at $e/2$, consistent with Eq. 5.9 for $n = 2$. For the long junction array it is not only important what the total charge on the device is but how it distributes onto the islands. At $q_0 = 0$, Eq. 5.4 predicts the charging energy

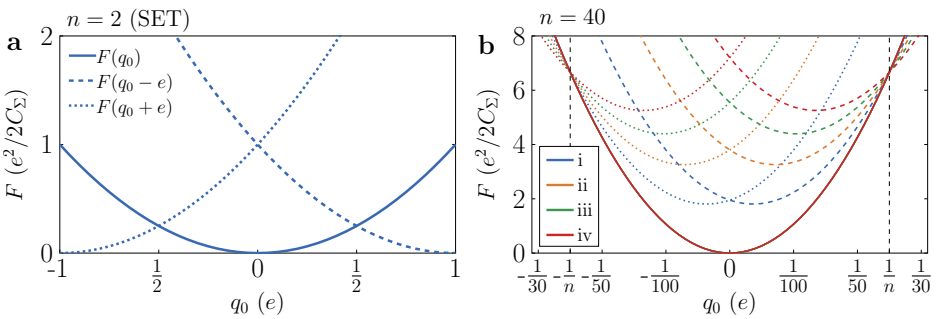


Figure 5.2: **Electrostatic free energy of tunnel junction arrays**, **a** A single island ($n = 2$) has a charging energy of $E_C = e^2/2C_\Sigma$ and a charge degeneracy point of $q_0 = e/2$. **b** An array with $n \gg 1$ has a charging energy of $E_C \approx e^2/C_\Sigma$. The effective charging energy depends on the island which is charged but all single electron charge states have a charge degeneracy at $q_i = e/n$. The plot designations are; i: $\mathbf{q} = \{\pm e, 0, 0, 0, ..., 0\}$, ii: $\mathbf{q} = \{0, \pm e, 0, 0, ..., 0\}$, iii: $\mathbf{q} = \{0, 0, \pm e, 0, ..., 0\}$, iv: $\mathbf{q} = \{0, 0, 0, \pm e, 0..., 0\}$. Dashed and dotted line designation as in **a**



for charging the $k$th island. When increasing an uniform offset charge from zero towards $\pm e/n$ and beyond, the Coulomb gap closes and reopens again on a small interval around $e/n$. Charge is quantized in units of $e$ in the single electronics regime, which is both true for the SET and the long array. For $n \gg 2$ it becomes unlikely that an array of tunnel junctions reaches the narrow regime of uniform island charge around $e/n$ by compensating an initial random offset charge, until all islands have offset charges close to $e/n$.

Even if all islands acquire a charge close to $e/n$, charge transport will be suppressed by stochastic reasons. For $q_0 = e/n$ there can be only one charge on the device without changing the electrostatic free energy. Thus, there are $n$ degenerate states: one with no excess charge on the device, and $n-1$ states with a single charge on island $k$. The probability of finding the system with a single charge on island $k$ at single charge degeneracy is thus $P(k) = 1/n$. For small bias voltage $V \ll E_C(k)$ and $T \to 0$, Eq. 2.41 becomes

$$\Gamma_k = \frac{\Delta F}{e^2 R_t} \tag{5.10}$$

At single charge degeneracy, $\Delta F$ is solely determined by the bias voltage over the $k$th junction, implying that $\Delta F = eV/n$. Towards $T \to 0$, charge tunneling along a positive free energy gradient is fully suppressed and the current over the device is given by

$$I = \sum_{i=1}^{n} P(i)\Gamma_i = \frac{V}{R_t n^2} \tag{5.11}$$

Here, all elements of the sum are zero, except for $i = k$. With $G = I/V$ and $G_t = 1/nR_t$ this just implies that the zero bias conductance for $T \to 0$ should be as large as

$$\left(\frac{G(0)}{G_t}\right)_{T\to 0} = \frac{1}{n} \tag{5.12}$$

The only way to reach a higher conductance than $1/n$ is the coherent tunneling of $n$ charges, meaning that a charge is tunneling over every junction at (exactly) the same

time, in the same direction (for $q_0 = e/n$). This is the only possible other isoenergetic process at $T \to 0$ since all other processes are gapped. However, this process is suppressed by $(R_t/R_Q)^n$ and very unlikely to happen for a sufficiently long array with intransparent junctions. Summarizing the consequences, $q_0 = e/n$ on every island will indeed drive the system out of Coulomb blockade but the probability to transfer a charge from source to drain is strongly suppressed leading to a significant conductance suppression for large $n$. The extreme cases discussed here can predict the general behaviour of the system. Calculating the exact conductance of an array with $n$ junctions in the presence of offset charge, as a function of bias and temperature, is treated numerically.

## 5.3. NUMERICAL MODEL

In order to calculate the conductance of a tunnel junction array with $n$ junctions, enclosing $(n-1)$ islands, in the presence of a charge configuration $\mathbf{q}^{\mathrm{T}} = [q_1, q_2, ..., q_{n-1}]$ with $q_i = n_i e + q_{0i}$, numerical single electronics is employed. For a given $n$, forward and backward tunneling over any junction $j_k$ (see Fig. 5.1) transforms the system from a charge state into one of $2n$ possible charge states. This gives rise to a huge state space and $\mathbf{\Gamma}$ (Eq. 2.44) is so large, that only an MCMC approach is feasible. Therefore, a computationally effective MCMC algorithms was written, mainly based on [138, 176]. The system is described by a Markov chain of randomly selected single charge tunneling events, altering $\mathbf{q}$ to $\mathbf{q}'$. For $\mathbf{q} \to \mathbf{q}'$, one can construct the matrix $\mathbf{Q}$ containing all possible $\mathbf{q}'$ for a given $\mathbf{q}$,

$$\mathbf{Q} = \begin{pmatrix} q_1 - e & q_1 + e & q_1 & \dots & q_1 & q_1 + e & q_1 - e & \dots & q_1 \\ q_2 & q_2 - e & q_2 + e & \dots & q_2 & q_2 & q_2 + e & \dots & q_2 \\ q_3 & q_3 & q_3 - e & \dots & q_3 & q_3 & q_3 & \dots & q_3 \\ \vdots & \vdots & \vdots & \ddots & \vdots & \vdots & \vdots & \ddots & \vdots \\ q_{n-1} & q_{n-1} & q_{n-1} & \dots & q_{n-1} + e & q_{n-1} & q_{n-1} & \dots & q_{n-1} + e \end{pmatrix} \tag{5.13}$$

The first column of $\mathbf{Q}$ corresponds to transport of an electron (hole) from (to) drain and vice versa for the last column. At any time the system is fully characterized by the electrostatic potential $\boldsymbol{\varphi}_i^{\mathrm{T}} = [\varphi_1, \varphi_2, ..., \varphi_{n-1}]_i$, with $i$ runing over the columns of $\mathbf{Q}$. The capacitance matrix $\mathbf{C}$ maps any potential to a charge configuration $\mathbf{C} \cdot \boldsymbol{\varphi}_i = \mathbf{Q}_i$. Thus

$$\mathbf{Q} = \begin{pmatrix} C_{\Sigma 1} & -C_2 & 0 & \dots & 0 \\ -C_1 & C_{\Sigma 2} & -C_3 & \dots & 0 \\ 0 & -C_2 & C_{\Sigma 3} & \dots & 0 \\ 0 & 0 & -C_3 & \dots & 0 \\ \vdots & \vdots & \vdots & \ddots & \vdots \\ 0 & 0 & 0 & \dots & C_{\Sigma n-1} \end{pmatrix} \begin{pmatrix} \varphi_{1,1} & \varphi_{1,2} & \dots & \varphi_{1,2n} \\ \varphi_{2,1} & \varphi_{2,2} & \dots & \varphi_{2,2n} \\ \varphi_{3,1} & \varphi_{3,2} & \dots & \varphi_{2,2n} \\ \varphi_{4,1} & \varphi_{4,2} & \dots & \varphi_{2,2n} \\ \vdots & \vdots & \ddots & \vdots \\ \varphi_{n-1,1} & \varphi_{n-1,2} & \dots & \varphi_{n-1,2n} \end{pmatrix} \tag{5.14}$$

with $C_{\Sigma k} = C_k + C_{k+1} + C_{gk}$ (see Eq. 5.1 and Fig. 5.1). The probability that one of the $2n$ tunneling processes is selected as the winner in a single step of the Markov-chain is weighted by its tunneling rate $\Gamma_i$. Thus, the tunneling event with the smallest tunneling

time $\Delta t_i = 1/\Gamma_i$ is most probably selected. The tunneling rates are calculated from the change in free energy $\Delta F_i$ accompanying the tunneling event with index $i$. The electrostatic potential difference between the islands before ($\varphi_k$) and after tunneling is [176]

$$\Delta F_i = \frac{1}{2}\sum_{k=1}^{n-1} C_{gk}\left(\varphi_{k,i}^2 - \varphi_k^2\right) + \frac{1}{2}\sum_{k=1}^{n} C_k\left(\varphi'_{k,i} - \varphi'_{k-1,i}\right)^2 - \frac{1}{2}\sum_{k=1}^{n} C_k\left(\varphi_k - \varphi_{k-1}\right)^2 \tag{5.15}$$

The contribution to $\Delta F_i$ from charging the leads is neglected. For $C_i = C_0$, one can use $\Delta F_i = e/2(\varphi'_{i\pm1} + \varphi'_{i\pm1} - \varphi'_i - \varphi'_i)$ following from Eq. 5.15 in this limit [176]. The tunneling rates $\Gamma_i$ are calculated with the orthodox theory (Eq. 2.41) of tunneling according to

$$\Gamma_i = \frac{1}{e^2 R_i}\frac{\Delta F_i}{1-\exp(-\Delta F_i/k_B T)} \tag{5.16}$$

The absolute tunnel current $I = e/\Delta t_i$ accompanies every single charge tunneling event. However, discrete current peaks introduce statistical noise, which is avoided by calculating $I$ with a variance reducing method [138, 178]. Here, the tunnel current, which is induced by tunneling of a single charge, is spread over all junctions. Accordingly, the total time of a Markov chain containing $N$ steps is calculated with the following expression

$$\Delta t = \sum_{p=1}^{N} \Delta t_p = \sum_{p=1}^{N}\left[\sum_{i=1}^{n}\left(\frac{1}{\Gamma_i^+ + \Gamma_i^-}\right)\right]_p \tag{5.17}$$

In thermal equilibrium, the current through every tunnel junction is equal $I = I_1 = I_2 = \ldots = I_N$, for any possible potential distribution $\{\varphi_i\}$. This allows to express the transported charge $\Delta Q$ during the period $\Delta t$ with the tunneling rates as follows

$$\Delta Q = \sum_{p=1}^{N} \Delta Q_p = e\sum_{p=1}^{N}\left[\frac{\sum_i\left(\Gamma_i^+ - \Gamma_i^-\right)R_i/R_\Sigma}{\sum_i\left(\Gamma_i^+ + \Gamma_i^-\right)}\right]_p \tag{5.18}$$

$R_\Sigma = \sum_i R_i$ is the resistance of the series tunnel junction array. The effect of calculating the current with all possible tunneling events provides stochastic sampling and thus reduced runtimes [138]. For calculating the differential conductance, the current $I = \Delta Q/\Delta t$ is calulated in a small bias interval in which the conductance is obtained by $G = \mathrm{d}I/\mathrm{d}V$. The asymptotic tunnel conductance is determined by $G_t = 1/R_\Sigma$.

## 5.4. THE UNIVERSAL CHARGING REGIME AT $k_B T > E_C$

To validate the MCMC model described in section 5.3, its results are first compared to the SET master equation tunneling model in the primary regime of $k_B T/E_C > 1$. For establishing a comparative discussion of the results, the dimensionless scaling factor[1]

$$u = \frac{2E_C}{k_B T} \tag{5.19}$$

is introduced. As already introduced in section 2.3.4, and first shown by Pekola et al. [56], the primary regime enables determination of temperature from the full width at half maximum of a charging curve according to $eV_{1/2} = \xi n k_B T$, with $\xi \approx 5.44$. Thus,

[1] The factor of two was introduced by Pekola et al. [56], where universal scaling factors for the tunnel conductance as function of temperature were defined with it. In later works the same scaling factors were used but the factor of two was dropped which has led to incorrect charging energy definition in some publications.

at temperature $1/u$, the FWHM of the charging curve, divided by $2\xi nE_C$, should just equal $1/u$. For comparison, full charging curves are calculated with the master equation tunneling model and the MCMC tunneling model for $n = 36$ and several temperatures in the primary temperature regime. The resulting curves are plotted in Fig. 5.3. As obvious

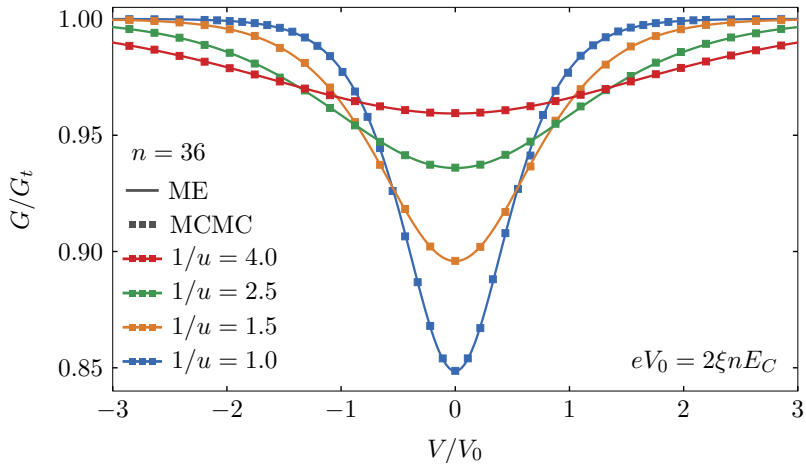


Figure 5.3: **Full width charging curves and zero bias conductance for $1/u \geq 1$ and $n = 36$, calculated with the master equation (ME) model and the Markov-chain Monte Carlo (MCMC) model.** Isothermal charging curves calculated with the MCMC model are drawn as squares and charging curves calculated with the ME model are drawn as solid lines. The bias voltage is scaled with $V_0 = 2\xi nE_C$, with $\xi \approx 5.44$. This produces curves, having a full width of $1/u$ at half maximum in the primary temperature regime.

from these, the MCMC tunneling model and the master equation tunneling model both reproduce the primary behaviour of CBTs in the universal regime. The normalized zero bias tunnel conductance $G(0)/G_t$ dip due to charging follows the series expansion [57]

$$\frac{G(0)}{G_t} \approx 1 - \frac{u}{6} + \frac{u^2}{60} - \frac{u^3}{630} \tag{5.20}$$

The expansion to the linear term in $u$ approximates $G(0)/G_t$ sufficiently well in the primary regime (down to $u \approx 1$). This behaviour is covered by the curves in Fig. 5.3 as well.

## 5.5. THE NONUNIVERSAL CHARGING REGIME AT $k_B T < E_C$

Beyond the universal regime of charging, the charging behaviour of tunnel junction arrays depends on the exact charge configuration with respect to the localization of excess charges and offset-charge on the islands. In this regime it is not appropriate to deduce the tunnel current with a master equation approach for $n = 2$ and an effective charging energy of $(n-1)e^2/nC_\Sigma$. For exploring the behaviour beyond the limits of the universal regime, the normalized differential conductance $G(V)/G_t$ is calculated for several temperatures $1/u$, reaching down far to $k_B T \ll E_C$, and for the limiting offset-charge cases of $q_0 = 0$ and $q_0 = e/n$. The result is summarized in Fig. 5.4, by plotting the charging curves versus the dimensionless voltage $eV/\Delta_C$, with the Coulomb gap of the array $\Delta_C = nE_C$.

For $1/u = 0.4$, the same charging curve is produced for $q_0$ and $q_0 = e/n$. This is consistent with the assumption that the lower temperature limit of the universal regime is around $1/u \sim 0.4$ [90]. For this temperature there is also a full consistency between the results of the MCMC tunneling model and the master equation tunneling model. For lower temperatures, a uniform offset charge of $q_0 = 0$ produces a stronger Coulomb blockade around zero bias, while for $q_0 = e/n$ the limiting conductance of $G(0)/G_t = 1/n$ is asymptotically reached. The $q_0 = 0$ case at $1/u = 0.001$, displayed in Fig. 5.4 a reaches

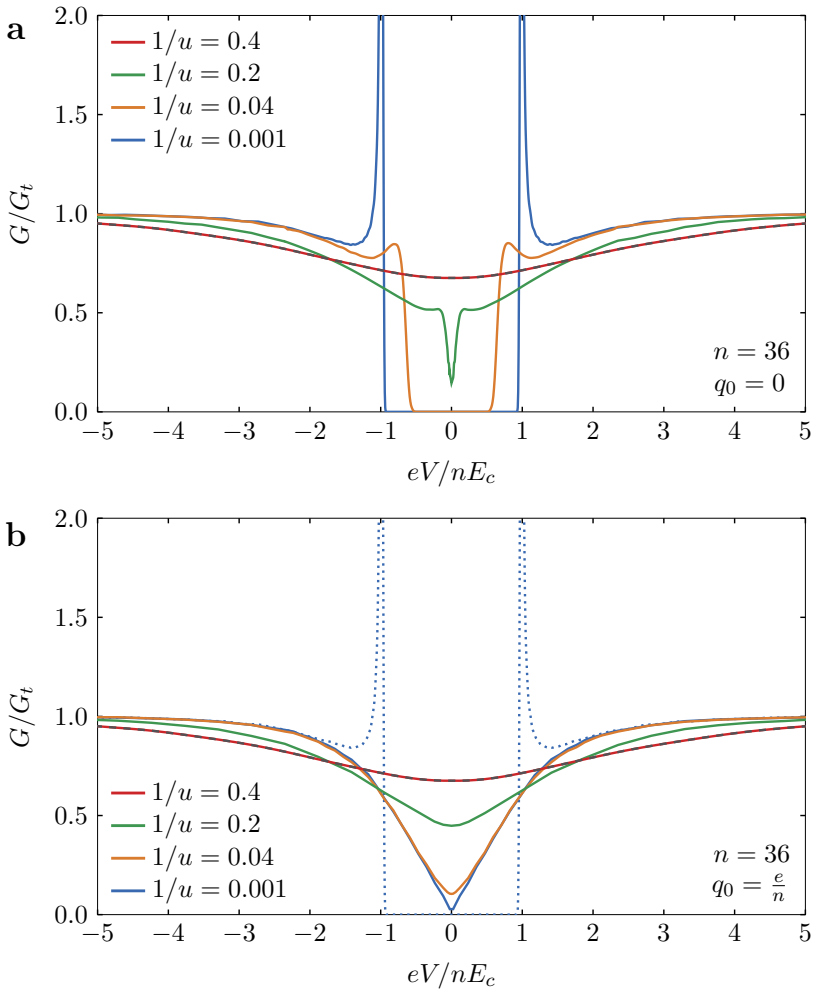


Figure 5.4: **Isothermal charging curves for $n = 36$, calculated with the Markov-chain Monte Carlo (MCMC) model for temperatures beyond the universal regime of charging. a** Tunnel junction array charging curves calculated with a uniform offset charge of $q_0 = 0$ on the islands, leading to maximum Coulomb blockade towards zero bias. **b** Charging curves for uniform offset charge of $q_0 = e/n$ on the islands of the junction array. In the ultralow temperature limit, a conductance of $1/n$ is asymptotically reached at zero bias. For both a and b the voltage is scaled with the Coulomb gap $nE_c$, which is reached for $1/iu \leq 0.001$ and zero offset charge.

full Coulomb blockade and was discussed earlier in the context of charge soliton propagation on tunnel junction chains at zero temperature, where the threshold voltage was found to be $\Delta_C = nE_C$, in agreement with the numerical results obtained in this work.

In the next step, the MCMC model is applied to probe the limits of the universal regime, in analogy to the approach in [132]. Therefore, the limiting cases of island offset charge $q_0$, being full Coulomb blockade with $q_0 = 0$, and no Coulomb blockade with $q_0 = e/n$, are addressed for $C_0 \gg C_g$. As in section 5.2, a constant $q_0$ means that all islands are occupied with the uniform offset charge $q_{0i} = q_0$. The zero bias tunnel conductance $G(0)/G_t$ is calculated with the MCMC model as a function of $k_B T/E_C$ for a SET ($n = 2$), as well as for junction arrays with $n = 20, 50, 100$. The results are plotted in Fig. 5.5 together with $G(0)/G_t$ calculated with the master equation tunneling model (ME) for $q_0 = 0$.

As can be seen, the MCMC model and the ME model give equal results for the SET case ($n = 2$) over the full temperature range, as it would be expected. For $n > 2$ the ME model deviates significantly in a way that the MCMC model predicts a significantly larger Coulomb blockade for $q_0 = 0$, as well as a tunnel conductance scaling with $G/G_t \to 1/n$ towards zero temperature for the case of $q_0 = e/n$. This result is based on the charging energy expression summarized in Fig. 5.2, where all $n-1$ possible states with a single excess electron and the empty chain have the same electrostatic energy if $q_0 = 1/n$. Since all other charge configurations are higher in energy, only these $n$ states are occupied at zero temperature, with an equal probability of $P = 1/n$, consequently leading to a normalized zero bias tunnel conductance given by (see Eq. 5.12). The stronger suppression of tunnel conductance for $q_0 = e/n$ with large $n$ puts a lower bound on the temperature down to $1/u \approx 0.01$ for all $n \gg 2$, while for a SET the temperature is within a defined band only for a small region at $1/u \approx 0.2$. On the high temperature side, a stronger Coulomb blockade of long arrays compared to a SET increases the temperature uncertainty.

Apparently, the tunnel conductance for $n \gg 2$ still follows the third order approximation of the ME result (Eq. 5.20) for $G(0)/G_t$ below $1/u = 0.4$. Thus, when defining the limits of the universal regime the work on the SET master equation tunneling model can be adapted and the acceptable error is defined as in [132] as 2.5 % deviation of the ME model to one of the limiting offset charge cases modelled with the MCMC model. For arrays not longer than $n = 50$, $G(0)/G_t$ is still universal down to $1/u \approx 0.3$. For short arrays, the limit of the universal regime is mainly determined by the $q_0 = e/n$, where a universal behaviour can be found for all $n$ down to $1/u \approx 0.2$. For $q_0 = 0$, the stronger Coulomb blockade of long arrays marks the limits of the universal regime such that e.g. for $n = 100$ the largest deviation from the third order approximation of $G(0)/G_t$ occurs for $q_0 = 0$.

The calculations for $q_0 = 0$ and $q_0 = e/n$ show that Coulomb blockade thermometers which are made of long arrays should perform well beyond the limit of $1/u = 0.4$, postulated in [132]. Furthermore it is not necessary to run MCMC algorithms to calibrate a Coulomb blockade thermometer beyond this limit. The limits of the universal regime found with the MCMC calculations in this work can be used as a valid temperature scale for any CBT while the tunnel conductance can be still calculated by a SET master equa-

tion tunneling model without offset-charge considerations. All higher order expansions of the zero bias tunnel conductance $G(0)/G_t$, as introduced in previous works, can be used down to a temperature of $1/u = 0.3$, marking a valid universal limitvalso for large $n$.

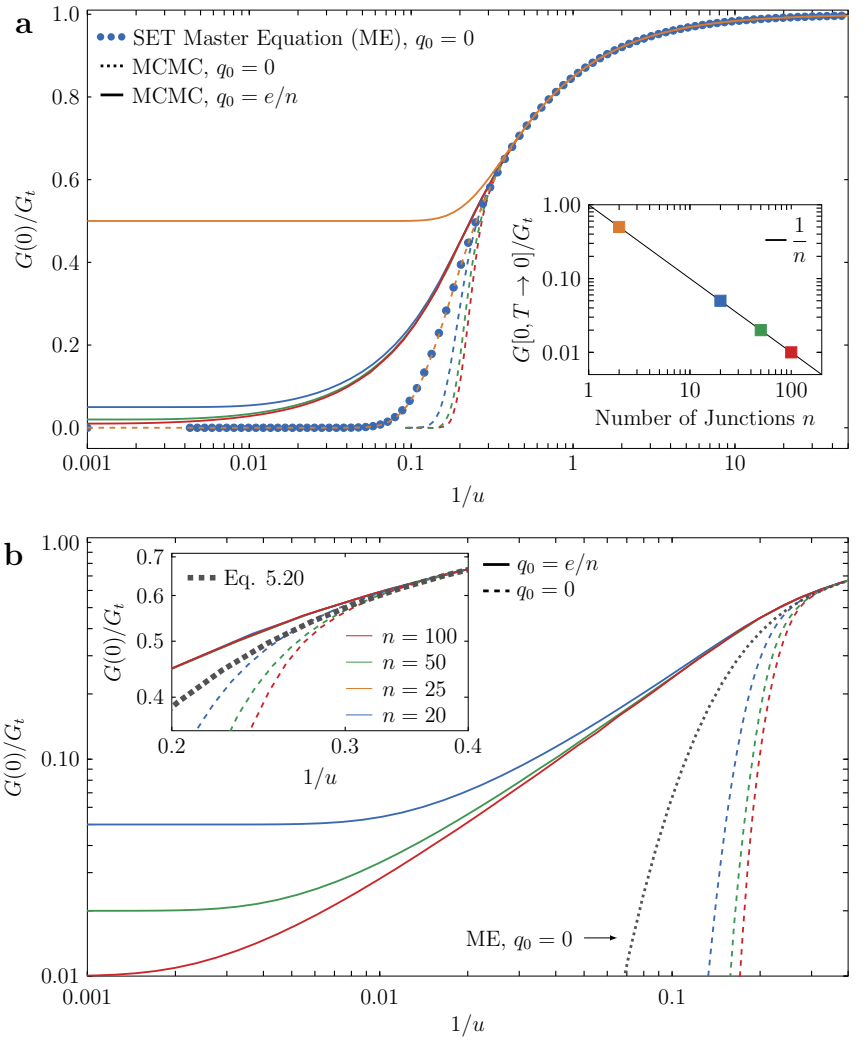


Figure 5.5: **The universal regime of charging for a linear array of $n$ tunnel junctions determined with the MCMC model. a** The zero bias tunnel conductance of a SET ($n = 2$), calculated with the MCMC model (solid orange lines), and agreeing well with the result of the master equation tunneling model (blue dotted line, only drawn for $q_0 = 0$). For isoenergetic tunneling which is reached at an offset charge $e/n$ the zero bias tunnel conductance at zero temperature is suppressed by 1/n, putting the limits of the universal regime to lower temperatures. Down to about $1/u \approx 0.3$ the tunnel conductance can be predicted with the SET model for $n \leq 50$. **b** Equal to **a** but the upper limit of temperature reduced to $1/u$ and $G(0)/G_t$ on a logarithmic scale. The zero bias tunnel conductance of the SET master equation model with $q_0 = 0$ is drawn as dotted line.

## 5.6. RANDOM OFFSET-CHARGES

To study the conductance behaviour of tunnel junction arrays under the influence of offset charges, the expectation value of the conductance $\langle G(0)/G_t \rangle$ is calculated in the presence of random offset charges. This initially raises the question what exactly random is in this respect, and how justified the assumption of a random offset charge is in general. To calculate the conductance of the CBT under realistic conditions, one has to find offset charge configurations which would also occur on a real device on which the island charge is not gate-controlled. For any thin film device, one normally has to deal with a significant number of trap charges and mobile donor charges. Very clean interfaces like the Si-$SiO_2$ interface have interface state densities of $1 \cdot 10^2$ $\mu m^{-2}$ [179–181]. Even if only a small amount of these charges are mobile, the offset charge on a floating island can be orders of magnitude larger than $e$. In a real device, where one or more of the islands are tunnel coupled to electrodes, this charge will be reduced by tunneling until a stable offset charge configuration is reached. For a SET this results in an offset-charge range of $q_0 = [-e/2, e/2]$, since any offset charge outside of this interval would enable a free energy decrease by tunneling of a charge $\pm e$. For a junction array with $n > 2$ it can be assumed that the system tends to compensate offset charge by tunneling, such that all island charges are at $|q_{0i}| < e$ but the limits at $\pm e/2$ can not be assumed since the configuration space is large and the system can be trapped in a local minimum of the electrostatic energy, while the global minimum is accessible over an activation energy.



For finding a realistic offset charge configuration based on the above considerations, the MCMC model is initialized with a random offset charge configuration, calculated from a uniform distribution of width $\pm 100e$, and a stable offset charge configuration is calculated by minimizing the free energy by a Markov-chain of randomly selected tunneling events. The charge configuration is taken as valid when all possible tunneling events out of this state increase the electrostatic free energy with $\Delta F_i > 0$. The results for arrays of several $n$ are shown in Fig. 5.6 by plotting the probability distributions of island charges $q_{0i}$, found after the minimization procedure. As can be seen in Fig. 5.6, island charges

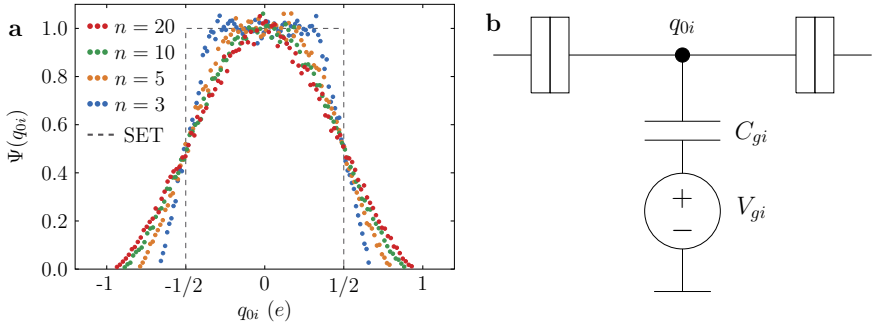


Figure 5.6: **Offset charge distributions leading to a thermodynamically stable state as a function of $n$. a** Offset charge distributions, calculated with a Markov-chain, minimizing $\Delta F$, for several $n$, and normalized to $e$. The offset charge distribution of a SET, not calculated but postulated as uniform between the limits $-e/2$ and $e/2$, is drawn as a dashed line for comparison. **b** Illustration of the location of the offset charge $q_{0i}$.

above $e$ do not occur, but values above $e/2$ are indeed found for $n > 2$. For modelling the tunnel conductance of a CBT with at a given offset charge configuration which was found to be thermodynamically stable, the zero bias tunnel conductance distribution $G(0)/G_t$ is calculated with the MCMC model. This procedure is repeated sufficiently often until a continuous tunnel conductance distribution $\{G(0)/G_t\}$ is obtained.

For a realistic result it is also important to take the effect of parallel chains of tunnel junctions, $m > 1$ into account (see Fig. 5.1). The conductance of the $n \times m$ junction array is the sum of the tunnel conductance of all $1 \times n$ arrays, with the probability of a specific conductance value depending on the conductance distribution $\{G(0)/G_t\}$. Consequently, the normalized tunnel conductance of an $n \times m$ array is calculated by constructing the distribution $\{G(0)'/G_t\}$ by randomly selecting $m$ values of $\{G(0)/G_t\}$ according to

$$\left\{\frac{G(0)'}{G_t}\right\}_j = \frac{1}{m}\sum_{i=1}^{m}\left\{\frac{G(0)}{G_t(i)}\right\}_i \tag{5.21}$$

5

For both cases the expectation value of the conductance $\langle G(0)/G_t\rangle$ and the standard deviation determine how likely it is to observe a specific conductance at a specific tem-

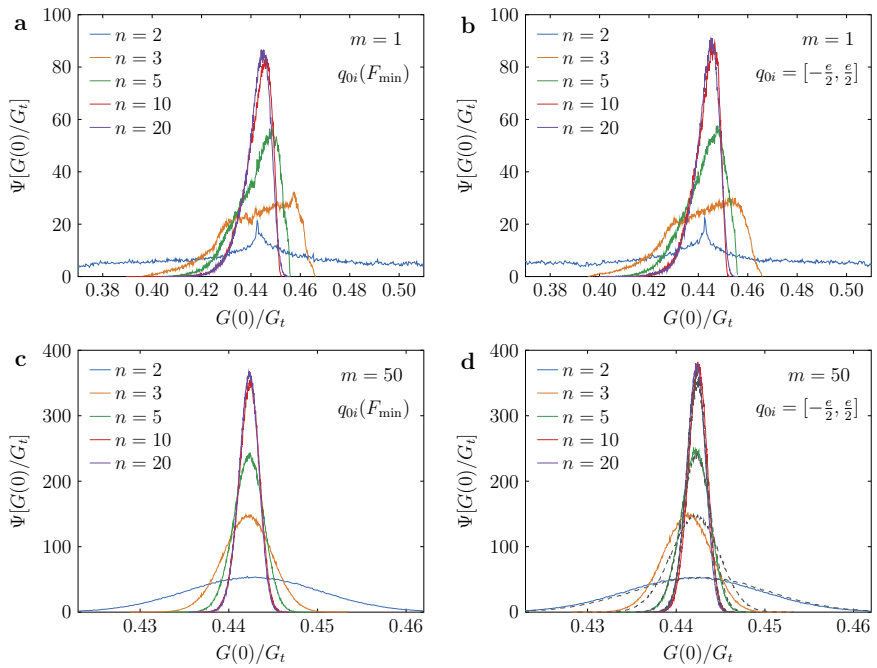


Figure 5.7: **Conductance distribution for tunnel junction arrays with different number of junctions in series $n$.** All distributions are normalized to 1, **a** In the nonuniversal regime the temperatures are chosen such that the expectation value of the conductance is centered. The temperatures are $1/u = 0.15$ ($n = 2$), $1/u = 0.18$ ($n = 3$), $1/u = 0.187$ ($n = 5$), $1/u = 0.189$ ($n = 10$) and $1/u = 0.190$ ($n = 20$). **b** The conductance distribution recalculated from the data in **a** with $m = 20$ arrays of $n$ linear junction arrays in parallel.

perature. Tunnel conductance distributions for arrays with $n = 2,3,5,10,20$ are calculated with the MCMC model and plotted in Fig. 5.7 for temperatures below the universal regime of tunneling. Since the conductance is nonuniversal with $n$, the temperatures are chosen such that $\langle G(0)/G_t \rangle$ is ver close for all $n$. All conductance distributions are calculated for $m = 1$ and $m = 50$, representing to extreme cases of a linear array, in which the conductance distributionis only determined by conductance broadening due to random offset charges, and a large number of linear arrays in parallel, in which the conductance distribution is strongly affected by $m$ as well. As expected from the considerations made in section 5.2, the conductance distribution for $m = 1$ narrows significantly when $n$ is increased. A saturation effect can be observed in Fig. 5.7 as the number of junctions above a specific treshold does not lead to a significantly narrower conductance distribution, as it would be expected due to a $e/n$ offset charge dependence: As long as $e/n$ is of the order of $e$, the device should have a significant response to variations in $n$.

By comparing the results calculated for offset charge configurations determined by minimizing the free energy with the results in which offset charges are limited to the interval $q_{0i} = [-e/2, e/2]$ (Fig. 5.7 c,d), one can see that the expectation value of the conductance and the overall shape of the conductance distribution is very similar, except for $n = 3$, where the expectation value is shifted to a lower conductance (see Fig. 5.7 d, the dashed in line in panel d corresponds to the distribution for $n = 3$ in panel c). As expected, the conductance distribution is further localized and smoothed by increasing $m$. Averaging over samples of any distribution will lead to a normal distribution around the same expectation value as it is visible in Fig. 5.7 for $m = 50$. This indicates that placing several chains of tunnel junctions offers far more beneficial aspects than just increasing the device conductance to a value which is acceptable for proper measurement instrumentation. Many chains in parallel significantly narrow the conductance distribution in the offset charge limit and shape the conductance distribution into a normal distribution.

The conductance distribution for finite $m$ and large $n$ over a wide temperature range is investigated by setting setting $n = 36$ and calculating the zero bias tunnel conductance distribution $G(0)/G_t$ between $1/u = 0.04$ and $1/u = 0.4$. At each temperature, the conductance distribution is calculated for several values of $m = 5,25,50,100$. The results are summarized in Fig. 5.8. As can be seen, $\langle G(0)/G_t \rangle$ has a well defined behaviour with temperature for all $m$. According to the error scale in the inset of Fig. 5.8 this would imply that for a large number of $m$ a CBT has a well defined relation of conductance to temperature even well beyond the limits of the universal regime found in section 5.5. By further decreasing the temperature, the conductance distribution is widened so much that the error becomes as large as the temperature. Adapting the error scale in the inset of Fig. 5.8 a, the temperature error of about 5 % is obtained at $1/u = 0.15$ for $m \geq 25$. This allows to extend the effective temperature range of CBTs, implemented as tunnel junction arrays with large $n$ and $m$, down to about half of the lower temperature limit of the universal regime (see Fig. 5.5). In this regime the behaviour of the tunnel junction arrays is not universal anymore, with mean conductance not only a function of temperature but also a function of $n$. This implies that if a CBT is to be operated in this regime, the tunnel conductance would be only accessible by a MCMC CBT model.

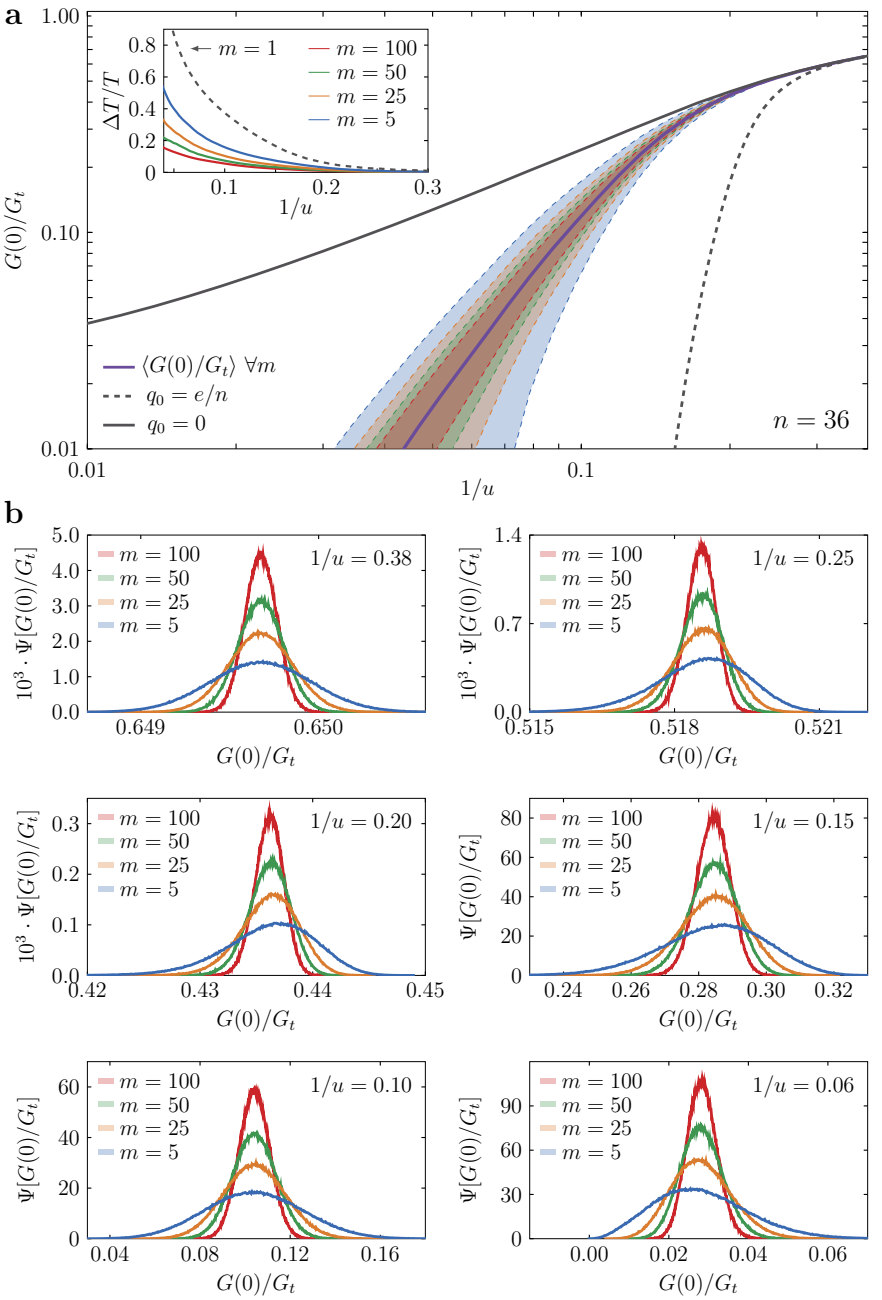


Figure 5.8: **Variance of the zero bias tunnel conductance of an array of $n \times m$ tunnel junctions beyond the universal regime, calculated with the MCMC model. a** The expectation value $\langle G(0)/G_t\rangle$ is plotted as a function of temperature, representing the mean value of the conductance distribution at a given temperature. A three standard deviations wide region around $\langle G(0)/G_t\rangle$ is plotted as filled region for different $m$. **Inset** Temperature error resulting from the finite width of the conductance distribution for different $m$. **b** Conductance distributions $\Psi\,[G(0)/G_t]$ for different $m$, plotted in separate panels. All distributions are normalized to 1.

## 5.7. NON-IDEALITIES IN REAL DEVICES

As shown in the previous section, offset charges can be mitigated by using devices with large $n$ and $m$. However, for realistic device modeling, the non-uniformity in the tunnel junction resistance $R_i$ and island coupling capacitance $C_i$ values has to be considered. The island capacitance mainly varies due to lithographic inaccuracy and film nonuniformities, while the tunnel resistance has an experimental uncertainty due to inhomogenous tunnel barrier formation. Usually one has standard deviations of $\Delta R \leq 10$ % and $\Delta C_\Sigma < 5$ % for a well developed process [141], with $C_{\Sigma,i} \approx 2C_i$.

First, the effect of capacitance disorder is considered by calculating a conductance histogram of an $n = 36$ and $m = 5$ device with a uniform distribution of junction capacitances with a width of $\Delta C$ (Fig. 5.9 a and b). Here, $\Delta C/C = 0$ corresponds to a homogeneous array, where the conductance distribution is governed by the random offset charges. Increasing $\Delta C$ results in a broadening of the conductance histogram as well as a quadratic systematic decrease in the expectation value. However the impact of $\Delta C$ on thermometry depends on the temperature, as we show in Fig. 5.9 a, where the rela-



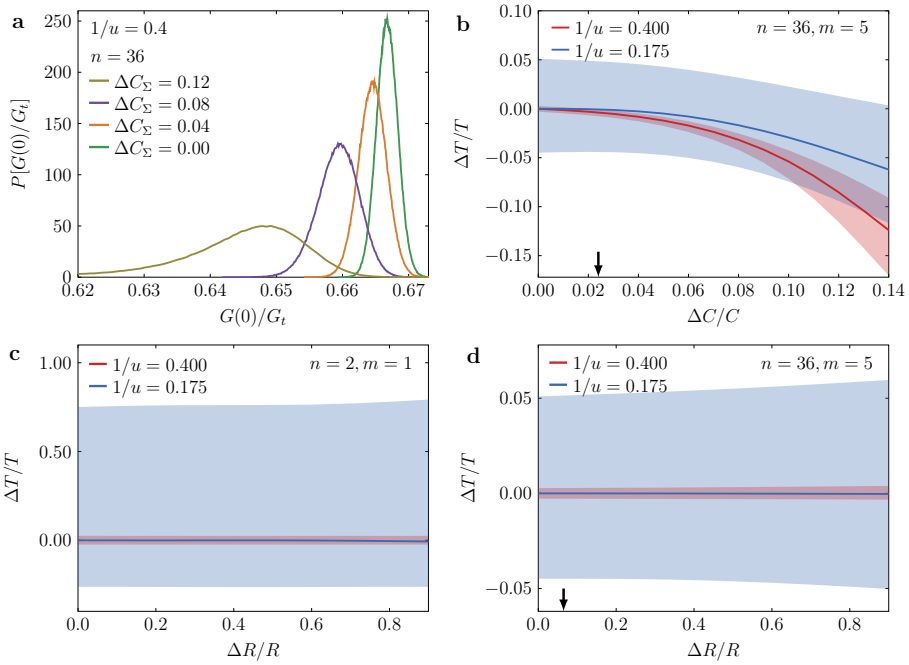


Figure 5.9: **Effect of nonuniformities in $R_i$ and $C_i$. a** Conductance distributions for different values of capacitance scattering at $1/u = 0.4$. The capacitances are assumed to be unifomly distributed around $C$ in an interval of $\Delta C$ **b** The systematic change in the temperature expectation value depicted as solid lines for $1/u = 0.4$ (red) and $1/u = 0.175$ (blue). The shaded regions denote the $3\sigma$ confidence intervals. **c** The systematic change in the temperature expectation value depicted as solid lines for $1/u = 0.4$ (red) and $1/u = 0.175$ (blue) in dependency of the resistance nonuniformity $\Delta R/R$ for a single island SET ($n = 1, m = 1$). The shaded regions denote the $3\sigma$ confidence intervals in temperature. **d** Same as c, but calculated for a junction array with $n = 36, m = 5$.

tive temperature error $\Delta T/T$ is displayed as the $3\sigma$ confidence interval as a function of $\Delta C/C$ at different temperatures. The results indicate that in the low temperature regime $1/u < 0.4$ and realistic capacitance variations of a few percent, the measurement error is dominated by the randomness of the offset charges.

Next, the effect of variations in the individual tunnel junction resistances is investigated, by performing the MCMC simulations with a uniform distribution of $R$ with a width of $\Delta R/R$ (Fig. 5.9 c and d). The resistance variations cause a weak quadratic decrease in the expectation value of the temperature, however even the extreme case of $\Delta R/R = 0.9$ yields a smaller systematic and statistical error than the capacitance disorder in the $\Delta C/C \sim 0.1$ regime. When comparing the $n = 2$ and $m = 1$ single island CBT with the $n = 36$ and $m = 5$ case the significant reduction in the statistical temperature error by increasing the array size can be seen. Not captured by the orthodox theory is coherent tunneling, which is occuring for $R_t \leq R_Q$.

## 5.8. CONCLUSIONS



In summary it was shown that the universal temperatureregime of a Coulomb blockade thermometer, in the limit of $C \gg C_g$, can be extended to $1/u \sim 0.3$ based on Markov-chain Monte-Carlo (MCMC) calculations without taking into account effects of random offset-charges. Currently, MCMC numerics provides the only available access to modelling collective charge carrier transport in tunnel junction arrays and thus a full range numerical model for CBTs. Drawbacks of MCMC implementations include longer runtimes, which is why the SET master equation tunneling model is still a model of choice down to the limits of the universal regime, found with the MCMC model.

By introducing random offset charges into the model, it can be shown that the accuracy of CBTs profits significantly from the stability of long tunnel junction arrays with respect to stability against random offset charges. The stability of tunnel junction arays against random offset charges enables Coulomb blockade thermometry far beyond the universal regime, while the error in temperature towards low temperatures is dominated by the increasing width of the conductance distribution. A CBT profits both from a large number of junctions in series and in parallel, since both localize the tunnel conductance distribution and extend the effective temperature range to lower values.

Non-idealities in the most important device parameters, being the tunnel junction resistance $R_i$ and the mutual capacitance of the islands $C_i$, are affecting the response of the device by increasing the temperature uncertainty of the device in the nonuniversal regime of charging. In the limits of the present treatment of the problem with MCMC algorithms in the orthodox theory of single electron tunneling, nonuniformities in the tunnel resistance show a negligible effect against nonuniformities in the island capacitance. Well proven fabrication techniques for tunnel junctions produce capacitance and resistance uncertainties well below limits of significance of these errors.

# 6

# On- and Off-Chip Nuclear Magnetic Cooling with Indium

*An experimentalist wishing to pursue research at low temperatures faces four technical difficulties: how to reach the low temperatures, how to measure it, how to reduce the external heat leak so that the low temperature can be maintained for a sufficiently long time, and how to transfer cold from one place to another. Many experimental methods have been developed to provide a satisfactory solution to these problems.*

Olli Lounasmaa (1930-2002)

This chapter is based on M. Sarsby, N. Yurttagül, A. Geresdi, *500 Microkelvin Nanoelectronics*, Nature Communications **11**, 1492 (2020)

## 6.1. INTRODUCTION

The conventional means of cooling nanoelectronic devices relies on the thermal coupling between thin-film phonons and conduction electrons, scaling with $\dot{Q}_{\text{e-p}} \propto T^5$ (see Eq. 2.4). In larger volumes, where electron phonon scattering is not the bottleneck of heat transport, the latter is limited by transmission of phonons over an acoustic boundary resistance into the insulating substrate, $\dot{Q}_{\text{p-p}} \propto T^4$ (see Eq. 2.2). Both thermalization processes rapidly diminish towards ultralow temperatures, limiting the lower limit of accessible temperatures for operating miniaturized devices by hot electron effects. In a typical dilution refrigerator, $T_{\text{p}} \geq 5$ mK, specially built systems reach 1.8 mK [50], limiting $T_e > T_p$ to the millikelvin regime. The lowest static electron temperature reached by electron-phonon thermalization on-chip is $T_e = 3.9$ mK in a metallic island [46], other experiments reached similar values [43, 131, 163] in semiconductor heterostructures.

This technological limitation can be avoided by integrating a nuclear refrigerant with the nanoelectronic device and performing magnetic refrigeration on the chip [45, 47], (see 4). This procedure enables a direct heat transfer $\dot{Q}_{e-n} = \alpha\kappa^{-1}B^2\,(T_e/T_n - 1)$ on the timescale of the spin-lattice relaxation time $\tau_1 = \kappa/T_e$ (see sections 2.1.3, 2.2.4, 4.1 for details). Nuclear magnetic cooling has been utilized to cool bulk metals down to nuclear spin temperatures well below 1 μK [23, 182]. If only nuclear Zeeman splitting is present, which is linear in field, the ultimate temperature is limited by the decreasing molar heat capacity, $C_n \propto B^2/T^2$, in the presence of finite heat leaks (see section 4.1). The small amount of nuclear refrigerant which can be integrated on-chip by film deposition techniques, in combination with the relatively large heat load on micro- and nanoelectronic devices, is a major problem for on-chip nuclear cooling, limiting the performance by the diminishing nuclear heat capacity due to Zeeman interaction at small magnetic fields.

The on-chip integrated nuclear heat capacity can be singnificiantly enhanced towards small magnetic fields and microkelvin temperatures, by using a nuclear refrigerant with non-magnetic splitting of the nuclear eigenenergies. Nuclear quadrupole and pseudoquadrupolar interaction, occuring in metallic nuclear paramagnets and intermetallics with van-Vleck susceptbility (see section 2.3.4) shows just the right temperature scaling of 0.1-1 mK, which is necessary stabilize the nuclear heat capacity at small magnetic fields or even in the absence of a magnetic field. On the other hand, bulk nuclear cooling stages have predominantly been built of Cu [20], owing to its high thermal conductivity, beneficial metallurgic properties and weakly coupled nuclear spins, which allows for magnetic refrigeration of the nuclear spins down to < 1 μK. However, the weak hyperfine interaction in Cu results in a decoupling of the electron system at much higher temperatures, ~ 100 μK, and nonmagnetic level splitting is fully absent in the nuclear energy spectrum. Chipscale nuclear magnetic cooling attempts with Cu [45, 47] consequently showed a weak performance in the presence of electronic heat load. Another material, a Van Vleck paramagnet, $PrNi_5$, has been used as a bulk nuclear refrigerant, exploiting its interaction-enhanced heat capacity in a temperature range of $T > 200$ μK [183] even in dry dilution refrigerators [54]. While $PrNi_5$ also shows a significant pseudoquadrupolar interaction and extremely fast spin-lattice relaxation, preparing the material as thin-film material for chipscale nuclear magnetic cooling is very difficult (see section 8.1.2).

For on-chip nuclear magnetic cooling applications In has been demonstrated to be a viable on-chip nuclear refrigerant (see chapter 4). Elemental In has a large nuclear magnetic moment, combined with a short spin-lattice relaxation time with $\kappa = 0.084-0.086$ K s, giving rise to a nuclear cooling performance ratio $\alpha/\kappa$ ratio 60 times better than Cu (see section 4.1). The large nuclear quadrupole coupling with $\hbar\omega_Q \approx 0.2$ μeV, corresponding to about 0.23 mK, ensures sufficient nuclear heat capacity by nonmagnetic spin splitting, even in the absence of a magnetic field. As Cu, In allows for on-chip integration of patterned thick films by electrodeposition from aequous salt solutions (see section 3.1.2) and is a versatile interconnect material for superconducting quantum circuits [30] and cryogenic applications due to its metallurgical properties. Experiments with on-chip nuclear refrigeration based on In microrefrigators showed a rapid consumption of the nuclear heat capacity by large molar heat leaks, which thus far limited the attainable electron temperatures above 3 mK both for Cu [45] and In as on-chip refrigerant. The short hold temperature hold times limit the practical applications of devices which are solely combined with miniaturized nuclear microrefrigerators. Thus, the key to achieve a sufficient thermal stability in the chipscale nuclear magnetic cooling process is the reduction of the external heat leak into the chip, such that it is just a sufficently small fraction of the heat of magnetization, accumulated over time. A recent work [47] has shown, that coupling the leads of a CBT to a set of parallel nuclear demagnetization stages, reduces the heat leak into a single CBT island to $< 0.1$ fW, yielding $T_e = 2.8$ mK by a combined on- and off-chip nuclear magnetic cooling approach with Cu, resulting in a hold time of about 1 h below 3 mK after nuclear demagnetization.



In this work a combined on- and off-chip nuclear demagnetization approach with In, surpassing the 1 mK limit in a nanoelectronic device is realized. An electron temperature below 500 μK is achieved by combining on-chip In cooling blocks with an off-chip parallel network of bulk In leads, attached to a Cu bulk stage. By demagnetization cooling of all components together, the heat leak to the nanoscale device is greatly reduced, enabling both a record low final electron temperature and long hold times in the microkelvin regime of several days. Signatures of a strong coupling of the In nuclei to an electric field gradient are revealed in terms of measuring the demagnetization efficiency under nearly adiabatic conditions. By demonstrating finite bias quantum transport experiments in the microkelvin regime, a working microkelvin refrigeration is established.

## 6.2. EXPERIMENTAL SETUP

For performing the nuclear cooling process on-chip and off-chip, a CBT with on-chip nuclear cooling functionality (see sections 3.1.1, 3.1.2 for details) is mounted into a custom made demagnetization stage. The design of the parallel nuclear cooling stages is described in section 3.3. The stage consists of a Cu stage, thermally anchored to the mixing chamber via a superconducting heat switch. A parallel set of off-chip stages, made of In wires, is utilized for cooling the leads of the device (see Fig. 6.1). The leads are precooled over epoxy film thermalization junctions (see section 3.3 for details), enabling single heat switch operation of parallel stages. Filtering of electromagnetic noise is implemented as described in section 3.3. The CBT is placed in the magnetic field center with the leads made out of thick In wires, comprising the parallel set of nuclear cooling stages, galvan-

ically disconnected from the Cu stage. The CBT is a $36 \times 15$ Al/$AlO_x$/Al tunnel junction ($780 \times 780$ nm$^2$ junction area) array, fabricated in an *ex-situ* scheme [141]. Since the tunnel junctions with $R_t \approx 35\,\mathrm{k}\Omega$ correspond to high thermal barriers and electron-phonon coupling diminishes strongly towards ULT, In cooling bars with $V = 50 \times 140 \times 25.4\ \mu\mathrm{m}^3$ (11.4 nmol) are electrodeposited on each island for local nuclear cooling. The used device has only 5 conducting lines, resulting in an $n \times m = 36 \times 5$ CBT array. With Coulomb blockade thermometry, the electron temperature can be measured during the nuclear magnetic cooling cycle. Crucially for temperature measurements during demagnetization cooling, CBTs exhibit no sensitivity to the applied magnetic field [134]. An overview of how the CBT is thermally anchored to the In nuclear cooling stages is shown in Fig. 6.1. For isothermal magnetization (see Fig. 2.3) of the islands, it is necessary to remove the high field heat of magnetization of the In cooling blocks from the islands and from the parallel set of In wires cooling the leads. Thermalization of the leads with the Cu stage (thermalized with the mixing chamber at $T_{\mathrm{MC}}$) is provided by the epoxy films with $\dot{Q}_{\mathrm{th}} = kA(T_L^4 - T_{\mathrm{MC}}^4)$ (see sections 3.3.2, 6.4). The heat of magnetization of the In islands on the CBT has to to flow over a thermal series resistance of, electron-nucleus scattering $R_{\text{e-n}}$, electron-phonon scattering $R_{\text{e-p}}$ or phonon-phonon scattering $R_{\text{p-p}}$, and the epoxy thermalization junctions. The large thermal resistance $R_{\mathrm{wf}}$ in parallel prevents any sig-



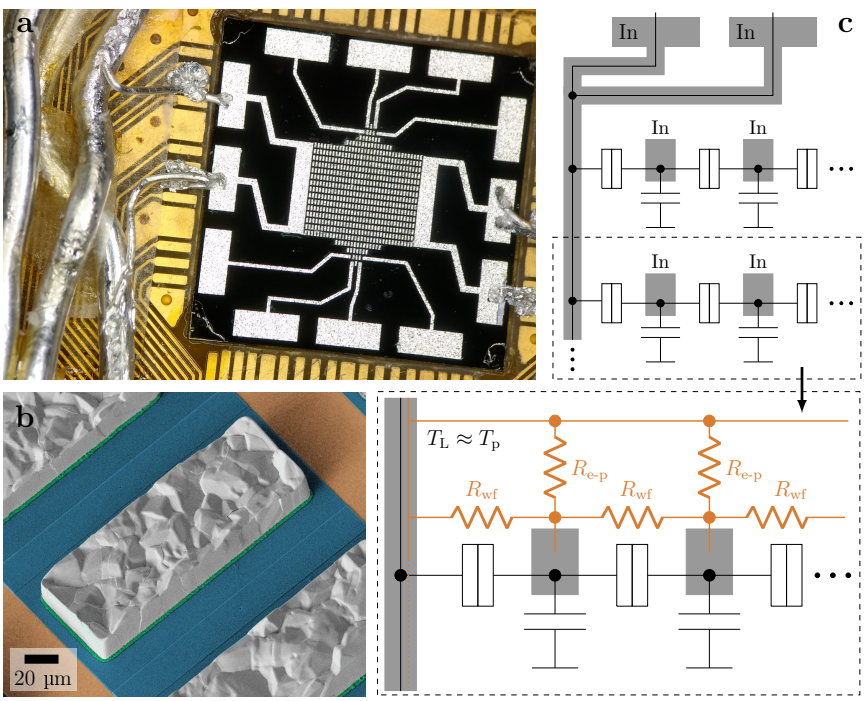


Figure 6.1: **Overview of on- and off-chip nuclear magnetic cooling with In. a** The CBT is electrically connected to the In stages by In-In cold welding. **b** In cooling bars are electrodeposited onto the islands for chipscale nuclear cooling. **c** Overview of the thermal coupling of the CBT islands to the In stages.

nificant heat flow over the junctions. At millikelvin temperatures either $R_{\text{e-p}}$ or $R_{\text{p-p}}$ is the thermal bottleneck for this process. In the limit of $T_e \leq 1$ mK, electron-phonon scattering becomes in turn so weak that the islands are only cooled the In fins integrated onto the islands of the CBT. In this regime $R_{\text{e-p}}$ and $R_{\text{wf}}$ (see Fig. 6.1), enabling the heat flow $\dot{Q}_{\text{e-p}} = \Sigma V \left(T_e^5 - T_p^5\right)$ and $\dot{Q}_{\text{wf}} = \frac{L_0}{2R}\left(T_e^2 - T_L^2\right)$ (see section 2.1 for details), are effectively open, thermally isolating the CBT towards cooling into the submillikelvin regime.

## 6.3. THERMOMETER CALIBRATION

With the device leads thermally anchored to the In stages, the CBT is self-calibrated by obtaining isothermal charging curves, with the temperature of the mixing chamber set to the corresponding temperature with a resistive heater (see section 3.4). In Fig. 6.2, the differential conductance, $G/G_t$, of the CBT is plotted against the bias voltage. The differential conductance is measured with a conventional low frequency lock-in technique at 19.3 Hz (see section 3.2.1). As described in section 2.3.4, a master equation model of single electron tunneling [56, 57] is used to find the electron temperature of each curve and the charging energy $E_C$ as a global fit parameter. With a total capacitance of each island $C_\Sigma$, the charging energy for a tunnel junction array of length $n$ is defined as $E_C = e^2/C_\Sigma \times (n-1)/n$ (see section 2.3.4 and Eq. 5.5). Fitting all curves to a common charging energy results in $E_C = 116.3 \pm 0.8$ neV, yielding $C_0 = 669.8 \pm 2$ fF. Remarkably, at a small magnetic field of $B = 45$ mT, required to suppress superconductivity, an electron temperature $T_e = 7.07 \pm 0.09$ mK is achieved. $T_e$ as a function of the mixing chamber temperature $T_{\text{MC}}$ shows a saturation behavior below 10 mK (inset of Fig. 6.2). In this regime Joule heating of the CBT at finite bias is corrected for as described in section 3.4 and [69]. A temperature-independent magnetoresistance between zero field and 12 T (see Fig. 3.3 d) is observed, which is accounted for during magnetic field ramps.



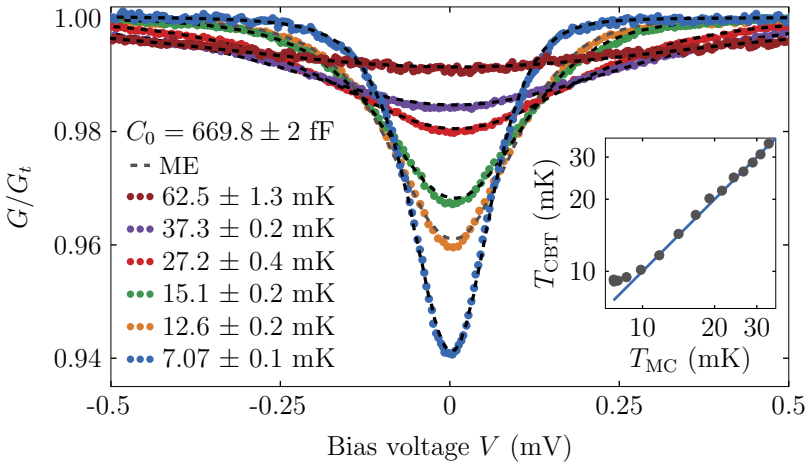


Figure 6.2: **Isothermal charging curves of the CBT used for on-chip nuclear cooling experiments.** the tunnel conductance $G$ is normalized with the asymptotic tunnel conductance $G_t$ and fitted to a master equation model (dashed). Inset: $T_{\text{CBT}}$, measured against the mixing chamber temperature (set with resistive heater).

## 6.4. NUCLEAR MAGNETIZATION EFFICIENCY

To perform the nuclear magnetization (precooling, see Fig. 2.3) process, the parallel set of In stages, thermally anchored to the CBT leads (see Fig. 6.1), is galvanically separated from the Cu bulk stage (see Fig. 3.10) and cooled by the mixing chamber through epoxy resin. Because of this, the characerization of the system with respect to nuclear magnetization is complicated compared to the simple case evaluated in section 4.3. The CBT islands are thermally coupled to the mixing chamber via the epoxy-resin layers, in series with the thermal resistance provided by electron-phonon scattering. On the other hand, the heat of magnetization of the macroscopic In wires has to flow only over the epoxy layers to the mixing chamber (In both cases the additional series resistance of the Al heat switch can be neglected when in the closed state). The temperature dynamics of the CBT during magnetization precooling will be dominated by either weakening electron phonon coupling between the CBT islands and the substrate, or a combination of an increasing heat release of the nuclear moments in the In wires upon further magnetization, in combination with a increasing thermal resistance of the epoxy resin layers for thermalization. Utilizing solely on-chip nuclear magnetic cooling without heat-switching between the coldfinger and the mixing chamber allowed to cool the CBT islands to the same base temperature at 13 T, as reached at low magnetic field (see section 4.3). To evaluate the limiting factors for precooling in the present case, the thermal bottleneck for nuclear magnetization of the CBT islands needs to be determined.



Since there is no thermometry performed on the bulk In stages, only the temperatures of the CBT and the mixing chamber are accessible. Due to the low electron temperature of 7 mK achieved at 45 mT it is assumed that at $T > 10$ mK the In stages are well thermalized with the electrons on-chip with $T_e \approx T_\mathrm{L}$, where $T_\mathrm{L}$ is the temperature of the leads as in Fig. 6.1. In order to evaluate the high field magnetization efficiency of the CBT and the In stages, the electron temperature $T_e$ is measured after ramping up the field to 12 T. The resulting temperature is plotted in Fig. 6.3 as function of time. The electron temperature reaches 12 mK after magnetizing the whole system for 180 h. $T_e(t)$ is fitted to a model which parameterizes the heat flow from the In leads to the mixing chamber via the epoxy layers with $\dot{Q}_\mathrm{th} = kA(T_\mathrm{L}^4 - T_\mathrm{MC}^4)$ (see section 3.3.3 for details). The nuclear heat capacity of the In stages, $C_{n,L}$, exceeds the nuclear heat capacity of the In integrated on-chip by several orders of magntiduce and is approximated by $C_{n,L} = n_\mathrm{L}\alpha B^2/T_\mathrm{L}^2$, with the molar Curie constant $\alpha = N_A I(I+1)\mu_n^2 g_n^2/3k_\mathrm{B}$. $C_{n,L}$ sets the reactance of the system according to $\dot{Q} = C_{n,L}\dot{T}_e$ and with $T_e \approx T_\mathrm{L}$ one arrives at the following differential equation for $T_e$

$$\frac{\partial T_e}{\partial t} = \left(\frac{kA}{n\alpha B^2}\right) T_e^6, \tag{6.1}$$

with $n_L = 2 \times 2$ mmol (see section 3.3.1). Integrating with respect to $T_e$ yields an expression for $T_e(t)$ to which the measured electron temperature during the magnetization process (Fig. 6.3) is fitted, yielding $k = 0.034$ W K$^{-4}$. This is compared to $k_0 = 1.28 \cdot 10^{-4}$ W K$^{-4}$, obtained as a reference for a $d \approx 30$ µm epoxy resin layer, separating two polished Cu specimens over a contact area of $A = 1.6$ cm$^2$. The exact insulator thickness $d$ and the total contact area $A$ for the bulk indium stages is not well defined because the In wires are rolled out on the epoxy resin layer and the PCB lossy transmission line filters are ther-

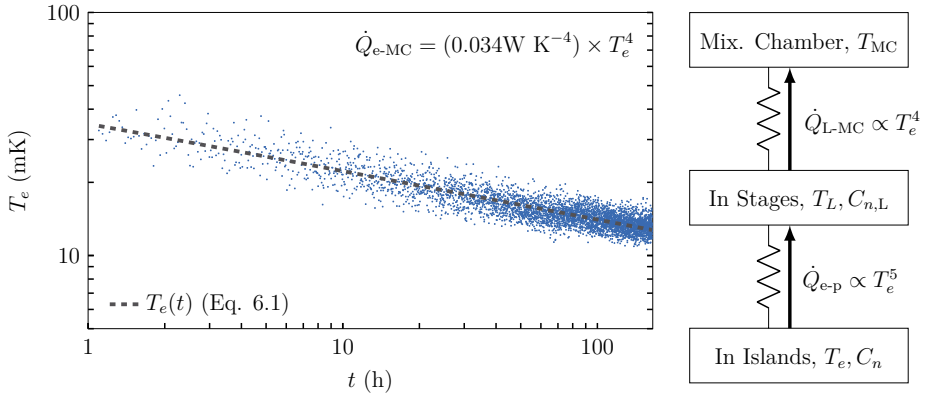


Figure 6.3: **Temperature of the CBT measured during nuclear magnetization at 12 T** The thermal coupling to the mixing chamber of the dilution refrigerator (at 5 mK), extracted from the measured electron temperature $T_e$, implies that the nuclear magnetization efficiency is limited by the thermal conductivity of the epoxy thermalization junctions and not weakening electron-phonon coupling on the miniaturized device.

mally anchored to the Cu stage over a large contact area via epoxy resin layers as well. A possible contribution to the large increase in thermal conductivity over the Cu-epoxy-Cu film thermalizers could be a larger effective surface area of the soft In compared to Cu, used for the thermal conductivity reference. The actual contact area between metals can be as low as only about $10^{-6}$ of the nominal contact area, due to microscopic irregularities of the metal surfaces [9]. While limited by the finite nuclear heat capacity of the bulk In stages, the CBT islands can be cooled to a temperature of about 12 mK in a field of 12 T, corresponding to a single island entropy removal of about 40% (see inset of Fig 4.3).



## 6.5. SUB-MILLIKELVIN MAGNETIC COOLING OF THE CHIP

The nuclear magnetic cooling cycle is initialized by precooling the device with a closed heat switch at $B_i = 12$ T. After magnetizing the nuclear spins for 164 h, the CBT reaches an electron temperature of $T_e \approx 12$ mK. For performing the nuclear demagnetization process, the Al heat switch (see section 3.3.1, Fig. 3.12) is opened and the magnetic field is ramped down to $B_f = 100$ mT with a decreasing rate $\dot{B}(t)$. The ramp rate is adapted with the magnetic field $B(t)$ according to $\dot{B} = -\alpha B(t)$, giving rise to $B(t) = B_i \exp(-\alpha t) + B_f$. By setting $\alpha = 2 \times 10^{-4}\text{s}^{-1}$, the ramp rate was sufficiently slow to to account for the nonlinear decrease of $G(0)/G_t$ towards lower temperatures, in combination with a narrower charging peak by offset bias compensation which involves tracking of the differential resistance in a small bias windows around zero. The resulting measured tunnel conductance around zero bias, $G(0)/G_t$, is plotted in Fig. 6.4 as a function of magnetic field. Towards reducing the magnetic field, $G(0)/G_t$ drops from its initial value of $> 0.9$ to a value as low as 0.38, indiciating a significant reduction of electron temperature and cooling of the CBT well below the universal regime (see section 5.5, Fig. 5.5). The master equation tunneling model (see section 2.3.4) can not be used over the whole range of the experiment because in the regime of $1/u \geq 0.3$, where the system is invariant to random island charges, is left (see section 5.5). In the limits of the universal regime and $C_0 = 0.67$ pF,

the temperature at the lower range limit of $1/u = 0.3$ (corresponding to $G(0)/G_t \approx 0.55$) corresponds to an electron temperature of 770 µK. This temperature is clearly reached without taking into account random offset charge effects. This demonstrates that 1 mK is the first time ever [24] surpassed inside a nanoelectronic device.

For obtaining the electron temperature on the CBT islands beyond the universal regime, $G(0)/G_t$ is modelled with the Markov-chain Monte-Carlo (MCMC) model introduced in section 5.2, including random offset charges for each island, as described in section 5.5. Using the MCMC approach, the expectation value of the differential tunnel conductance $\langle G(V,T_e)/G_t \rangle$ of the junction array is calculated for 10000 gate charge configurations, at a given $T_e$ and bias voltage $V$, resulting in a histogram of the CBT conductance as a sum

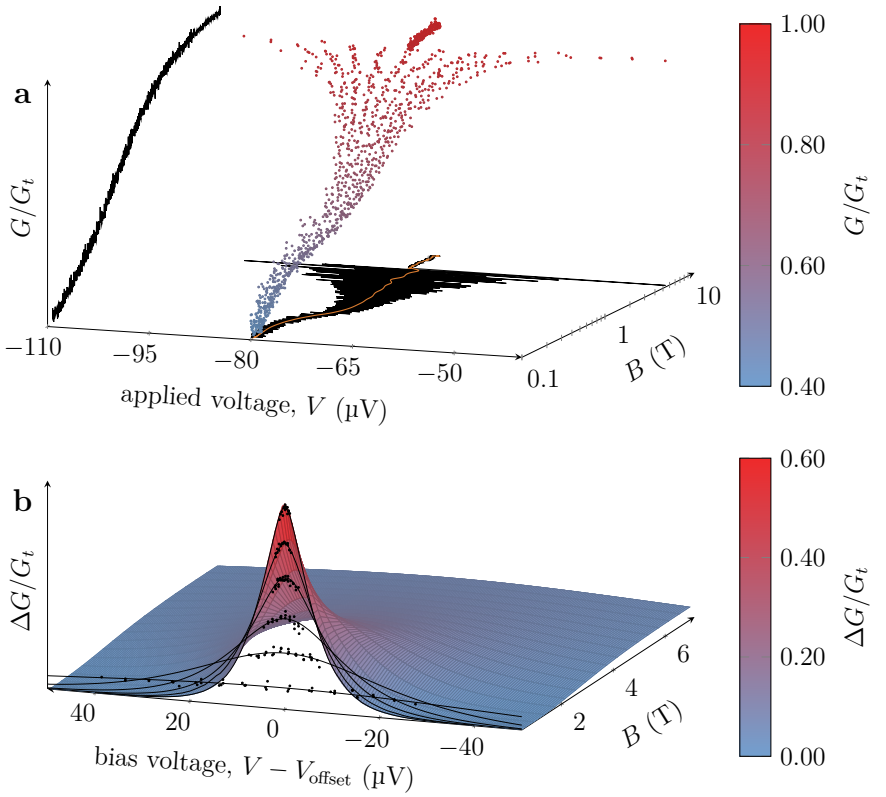


Figure 6.4: **Overview of the dynamic offset-bias compensation and thermometry procedure for sub-1mK CBT thermometry. a** The measured tunnel conductance $G$, obtained during nuclear demagnetization from 12 mK and 12 T to 0.1 T , is normalized to the tunnel conductance in the Ohmic regime $G_t$ and plotted as a function of measured voltage and magnetic field during demagnetization. Offset-bias is compensated by measuring the differential resistance $R = \Delta V/\Delta I$ in a small bias window and determining the offset-bias $V_{\mathrm{offset}}$ corresponding to the slope of the charging peak. The voltage increments for scanning the differential resistance are dynamically adapted with the curvature of the charging peak. **b** The measured differential conductance around zero bias is compared to a master equation model (see section 2.3.4) and the MCMC model (see sections 5.3, 5.5 for details) of single electron tunneling in a tunnel junction array of $n = 36$ junctions in series.

of $m = 5$ randomly selected line conductances. $G(V)/G_t$ traces, measured over a small bias window at constant temperatures, are fitted to either the master equation tunneling model for $G(0)/G_t \geq 0.55$ or the MCMC model for $G(0)/G_t < 0.55$. Some of the calculated charging curves are plotted together with measured charging peaks in Fig. 6.4. As can be seen by comparing the results of the single-electronics model with the tunnel conductance suppression in the small bias window used for bias offset tracking, the curvature around zero bias is well reproduced with both the master equation tunneling model and the MCMC model for single electron transport, validating the functionality of the CBT.

The electron temperature $T_e$, obtained from the zero-bias conductance $G(0)/G_t$, measured during the field ramp, is plotted in Fig. 6.5 and Fig. 6.6 as a function of time. In Fig. 6.6 the electron temperature is plotted only for the field ramp and the warmup period. From the stable base temperature of $T_e \approx 12$ mK, reached after the long magnetization process at 12 T, the electron temperature drops in accordance with the drop of the magnetic field while ramping down the field. After finishing the field ramp, a lowest electron temperature $T_e = 421 \pm 35$ µK is found, followed by a slow increase of the electron temperature with time. The warmup rate is as low as $\dot{T}_e = 1.7$ µK/h, giving rise and a hold time of 85 h with $T_e < 700$ µK, indicating a significant nuclear spin heat capacity seen by the electrons on the CBT islands. This duration was not limited by the finite nuclear heat capacity on chip, but by the periodic cryogenic liquid transfer to the host cryostat, inducing mechanical vibrations and consequently a rapid warmup of the device. Other than in the on-chip cooling experiments (see Fig. 4.5) there is no rapid temperature upturn but continuous cooling towards further reduction of the magnetic field.



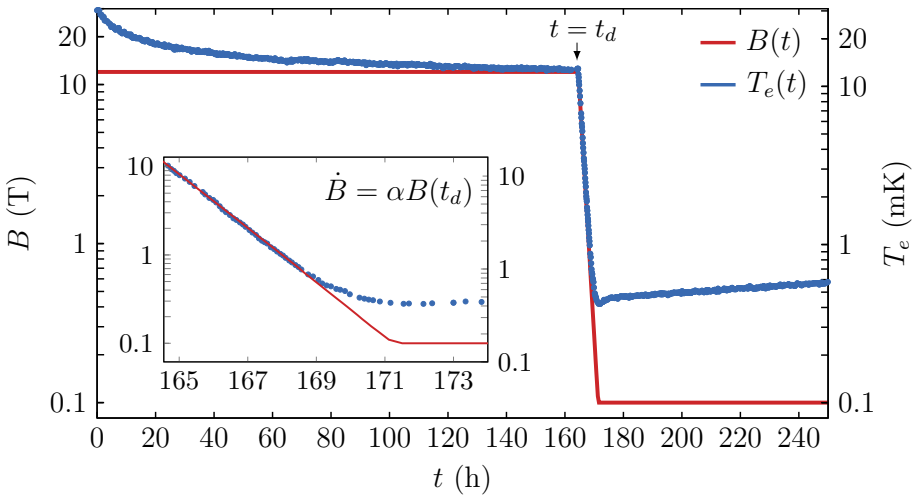


Figure 6.5: **Microkelvin refrigeration of electrons measured with the CBT.** Temperature and magnetic field as a function of time for the full nuclear cooling cycle (see also Fig. 2.3 for details), reaching an electron temperature of $T_e = 421 \pm 35\,\mu$ K after demagnetization from 12 T to 100 mT. The electron temperature stays below 700 µK for more than 90 h during the warmup. **Inset** temperature and magnetic field as a function of time only for the demagnetization and a short, 2 h long part of the warmup after reaching the minimum temperature.

In Fig. 6.6 the measured electron temperature is plotted as a function of time, with the time zeroed at $t_d$, being the time of the magnetic field ramp start (see Fig. 6.5). In panel a the measured electron temperature is plotted together with a calculated nuclear spin temperature, assuming a fully adiabatic demagnetization process. Other than in chapter 4, the quadrupolar contribution to the nuclear entropy is not treated as a small perturbation but included in terms of a residual magnetic field of $B_{\text{int}} = 295$ mT (see Eqs. 6.3

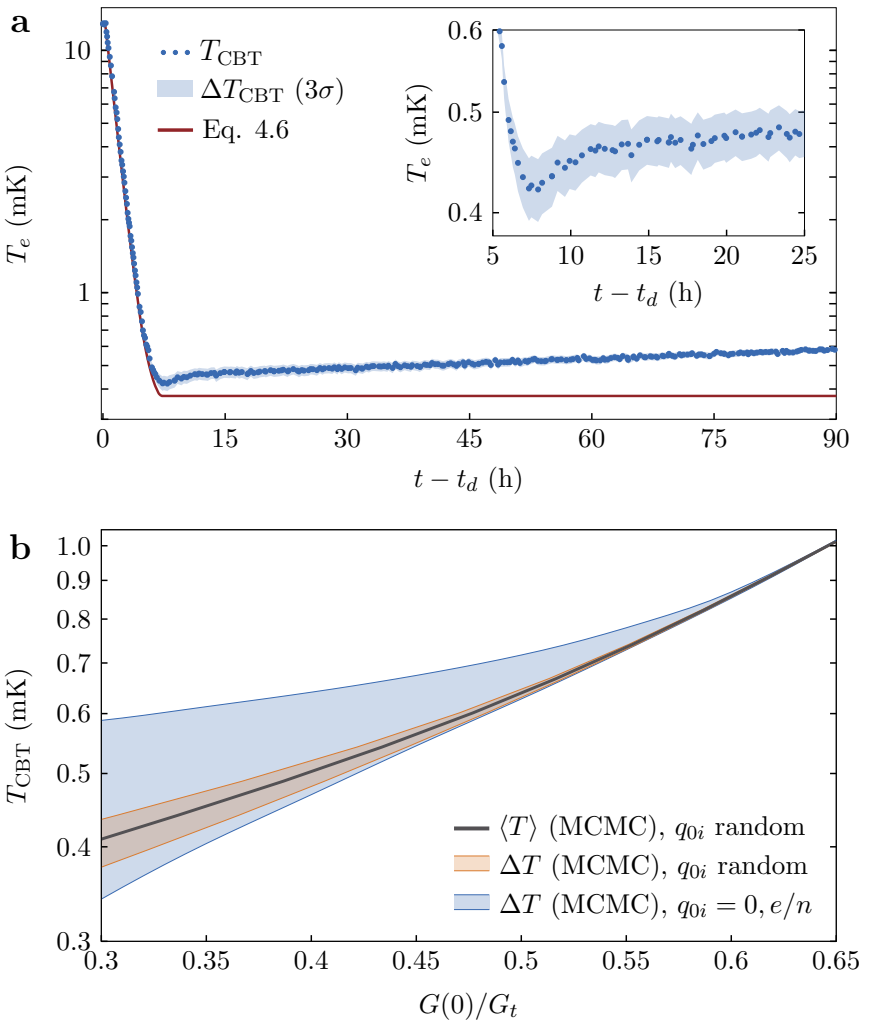


Figure 6.6: **Nuclear Demagnetization to < 1 mK and warmup of the CBT islands with the residual heat leak.** **a** The measured and calculated (Eq. 6.2) electron temperature during demagnetization and warmup is plotted versus time. The temperature error is plotted as shaded region in three standard deviations. **b** The error scale due to random offset charges is plotted as orange shaded region around the temperature expectation value (black solid line). For comparison the temperature uncertainty bands according to the universal regime for the limits of zero offset charge ($q_{0i} = 0$) and charge degeneracy ($q_{0i} = e/n$) are plotted as blue shaded regions.

and 6.4). When assuming $T_e = T_n$, the electron temperature should evolve as

$$T_e(B) = \frac{\sqrt{B(t)^2 + B_{\text{int}}^2}}{B_i} T_{e,i} \tag{6.2}$$

With $T_{e,i} = 12$ mK. Remarkably, the measured electron temperature follows an adiabatic model down to a field of 0.8 T, where the measured electron temperature splits off (inset of Fig. 6.5). The lowest electron temperature of $421 \pm 35$ μK is close to the expected value of 375 μK for an ideal process. In Fig. 6.6 the temperature error is plotted as shaded region around the temperature expectation value. The error in $T_e$ results from the error of $C_0$ and the conductance uncertainty due to random offset-charges. If the temperature uncertainty is defined by the limits of isoenergetic tunneling ($q_0 = e/n$) and full blockade ($q_0 = 0$) (see section 5.4 for details), the maximum temperature uncertainty interval at the lowest reached conductance is $\Delta T = [350\,\mu\text{K}, 600\,\mu\text{K}]$. When calculating the width of the tunnel conductance distribution with the MCMC model, assuming random offset charges, the error band here reduces to the region shown in the inset of Fig. 6.6 a.

## 6.6. RESIDUAL FIELD AS NUCLEAR QUADRUPOLE HEAT CAPACITY APPROXIMATION



The thermal stability demonstrated in Fig. 6.5 and 6.6 results from a combination of large nuclear heat capacity on-chip (enhanced by quadrupolar coupling) with a small heat leak, provided by the In nuclear stages, cooling the leads and the substrate. For evalulating the performance of the stage, the order of background heating in the present experiment needs to be compared with previously reported values [44, 47]. To estimate the heat leaks in on-chip nuclear cooling attempts (see section 4.5) the quadrupolar coupling was included by neglecting all off-diagonal elements in the Hamiltonian, resulting from magnetic coupling of different spin states by the electric field gradient. This is not possible under conditions as $T_n < 1$ mK and $B = 100$ mT anymore. To avoid a rigorous treatment of the quadrupolar coupling for the present experiments, the latter is included as residual field in the model. For this the quadrupolar specific heat is expanded to [184]

$$C_Q = \frac{11R}{480}\left(\frac{eV_{zz}Q}{k_B T}\right)^2 - \frac{11R}{5760}\left(\frac{eV_{zz}Q}{k_B T}\right)^3 + \ldots \tag{6.3}$$

Neglecting all terms of higher order, $C_Q$ has the same $T^{-2}$ temperature dependence as the Schotty approximation of the Zeeman heat capacity, $C_Z = RI(I+1)g^2\mu_n^2(B/k_B T)^2/3$, which allows to approximately express $C_Q$ in terms of an internal magnetic field $B_{\text{int}}$ as

$$B_{\text{int}} = \frac{33e^2V_{zz}^2Q^2}{480g_n^2\mu_n^2 I(I+1)} \tag{6.4}$$

While it is important to note that this field description can not be used to calculate the quadrupolar coupling strength, as one might guess from Eq. 6.4 (a treatment is provided in chapter 7), Eq. 6.3 is sufficient to estimate the order of the heat leak into a single In island. For determining $B_{\text{int}}$ it is used that the system behaves adiabatic on short

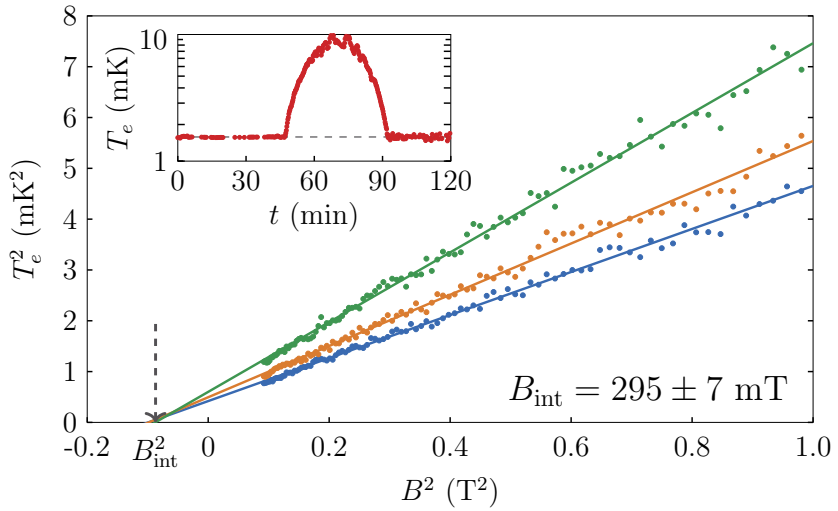


Figure 6.7: **Experimental determination of the residual field in the Zeeman regime.** The magnetic field is ramped up and down on a short timescale on which the system performs nearly adiabatic at different startin temperatures. The residual field is obtained by extrapolating temperature versus $B^2$. **Inset** Electron temperature obtained during a magnetic field ramp (between 1 T and 10 T), plotted against time.



timescales: Since Eddy-currents on-chip can be neglected, a cyclic change of the magnetic field is resulting in a nearly reversible process. (see inset of Fig. 6.7, where a measurement run starting with $B_i = 1$ T and $T_{e,i} = 1.57 \pm 0.01$ mK, up to 10 T, is shown). In the adiabatic regime the internal field $B_{\mathrm{int}}$ can then be obtained by ramping the magentic field up and down in different temperature ranges and extrapolating the measured temperatures to zero. A series of $T_e(B)$ curves is displayed in Fig. 6.7. Notably, $T_e^2(B^2)$ follows a linear proportionality, with a negative intercept, giving rise to $B_{\mathrm{int}} = 295 \pm 7$ mT, which approximates the effect of the quadrupolar coupling on the nuclear spin eigenenergies in the absence of a magnetic field. Based on the obtained internal field, the heat leak into a single island of the CBT is obtained as $\dot{Q}_{\mathrm{res}} = -n\alpha B_{\mathrm{tot}}^2 \frac{\mathrm{d}(1/T_e)}{\mathrm{d}t}$, for $n$ moles of In per island an $\mathrm{d}(1/T_e)/\mathrm{d}t$, the inverse warmup rate (obtained from Fig. 6.6). At $B = 100$ mT, $\dot{Q}_{\mathrm{res}} = 26.7$ aW/island is obtained, of the same order of magnitude as the heat leak per island, found in an chipscale nuclear magnetic cooling experiments using Cu [47].

## 6.7. FINITE BIAS TRANSPORT AT MICROKELVIN ELECTRON TEMPERATURES

The long electron temperature hold times at microkelvin temperatures (see section 6.5) imply that the nuclear spin reservoirs, represented by the In microrefrigerators on the CBT islands, provide a thermal bath with a large heat capacity and a strong coupling to the electrons. The heat which can be exchanged between conduction electrons at temperature $T_e$ and nuclear spins at temperature $T_n$ can be estimated by $\dot{Q}_{\text{e-n}} = C_n/\kappa \times (T_e^2 - T_n^2)$, where $\kappa = \tau/T_e$ is the Korringa constant, $\tau$ the spin-lattice relaxation time, and

$C_n$ the molar nuclear spin heat capacity (see also section 2.1.3). This indicates that hot electron effects should be completely absent once the islands are cooled by the nuclear spins and not by phonons anymore. At given heat load $\dot{Q}_0$ on the electrons, combined of the background heat leak and energy dissipated by the junction voltage $V_k = V_{\mathrm{bias}}/n$, the electron temperature will be raised above the nuclear spin temperature, reaching

$$T_e = T_n + \frac{\kappa \dot{Q}_0}{C_n T_n}, \quad \dot{Q}_0 \approx \frac{V_k^2}{R_t} \tag{6.5}$$

with $R_t \sim 35\,\mathrm{k\Omega}$ for the present device. With the performance of the nuclear refrigeration system, 10 nmol In nuclear spins should have a heat capacity of $C_n \sim 0.5\,\mu\mathrm{J/K}$ (see Fig. 2.5) at $T_n \sim 500\,\mu\mathrm{K}$. With $\kappa = 0.085$ K s for In, a self-heating of $\kappa/C_n T_n \approx 10\,\mu\mathrm{K/fW}$ should occur. Interestingly, other than in dilution refrigeration, the effective cooling power on the electrons is not rapidly decreasing, but increasing towards lower temperatures. The reason is that the nuclear heat capacity at 100 mT is increasing towards reducing the temperature well below 1 mK. This means that in the case of diminishing nuclear heat capacity one would not observe the usual self-heating effects but rather see a dramatic warmup when one operates the system at the tail of the nuclear heat capacity where $C_n$ drops quickly towards higher temperatures according to $C_n \propto 1/T^2$ (see Fig. 7.3 and 7.6). This enormous thermal budget, when operating the system close to the nuclear heat capacity maximum as in the present case, allows to study the charging behaviour of the junction arrays beyond the SET regime by fully suppressing charging and obtaining full scale charging curves at microkelvin temperatures.



For probing electron thermalization at finite bias, nuclear cooled charging curves are measured in order to to obtain the temperature from a full charging curve fit. For this, the nuclear magnetic cooling process is performed by precooling the system to 12 mK and ramping down the field to 0.1 T, resulting in a CBT temperature < 500 μK. While the nuclear spins are slowly warming up with the background heat leak (see Fig. 6.5 and Fig.6.6), isothermal charging curves are obtained by sweeping the voltage bias and measuring the differential conductance of the CBT. The resulting curves are only fitted for the electron temperature while the charging energy is fixed to the value of $E_C = e^2/C_\Sigma \times (n-1)/n$ with $C_0 = 669.7$ fF, obtained in the high temperature calibration (Fig. 6.2). For charging curves with $G(0)/G_t > 0.6$, the curves are fitted with a master equation tunneling model. For $G(0)/G_t < 0.6$ the curves are fitted with the MCMC model, including random offset charges (see section 5.6). The results of the fitting procedure are summarized in Fig. 6.8. Remarkably, there is a good agreeement of the measured charging curves with both of the single-electronic models for all temperatures. All isotherms fitted with the MCMC model at microkelvin temperatures show an excellent agreement with the model over the whole investigated bias range, validating the strong thermal coupling of the electrons to the nuclear spins and demonstrating the applicability of the MCMC model with random offset charges for Coulomb blockade thermometry. Other than in the high temperature regime $k_B T/E_C \geq 1$, where CBTs are primary thermometers, they are only working as self-calibrated secondary thermometers at temperatures as low as $k_B T/E_C < 1$ due to higher order terms in the high temperature expansion of the tunneling rates (see section 2.3.4). In the inset of Fig. 6.8 the FWHM of

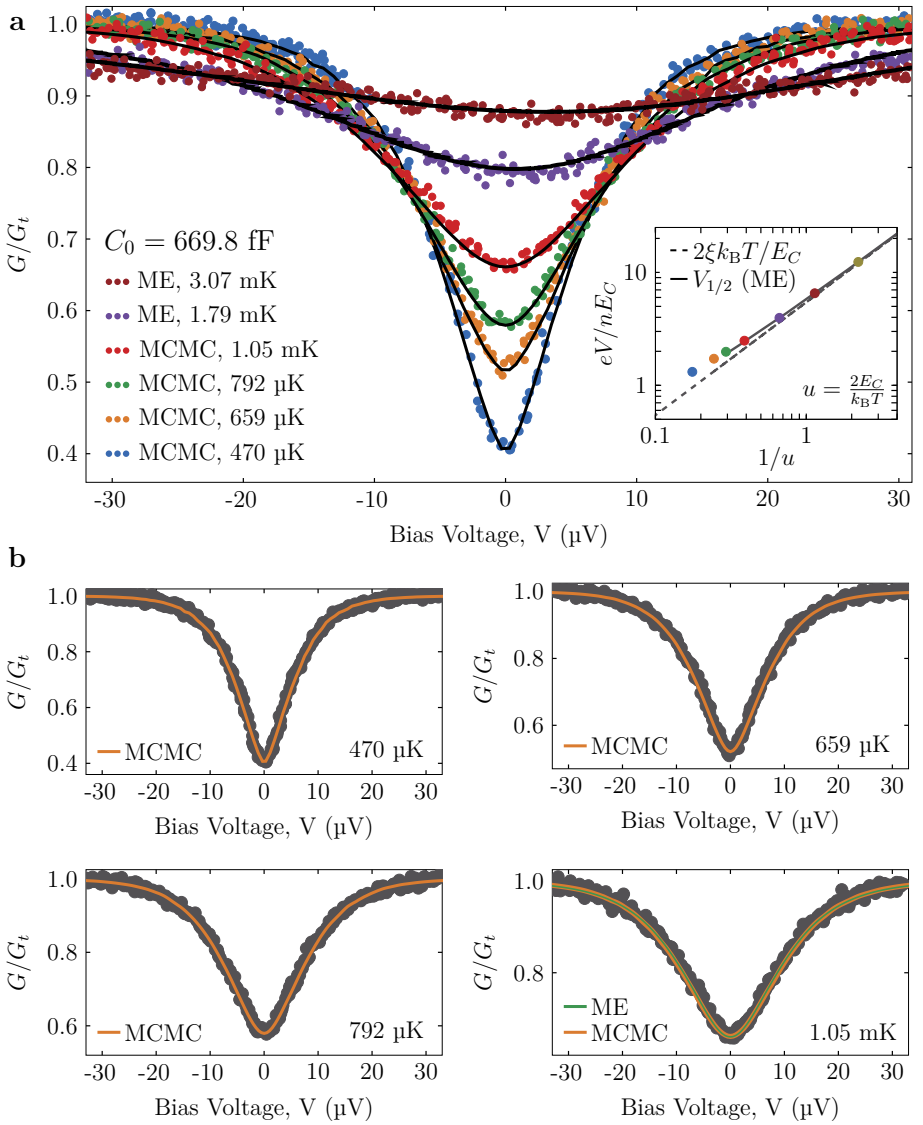


Figure 6.8: **Finite bias charging curves obtained down to $T_e \leq 1$ mK. a** A series of isothermal charging curves is taken (plotted as colored dots), and fitted to either the SET master equation tunneling model (ME) or the Markov-chain Monte-Carlo model (MCMC) including random offset-charges. Which method was used for the fit and the resulting temperature is denoted in the legend. The fits are all drawn as solid black lines. **Inset** The full width at half maximum (FWHM) of the measured charging curves plotted as function of temperature together with the first order approximation of the SET master equation model and the calculated FWHM with the master equation tunneling model down to $1/u$, with $u = 2E_C/K_B T$. **b** The four coldest charging curves from panel a plotted in separate figure panels in order to provide a better overview of the MCMC fit accuracy. The charging curve at $T_e = 1.05$ mK is also fitted with the SET master equation tunneling model for comparison, revealing an excellent agreement of the MCMC model and the ME model in the validity range of the ME model.

the charging curves, measured between 470 μK and 9 mK, is plotted against the primary range FWHM with $eV_{1/2} \approx 5.44nk_{\mathrm{B}}T$, as well as the FWHM of charging curves calculated with the master equation tunneling model down to $1/u = 0.3$. As can be seen, the FWHM of the charging curves at < 1 mK, calculated with the MCMC model, is very close to the results of the SET master equation model in its validity range. The proven absence of thermal non-equilibrium effects shows that nuclear cooling does not only offer submillikelvin electron temperatures on the miniaturized scale, but also brings mesoscopic transport into a new regime of thermal stability. In the electron-phonon limit, hot electron effects were observed already at 10 mK, even with the large In cooling bars available for electron-phonon thermalization. When cooled by a nuclear refrigerant the electrons are thermally strongly coupled to nuclear spins, even at a few hundred microkelvin.

## 6.8. CONCLUSIONS

In conclusion, nuclear magnetic cooling of electrons in a miniaturized electronic device down to electron temperatures below 1 mK, reaching an ultimate temperature of $T_e = 421 \pm 35$ μK, was experimentally demonstrated. Utilizing an on and off-chip nuclear refrigeration technique, exploiting the strong electron-nucleus coupling of In, 85 h of hold time in the microkelvin range could be achieved, opening up the unexplored, temperature regime for nanoelectronic devices and quantum transport experiments.



A nonmagnetic splitting of the nuclear spin energy spectrum could be observed by measuring a residual field of 295 mT of the on-chip integrated In refrigerant in the adiabatic regime. This supports the assumption of the beneficial effect of nonmagnetic level splitting on the nuclear cooling performance of chipscale nuclear refrigerators. Further experiments are needed, in order to identify the observed level splitting to be caused by nuclear quadrupole interaction with the expected interaction energy scale in indium.

By performing finite bias transport measurements at microkelvin temperatures, it was shown that microkelvin refrigeration of electrons in miniaturized structures is still effective when Joule heating puts an additional heat load on the electron system. The ability to perform finite bias measurements enabled the exploration of charging in tunnel junction arrays beyond the universal charging regime, at microkelvin temperatures. The results confirm the thoughts made in chapter 5, that long arrays of tunnel junctions are significantly stable against conductance randomization due to random offset-charges, even beyond the SET regime. This makes Coulomb blockade thermometry much more versatile than it was expected to be according to currently established models, and further supports its applicability for microkelvin thermometry on the miniaturized scale.

Microkelvin refrigeration of nanoelectronic devices opens new avenues for quantum devices, metrological applications and quantum sensing in the ultra-low electron temperature regime. Scalable methods of nuclear refrigerant integration, in combination with using novel implementations of conventional nuclear cooling techniques to refrigerate the surroundings of miniaturized electronic circuits, as demonstrated in this work, could lead to novel refrigeration techniques, extending far into the unexplored microkelvin temperature regime for performing ultracold quantum transport measurements.

## 6.9. Additional Datasets

Fig. 6.9 shows the results of a nuclear magnetic cooling cycle performed with the Al heat switch (see section 3.3) continuously open. Normally the heat switch is closed for performing the nuclear magnetization (precooling) step in which the heat of magnetization needs to be absorbed by the mixing chamber. As can be seen in in Fig. 6.9, precooling through an open heat switch results in rather large starting temperature of 60 mK, reached after about 150 h. At the same time the mixing chamber cools to 6.6 mK, indicating a very small thermal conductance through the heat switch. Upon ramping down

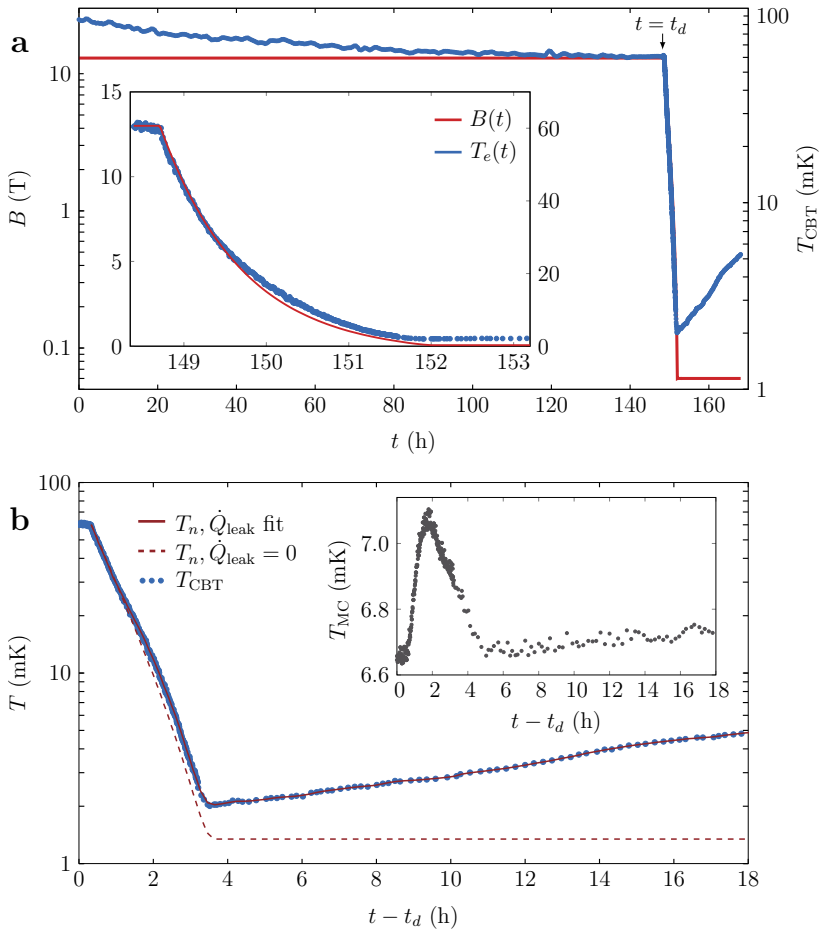


Figure 6.9: **Nuclear demagnetization cycle obtained with the heat switch open. a** Electron temperature measured with the CBT and magnetic field plotted against time for a full nuclear cooling cycle including the magnetization, demagnetization and warmup with the heat switch constantly open. The starting temperature is 60 mK at a starting field of 13 T, reaching a lowest temperature of 1.9 mK upon demagnetization to 60 mT. **b** Closer overview of the demagnetization and the warmup with the time zeroed at $t_d$. The measured electron temperature is fitted to a model for determining the electronic heat leak and compared to an adiabatic process.

the field, the electron temperature drops to 1.9 mK, staying below 5 mK for more than 12 h during the warmup. For a significant part of the field ramp the reduction of the electron temperature $T_e \approx T_n$ follows an adiabatic model for the nuclear spin temperature. The mixing chamber stays at about 6.7 mK > $T_e$ during the whole warmup period. Comparing the warmup rate with an adiabatic model gives a heat leak of 45 aW. Here it is important to note that at $T_e > 1$ mK the coupling of the islands to the off-chip In stages might become significiant (see also Fig. 7.6), with the stage cooling the electrons as well.

In Fig. 6.10 shows isothermal charging curves obtained during warmup of a nuclear cooled chip (precooled with an open heat switch). The isotherms are fitted to the SET master equation tunneling model, without self-heating correction. The fit results in $C_0$ = 668.4±3.2 fF, within error bands of the island capacitance of $C_0$ = 669.7±2.0 fF, previously obtained by self-calibration of the device at different mixing chamber temperatures.

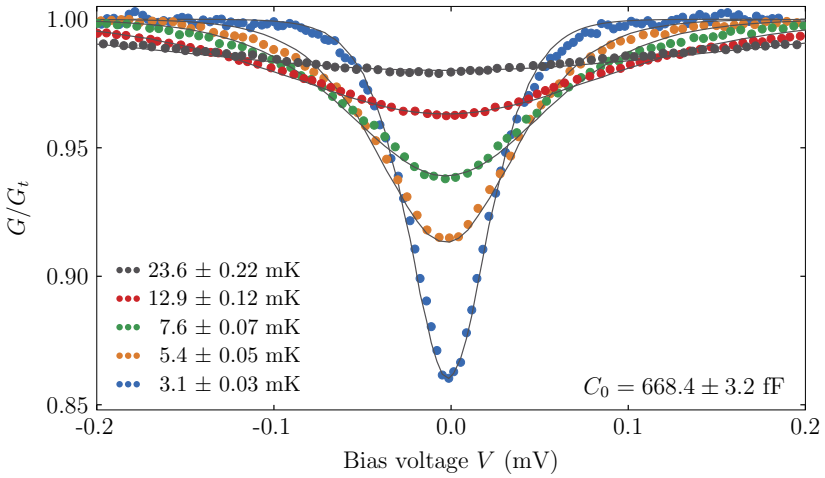


Figure 6.10: **Isothermal CBT charging curves with the islands of the CBT cooled by nuclear stages.** Measured CBT conductance $G/G_t$ (colored dots) plotted as a function of voltage bias. The SET master equation fits are drawn as gray solid lines. Nuclear cooling with the heat switch open extends the self-calibration temperature range from 7 mK in a phonon cooled system with finite bias self-heating (Fig. 6.2) down to 3 mK. In case of nuclear cooling the electrons behave isothermal (within CBT detection limits) over the used voltage bias range.

Fig. 6.11 a shows a series of full nuclear magnetic cooling cycles performed between $B_i$ = 12 T, $T_i$ = 20 mK and $B_f$ = 200 mT. The timescale of the precooling and warmup periods is adapted to a working day cycle. Fig. 6.11 b evaluates the nuclear cooling cycles in an entropy-temperature diagram. The entropy and nuclear heat capacity are calculated according to section 7.3 using a quandrupolar coupling of $\omega_{Q,R}/2\pi$ = 45 MHz and assuming polycrystalline In as nuclear coolant on-chip. Remarkably, the electron temperature reached right after demagnetization is very close to the expected temperature assuming a fully adiabatic process. The principle of using a nuclear cooling cycle for cooling conduction electrons on the chipscale can be well understood from Fig. 6.11 b in combination with Fig. 2.3): The field is ramped up to $B_i$ in step 1 where the nuclear spins are precooled to $T_i$. The heat $Q_2$ is removed from the nuclear spins into the mixing

chamber. The nuclei are prepared at the nuclear base temperature $T_f$ by an isentropic rampdown of the field to $B_f$. The nuclear spins absorb the heat $Q_1$ from the electrons by spin-spin scattering while warming up themselves. When the system is not needed at the nuclear base temperature anymore the field is ramped up to $B_i$ and the nuclear spin magnetization is recovered by cooling to $T_i$. The shown cycling behaviour with reproducible cycles is a prerequisite for the development of nuclear refrigerators with continuous cooling power, based on cycling separate working substance in phase shifted cycles [185–187].

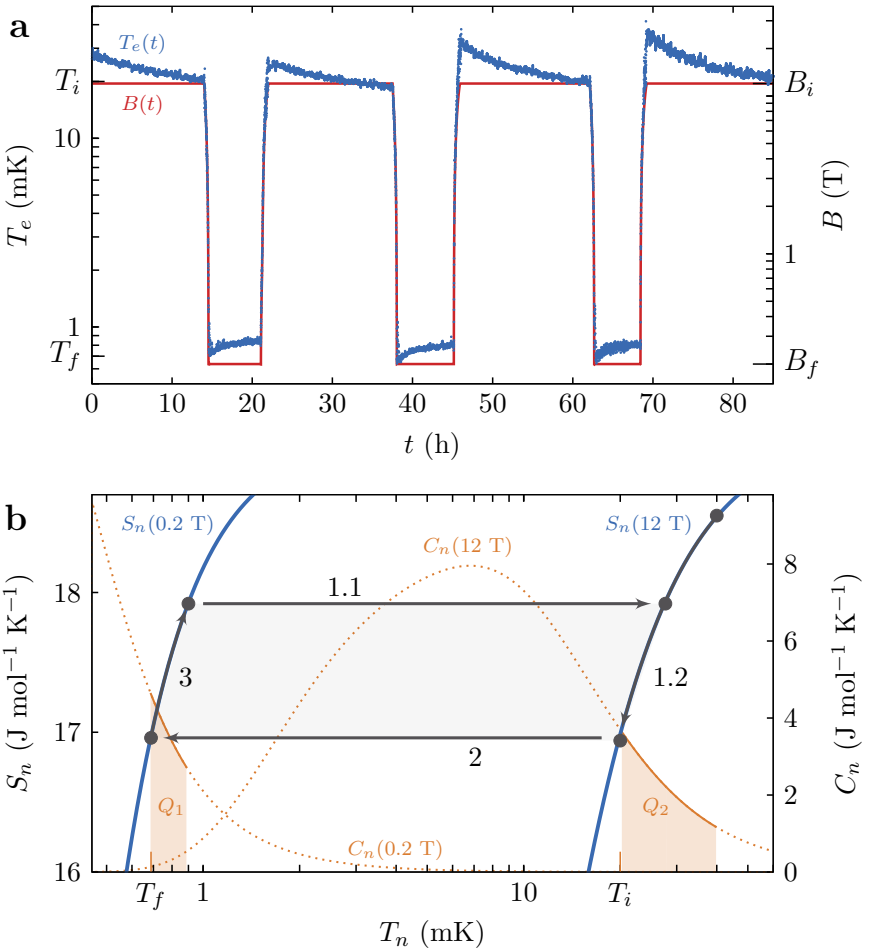


Figure 6.11: **Cycling the nuclear magnetic cooling process. a** Electron temperature measured with the CBT and magnetic field are plotted againts time for three full nuclear cooling cycles. The field is ramped between $B_i = 12$ T and $B_f = 200$ mT. **b** Evaluation of the nuclear cooling cycle shown in a in an entropy-temperature diagram. The single island nuclear spin entropy $S_n$ and nuclear heat capacity $C_n$ are plotted against the nuclear spin temperature. The figure is plotted in the same style as Fig. 2.3 with the shown features fully equivalent.

# 7

# Quadrupole Enhanced Nuclear Magnetic Cooling

*Door meten tot weten*

Heike Kamerlingh Onnes (1853-1926)

## 7.1. INTRODUCTION

A technological obstacle, hindering effective cooling of miniaturized electronic devices to submillikelvin temperatures, is the diminishing thermal coupling of conduction electrons in small volumes to phonons (see section 2.1), in combination with the electronic heat load due to dissipation of applied bias and electromagnetic noise. Nuclear magnetic cooling [6, 16] (section 2.2.4), offers a cooling path for electrons which bypasses the need for electron-phonon scattering by utilizing the spin-lattice relaxation of nuclear spins with conduction electrons (see section 2.1.3). Heat exchanged with conduction electrons via spin-spin scattering, as the main thermal relaxation channel for a magnetized nuclear spin system, scales with $\dot{Q}_{\text{e-n}} \propto T_e T_n$, compared to the $\dot{Q}_{\text{e-p}} \propto T_e^5$ dependence of electron-phonon scattering (see also Eqs. 2.4, 2.14). This cooling scheme is technologically realized by on-chip nuclear magnetic cooling, where a metal with suitable nuclear magnetic properties is brought into galvanic contact with the device by integrating it in usual micro- and nanoprocess technology metallization schemes [45]. By additional thermal anchoring of the device leads to bulk nuclear cooling stages, the external heat load on the nuclear spins becomes so small, that microkelvin refrigeration becomes feasible [47]. In this work, an on-chip nuclear magnetic cooling scheme, based on thick-film integration of In as metallic nuclear working substance, reached an electron temperature of $3.2 \pm 0.1$ mK (section 4.4) and was extended by off-chip nuclear cooling the device leads, resulting in an electron temperature of $421 \pm 30$ µK (section 6.5).

Since nuclear cooling is a single-shot technique, it is not only important to reach a desired temperature but to stabilize it against external heat load. The temperature hold time depends on the nuclear spin heat capacity of the working substance. The superior thermal stability of In against conventional refrigerants manifested itself in temperature hold times below 1 mK, reaching several days (see Fig. 6.6). This is in turn caused by the significant nonmagnetic splitting of the nuclear eigenenergies, occuring in metallic In. Miniaturized nuclear magnetic cooling has an intrinsic difficulty, which is the diminishing nuclear heat capacity $C_n \propto B^2/T_n^2$, provided by the finite Zeeman splitting of $\hbar\omega_0 = g_n \mu_n B$ of the nuclear eigenenergies, becoming a limiting factor at small magnetic fields. Metallic In belongs to a class of materials in which large nucleons with an anisotropic charge distribution are combined with a noncubic crystal structure, imposing an electric field gradient on the nuclei and thus a large quadrupolar splitting of the nuclear eigenenergies. Pure quadrupolar splitting is described by the Hamiltonian given by Eq. 2.22, imposing an energy splitting of $(6m \pm 3)\hbar\omega_Q$ between nuclear spin eigenstates with quantum number $m$ and $m \pm 1$. The absolute value of the quadrupole coupling depends on the electrostatic environment of the nuclei as $\hbar\omega_Q = eQV_{zz}/4I(2I-1)$, with the material dependent electric field gradient $V_{zz}$, and the nuclear quadrupole moment $eQ$. Once Zeeman splitting surpasses quadrupole splitting, the nuclear eigenspectrum is mainly determined by the non-equidistant eigenvalues of Eq. 2.22, and residual Zeeman splitting occurs as small perturbation for $\omega_0 \ll \omega_Q$. This is illustrated in Fig. 7.1: in the absence for nonmagnetic level splitting (Fig 7.1 a), the nuclear eigenenergies split in a magnetic field into 2I+1 equidistant energy levels, separated by $\hbar\omega_0$. In the presence of nuclear quadrupole coupling (Fig 7.1 b), the splitting between ground state and first excited state is $(6I-3)\hbar\omega_Q$ ($V_{zz} < 0$) or $6\hbar\omega_Q$ ($V_{zz} > 0$) at zero magnetic field.

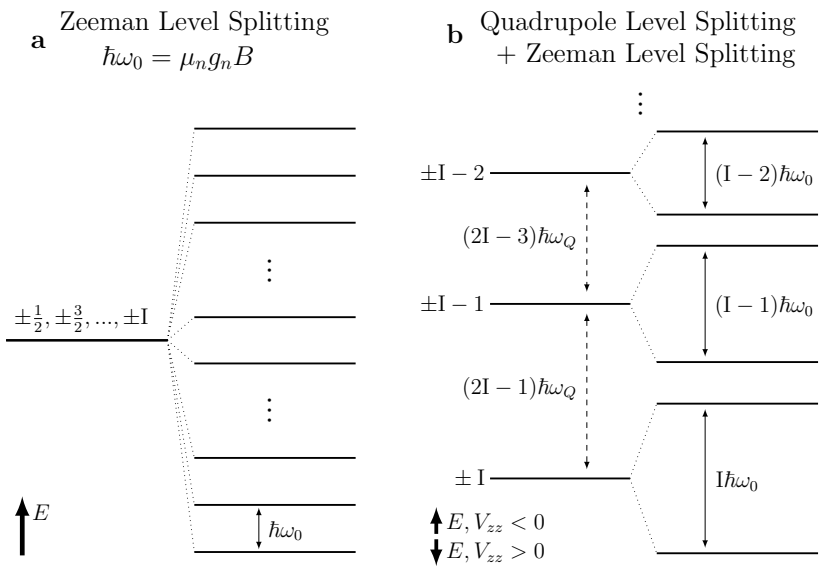


Figure 7.1: **Illustration of nuclear level splitting in the case of Zeeman interaction and Zeeman interaction combined with quadrupole interaction**. **a** Pure Zeeman splitting with equidistant energy levels. separated by $\hbar\omega_0 = \mu_n g_n B$. **b** Zeeman splitting and quadrupole splitting, depending on $\hbar\omega_Q = eQV_{zz}/4I(2I-1)$, with non-equidistant levels at small field. The energy axis is chosen in dependecy of the sign of $V_{zz}$, illustrating that either −I comprises the ground state of the system ($V_{zz} < 0$), or the the state with highest energy ($V_{zz} > 0$).



If one wants to utilize quadrupole enhancement of the nuclear heat capacity for scalable nuclear cooling on the miniaturized scale, the contribution of the quadrupole interaction to the thermodynamic properties of the nuclei has to be known. In case of metallic In, the asymmetry parameter $\eta$ is zero and thus, according to Eq. 2.22, the nuclear energy spectrum the absence of a magnetic field is fully determined when the absolute values of $V_{zz}$, $eQ$ and their signs are known. The absolute value of $eQV_{zz}/h$ is experimentally accessible by nuclear quadrupole resonance (NQR) or low-temperature specific heat measurements. NQR studies of In at 4.2 K revealed 45.19 MHz [104] and 45.24 MHz [103], ultralow temperature calorimetry resulted in 47.8 MHz [184]. According to these values, the separation between ground state and first excited state is as large as ~ 0.4 mK, making In an attractive material for quadrupole enhanced nuclear magnetic cooling to submillikelvin temperatures. The sign of $\hbar\omega_Q$ is determined by the sign of the z-component of the electric field gradient tensor, $eV_{zz}$, in its eigenbasis. The sign of $V_{zz}$ in In has been obtained experimentally by NQR studies in In-alloys [104, 188–190], $\gamma$ ray anisotropy from the $^{114}$In isotope [191], or specific heat measurements at ultralow temperatures [184, 192]. All works obtained a negative sign of $V_{zz}$, except the most recent, inferring a positive value for $V_{zz}$ [192]. The sign of the electric field gradient has a decisive impact on the nuclear level fine structure, and uncertainty in $V_{zz}$ imposes an uncertainty on the exact temperature scale of the quadrupolar heat capacity.

This work is aimed at the study of the nuclear energy level spectrum of on-chip integrated In as nuclear refrigerant at submillikelvin temperatures. The short spin-lattice relaxation time of In makes the nuclear spin temperature on the mesoscopic scale accessible by measuring the temperature of the conduction electrons in a defined metallic volume. For this purpose, a Coulomb-blockade thermometer is utilized. The absolute value of $\hbar\omega_Q$ and its sign are determined by tuning the nuclear level splitting with a magnetic field, while measuring the spin temperaure. The specific heat is measured by nanocalorimetry and compared to model values. The obtained parameters allow for a quantitative prediction of the nuclear magnetic cooling performance of nuclear microrefrigerators for chipscale nuclear magnetic cooling based on In, making the cooling techniques which were introduced in chapter 4 and chapter 6 a fully scalable approach.

## 7.2. EXPERIMENTAL SETUP AND TRANSPORT MEASUREMENT SCHEME FOR INDIUM NANOCALORIMETRY

Coulomb-blockade thermometry [56, 57] and nuclear cooling on-chip is utilized to study the ULT specific heat of In. The CBT is made by fabricating arrays of Al-$AlO_x$ tunnel-junctions (see section 3.1.1) and has a charging energy of $E_C = e^2/C_\Sigma \times (n-1)/n$, with $n = 36$ and $C_0 = 669.8 \pm 2$ fF. The differential conductance of the CBT is measured using standard low frequency lock-in techniques in a four-wire geometry. Polycrystalline In (50 µm×140 µm×25.4 µm) is integrated onto each island, formed between the tunnel junctions, by electrochemical depositon from a custom $In(SO_3NH_2)_3$ bath for local nuclear magnetic cooling. The grain structure is refined by using a pulsed electrodeposition scheme (see section 3.1.2 for implementation details). An overview of the experimental setup, including experimental measurement schemes, is shown in Fig. 7.2.

The In microrefrigerators are thermally only weakly coupled to each other, due to the large electrical resistance provided by the tunnel junctions ($R_t \approx 35$ kΩ), and weakly coupled to substrate phonons at < 1 mK, due to the small volume of the In cooling bars (see Fig. 6.1). Microkelvin refrigeration of the CBT islands is enabled by a combined on- and off-chip nuclear magnetic cooling scheme (see sections 4.2, 6.2, 6.5), providing a low residual heat leak as low as 27 aW into a single island of the CBT (see section 6.6). Further details regarding the on- and off-chip cooling stage can be found in section 6.2.

At finite magnetic field, the nuclear level splitting in each crystallite is defined by the strength of the magnetic field and the orientiation of the electric field gradient with respect to the magnetic field direction (Fig 7.2 b). A variation of the magnetic field leads to an isentropic temperature change, which significantly depends on the nuclear quadrupole coupling strength in the presence of nonmagnetic level splitting (Fig 7.2 c). This temperature of the nuclei $T_n$ is experimentally accessible via the CBT, given the strong electron-nucleus coupling, in combination with the large nuclear specific heat.

The nuclear heat capacity is accessible by on-chip calorimetry, using the tunnel junctions as heaters. The heating $\dot{Q}_0$ can be precisely adjusted since the CBT is biased in a four wire configuration and can self-compensate a voltage bias offset. Sufficiently far in

the submillikelvin temperature regime, the diminishing electron phonon coupling thermally decouples the islands from the substrate and the electronic heat load is solely applied to the nuclear spins. These absorb the specific heat according to their specific heat $C_n(\theta, B)$, which then becomes measurable via $C_n = \partial Q_0 / \partial T_n$. The obtained specific heat is compared to values obtained by solving Eq. 2.22, as described in the next section.

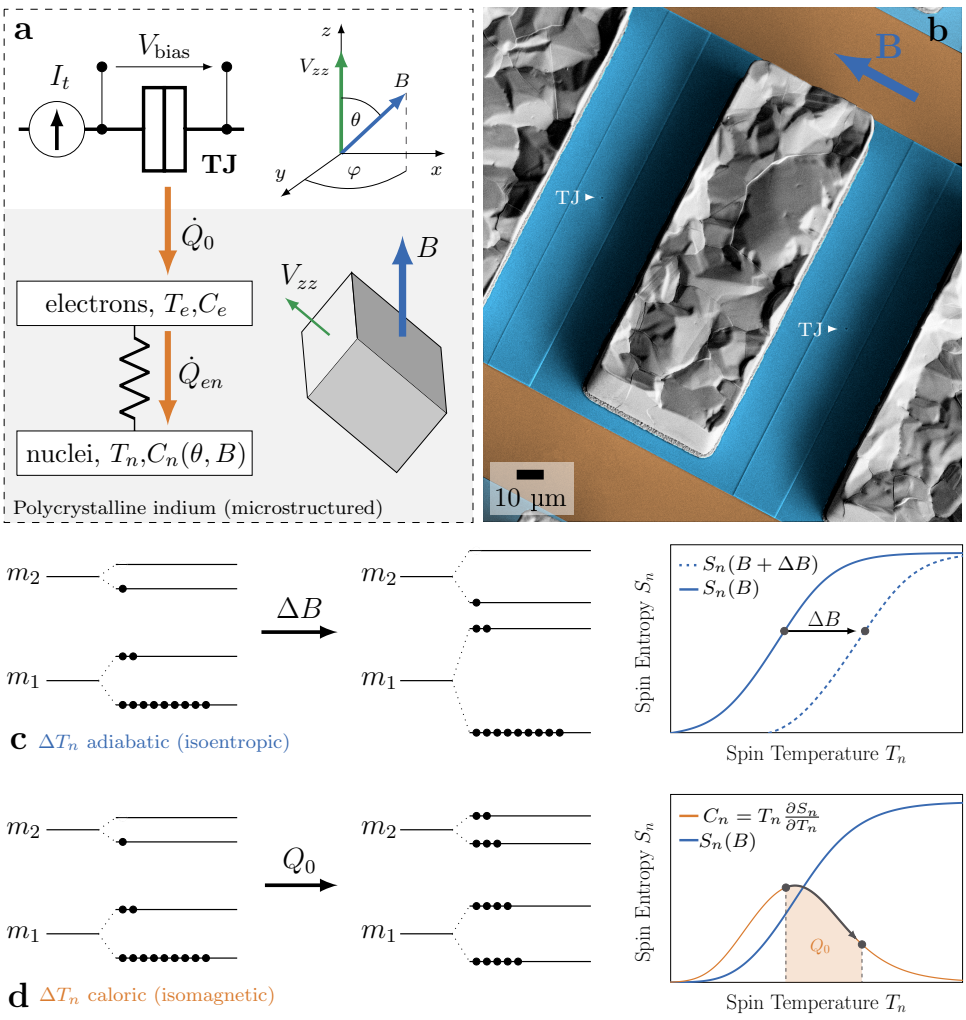


Figure 7.2: **Device setup for characterizing the thermodynamics of nonmagnetic level splitting in miniaturized, polycrystalline In nuclear magnetic refrigerators. a** Schematic overview of the heat flow into the magnetized nuclear spin system when energy is dissipated at the tunnel junctions (TJ). The heat capacity is determined by the strength of the magnetic field and the orientation between the magnetic field and the electric field gradient in the crystals. **b** SEM micrograph of a single CBT island. **c** Illustration of an adiabatic temperature change by tuning the nuclear level splitting with a magnetic field in the absence of parasitic heating. **d** Illustration of a caloric temperature change by heating the nuclear spins at constant magnetic field.

## 7.3. MODELLING THE QUADRUPOLAR LEVEL SPLITTING IN POLYCRYSTALLINE INDIUM

For obtaining the strength and nature of the quadrupolar coupling from measured observables, a model for calculating the nuclear entropy $S_n$ and nuclear heat capacity $C_n$ of polycrystalline In in the presence of quadrupole splitting is made. In the previous chapters this problem was avoided by either only modelling the system at large magnetic fields, while taking the quadrupole splitting as small perturbation (chapter 4), or expanding the heat capacity to quadratic terms in $B$ (chapter 6). For a proper calculation of the nuclear heat capacity at any field and temperature, one has to find a common basis for the quadrupole interaction and the Zeeman interaction, in which the spectrum is defined by the nuclear spin eigenbasis $\{|m\rangle\}$. Herefore, a single island is divided into $N$ grains with $N_i/N$ number of spins, where $N = V/V_m$ is the total number of spins per island, obtained by the measured volume $V$ (see Fig. 3.7), and the molar volume $V_m$. Each grain has a specific orientation $(\varphi,\theta)$ of the z-basis of the electric field gradient tensor to the magnetic field direction. In the z-basis of the electric field gradient tensor one has

$$\mathbf{H}_\mathrm{Q} = \frac{\hbar\omega_{Q,R}}{\delta}\left[3\mathbf{I}_z^2 - \mathbf{I}^2 + \eta\left(\mathbf{I}_x^2 - \mathbf{I}_y^2\right)\right] \tag{7.1}$$

with $\hbar\omega_{Q,R} = eV_{zz}Q$ [1], $\delta^{-1} = 4I(2I-1)$ and $I = 9/2$, $\eta \approx 0$ for In. For $V_{zz} > 0$, the ULT nuclear heat capacity is determined by the transition $I \to I-1$ while for $V_{zz} < 0$ the heat capacity is scaled by $1/2 \to 3/2$. At finite magnetic field $\mathbf{B}$, the Zeeman levels are given by

$$\mathbf{H}_Z = -\mu_n g_n \mathbf{B}\cdot\mathbf{I} \tag{7.2}$$

with the nuclear magnetic moment $\mu_n = 5.05\cdot10^{-27}$ J T$^{-1}$ and the nuclear g-factor as large as $g_n = 1.23$ for $^{115}$In and $^{113}$In. As can be seen from Eq. 7.1 and Eq. 7.2, the magnetic field is determining the basis in the Zeeman operator while the quadrupole Hamiltonian is defined in the principal axis system of the electric field gradient tensor. The matrix elements of the spin operator $\mathbf{I}$ components (with dimension $m\times m$) are

$$\langle m'|\mathbf{I}_x|m\rangle = +\frac{1}{2}\left(\delta_{m',(m+1)} + \delta_{(m'+1),m}\right)\sqrt{I(I+1)-m'm}, \tag{7.3}$$

$$\langle m'|\mathbf{I}_y|m\rangle = -\frac{\mathrm{i}}{2}\left(\delta_{m',(m+1)} - \delta_{(m'+1),m}\right)\sqrt{I(I+1)-m'm}, \tag{7.4}$$

and $\langle m'|\mathbf{I}_z|m\rangle = \delta_{m,m'}$ with the Kronecker delta $\delta_{ij}$. The Zeeman Hamiltonian $\mathbf{H}_Z$ is then transformed into the basis of the electric field gradient tensor with $\mathbf{H}'_Z = \mathbf{U}^\dagger\mathbf{H}_Z\mathbf{U}$, where $\mathbf{U}$ is a unitary transformation aligning the magnetic field direction with the direction of $V_{zz}$. The eigenvalues $\varepsilon_m = \langle m|\mathbf{H}|m\rangle$ of $\mathbf{H} = \mathbf{H}_Q + \mathbf{H}'_Z$ with spin quantum number $m$ determine the occupation of the nuclear eigenenergies with the partition function

$$Z_i = \left[\sum_{m=-I}^{I}\exp\left(-\frac{\varepsilon_m}{k_\mathrm{B}T_n}\right)\right]^{N_i} \tag{7.5}$$

[1] For comparability reasons we use the historic notation for the coupling energy $\hbar\omega_Q\cdot 4I(2I-1)$ to make results comparable to previous works. For illustrative purposes $\hbar\omega_Q$ is still used in Fig. 7.1 and Fig. 7.3

It is not assumed that there is a preferred lattice orientation of the grains, since electrodeposition is known to produce incoherent films. Thus it is assumed that the grains are fully randomly oriented with respect to the basis of the electric field gradient tensor in relation to the magnetic field. The grain entropy at a given magnetic field is

$$S_{n,i} = k_\mathrm{B}\left[\frac{\partial(T_n \log Z_i)}{\partial T_n}\right]_B \tag{7.6}$$

For calculating the total entropy $\overline{S}_n$ and specific heat $\overline{C}_n$ of the system from the grain entropy, it can be used that both entropy and specific heat are extensive state variables. Consequently, the total specific heat will result from a sum of grain entropies as

$$\overline{C}_n = T_n\left(\frac{\partial \overline{S}_n}{\partial T_n}\right)_B, \qquad \overline{S}_n = \sum_{i=1}^{N} N_i S_{n,i} \tag{7.7}$$

Due to the tetragonal crystal symmetry of In, there is $Z(-\theta) = Z(\theta)$ which allows to express the total heat capacity of the system as average over the range $\theta = \{0, \pi/2\}$ for different $\phi$, here iterated in steps of $\pi/2N$. Calculated values for $C_n$ (Eq. 7.7) are plotted

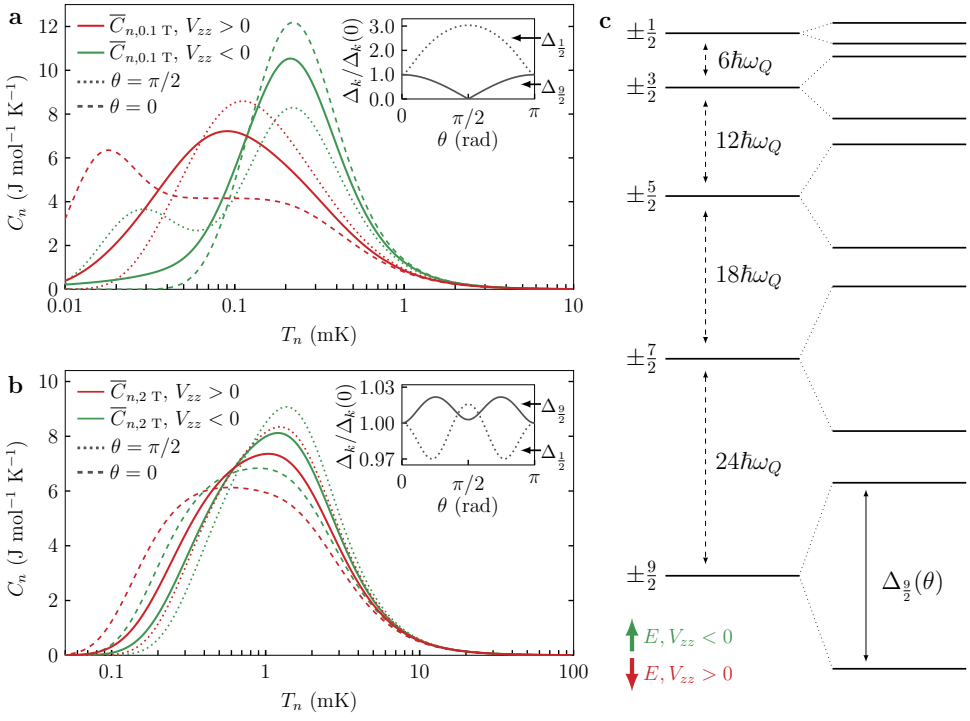


Figure 7.3: **Nuclear heat capacity of single crystalline and polycrystalline indium**. **a** Specific heat $C_n$ of In at $B = 100$ mT, plotted against $T_n$ for single grains with angles $\theta = 0$ and $\theta = \pi/2$, and for a polycrystal in the interval $\theta = \{0, \pi/2\}$. Inset: Splitting of the 1/2 and the 9/2 state plotted against $\theta$. **b** Same as panel a, but for $B = 2$ T. **c** Level diagram, illustrating the nuclear quadrupole splitting in In, in combination with Zeeman splitting and an angle $\theta$ between the direction of the magnetic field and the electric field gradient.

in Fig. 7.3 at different magnetic fields, in the interval $\{0, \pi\}$, and for a positive and a negative electrical field gradient respectively. For the quadrupole coupling, the value of $\omega_{Q,R}/2\pi = 45$ MHz is taken, representing a value well reproduced with nuclear quadrupole resoncance spectroscopy at 4.2 K [103, 104]. A schematic of the expected nuclear level splitting is drawn in Fig. 7.3 c. As can be seen in Fig. 7.3 a and Fig. 7.3 c, the splitting of the 9/2 state, which is the ground state for $V_{zz}$, goes to zero for $\theta = \pi/2$ and $g_n\mu_n B < \hbar\omega_Q$. As obvious from Fig. 7.3, the sign of the electric field gradient in polycrystalline In should be distinguishable by calorimetry and adiabatic magnetization/demagnetization cycles in a temperature interval of $T_n, T_e < 1$ mK, well reachable by nuclear demagnetization.

## 7.4. ADIABATIC MEASUREMENT OF THE COUPLING $\hbar\omega_Q$

The expected effect of nuclear quadrupole coupling in the In microrefrigerators on the CBT islands (see Fig. 7.2) is a significant enhancement of the nuclear specific heat at low fields, combined with weak coupling of the island electrons to the bulk indium stages, scaling with $\propto T_e^5$ (see also Eq. 7.12), and a strong electron-nucleus coupling. Under these conditions, $\hbar\omega_Q$ of the In islands can be deduced from measured electron temperatures during adiabatic magnetization/demagnetization cycles (see Fig. 7.2 d). In the adiabatic regime, the nuclear spin temperature dynamics in a varying magnetic field is solely determined by the nuclear energy spectrum, and deviations from equidistant Zeeman nuclear level splitting manifests as a deviation from a constant $\partial T_n/\partial B = T_n/B$.

To measure $\hbar\omega_Q$, the CBT is prepared at a low starting temperature by performing nuclear cooling from 20 mK and 12 T to 0.3 T and 870 μK. The field is then slowly ramped between 0.3 T and 2 T, while the electron temperature is monitored by measuring the zero bias tunnel conductance of the CBT. The result is summarized in Fig. 7.4 a. Adiabacity is approved by the reversible behaviour of the electron temperature with field ramps in opposite directions (Fig. 7.4 a), showing neither warming nor cooling of the electrons (from the scale, later established in Fig. 7.8 it is expected that the system behaves well adiabatic with a cooling rate of ~ 1 nK/s at a temperature of $T_n, T_e \approx 4$ mK).

The measured electron temperatures $T_e$ are fitted to the model described in section 7.3 under adiabatic conditions, in order to obtain the absolute value of $\hbar\omega_Q$, as well as the sign of $V_{zz}$ at once. This is possible because the system responds in a much more pronounced way to the sign of the electric field gradient in given limits of $|\hbar\omega_Q|$: changing the sign of $V_{zz}$ at given $\omega_Q$ inverts the whole energy spectrum of the nuclei, resulting in a significant shift of the nuclear heat capacity to lower temperatures (see Fig. 7.4 b). Fitting the data with a negative field gradient, as it was obtained already from the calorimetry data in section 7.5 (see Fig. 7.6), results in an absolute coupling of $|\omega_{Q,R}|/2\pi = 47.1$ MHz, within boundaries of previously reported values between 45.19 MHz [104] and 47.8 MHz [184], obtained by nuclear quadrupole resonance spectroscopy at 4 K and calorimetry of bulk In at ultralow temperatures respectively. The measured electron temperature can be only explained by a positive field gradient if $|\hbar\omega_Q|$ is lowered far below usually measured values. If an uncertainty range is defined by the standard deviation of all measured quadrupole splitting constants in history, the nuclear entropy has to be evaluated with respect to the field gradient in a range of $|\omega_{Q,R}|/2\pi = 47.09 \pm 3.96$ MHz (Fig. 7.4 b).

It can be seen that the uncertainty in $|\hbar\omega_Q|$ is of the order of the uncertainty in measured temperature and is clearly too small to allow the assumption of a positive electric field gradient, if previously obtained coupling energies are inferred. The negative sign of the electric field gradient is in agreement with the sign of the field gradient obtained by measuring the nuclear heat capacity between 0.5 mK and 2 mK as well as with NQR

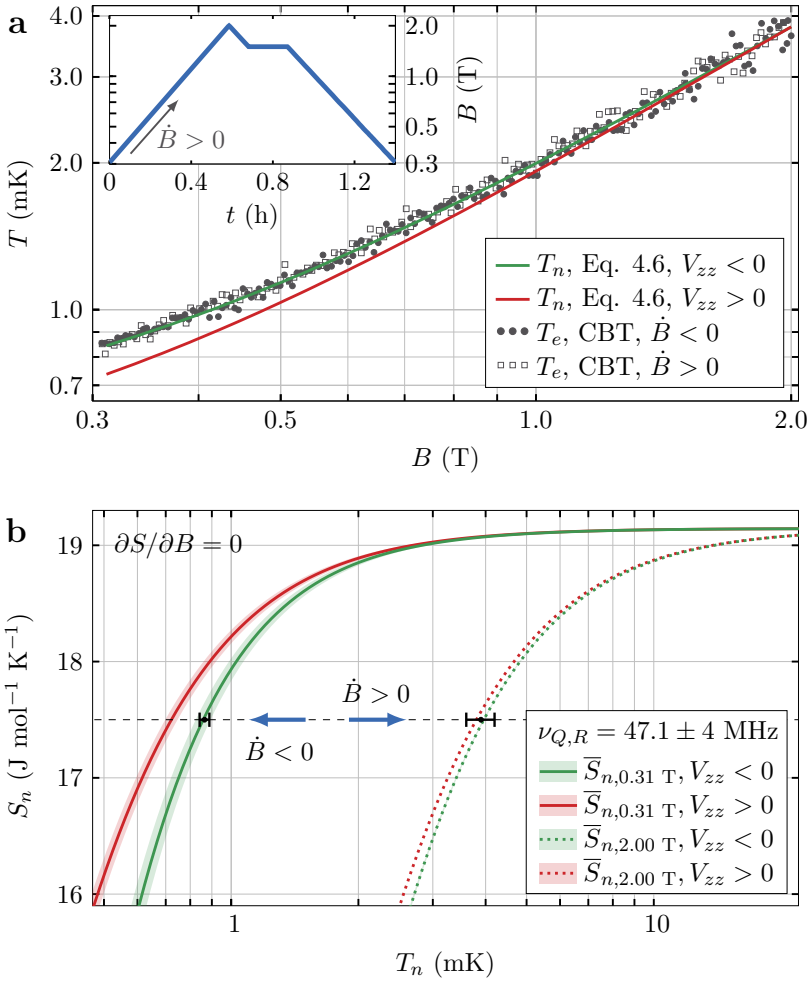


Figure 7.4: **Determination of the nuclear quadrupole coupling strength of polycrystalline In in the adiabatic regime. a** Temperature measured with the CBT is plotted as a function of magnetic field for the upsweep from 0.3 T to 2 T (dB/dt>0) and the downsweep from 2 T to 0.3 T (dB/dt>0). From the initial starting temperature and magnetic field the nuclear spin temperature is calculated with Eq. 7.11 and plotted against the magnetic field. The inset of panel a shows the magnetic field applied to the device as a function of time. **b** Measured starting end end temperatures of the field sweep in a plotted in a $S,T$ diagram with the nuclear spin entropy $S_n$ and - temperature $T_n$. The entropy is calculated for a positive and a negative electric field gradient in a defined error band for the coupling $|\hbar\omega_Q|$. The temperature uncertainty at 0.3 T and 2 T, according to three standard deviations from a local temperature mean in panel a, is indicated by drawing horizontal error bars.

measurements on In specimens at 4.2 K. Measuring the sign of the electric field gradient in the adiabatic regime produces reliable results, because the nuclear heat load as well as the total amount of moles are eliminated as uncertainty parameters.

## 7.5. CALORIMETRIC MEASUREMENT OF THE QUADRUPOLE COUPLING STRENGTH

The specific heat $C_n$ of the In nuclei can be obtained by nanocalorimetry, using the tunnel junctions of the CBT as on-chip heaters (see also 7.2 c for details). This requires to provide a well defined heating level by dissipation of the tunnel current $I_t$ at defined voltage bias $V$ and a careful evaluation and elimination of non-idealities, being parasitic heat flow from the island to the substrate $\dot{Q}_{\text{e-s}}$, parasitic heating by the finite heat leak $\dot{Q}_{\text{res}}$, and parasitic heat exchange between the islands. A CBT island at temperature $T_i$, with a voltage bias $V_k = V/n$ over each of its $n$ junctions, exchanges heat with the neighbouring islands at temperatures $T_{i\pm1}$ and the environment according to [42]

$$\dot{Q}_{\text{island}} = \frac{1}{e^2 R_t} \sum_{\pm} \int_{-\infty}^{\infty} \mathrm{d}E\, E \left[ f(E \pm eV_k, T_{i+1}) - f_i(E, T_i) \right] + \dot{Q}_{\text{res}} \pm \dot{Q}_{\text{e-s}} - \dot{Q}_{\text{e-n}} \tag{7.8}$$

With the Fermi-Dirac distribution $f(E)$ given by Eq. 2.37. While $\dot{Q}_{\text{e-n}}$ should be negative as long as the nuclei have a finite heat capacity, the sign of $\dot{Q}_{\text{e-s}}$ depends on the substrate temperature $T_s$ (refrigerated by cold nuclei in the bulk In stages as depicted in Fig 6.1). The integral can be solved with the identity $\int_0^\infty x\mathrm{d}x/(\mathrm{e}^x + 1) = \pi^2/12$, resulting in

$$\dot{Q}_{\text{island}} = \frac{V_k^2}{R_t} + \sum_{\pm} \frac{L_0}{2R_t} \left( T_{i+1}^2 - T_i^2 \right) + \dot{Q}_{\text{res}} \pm \dot{Q}_{\text{e-s}} - \dot{Q}_{\text{e-n}} \tag{7.9}$$

With the Lorentz number $L_0 = \pi^2 k_{\text{B}}^2/3e^2$. The first term, $V_k^2/R_t$, is the dissipation of the tunnel current of a junction, shared exactly half-half between the adjacent islands [69]. The second term is the heat flow over the resistive junction according to the Wiedemann-Franz law (Eq. 2.1). In this case, the latter can be neglected, since each island is thermally well isolated with junction resistances of $R_t \sim 35\ \text{k}\Omega$. The temperature difference between the islands should be small due local nuclear cooling on the islands, enabling $T_k \approx T_{k\pm1}$. Joule heating by the junctions can be adjusted such, that the total heat balance of a single island fully determined by Joule-heating, electron nucleus coupling, and the electron-(substrate) phonon coupling according to $\dot{Q}_{\text{island}} = V_k^2/R_t \pm \dot{Q}_{\text{e-s}} - \dot{Q}_{\text{e-n}}$, with $V_k^2/R_t \gg Q_{\text{res}}$. In the regime $T_e < 1$ mK electron-phonon coupling should be so weak ($\dot{Q}_{\text{e-s}} \propto T^x$, with $x \geq 4$), that the nuclear heat capacity can be extracted with

$$\left( \frac{\partial T_n}{\partial t} \right)_B = \frac{V_k I_t}{C_n(B, T_n)} \tag{7.10}$$

Nanocalorimetry of the In islands is implemented by measuring $V_k$, $I_t$, and $T_n$ with the CBT, while the short spin-lattice relaxation time of In ensures $T_e \approx T_n$. A measurement of the electron temperature $T_e$, before and after applying a heat pulse $Q_0$ to the system, yields a finite difference approximation of the nuclear specific heat $C_n = \partial Q_0/\partial T_n$.

To initialize the experiment, the CBT is precooled to 14 mK in a field of 12 T, followed by a slow reduction of the magnetic field to 115 mT. During demagnetization, the electron temperature is obtained in secondary operation mode (see Fig. 7.5 a and b). After a waiting period (several hours), the electron temperature reaches a value of $576.8 \pm 11.1$ µK. Now, Joule-heating, $\dot{Q}_0 = V_k I_t$, is applied to the islands by sweeping the bias voltage, inducing well defined heating pulses with $Q_p = 2.00 \pm 0.01$ pJ/pulse. This ensures $I_t V_k \gg \dot{Q}_{\mathrm{res}}$, assuming an uncontrollable background heat leak of $\dot{Q}_{\mathrm{res}} \sim 27$ aW (see section 6.6). Measuring the electron temperature from full CBT charging curves is enabled by sweeping the bias voltage through zero.

The procedure is illustrated in Fig. 7.5 c, where the measured differential conductance during several heat pulses is plotted against time. When the applied heat reaches a significant value (> 0.1 fW), the conductance of the CBT returns to its Ohmic value $G_t$. When the heat is reduced between two pulses, the nonlinear response in $G$ allows to deduce the electron temperature very precisely from the full charging curve of the device.

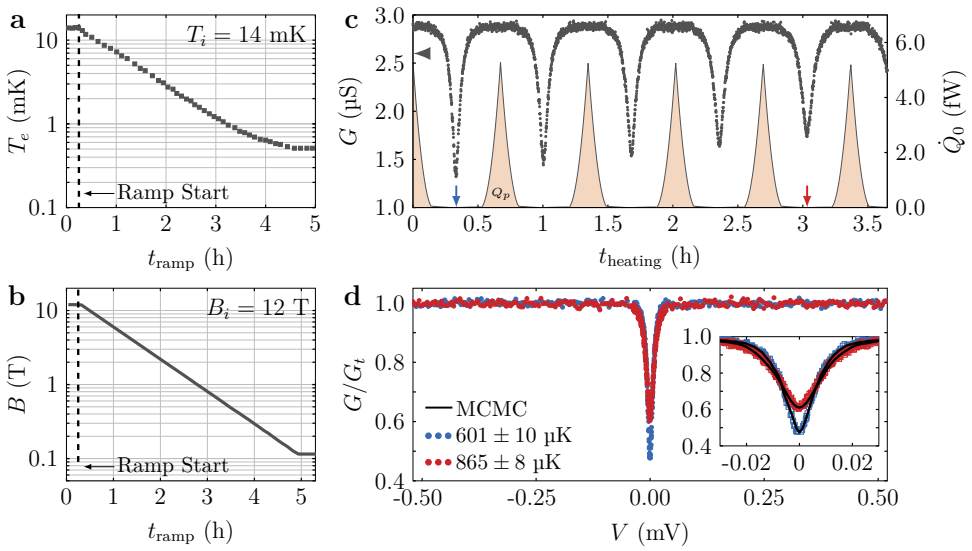


Figure 7.5: **Nuclear cooling and caloric change of the measured electron temperature by heat pulses. a** Electron temperature $T_e$, measured during nuclear demagnetization from 12 T and 13 mK to 115 mT **b** Magnetic field during demagnetization as function of time. **c** Differential conductance, $G$, measured during application of the heating pulses $\dot{Q}_0 = V_k I_t$, with $Q_p = 2$ pJ/pulse. **d** Two isothermal charging curves, obtained during heating the In islands. The curves are obtained at the times marked in the corresponding colors in panel *c*.

For comparison, the nuclear spin heat capacity at constant magnetic field $B$ is calculated with the averaging procedure described in section 7.3. From the starting value of $T_n = 580$ µK and the heat input $\dot{Q}_0 \approx V_k^2/R_t$, $T_n(t)$ and $T_e(t)$ are calculated at given specific heat $C_n$ and magnetic field as solutions of Eq. 4.6 and Eq. 4.7. The quadrupolar coupling is included by calculating the specific heat $C_n$ of the In nuclei with the previously obtained value of $\omega_{Q,R}/2\pi = 47.1$ MHz. The Korringa constant is taken in the magnetic limit as $\kappa = 0.085$ Ks, also holding for purely quadrupolar level splitting [80].

The results of the on-chip calorimetry are plotted Fig. 7.6. It is at first sight remarkable that even with a average heating of the order of fW into each island, the electron temperature can be kept below 1 mK for about 5 h (see Fig. 7.6 a). This can be attributed to the large specific heat of the In nuclei on the CBT islands, as can be clearly seen in Fig. 7.6 b. The measured electron temperature $T_e$ shows a turnover at $T_e \approx 2$ mK, where the system aquires a large heat capacity than just expected from the single island heat

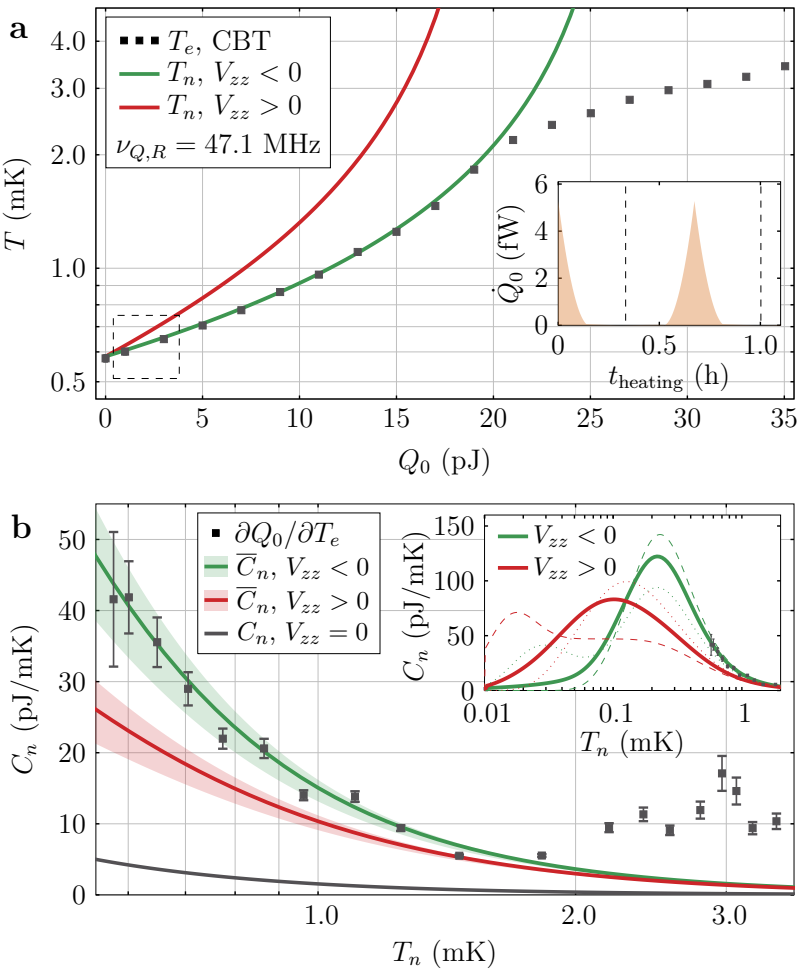


Figure 7.6: **Calorimetric measurement of the single island specific heat. a** Electron temperature $T_e$, measured during the forced warmup, plotted against the amount of the totally applied heat, $Q_0$, to the island. For comparison, $T_n$ is calculated with Eq. 4.7 for $V_{zz} > 0$ and $V_{zz} < 0$. Inset: electronic heat load, mediated by the bias voltage, plotted as a function of time $t_{\mathrm{heating}}$, during an inital period which is marked by a dashed rectangle in the main panel. The heat into the island is applied as heat pulses with magnitude $Q_p = 2$ pW, integrated over $\dot{Q}_0$ within limits of the length of a single pulse. **b** Specific heat of the In nuclei, obtained from the data in panel a, and calculated specific heat (Eq. 7.7) for $V_{zz} > 0$, $V_{zz} < 0$, and $V_{zz} = 0$, with shaded confidence intervals from angle averaging, plotted as function of the nuclear spin temperature $T_n$.

capacity. Below this temperature, the electron temperature as a function of absorbed heat follows the expected quadrupolar nuclear heat capacity sufficiently well. Here, it is important to note that there was no fit parameter defined: The angle distribution of the electric field gradient direction was assumed to be fully random and the total mass of the indium refrigerators was taken from the measured island volume (see section 2.1.3 for details). The resulting negative field gradient is in contradiction to the positive field gradient reported by [192], but in agreement with the negative field gradient observed in all other works on the topic [103, 104, 184, 188, 189, 191]. Other than in [192], where a polycrystalline sample consisting only of a few grains was used, a completely randomly oriented c-axis in the tetragonal In crystallites with respect to the field is more justified in the present experiment, since as obvious in Fig. 7.2. The electron temperature is obtained from charging on the whole tunnel junction array, averaging the specific heat of the In cooling bars over hundreds of islands, each containing a large number of In grains. Furthermore, no preferred lattice orientation of the films can be assumed, since coherent growth does rarely occur in the electrochemical deposition methods used here.

## 7.6. ELECTRON-PHONON COUPLING AT FINITE MAGNETIC FIELD

The crossover from cooling with nuclear spins alone to heat removal to the substrate, observed during single island calorimetry experiments (see Fig. 7.6 a), allows to estimate the strength of the coupling of electrons in the In islands to the substrate, which is dominated by either electron-phonon scattering in the In cooling bars or phonon-phonon scattering at the film-substrate interface (see sections 2.1, 6.2 for details). The substrate should be well thermalized with the bulk In stages, which are thermally anchored to the device leads. Since the In films have a thickness of several tens of µm one could expect that the thermal resistance to the substrate is dominated by phonon scattering at the In film-substrate interface [67]. However, the temperature is so low that the dimensions of the In islands ($50 \times 140 \times 25.4\ \mu m^3$) are of the of order of the thermal phonon wavelength in In with a value of $\lambda_p = h v_s / k_B T = 117\ \mu m$ at 500 µK, with $v_s = 1.22 \cdot 10^3\ m\ s^1$ (see Tab. 2.1). This implies that the islands could indeed behave like phonon low-dimensional systems. The nature of the coupling to the substrate can be probed by measuring the coupling strength between film and substrate as a function of electron temperature.

In order to obtain the coupling efficiency, the electron temperature, measured in the on-chip calorimetry experiments (Fig. 7.6 b) as a function of heat, $Q_0$, is fitted to a coupling model $\dot{Q}_{e-s} = \alpha \left( T_e^x - T_s^x \right)$, where $\dot{Q}_{\text{e-n}} = V_k I_t - \dot{Q}_{\text{e-s}}$ allows to determine $\dot{Q}_{\text{e-s}}$ above the crossover temperature from nuclear cooling alone to electron-phonon cooling. Since the temperature of the substrate $T_s$ is not measured, it comprises a fit parameter, together with $\alpha$, $x$. As long as the substrate is cooled to well below 1 mK, the substrate temperature should have a negligible impact on the result because the temperature of the islands is raised above a stable base temperature of the bulk stages of the order of a few hundred microkelvin, implying that $\dot{Q} \approx \alpha T_e^x$. To account for the unknown substrate temperature, all data are fitted for substrate temperatures in the range of $T_s = 0.1 - 1$ mK. To account for the unknown electron-substrate coupling mechanism, the data are fitted for the clean

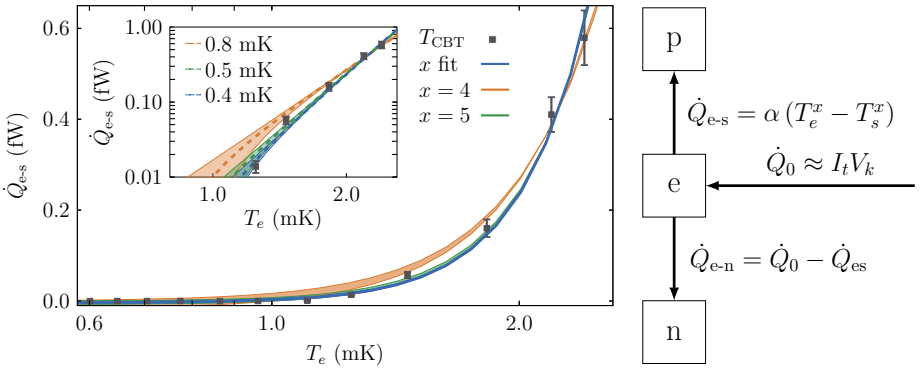


Figure 7.7: **Measured electron temperature plotted against the calculated heat transfer to the substrate and fitted to a substrate coupling model.** The heat flow from the electrons to the substrate $\dot{Q}_{\text{e-n}} = V_k I_t - \dot{Q}_{\text{e-s}}$ (see main text and section 7.5) is plotted against the electron temperature plotted in Fig. 7.6 b and fitted to a coupling model indicated on the right of the figure panel. The fit is performed for substrate temperatures of $T_s = 0.1 - 1$ mK, with $T_s$ stepped in an interval of 0.1 mK. The fits with different substrate temperatures are indicated as shaded regions. **Inset** $\dot{Q}_{\text{e-s}}$ plotted against $T_e > 1$ mK. The dashed lines correspond to the substrate temperatures providing the best fit to the data for the corresponding model above the crossover temperature.

cases $x = 4$ (phonon-phonon coupling, Eq. 2.2) and as well as $x = 5$ (electron-phonon coupling, Eq. 2.4). In these cases, the coupling constant is either $\alpha_{p-p} = kA$, with the contact area $A = 50 \times 140\,\mu\text{m}^2$, or $\alpha_{e-p} = \Sigma V$, with the In volume $V = 50 \times 140 \times 25.4\,\mu\text{m}^2$. For $x = 4$, the data can be best fitted with $k = (2.44 \pm 0.03) \cdot 10^3$ W K$^{-4}$ m$^{-2}$, $x = 5$ results in $\Sigma = (4.26 \pm 0.03) \cdot 10^{10}$ W K$^{-5}$ m$^{-3}$. While $k$ and $\Sigma$ are of the right order of magnitude in both cases, the phonon-phonon coupling model is inconsistent with a constant substrate temperature: Fitting the data with $x = 4$ requires that $T_s$ is lowest at $T_e < 1$ mK and highest $T_s$ above 1 mK (see Fig. 7.7). The large substrate temperatures, fitting the data well at higher temperatures, would imply a positive heat flow from the substrate to the electrons on the chip which was clearly not observed. The data could be modelled with a phonon-phonon coupling if the substrate temperature is assumed not to be stable during the experiment. However, this would be clearly inconsistent with the results obtained in previous experiments (see Figs. 6.5, 6.6). An electron-phonon coupling model fits the data good for a constant substrate temperature of $T_s = 0.5$ mK. A free fit gives $x = 5.53 \pm 0.05$ and $\alpha / V = (2.38 \pm 0.59) \cdot 10^{11}$ W K$^{-5.53}$ m$^{-3}$, consistent over the whole temperature range with a constant substrate temperature of $T_s = 0.4$ mK. This indicates that the main thermal relaxation path at high temperatures is electron-phonon coupling, but signfificantly weaker than expected from the free electron model with a temperature scaling of about $T^{5.5}$. Interestingly, exponents of $> 5$ are predicted for electron-phonon coupling in geometries which are restricted for phonon degrees of freedom (see Eq. 2.6).

The weak coupling of the electrons on-chip to the environment at $T_s$ enables operating the system in the adiabatic regime, since the heat balance of the CBT and its environment, when its temperature is modified with a magnetic field, is not dominated by background heat leaks, but the strengthening coupling to its environment. In the adiabatic limit, $T_n$ can be solely modeled by means of a constant molar nuclear entropy $S_n$. Due

to $\dot{Q}_{\text{res}} \ll C_n \dot{T}_n$, the nuclear spin temperature $T_n$ can only be modified by changing the magnetic field $B$ (as experimentally shown in section 7.4) according to

$$\mathrm{d}T_n = \left(\frac{\partial T_n}{\partial B}\right)_S \mathrm{d}B, \tag{7.11}$$

enabling tuning of the electron temperature with a magnetic field under isentropic conditions. Depending on the strength of the magnetic field, the quadrupolar heat capacity of In (see Fig. 7.3 and Fig. 7.6) has a maximum between 100 µK and 200 µK, implying that there will be an upper limit of the adiabatic regime which is determined by finite coupling of the islands to the substrate. A small temperature difference between substrate and islands will increase with increasing the magnetic field until it becomes so large that the temperature difference between electrons on the island and the substrate results in a significant heat flow $\dot{Q}_{\text{e-s}}$ to the substrate. The heat flow of electrons on the island at $T_e$ to the substrate at $T_s$, after increasing the field from $B_i$ to $B_f$ can be estimated by

$$\dot{Q}_{\text{e-s}}(B) = \alpha\left[\left(T_e\frac{B_2}{B_1}\right)^x - \left(T_s\frac{B_2}{B_1}\right)^x\right] = \alpha\left(\frac{B_2}{B_1}\right)^x\left(T_e^x - T_s^5\right) = \left(\frac{B_2}{B_1}\right)^5\dot{Q}_{\text{e-s}} \tag{7.12}$$

Here $B_1 = \left[B_{\text{int}}^2 + B_i^2\right]^{1/2}$ and $B_2 = [B_{\text{int}}^2 + B_f^2]^{1/2}$ with $B_{\text{int}} = 295$ mT (see section 6.6). The cooling power of the substrate on a single island, when the working point is set to $(B, T)$, can thus be estimated by $\dot{Q}_{\text{e-s}}(B) \approx \lambda(B_2/B_1)^{5.5}T_e^{5.5}$, under the condition that $T_s$ is sufficiently smaller than $T_e$. At temperatures $T_e(B_f)$ and $T_s(B_f)$, the substrate cooling power gives rise to a warmup rate of the nuclei with specific heat $C_n$, given by

$$\dot{Q}_{\text{e-s}} = C_n\frac{\partial T_n}{\partial t} \tag{7.13}$$

To probe the adiabatic regime with Eq. 7.12, the is CBT prepared at a temperature of $T_i = 1.22$ mK and a magnetic field of $B_0 = 500$ mT by nuclear demagnetization (Fig. 7.8 a). This working point corresponds to a situation where the nuclear quadrupole coupling is signficantly screened by Zeeman splitting and the thermal energy $k_{\text{B}}T_e$. Then,

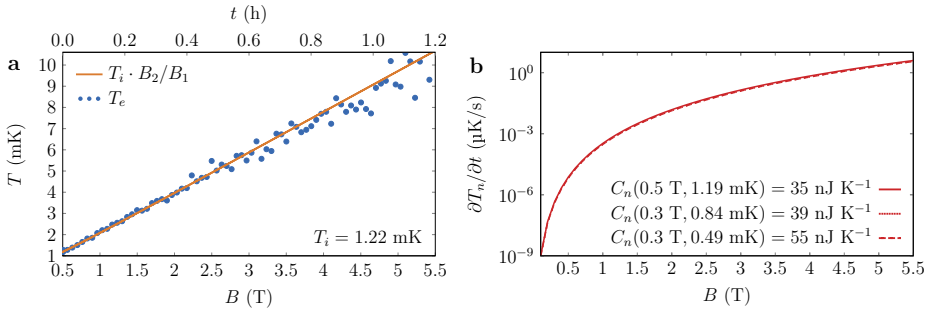


Figure 7.8: **Probing the limits of adiabatic temperature tuning with magnetic field strength. a** The measured electron temperature plotted as a function of applied magnetic field strength, starting from a working point at (1.22 mK, 0.5 T). **b** The cooling rate of nuclei due to off-chip coupling calculated with Eq. 7.13 and plotted as a function of magnetic field for different starting points in $(B, T_n)$ space, giving rise to a starting value $C_n(B, T_n)$

the magnetic field strength is slowly increased up to 5.5 T while the electron temperature is tracked. For magnetic fields up to about 3 T, the measured electron temperature follows an ideal adiabatic model according to $T_e(B_f) = T_i \times B_2/B_1$. At higher fields, the measured temperature seems to drop off towards lower values. Here, the scattering of the temperatures due to the small AC excitation chosen for measuring the differential conductance of the CBT, prevents the drawing of clear conclusions. The cooling rate imposed by $\dot{Q}_{\text{e-s}}$ is calculated with Eq. 7.13 and plotted for magnetic fields between 0.1 T and 5.5 T in Fig. 7.8 for different working fields and working temperatures (The other two working points in Fig. 7.8 b correspond to the experiments discussed in section 7.5 and section 7.6). The nuclear heat capacity of a single In island with $n = 11.4$ nmol is of the order of several tens of nJ/K with the chosen demagnetization efficiency (see Fig. 7.7 and Fig. 2.5). Significant cooling rates over the timescale of hours are reached with $\partial T_n/\partial t > 0.1\,\mu$K/s at a few mK, guaranteeing operation in the adiabatic regime up a lower boudary of 3 T, limited by the temperature accuracy of the CBT at low AC excitations (see Fig. 7.8 a).

## 7.7. CONCLUSIONS

A nanocalorimetric analysis of the In microrefrigerators revealed a nuclear specific heat, determined by $\omega_{Q,R}/2\pi = 47.1$ MHz and $V_{zz} < 0$. This result is well in line with previously obtained values and identifies the nonmagnetic nuclear level splitting, observed in the experiments discussed in sections 6.5 and 6.6, and parameterized as a residual field of 295 mT (see Fig. 6.7), as pure quadrupolar. The large specific heat of the on-chip coolant, enabling microkelvin refrigeration of a nanoelectronic device with temperature hold times of several days (see Fig. 6.5 and Fig. 6.6) can thus be attributed to a significant enhancement of the nuclear level splitting at the corresponding magnetic field. The identification of the specific heat of the system as solely resulting from the on-chip integrated nuclear refrigerant justifies the applicability of a single island model for the nuclear heat capacity and approves the the small heat leaks in similar on- and off-chip nuclear demagnetization experiments (see section 6.6 for details) as a feature of cooling the leads of the CBT with a parallel set of bulk In stages. The specific heat measurements also revealed an extremely weak thermal coupling of the electrons on the island of the CBT to the environment, scaling with $\dot{Q}_{\text{e-s}} \propto T_e^{5.5}$, most probably enabled by electron-phonon scattering inside the metallic islands. These results confirm the initial assumptions made that electron-phonon coupling is insufficient to provide submillikelvin refrigeration of electrons in miniaturized structures.

For chipscale nuclear magnetic cooling material integration schemes, as utilized in this work, the obtained results imply that device integration of electrodeposited In microrefrigerators is a fully scalable approach. Scalable here means that one is able to design the thermal budget accompanied by integrating a defined amount of nuclear refrigerant very well, even including the effect of nonmagnetic nuclear level splitting for nuclear magnetic cooling on the miniaturized scale. In summary, this fully approves the principle of quadrupole enhanced nuclear cooling which was postulated in this work, opening a wide variety of possbilities for microkelvin refrigeration of nanoelectronic circuits.

# 8

# SUMMARY AND OUTLOOK

*There is nothing impossible to him who will try*

Alexander the Great (356 B.C. - 323 B.C.)

## 8.1. TECHNOLOGY OF MICROKELVIN NANOELECTRONICS

The development and successful implementation of on-chip integrated and parallel stage nuclear magnetic cooling for microkelvin nanoelectronics can be seen as a primer for future developments in this field. Concepts developed in this and similar works [45, 47] can be adapted for this purpose. These main concepts are on-chip integration of metallic nuclear paramagnets as film material, and cooling the device leads with a parallel set of macroscopic nuclear refrigerators. Further developments on bulk stages for cooling the leads (see section 3.3) are an improvement of the heat transfer from the parallel nuclear cooling stages to the main stage via thin-film thermalization (see section 3.3.3). Increasing the effective thermalization area and reducing the thickness of the insulating films, over which the bulk stages are precooled, can possibly enable lower starting temperatures for the nuclear demagnetization process, as obtained here (see section 6.3). At a certain limit of the barrier thickness, surpassing the thermal wavelength of phonons in the neighbouring materials signficiantly, one could profit from phonon tunneling [193].

Besides this, the main focus of this section is put on the development of material integration schemes, enabling efficient refrigeration of miniaturized electronic devices to microkelvin electronic temperatures. The concepts proposed here for realizing on-chip integrated microrefrigerators or low resistance interconnects are analogous to IC (integrated circuits) metallization and 3D integration schemes. These give rise of two possible ways of nuclear cooling on the chipscale. **1) Direct (on-chip) nuclear cooling**, by integration of the nuclear refrigerant as metallic film, as done in this work. Direct nuclear cooling allows to cool even thermally well isolated regions of the chip efficiently. The technique needs to be accompanied by cooling the device leads and the magnetic field used for nuclear cooling has to be compatible with magnetic fields driving the device. **2) Remote nuclear cooling** utilizes a macroscopic nuclear stage, galvanically connected to the device leads. In this approach the electronic heat load on-chip has to be transferred from the device to an off-chip stage, requiring that the thermal resistance to the device is low enough. Metallic nuclear paramagnets are integrated as thick film interconnect materials, serving as nuclear microrefrigerators for thermally isolated regions of the chip (1), or as low-impedance interconnects to macroscopic off-chip nuclear stages (2).



### 8.1.1. FUTURE NUCLEAR REFRIGERANT INTEGRATION SCHEMES

For any nuclear refrigerant (NR) integration process, the main constraint is a sufficiently small electrical resistance between the nuclear microrefrigerator and the electronic system to be cooled (see Fig. 2.2). If interconnects with a low enough electrical resistance can be routed off-chip, the device can be cooled by an off-chip stage only, which enables remote nuclear magnetic cooling. If the latter is not possible, the NR volume has to be sufficiently large with respect to the nuclear heat capacity to provide the necessary thermal stability at microkelvin temperatures. The corresponding nuclear cooling properties can be tailored by material choice (see Tab. 8.1 and Tab. 2.2). Integrating thick metallic films on top of miniaturized devices is a main task in IC fabrication, where wiring is provided on the chip. Thus, NR integration schemes can be developed in analogy with existing methodologies. Two basic schemes for on chip metallic wiring, suitable for efficient NR integration, are depicted in Fig. 8.1. Both are discussed in the following.

The back end NR integration scheme (Fig. 8.1 a) is fully analogous to common back end of line processes used for wiring after IC fabrication. The back end scheme involves capping of the device with an interlayer dielectric (ILD) to provide galvanic separation from the interconnect layers. The nuclear refrigerant is electroplated into trenches, etched into a second (thick) ILD, and is galvanically connected to the device via metallic contact plugs in case the nuclear refrigerant is not making a good electrical and thermal contact to the device leads (or builds unwanted alloys with the lead material). Plating the nuclear refrigerant into a patterned dielectric allows to integrate extremely thick NR films with very large aspect ratio. The electrical resistance over the contact plugs has to be sufficiently small that it does not add a significant series resistance towards the device. The back-end scheme can be implemented with any suitable metallic nuclear paramagnet by direct masked electroplating, as already demonstrated in this work (see section 3.1.2). A benefit of back end schemes is that interconnects can be routed in several layers, stacked on top of each other. This however requires planarization steps which are not possible with soft metals like In. These constraints are not there is only a single back-end layer is used. In the latter case any material can be integrated, with the achievable amount of material depending in both of the cases on the available area on the chip surface.

Another approach to integrate signficiant amounts of nuclear refrigerant onto a chip is the implementation of electroplated through substrate vias (TSVs), as illustrated in Fig. 8.1 b. In this process, holes are etched or milled into the substrate and the space is filled by metal electrodeposition afterwards. Void free filling of TSVs, which were previously created by deep reactive ion etching, is mainly demonstrated for electroplated Cu films [194], but can be achieved with other nuclear paramagnetic metals in the same way. Integrating the nuclear refrigerant into the substrate would allow to use large amounts of NR. For example, a 50 µm TSV through a 0.5 mm thick substrate can be filled with about

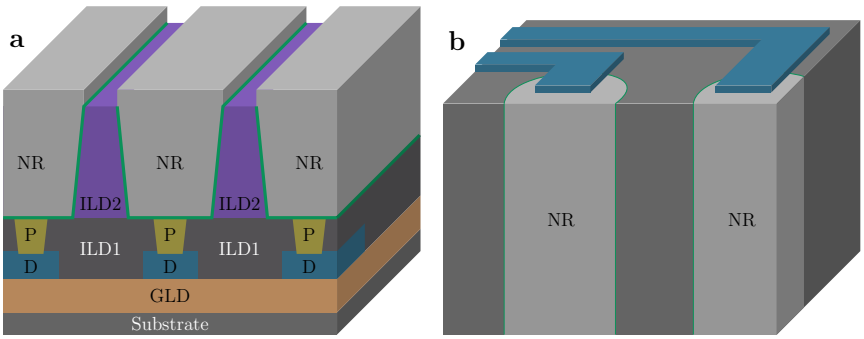


Figure 8.1: **Integration schemes for metallic nuclear paramagnetic films for on-chip integrated nuclear magnetic cooling**. **a** Back end scheme: thick films of nuclear refrigerant (NR) are integrated in a typical back-end of line (BEOL) process using thick interlayer dielectrics (ILD) and contact plugs (P) for top-down contacting to the devices (D). The devices are fabricated on a suitable substrate and may be further isolated from the substrate by a dielectric separation layer (GLD). **b** TSV scheme: through holes (through-vias) are etched or drilled into the substrate followed by conformal deposition of the seed layer and filling of the vias with a metallic nuclear refrigerant. Devices can be afterwards fabricated on a planar substrate.

140 nmol of Cu, which is an order of magnitude larger than the integrated 11 nmol of In per CBT island achieved in this work. Despite the weak hyperfine interaction and absence of nuclear quadrupole coupling, on-chip (or better in-chip) nuclear cooling with Cu would become interesting again (see section 8.1.2, Tab. 8.1). TSVs are also a main building block of 3D integrated superconducting quantum bit architectures [30], which could enable interesting opportunities for cooling these systems. Using In for wiring and on-chip nuclear cooling would have the additional benefit that the leads can be connected to the off-chip stage via room temperature metal welding (see Fig. 3.13).

### 8.1.2. MATERIALS FOR MINIATURIZED NUCLEAR COOLING

A decisive impact on the performance of on-chip integrated nuclear cooling is brought by the choice of the nuclear refrigerant. As introduced in section 2.2.4, the material requirements for on-chip refrigerants and refrigerants used in bulk nuclear stages are completely different. The important material properties of an on-chip refrigerant are the volume nuclear heat capacity $C_V(T_n, B) = C_n(T_n, B)/V_m$, with the molar nuclear spin heat capacity $C_n(T_n, B)$, the molar volume $V_m$, and the spin lattice relaxation time $\tau$, at a given spin temperature $T_n$ and magnetic field $B$. The nuclear heat capacity has a maximum (see Fig. 2.5) at a material and magnetic field dependent spin temperature $T_R$, corresponding to the thermal energy scale of the nuclear level splittings. At a given magnetic field $B$, the system can be tuned to its maximum by cooling to $T_n = T_R(B)$ . At this optimal operation point, the nuclear refrigerant has its maximum cooling power

$$\dot{Q}_{\max,V}(B) = \left[C_V(T_R, B) \cdot T_R^2/\kappa\right](T_e - T_R) \tag{8.1}$$

on the conduction electrons. Here, $\kappa$ is the Korringa constant with $\tau = \kappa/T_e$. The distinct material dependence of $T_R$ makes $\dot{Q}_{\max}$ a good parameter to compare different nuclear refrigerants. Since nuclear cooling is a single-shot technique, characterized by a finite nuclear heat capacity, nuclear refrigerants need to be benchmarked with respect to temperature hold time too. Approximating $C_V$ as constant in the interval between $T_R$ and $2T_R$, the nuclear spin system will warm up from $T_R$ to $2T_R$ by absorbing

$$Q_{\max,V}(B) \approx C_V(T_R, B) \cdot 2T_R \tag{8.2}$$

Some applicable metallic nuclear paramagnets for microkelvin refrigeration of nanoelectronic circuits are compared in Tab. 8.1 with respect to $\dot{Q}_{\max,V}(B_c)$, corresponding to the lowest $T_R$ achievable by demagnetizing the nuclear spins to the critical end field $B_c$. In this context, $B_c$ is the smallest attainable magnetic field for the material, and thus either the critical temperature for the superconducting phase transition of the conduction electrons or the nuclear Curie temperature. For comparison, $\dot{Q}_{\max,V}(B)$ is also compared at 5 T, which would be a typical field value for quantum Hall measurements.

Tab. 8.1 can be used as a design guide for implementing nuclear microrefrigerators and/or remote nuclear stages for off-chip cooling of nanoelectronic circuits. From there it is clear that In is the most suitable nuclear refrigerant for cooling microstructures with volumes of the order of $10^4 - 10^5$ µm$^3$ to temperatures between 100 µK and 1 mK, since it can be integrated as film material from an elemental plating bath and has a good com-

Table 8.1: **Material properties important for chipscale nuclear magnetic cooling of some selected materials.** The critical fields are intrinsic fields by Ruderman-Kittel induced nuclear spin ordering (Cu: 0.5 mT, Sc: 0.5 mT, La: 0.5 mT, Sb: 0.5 mT, $PrNi_5$: 0.5 mT), where all of the latter materials are not superconducting, or superconductivity (In: $B_c = 28$ mT). For all other material properties used, the reader is referred to Tab. 2.2.

| | $T_R$ (μK) | $C_V(T_R, B_c) \cdot T_R^2/\kappa$ (fW/μm$^3$) | $C_V(T_R, B_c) \cdot 2T_R$ (aJ/μm$^3$) | $C_V(T_R, 5\,\mathrm{T}) \cdot T_R^2/\kappa$ (fW/μm$^3$) | Plating |
|---|---|---|---|---|---|
| Cu | 0.18 | $1.3 \cdot 10^{-4}$ | 0.29 | 1.24 | [194] |
| Sc | 13 | 0.46 | 9.11 | 113.8 | [195] |
| La | 42 | $2.6 \cdot 10^{-3}$ | 27.5 | 3.06 | [196] |
| In | 230 | 1.45 | 240 | 18.97 | [197, 198] |
| Sb | 248 | $5.4 \cdot 10^{-3}$ | 174 | 0.55 | [199, 200] |
| $PrNi_5$ | 343 | 86.8 | 52.2 | $1.34 \cdot 10^4$ | [201] (Pr) |

bination of nuclear cooling power and heat capacity at submillikelvin temperatures. Remaining obstacles with using In are that it is a superconductor with a critical field of 28 mT, it is very soft and plated films do not have a smooth surface. $PrNi_5$ is an attractive material due to its extremely short spin lattice relaxation time (see Tab. 2.2), but is extremely difficult to prepare as a film material by electrochemical deposition methods, since $Pr^{3+}$ is a very unnoble metal with a reduction potential of -3.1 V, and needs to be plated as an alloy with Ni in an exact stochiometry. Sc can be a suitable material for nuclear microrefrigators in the range of 10-100 μK, but also suffers from a large negative resuction potential of -2.1 V (of $Sc^{3+}$), requiring plating from a non-aequous bath. For remote nuclear cooling with a bulk stage, where small volumes are not an issue, Cu should perform well as a nuclear refrigerant. It is not expected that any other elemental nuclear paramagnet will show superior performance to In in terms of nuclear cooling on chip.

Superior materials could be provided by metal alloys, in which metals with beneficial nuclear magnetic properties are alloyed in such a way that the quadrupole splitting of the nuclear spin levels is in the temperature regime of interest. By alloying, one can also reduce the critical field of superconductors significantly or make the material normal conducting in the desired temperature range. A starting point could be In alloys with a non-cubic crystal structure. Electrodeposition of metallic alloys with tuning the alloy composition is possible. The utilization of materials with van-Vleck paramagnetism would be a signficant improvement, however also the largest challenge in terms of chip integration because known van-Vleck paramagnets are intermetallics of lanthanoids for which electrodeposition with the necessary material quality is extremely challenging.

### 8.1.3. COOLING OF LOW-DIMENSIONAL SEMICONDUCTORS

Low-dimensional semiconductors are typical systems in which chipscale nuclear magnetic cooling would need to be applied to cool quantum devices into the microkelvin regime. A wide variety of quantum devices can be realized in planar semiconductor heterostructures, comprising two-dimensional electron gases (2DEGs), which are electrically 2D systems. These systems are also ideal platforms for on-chip nuclear mag-

netic cooling since for an as grown 2DEG stack, the conducting channel extends over the whole chip area. This makes it possible to locally realize large electronic reservoirs in which charge carriers in the 2DEG can be brought into thermal equilibrium with cold nuclear spins in the on-chip refrigerant. The nuclear refrigerant can be plated onto existing metallic contacts to the 2DEG in a back end integration scheme as introduced in section 8.1.1. If the contact resistance between the metallic contact to the 2DEG and the semiconductor channel is not limiting the thermalization of electrons in the 2DEG with the nuclear spins in the plated nuclear refrigerant, the contacts can be used as thermalization spots for cooling further regions of the 2DEG. With a suitable metallization scheme, often involving diffusion processes, contact resistivities of the order of $10^{-7}-10^{-5}\,\Omega\,\mathrm{cm}^2$ can be achieved for bulk III-V semiconductors [202, 203], while for AlGaAs/GaAs 2DEGs still values down to $10^{-4}\,\Omega\,\mathrm{cm}^2$ can be reached [204], which should enable efficient thermalization with the nuclear refrigerant. The length scale over which the conduction electrons in the semiconductor device thermalize with the contacts is determined by the inelastic mean free path $\lambda$ of the charge carriers. On length scales smaller than $\lambda$, conduction electrons in the 2DEG will be cooled to the lead temperature (Fig. 8.2).

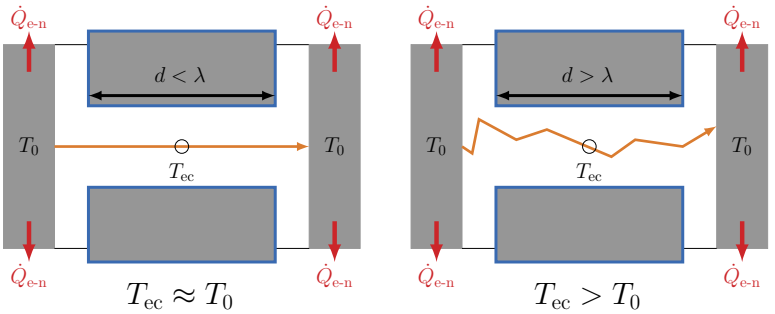


Figure 8.2: **Cooling of a two-dimensional electron gas by nuclear magnetic cooling**. The electrical contact regions at temperature $T_0$ are thermalized with a nuclear refrigerant either by direct or remote nuclear magnetic cooling. A channel region is defined by gates (gray with blue borders) **a** If the mean free path $\lambda$ is longer than the contact separation the conducting channel is perfectly thermalized with the leads. **b** If the contact separation exceeds $\lambda$ a local thermal equilibrium will be established inside the channel.

Structures of lower dimensionality such as quantum wires (1D) and quantum dots (0D) can be defined in a 2DEG by depletion of charge carriers with a gate, or patterning of the 2DEG. Cooling a quantum wire can be achieved when the wire length does not exceed the inelastic mean free path, since a local thermal equilibrium is never reached in a ballistic channel [205]. Thus, inside these channels, the temperature of the electronic reservoirs, which are effectively cooled by the nuclear microrefrigerators, will be retained. Problematic for any cooling technique are quantum dots, which are only tunnel coupled to the reservoirs and thus thermally well isolated from these. A SET can be cooled by a floating island of a metallic nuclear refrigerant, as it was done in this work for the CBT islands. If the charging energy of the dot is defined by discretization of electronic states due to the dot geometry, it can not be brought into galvanic contact with a large metallic volume. If the dot is not the active device but is only used for sensing it might however not be strictly necessary to cool it to the temperature of the reservoirs.

## 8.2. ULTRALOW TEMPERATURE REFRIGERATION FOR TOPOLOGICAL QUANTUM COMPUTATION

Topological quantum computation [34–36, 206, 207] is an approach for quantum information processing in which quantum gates are intrinsically fault tolerant unitary transformations of exchanges of non-Abelian anyons with a topological degeneracy. Quantum operations between degenerate eigenstates of the system are thus adiabatic and a qubit based on non-Abelian anyons is topologically protected by an energy gap $\Delta$ (topological gap), depending on the physical nature of the topological phase. Errors are occuring due to excitations of quasiparticles with a rate $\Gamma \simeq (k_B T/\Delta)\exp(-\Delta/k_B T)$ [34]. Reaching lower electron temperatures is not only an opportunity to protect quantum information stored in a topological phase with a small excitation gap against thermal excitations of quasiparticles, but could also enable alternative ways for engineering a topological phase hosting non-Abelian anyons into low-dimensional semiconductors. Concepts for utilization of microkelvin nuclear magnetic cooling of low-dimensional solid state systems, hosting topological states, are discussed in the following sections.

### 8.2.1. FRACTIONAL QUANTUM HALL STATES

In strongly correlated two-dimensional electron gases, several fractional quantum Hall states [208, 209], appearing at high magnetic fields, are expected to have quasiparticle excitations which could be non-Abelian anyons. Fractional quantum Hall states appear when electron-electron interactions in a two-dimensional electron gas are not screened by disorder and at low enough temperature. Of particular interest here is the fractional quantum Hall state at filling factor $\nu = 5/2$, which is assumed to support Ising anyons [210]. Ising anyons are equivalent to Majorana zero modes (MZMs) in terms of topological quantum computation. A quantized Hall plateau at $\nu = 5/2$ was first observed by cooling a GaAs 2DEG to 25 mK [49]. With a nuclear stage of 5 mol $PrNi_5$ at 2 mK, cooling of a GaAs 2DEG with mobility $17 \cdot 10^6$ cm$^2$ V$^{-1}$ s$^{-1}$ to 4 mK could be achieved, enabling an exact quantization of the $\nu = 5/2$ plateau [43, 211]. The expected quasiparticle charge of $e/4$ [34] could be confirmed too [212]. Further studies of the 5/2 state are expected to profit significantly from stable and lower electron temperatures, not limited by electron-phonon scattering [213], as they can be provided by chipscale nuclear magnetic cooling.

The very fragile fractional quantum hall state at filling factor $\nu = 12/5$ could provide Fibonacci anyons which would be universal in topological quantum computation [34]. Signatures of the 12/5 state have been seen only in a few experiments so far, indicating a thermally fragile state [214–216]. Reaching lower and well defined electron temperatures could provide better experimental boundary conditions for studying this state. In general, lowering electron temperatures beyond further limits provides exponential suppression of excitations above the excitation gap $\Delta$, even when $\Delta$ can not be well tuned. The improper control of $T_e$ is a proven problem in electron-phonon cooled systems. If the electron temperature can be reduced down to $T \leq 100$ µK and below, stabilized by strong electron-nucleus coupling in the leads, an order of magnitude difference between and $\Delta$ and $T_e$ can be provided even under non-ideal conditions regarding $\Delta$.

Quantum Hall plateaus are observed at fields according to $\nu = n_e h/eB$, with the electron density $n_e$. This allows to reduce the magnetic field, necessary for observing the fractional quantum hall states at $\nu = 5/2$ and $\nu = 12/5$ by increasing the carrier density. In the case of direct nuclear magnetic cooling of the 2DEG via the leads, the magnetic field is driving the nuclear cooling process and the quantum Hall experiment at the same time. Remote nuclear cooling using low resistance interconnects, not made out of a nuclear paramagnetic metal could enable the decoupling of the nuclear cooling cycle and the magnetic field applied to the 2DEG. Another possbility would be to use the Overhauser field provided by Ruderman-Kittel interaction of the nuclear spins (see next section), expected to occur in III-V seminconductor 2DEGs at microkelvin temperatures [217].

According to the proposals for effective nuclear cooling of low-dimensional systems based on 2DEGs (section 8.1), schemes for realizing a topological qubit based on nonabelions in the fractional Hall regime [33, 34] harmonize well with microkelvin cooling of the corresponding device. A proposed device is based on a quantum Hall bar structure with two individually gated regions in the center and tunneling gates, connecting edge states. Edge states in the fractional quantum hall regime show ballistic transport over long length scales and should be well thermalized with the leads, which can be themeselves thermally anchored to a large nuclear spin bath for local cooling. In [33] an error rate $(k_B T/\Delta)\exp(\Delta/k_B T) < 10^{-30}$ is postulated for an electron temperature of $T = 5$ mK and $\Delta/k_B = 500$ mK, which are both rather optimistic assumptions, given that the electron temperature reached in similar devices is usually well above 10 mK and $\Delta/k_B$ varies with carrier density and film quality down to 10 mK [218]. By cooling the electrons with nuclear magnetic cooling, one would not rely on extremely high charge carrier mobilities which are not always easy to sustain in real devices and could work at lower carrier densities, necessary for gating. For the 12/5 state with $\Delta/k_B < 100$ mK even for the highest mobility AlGaAs/GaAs 2DEGs, microkelvin refrigeration would enable fault-tolerant quantum computation, given that the parafermion nature of the 12/5 state is approved.



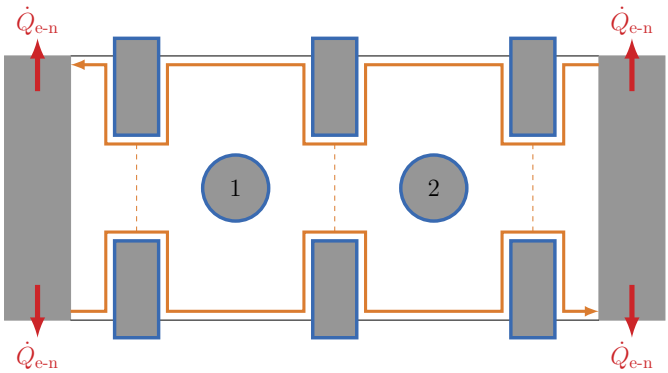


Figure 8.3: **Proposed device layout for a topological qubit based on the 5/2 fractional quantum Hall state, reproduced from [33].** The structure consists of point contacts over which quasiparticles tunnel between the edge states (drawn in orange). The charge on the central antidots (gated regions, labeled with 1 and 2) is controlled with gates (drawn with blue borders). The leads are cooled by nuclear refrigerants.

### 8.2.2. SELF-SUSTAINED TOPOLOGICAL PHASE IN 1D

Majorana zero modes (MZMs) were postulated to occur in topological superconductors, signatures were found in engineered systems based on semiconductor nanowires [219, 220]. Engineering a topological phase into a semiconductor nanowire, proximitized with a s-wave superconductor, requires a helical spin-texture, required for realizing a p-wave type superconductivity. A helical spin-texture can be created by a helical magnetic field $\mathbf{B}(\xi) = (\sin k_h\xi, \cos k_h\xi, 0)^{\mathbf{T}}$, with the field rotating with a period of $2\pi/k_h$ around the free axis $\xi$ of the 1D conductor. A topological phase transition takes place when a pairing potential $\Delta_s$ is switched on. The corresponding single particle hamiltonian is

$$H_0 = \left(\frac{p_\xi^2}{2m} - \mu\right)\tau_3 + \frac{g\mu_B}{2}\mathbf{B}(\xi)\boldsymbol{\sigma} \quad , \qquad H_s = \Delta_s\tau_1 \tag{8.3}$$

$\sigma_i$ and $\tau_i$ are pauli matrices in spin- and particle-hole space, $\mu$ is the chemical potential. $\mathbf{B}$ can be mapped to a homogenous field [221, 222] by unitary transforming Eq. 8.3 with $U(\xi) = \exp(i\phi\sigma_{xy})$ where $\sigma_{xy} = (\mathbf{B}\times\mathbf{e}_z)\cdot\boldsymbol{\sigma}/|\mathbf{B}\times\mathbf{e}_z|$ and $\cos\phi/2 = \mathbf{B}\cdot\mathbf{e}_z/|\mathbf{B}|$, then

$$U^\dagger H_0 U = \left(\frac{p_\xi^2}{2m} - \mu' + \alpha p_\xi\sigma_2\right)\tau_3 + \frac{g\mu_B}{2}|\mathbf{B}|\boldsymbol{\sigma_3} \quad , \qquad H_s = \Delta_s\tau_1 \tag{8.4}$$

With $\alpha = \hbar k_h/2m$. The transformation introduces a term, lineary coupling spin to momentum. Eq. 8.4 is up to a factor of 2 in the spin-momentum term identical to the Hamiltonian of a particle in a 1D conductor with Rashba spin-orbit interaction in a homogenous magnetic field. Hence, the current state of the art system for a 1D topological phase is a semiconductor nanowire with spin-orbit interaction and a magnetic field.

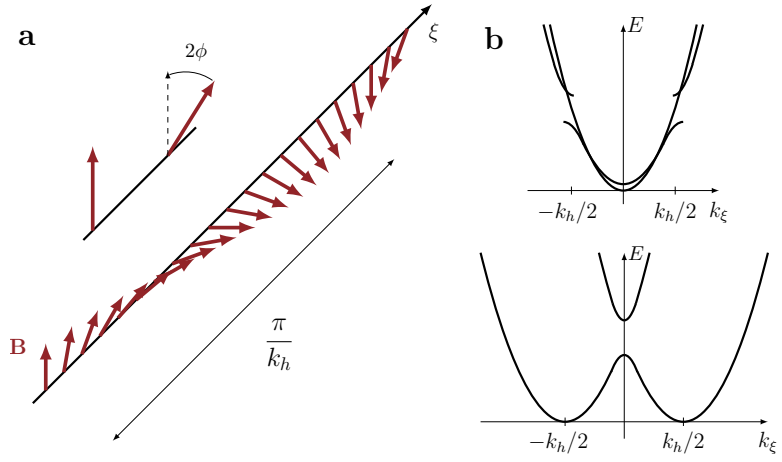


Figure 8.4: **Illustration of the magnetic field profile in Eq. 8.3 and 8.4 and band schemes**. **a** Helical magnetic polarization winding around the wire axis $\xi$ with period $\pi/k_h$ and defining a local spin basis. **b** The helical magnetization results in a spin dependent gapping of electronic states around $k_h/2$. **Top right panel**: Eigenspectrum of Eq. 8.3 (original basis), **Bottom right panel**: Eigenspectrum of Eq. 8.4 (transformed basis).

In view of the original basis (Eq. 8.3) it is obvious that with $k_F = k_h/2$ the appearance of the spin-dependent gap can be interpreted as a Peierls-instability of the conductor, gapping only half of the conducting modes and turning the system into an helical conductor when a (spin-selective) backscattering between the Fermi-points is switched on by the periodic potential provided by the spin helix. The energy where the helical gap opens up is determined by the pitch of the helical magnetic field. A possibility to create a magnetic helix in a 1D system is offered by the interplay of conduction electrons and nuclear spins in a one-dimensional nuclear paramagnet, occuring in non-interacting systems at extremely low electron temperatures [156, 223]. Conduction electrons can couple nuclear spins by Ruderman-Kittel interaction in a way that they are ferromagnetically locked in the two reduced dimensions and the nuclear magnetic polarization winds as a helix with pitch $\pi/k_F$ around the free axis. This helical nuclear magnetization acts back on the electrons, inducing an anisotropy in their spin susceptibility, in turn stabilizing the helical nuclear spin polarization. The Ruderman-Kittel interaction locks the pitch of the helical nuclear spin polarization to $k_F$ and makes the system self tuning into the helical gap, given by $\Delta_m = A_0 I$, with $A_0$ the strength of the isotropic hyperfine interaction. The helical nuclear spin polarization corresponds to a ground state, stabilized by the conduction electron susceptibility against scattering with momentum transfer $2k_F$. The latter is strongly pronounced in 1D systems. At finite temperature the helical ground state is destabilized by magnons, and thus a magnon excitation gap gives rise to the nuclear Curie-temperature $T_c$, given by $kT_c \approx I^2 J_{2k_F}$, with $I$ the nuclear spin, and $J_{2k_F} \propto -A_0^2 \chi(2k_F)$, parameterizing the Ruderman-Kittel interaction at $\Delta k = 2k_F$, with the 1D static electron spin susceptibility $\chi(2k_F)$ [161, 224]. $T_c$ and $\Delta_m$ are both expected to be enhanced by repulsive electron-electron interactions [156, 222, 224].

Signatures of helical nuclear ordering in 1D can be probed by conductance measurements in the ballistic regime. Below $T_c$, conductance through a ballistic helical 1D channel drops by a factor of 2 due to backscattering between $+k_F$ and $-k_F$ for half of the conducting modes (Fig. 8.5). A clear observation of conductance reduction of exactly a factor of 2 is only expected when the transmission coefficient for the gapped states is close to zero, requiring a distinct length of the one-dimensional conductor. With only the first subband occupied, this leads to conductance reduction from $2e^2/h$ to $e^2/h$. In a magnetic field, helical transport should be observable for fields smaller than the Overhauser field $B_c = \Delta_m/g_e\mu_B$, with $B_c$ further enhanced by electron interactions. A potential difference over the channel opens additional phase space for backscattering in one specific direction by a population difference for the ungapped modes [225]. Spin-flip backscattering of electrons leads to a conical nuclear-spin polarization and the helical polarization should vanish already at $eV \approx kT_c$, where the helical state is destroyed by heating electrons above $T_c$. If the chemical potential is tuned into the second subband, the electron system becomes susceptible against scattering with momentum transfer $2k_{F1}$, $2k_{F2}$ or either combinations of $k_{F1} + k_{F2}$ [226]. In this case, helical order can only exist if either two helices $2k_{F1}$ and $2k_{F2}$ are superimposed (Fig 8.5) or there is a single helix at momentum $k_{F1} + k_{F2}$ (8.5). In the latter case the two helices set in at different temperatures, exhibiting a stepwise reduction from $4e^2/h$ to $3e^2/h$ after the formation of the first helix, and $2e^2/h$ when the second helix is formed. Experimental signatures of a helical

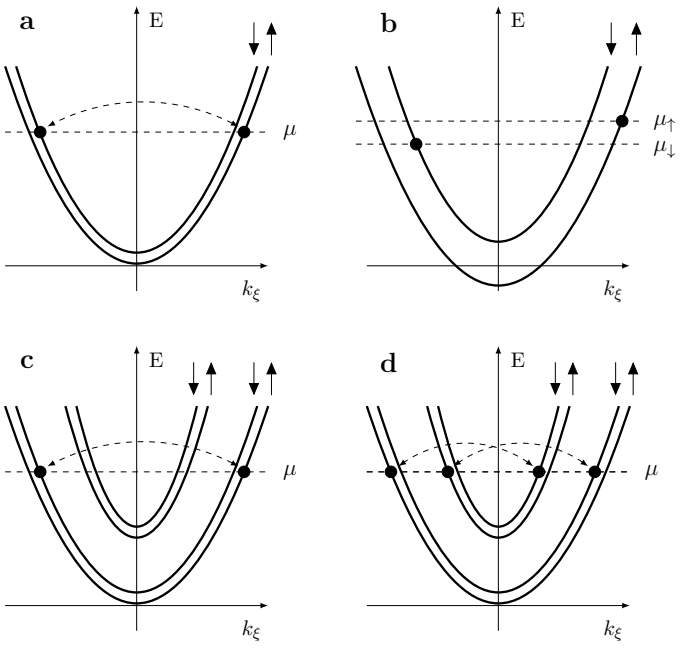


Figure 8.5: **1D electron spin susceptibility**. **a** Resonant backscattering with $2k_F$ between half of the conducting modes. **b** Finite bias $eV = \mu_\uparrow - \mu_\downarrow > 0$, inducing a uniform nuclear spin polarization. **c** Intraband resonant backscattering in the two-subband regime **d** Interband resonant backscattering in the two-subband regime.

nuclear spin polarization are reported for cleaved edge overgrown GaAs nanowires [227].

Concerning superconductivity, one would expect that superconductivity and helical nuclear order can not coexist because pairing of conduction electrons also gaps out states around the Fermi-energy which keep up the Ruderman-Kittel interaction. But the length scale on which the magnetization in a RKKY helical nuclear magnet changes direction is set by the electron wavelength which can be shorter than the coherence length of the superconductor. In this case the electron spin susceptbility can be approximated by [161]

$$\chi(k) \approx -\frac{k_F}{8\pi a \mu_F} \ln\left(\frac{\exp(1/2+\gamma)}{\sqrt{\Delta_s^2/\mu_F^2 + (1-k/2k_F)^2/2}}\right) \tag{8.5}$$

With the Euler gamma constant $\gamma \approx 0.58$, the chemical potential $\mu_F$ and the lattice constant $a$. $\chi_F$ is plotted in Fig. 8.6, clearly revealing a Fermi-edge singularity for small values of $\Delta_s$. That phases of RKKY mediated nuclear spin polarization and superconductivity can coexist is already known from bulk metals at microkelvin temperatures [22], where coexisting phases could be even observed in alloys of simple metals. This offers an exciting new possbility to induce a topological phase transition in a 1D conductor. Due to the smallness of nuclear magnetic moments, $T_c$ is expected to be so low, that once full nuclear-order is established, the system ends up deep in the topological

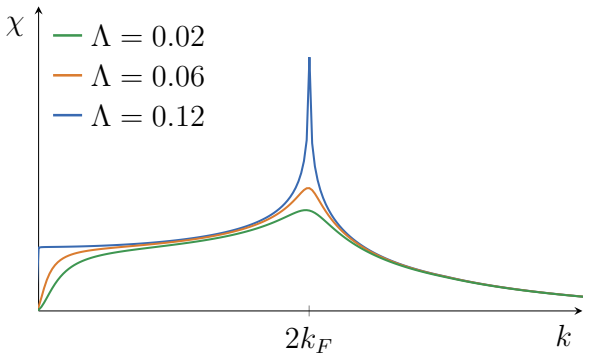


Figure 8.6: **1D electron spin susceptibility**. Static electron spin susceptibility plotted versus $k$ for different values of $\Lambda = \mu_F/\Delta_s$. The Fermi edge singularity (sharp peak at $2k_F$) is recovered for large values of $\Lambda$.

phase as a ground-state, without further tuning of the chemical potential required [228]. Majorana zero modes (MZMs) should appear at the ends of the wire once superconductivity is induced in the helical nuclear magnet. Inducing a topological phase transition in a nanowire with nuclear-spin ordering raises some additional boundary conditions: The system has to maintain the Ruderman-Kittel interaction in the presence of superconductivity which is possible as long $\Delta_m > \Delta_s$, with the induced superconducting gap $\Delta_s$. The system becomes gapless at $\Delta_m = \Delta_s$, marking the closing and opening of an energy gap and thus a transition between a topological phase and a non topological phase [161]. The electron temperature plays a decisive role, apart from only stabilizing the Ruderman-Kittel interaction, but deciding wether the system can tune itself into the topological phase or not [222]. An occupation of states on the edge of the helical gap in the presence of particle-hole symmetry is equal to a gap-closing and thus a phase transition to a non-topological phase. In order to prevent this, the thermal budget should be low enough that states on the edges of the smallest gap in the system (which has to be $\Delta_s$) can not be occupied. This raises $kT_c \ll \Delta_s$ as a condition for a self-tuning topological phase. This is not satisfied for most of the proposals for helical magnetic superconductors based on small gap superconductors and localized moments of electronic paramagnets, but should always hold well for nuclear spins as localized magnetic moments.

If conduction electrons are transmitted into a superconducting contact via the one-dimensional helical channel, Andreev-reflection is supressed and thus also the subgap current. This allows an identification of a helical state by conduction supression instead of the measurement of finite conductance, which can be cumbersome if ballistic conductance is affected by poor contacts or disorder. Superconductivity in the wire switches the conductance reduction of $2e^2/h$ to $e^2/h$ to $4e^2/h$ and zero in the helical regime. If a supercurrent can be observed at higher temperatures at zero magnetic field and drops to zero when the temperature is reduced below the nuclear Curie temperature, it would be a clear signature of a helical state in the nanowire. Furthermore, it is expected that signatures of a topological phase in the superconductor are also expected to appear in the full ballistic regime [229]. If the superconductor is in the topological phase the con-

ductance due to Andreev-reflection should not be supressed anymore but show a value of $2e^2/h$ which is a topological invariant and thus ivariant to the effects of disorder.

From all semiconductor materials available as sufficient quality nanowires, InSb and InAs are especially suited for inducing helical nuclear spin order. In has a very high nuclear magnetic moment ($I = 9/2$, $\mu = 5.5\mu_n$ whereas strong hyperfine interaction ($A_0 =$ 0.11 meV [230], $\kappa = 0.09$ K s [9]) which provides $\Delta_m \approx 0.3 - 0.5$ meV and $T_C \approx 7$ mK for $\mu_F = 1$ meV. GaAs is beneficial in terms of carrier mobility, with $A_0 = 0.09$ meV and $I = 3/2$ for GaAs, one arrives at $T_C \sim 800$ µK and a helical gap of $\Delta_m \sim 0.1 - 0.2$ meV. Thus, tuning a GaAs 1D conductor into the helical regime (without effects of electron correlations), would require microkelvin refrigeration. For inducing superconductivity, Al ($\Delta_s \approx 0.2$ meV) is a suitable candidate. Al is the state of the art material in Majorana devices based on semiconductor nanowires and epitaxially grown shells on InAs give hard induced gaps close to the bulk value [231]. In 2DEGs the induced gap can be further reduced by tuning the tunnel coupling between superconductor and semiconductor, which could also be interesting for this application. Here no restrictions have to be made with respect to field compatibility which allows the use of thick epitaxial shells. It should be generally favorable to tune the chemical potential high because local charges are screened due to a higher carrier density and the Ruderman-Kittel interaction is stabilized in the presence of superconductivity. Thus, thinner wires with a stronger confinement are interesting, which allow for a larger tuning range of the chemical potential and furthermore enhance repulsive electron-electron interactions. Due to the self-tuning effect the "masking" of the helical gap due to gradients in the electrostatic potential along the channel [232] should be less pronounced, providing beneficial conditions for observing experimental signatures of helical transport. Rashba spin-orbit interaction is not expected to destabilize helical nuclear spin order once established [222].

## 8.3. FURTHER OPPORTUNITIES OF MICROKELVIN PHYSICS



The possibility to reach sub 1 mK electron temperatures in miniaturized structures is expected to provide a platform for discovery of new physical phenomena on the mesoscopic scale but also to enable improvements in established nanoelectronic device technologies. Full-nuclear spin polarization by Ruderman-Kittel interaction without an external magnetic field could be reached in GaAs two-dimensional electron gases at temperatures between 0.1 - 1 mK [217], depending on the strength of electron-electron interactions (The same physics leading to helical nuclear spin ordering in 1D nuclear paramagnets were discussed in the foregoing section). In such a system, thermal fluctuations of the Overhauser field are fully suppressed, offering interesting possibilities for e.g. localized spin devices. The error rate of various quantum devices, including single electron charge pumps [233, 234] and superconducting quantum circuits [235] could improve by more effective thermalization of the charge carriers. Other interestic possibilites are the study of novel electronic states as topological ordered states [158] or p-wave superconductivity [159], limits of quantum coherence in solid state devices on the macroscopic scale [236], spatial phase coherence of charge charriers [24]. Apart from known physics, reducing thermal excitations to yet unreached energy scales may reveal completely unexpected physical phenomena on the miniaturized scale.

## 8.4. SUMMARY OF THE WORK AND CONCLUDING REMARKS

Chipscale nuclear cooling of a nanoelectronic device was implemented and studied, with the aim of developing a scalable microkelvin refrigeration technique for miniaturized electronic devices. Electrodeposition of thick In films onto the islands of a Coulomb blockade thermometer (CBT) and performing the nuclear magnetic cooling cycle on-chip provided electron temperatures down to 3.2 mK with short hold times, as in previous on-cip nuclear cooling attempts (section 4.6). For overcoming parasitic heating limitations, a novel scheme of nuclear cooling of the device leads with a parallel set of In nuclear stages, involving thermalization over thin, insulating films (section 3.3.3, section 6.4) was implemented. On- and off chip nuclear cooling resulted in a record low temperature of $421 \pm 35$ μK and hold time below 1 mK of more than 80 h. Finite bias transport down to 470 μK demonstrated the viability and successful implementation of a microkelvin refrigeration technique for transport experiments. A systematic study of the nuclear magnetic properties of the In microrefrigerators revealed non-equidistant nuclear eigenenergies dominated by electric quadrupole splitting, in agreement with nuclear quadrupole resonance studies of bulk In. This implies, in combination with the nuclear cooling performance obtained on-chip, a successful utilization of higher order nuclear multipole moments for nuclear refrigeration as a key to a stable and scalable microkelvin refrigeration technique for nanoelectronic circuits.

This work also provided new insights into the thermal charging of single-electronic circuits in the presence of island offset charge. By implementing a Markov-chain Monte-Carlo algorithm for modeling linear arrays of tunnel junctions the limits of universal regime of charging for Coulomb blockade thermometry were redefined. It was shown that the offset-charge stability of tunnel junction arrays extends the thermometer range of CBTs far below previously accepted limits. Offset-charge insensitive Coulomb blockade thermometry was demonstrated beyond previously accepted temperature limits by fitting CBT charging curves, obtained at microkelvin temperatures with the MCMC model and without a recalibration of the device. With the outcome of this work Coulomb blockade thermometry currently stands out as the only nanoelectronic thermometry technique for which thermometry in the microkelvin temperature scale is documented.



The outcome of the work is a microkelvin refrigeration technique for nanoelectronic circuits, readily applicable to various device technologies. If applied to microkelvin refrigeration of semiconductor nanoelectronics, several emerging fields of solid state quantum electronics should profit significantly from this new technological possibility. Here, microkelvin refrigeration is especially expected to provide new opportunities for the novel field of topological quantum computation. But apart from known solid-state phenomena, microkelvin cooling on the miniaturized scale could also result in unexpected discoveries: new physical discoveries like superconductivity or the quantum Hall effect were often made right after a new, unexplored temperature regime was opened. While bulk materials are already well studied at microkelvin temperatures, the submillikelvin temperature scale is a fully unexplored regime for nanoscale systems. With the knowledge that many exotic states of solid matter are only appearing in low-dimensional electron systems, there is surely still plenty of room at the bottom for microkelvin physics.

# 9

# BIBLIOGRAPHY


[1] H. Kammerlingh Onnes, *On the Change of Electric Resistance of Pure Metals at very Low Temperatures IV: The Resistance of Pure Mercury at Helium Temperatures,* Comm. Phys. Lab. Univ. Leiden (1911).

[2] H. Kammerlingh Onnes, *On the Change of Electric Resistance of Pure Metals at very Low Temperatures V: The Dissapearance of the Resistance of Mercury,* Comm. Phys. Lab. Univ. Leiden (1911).

[3] H. Kammerlingh Onnes, *On the Change of Electric Resistance of Pure Metals at very Low Temperatures VI: On the Sudden Change in the Rate at which the Resistance of Mercury Dissapears,* Comm. Phys. Lab. Univ. Leiden (1911).

[4] S. Balibar, *The Discovery of Superfluidity,* J. Low Temp. Phys. **146**, 441 (2007).

[5] C. Kittel, *Einführung in die Festkörperphysik*, 14th ed. (Oldenbourg, 2004).

[6] P. Debye, *Einige Bemerkungen Zur Magnetisierung bei Tiefer Temperatur,* Annalen der Physik **386**, 1154 (1926).

[7] W. Giauque, *Thermodynamic Treatment of Certain Magnetic Effects: A Proposed Method of Producing Temperatures Considerably Below 1 Degree Absolute,* J. Am. Chem. Soc. **49**, 1864 (1927).

[8] R. Hudson, *Principles and Application of Magnetic Cooling*, Vol. 1 (North-Holland, 1972).

[9] F. Pobell, *Matter and Methods at Low Temperatures*, 3rd ed. (Springer, 2006).

[10] O. Lounasmaa, *Experimental Principles and Methods Below 1 K*, Vol. 1 (Academic, 1974).

[11] D. Betts, *Refrigeration and Thermometry Below One Kelvin*, Vol. 1 (Sussex University Press, 1989).

[12] K. von Klitzing, G. Dorda, and M. Pepper, *New Method for High-Accuracy Determination of the Fine-Structure Constant Based on Quantized Hall Resistance,* Phys. Rev. Lett. **45**, 494 (1980).

[13] N. Kurti, F. H. Robinson, F. Simon, and D. Spohr, *Nuclear Cooling,* Nature **178**, 450 (1956).

[14] E. Ambler and R. Hudson, *Magnetic Cooling,* Reports on Progress in Physics **18**, 251 (1955).

[15] P. Debye, *Abkühlung Durch Adiabatische Entmagnetisierung,* Annalen der Physik **32**, 85 (1938).

[16] C. J. Gorter, *Kernentmagnetisierung,* Phys. Z. **35**, 923 (1934).

[17] F. Pobell, *Fortschritte auf dem Weg zum Absoluten Nullpunkt,* Phys. Bl. **36**, 176 (1980).

[18] R. Müller, C. Buchal, H. Folle, M. Kubota, and F. Pobell, *Refrigeration into the Microkelvin Range,* Phys. Lett. **75A**, 164 (1980).

[19] G. Pickett, *Cooling Metals to the Microkelvin Regime, Then and Now,* Physica B **280**, 467 (2000).

[20] K. Andres and O. Lounasmaa, *Recent Progress in Nuclear Cooling*, Vol. 8 (Elsevier, 1982).

[21] A. Oja and O. Lounasmaa, *Nuclear Magnetic Ordering in Simple Metals at Positive and Negative Nanokelvin Temperatures,* Rev. Mod. Phys. **69** (1997).

[22] T. Herrmannsdörfer, S. Rehmann, M. Seibold, and F. Pobell, *Das Wechselspiel von Kernmagnetismus und Supraleitung,* Physikalische Blätter **53**, 987 (1997).

[23] T. Knuuttila, J. Tuoriniemi, K. Lefmann, K. Juntunen, F. Rasmussen, and K. Nummila, *Polarized Nuclei in Normal and Superconducting Rhodium,* Journal of Low Temperature Physics **123**, 65 (2001).

[24] G. Pickett and C. Enss, *The European Microkelvin Platform,* Nature Reviews Materials **3**, 18012 (2018).

[25] M. Nielsen and I. Chuang, *Quantum Computation and Quantum Information*, Vol. 1 (Cambridge University Press, 2000).

[26] D. Deutsch, *Quantum Theory, the Church-Turing Principle and the Universal Quantum Computer,* Proc. R. Soc. London, Ser A **400**, 97 (1985).

[27] R. Feynman, *Quantum Mechanical Computers,* Found. Phys. **16**, 507 (1986).

[28] P. Shor, *Polynomial-Time Algorithms for Prime Factorization and Discrete Logarithms on a Quantum Computer,* Journal of Computing **26**, 1484 (1997).

[29] J. Clarke and F. Wilhelm, *Superconducting Quantum Bits,* Nature **453**, 1031 (2008).

[30] D. Rosenberg, D. Kim, R. Das, D. Yost, S. Gustavsson, D. Hover, P. Krantz, A. Melville, L. Racz, G. O. Samach, S. J. Weber, F. Yan, J. L. Yoder, A. J. Kerman, and W. D. Oliver, *3D Integrated Superconducting Qubits,* npj Quantum Information **3**, 42 (2017).

[31] X. Liu and M. Hersam, *2D Materials for Quantum Information Science,* Nature Reviews Materials **4**, 669 (2019).

[32] H. Engel, L. Kouwenhoven, D. Loss, and C. Marcus, *Controlling Spin Qubits in Quantum Dots,* Quantum Information Processing **3**, 115 (2004).

[33] S. Das Sarma, M. Freedman, and C. Nayak, *Topologically Protected Qubits from a Possible Non-Abelian Fractional Quantum Hall State,* Phys. Rev. Lett. **94**, 166802 (2005).

[34] C. Nayak, S. Simon, A. Stern, M. Freedman, and S. Das Sarma, *Non-Abelian Anyons and Topological Quantum Computation,* Rev. Mod. Phys. **80**, 1083 (2008).

[35] A. Stern, *Non-Abelian States of Matter,* Nature **464**, 187 (2010).

[36] S. Das Sarma, M. Freedman, and C. Nayak, *Majorana Zero Modes and Topological Quantum Computation,* NPJ Quantum Information **1**, 15001 (2015).

[37] J. W. Ekin, *Experimental Techniques for Low-Temperature Measurements* (Oxford, 2006).

[38] G. Ventura and L. Risegari, *The Art of Cryogenics* (Elsevier, 2008).

[39] G. Ebert, K. von Klitzing, C. Probst, E. Schuberth, K. Ploog, and G. Weimann, *Hopping Conduction in the Landau-Level Tails in GaAs-AlGaAs Heterostructures at Low Temperatures,* Solid State Commun. **45**, 625 (1983).

[40] A. Feshchenko, L. Casparis, I. Khaymovich, D. Maradan, O. Saira, M. Palma, M. Meschke, J. Pekola, and D. Zumbühl, *Tunnel-Junction Thermometry down to Millikelvin Temperatures,* Phys. Rev. Appl. **4**, 034001 (2015).

[41] F. Wellstood, C. Urbina, and J. Clarke, *Hot-Electron Effects in Metals,* Phys. Rev. B **49**, 5942 (1994).

[42] M. Meschke, J. Pekola, F. Gay, R. Rapp, and H. Godfrin, *Electron Thermalization in Metallic Islands Probed by Coulomb Blockade Thermometry,* J. Low Temp. Phys. **134**, 1119 (2004).

[43] J. Xia, E. Adams, V. Shvarts, W. Pan, H. Stormer, and D. Tsui, *Ultra-Low Temperature Cooling of Two-Dimensional Electron Gas,* Physica B: Condensed Matter **280**, 491 (2000).

[44] L. Casparis, M. Meschke, D. Maradan, A. C. Clark, C. P. Scheller, K. K. Schwarzwälder, J. P. Pekola, and D. Zumbühl, *Metallic Coulomb Blockade Thermometry Down to 10 mK and Below,* Rev. Sci. Instr. **83**, 083903 (2012).

[45] D. Bradley, A. Guénault, D. Gunnarsson, R. Haley, S. Holt, A. Jones, Y. A. Pashkin, J. Penttilä, J. Prance, M. Prunnila, and L. Roschier, *On-Chip Magnetic Cooling of a Nanoelectronic Device,* Scientific Reports **7**, 45566 (2017).

[46] D. Bradley, R. George, D. Gunnarsson, R. Haley, H. Heikkinen, Y. Pashkin, J. Penttilä, J. Prance, M. Prunnila, L. Roschier, and M. Sarsby, *Nanoelectronic Primary Thermometry below 4 mK,* Nature communications **7**, 10455 (2016).

[47] M. Palma, C. Scheller, D. Maradan, A. Feshchenko, M. Meschke, and D. Zumbühl, *On-and-off Chip Cooling of a Coulomb Blockade Thermometer Down to 2.8 mK,* Appl. Phys. Lett. **111**, 253105 (2017).

[48] G. Nicoli, P. Märki, B. Bräm, M. Röösli, S. Hennel, A. Hofmann, C. Reichl, W. Wegscheider, T. Ihn, and K. Ensslin, *Quantum Dot Thermometry at Ultralow Temperature in a Dilution Refrigerator with a $^4$He Immersion Cell,* arXiv **1909.10906** (2019).

[49] R. Willett, J. Eisenstein, L. Störmer, D. Tsui, A. Gossard, and J. English, *Observation of an Even-Denominator Quantum Number in the Fractional Quantum Hall Effect,* Phys. Rev. Lett. **59**, 1776 (1987).

[50] D. Cousins, S. Fisher, A. Guénault, R. Haley, I. Miller, G. Pickett, G. Plenderleith, P. Skyba, P. Thibault, and M. Ward, *An Advanced Dilution Refrigerator Designed for the New Lancaster Microkelvin Facility,* J. Low Temp. Phys. **114**, 547 (1999).

[51] G. Frossati, *Experimental Techniques - Methods for Cooling Below 300 mK,* J. Low Temp. Phys. **87**, 595 (1992).

[52] G. Vermeulen and G. Frossati, *Powerful Dilution Refrigerator for Use in the Study of Polarized Liquid $^3$He and Nuclear Cooling,* Cryogenics **27**, 139 (1986).

[53] A. C. Clark, K. K. Schwarzwälder, T. Bandi, D. Maradan, and D. M. Zumbühl, *Method for Cooling Nanostructures to Microkelvin Temperatures,* Review of Scientific Instruments **81**, 103904 (2010).

[54] G. Batey, A. Casey, M. N. Cuthbert, A. J. Matthews, J. Saunders, and A. Shibahara, *A Microkelvin Cryogen-Free Experimental Platform with Integrated Noise Thermometry,* New Journal of Physics **15**, 113034 (2013).

[55] F. Giazotto, T. Heikkilä, A. Luukanen, A. Savin, and J. Pekola, *Opportunities for Mesoscopics in Thermometry and Refrigeration: Physics and Applications,* Rev. Mod. Phys. **78**, 217 (2006).

[56] J. P. Pekola, K. P. Hirvi, J. P. Kauppinen, and M. Paalanen, *Thermometry by Arrays of Tunnel Junctions,* Phys. Rev. Lett. **73**, 2903 (1994).

[57] S. Farhangfar, K. Hirvi, J. Kauppinen, J. Pekola, and J. Toppari, *One Dimensional Arrays and Solitary Tunnel Junctions in the Weak Coulomb Blockade Regime: CBT Thermometry,* J. Low Temp. Phys. **108**, 191 (1997).

[58] B. van Wees, H. van Houten, C. Beenakker, J. Williamson, L. Kouwenhoven, D. van der Marel, and C. Foxon, *Quantized Conductance of Point Contacts in a Two-Dimensional Electron Gas,* Phys. Rev. Lett. **60**, 848 (1988).

[59] J. Pendry, *Quantum Limits to the Flow of Information and Entropy,* J. Phys. A: Math. Gen. **16**, 2161 (1982).

[60] S. Jezouin, F. Parmentier, A. Anthore, U. Gennser, A. Cavanna, Y. Jin, and F. Pierre, *Quantum Limit of Heat Flow Across a Single Electronic Channel,* Science **342**, 601 (2013).

[61] O. Chiatti, J. Nicholls, Y. Proskuryakow, N. Lumpkin, I. Farrer, and D. Ritchie, *Quantum Thermal Conductance of Electrons in a One-Dimensional Wire,* Phys. Rev. Lett. **97**, 056601 (2006).

[62] M. Meschke, W. Guichard, and J. Pekola, *Single-Mode Heat Conduction by Photons,* Nature **444**, 187 (2006).

[63] M. Banerjee, M. Heiblum, A. Rosenblatt, Y. Oreg, D. Feldman, A. Stern, and V. Umansky, *Observed Quantization of Anyonic Heat Flow,* Nature **545**, 75 (2017).

[64] A. Timofeev, M. Helle, M. Meschke, M. Möttönen, and J. Pekola, *Electronic Refrigeration at the Quantum Limit,* Phys. Rev. Lett. **102**, 200801 (2009).

[65] K. Schwab, E. Henriksen, J. Worlock, and M. Roukes, *Measurement of the Quantum of Thermal Conductance,* Nature **404**, 974 (2000).

[66] E. Swartz and R. Pohl, *Thermal Boundary Resistance,* Rev. Mod. Phys. **61**, 605 (1989).

[67] L. Wang, O. Saira, D. Golubev, and J. Pekola, *Crossover Between Electron-Phonon and Boundary Resistance Limited Thermal Relaxation in Copper Films,* arXiv **1903.10848** (2019).

[68] M. Dixon, F. Hoare, T. Holden, and D. Moody, *The Low-Temperature Specific Heats of Some Pure Metals,* Proc. Roy. Soc. A **285**, 561 (1965).

[69] R. Kautz, G. Zimmerli, and J. Martinis, *Self-Heating in the Coulomb Blockade Electrometer,* J. Appl. Phys. **73**, 2386 (1993).

[70] L. Isaacs, *Low-Temperature Specific Heat of Gold, Silver and Copper,* J. Chem. Phys. **43**, 307 (1965).

[71] A. Steinbach, J. Martinis, and M. Devoret, *Observation of Hot-Electron Shot Noise in a Metallic Resistor,* Phys. Rev. Lett. **76**, 3806 (1996).

[72] P. Echternach, M. Thoman, C. Gould, and H. Bozler, *Electron-Phonon Scattering Rates in Disordered Metallic Films below 1 K,* Phys. Rev. B **46**, 10339 (1992).

[73] H. O Neal and N. Phillips, *Low-Temperature Heat Capacities of Indium and Tin,* Phys. Rev. **137**, 748 (1964).

[74] S. Qu, A. Cleland, and M. Geller, *Hot Electrons in Low-Dimensional Phonon Systems,* Phys. Rev. B **72**, 224301 (2005).

[75] J. Liu and N. Giordano, *Electron-Phonon Scattering Times in Thin Sb Films,* Phys. Rev. B **43**, 3928 (1991).

[76] J. DiTusa, K. Lin, M. Park, M. Isaacson, and J. Parpia, *Finite-Size Effects in the Low-Temperature Resistivity of CuCr Films,* Phys. Rev. Lett. **68**, 678 (1992).

[77] D. Schmidt, R. Schoelkopf, and A. Cleland, *Photon-Mediated Thermal Relaxation of Electrons in Nanostructures,* Phys. Rev. Lett. **93**, 045901 (2004).

[78] J. Muhonen, M. Meschke, and J. Pekola, *Micrometre-Scale Refrigerators,* Rep. Prog. Phys. **75**, 046501 (2012).

[79] J. Korringa, *Nuclear Magnetic Relaxation and Resonance Line Shifts in Metals,* Physica **16**, 601 (1950).

[80] D. MacLaughlin and J. Williamson, *Nuclear Spin-Lattice Relaxation in Pure and Impure Indium - Normal State,* Phys. Rev. B **4**, 60 (1971).

[81] L. Pollack, E. Smith, J. Parpia, and R. Richardson, *Determination of the Electric Field Gradient and Relaxation Time Measurements in Scandium Metal at Very Low Temperature,* J. Low Temp. Phys. **87**, 753 (1992).

[82] D. MacLaughlin and J. Butterworth, *Nuclear Spin-Lattice Relaxation in Indium Metal by NQR,* Phys. Lett. **23**, 291 (1966).

[83] M. Nahum, T. Eiles, and J. Martinis, *Electronic Microrefrigerator Based on Normal-Insulator-Superconductor Tunnel Junction,* Appl. Phys. Lett. **65**, 3123 (1994).

[84] M. Leivo, J. Pekola, and D. Averin, *Efficent Peltier Refrigeration by a Pair of Normal Metal-Insulator-Superconductor Junctions,* Appl. Phys. Lett. **68**, 1996 (1996).

[85] A. Savin, M. Prunnila, P. Kivinen, J. Pekola, J. Ahopelto, and A. Manninen, *Efficient Electronic Cooling in Heavily Doped Silicon by Quasiparticle Tunneling,* Appl. Phys. Lett. **79**, 1471 (2001).

[86] A. Savin, M. Prunnila, J. Ahopelto, J. Kivinen, P. Törmä, and J. Pekola, *Application of Superconductor-Semiconductor Schottky Barrier for Electron Cooling,* Physica B **1481**, 329 (2003).

[87] E. Mykkänen, J. Lehtinen, L. Grönberg, A. Shchepetov, A. Timofeev, D. Gunnarson, A. Kemppinen, A. Manninen, and M. Prunnila, *Thermionic Junction Devices Utilizing Phonon Blocking,* Science Advances **6** (2020).

[88] H. Nguyen, M. Meschke, H. Courtois, and J. Pekola, *Sub-50 mK Electronic Cooling with Large-Area Superconducting Tunnel Junctions,* Phys. Rev. Appl. **2**, 054001 (2004).

[89] J. Pekola, J. Koski, and D. Averin, *Refrigerator Based on the Coulomb Barrier for Single-Electron Tunneling,* Phys. Rev. B **89**, 081309 (2014).

[90] A. Feshchenko, J. Koski, and J. Pekola, *Experimental Realization of a Coulomb Blockade Refrigerator,* Phys. Rev. B **90**, 201407 (2014).

[91] H. Edwards, Q. Niu, and A. de Lozanne, *Quantum Dot Refrigerator,* Appl. Phys. Lett. **63**, 1815 (1993).

[92] H. Edwards, Q. Niu, G. Georgakis, and A. de Lozanne, *Cryogenic Cooling Using Tunneling Structures with Sharp Energy Features,* Phys. Rev. B **52**, 5714 (1995).

[93] J. Prance, C. Smith, J. Griffiths, S. Chorley, D. Anderson, G. Jones, I. Farrer, and D. Ritchie, *Electronic Refrigeration of a Two-Dimensional Electron Gas,* Phys. Rev. Lett. **102**, 146602 (2009).

[94] F. Dolcini and F. Giazotto, *Adiabatic Magnetization of Superconductors as a High-Performance Cooling Mechanism,* Phys. Rev. B **80**, 024503 (2009).

[95] S. Manikandan, F. Giazotto, and N. Jordan, *Superconducting Quantum Refrigerator - Breaking and Rejoining Cooper Pairs with Magnetic Field Cycles,* Phys. Rev. Appl. **11**, 054034 (2019).

[96] B. Suits, *Nuclear Quadrupole Resonance Spectroscopy, Chapter 2 in Handbook of Applied Solid State Spectroscopy*, Vol. 1 (Springer, 2006).

[97] R. Hollingworth and S. Hacobian, *The Theory of the Nuclear Quadrupole Interaction in Terms of Irreducible Tensors,* Aust. J. Chem. **25**, 683 (1972).

[98] K. Andres, *Hyperfine Enhanced Nuclear Magnetic Cooling,* Cryogenics **18**, 473 (1978).

[99] A. Anderson and A. Redfield, *Nuclear Spin-Lattice Relaxation in Metals,* Phys. Rev. **116**, 583 (1959).

[100] L. Pollack, E. Smith, R. Mihailovich, J. Ross, P. Hakonen, E. Varoquaux, J. Parpia, and R. Richardson, *NQR Studies of Scandium Metal at Low Temperatures,* Physica B **165**, 793 (1990).

[101] R. Barnes, F. Borsa, S. Segel, and D. Torgeson, *Knight Shift Anisotropy in Scandium and Yttrium and Nuclear Quadrupole Coupling in Scandium,* Phys. Rev. **137**, 1828 (1964).

[102] J. Ross, F. Fradin, L. Isaacs, and D. Lam, *Magnetic and Nuclear-Resonance Properties of Single-Crystal Scandium,* Phys. Rev. **183**, 645 (1969).

[103] R. Hewitt and W. Knight, *Nuclear Quadrupole Resonance in Metallic Indium,* Phys. Rev. Lett. **3**, 18 (1959).

[104] W. Simmons and C. Slichter, *Nuclear Quadrupole Absorption in Indium Metal,* Phys. Rev. **121**, 1580 (1961).

[105] E. Genio, J. Xu, T. Lang, G. Ihas, and N. Sullivan, *Nuclear Spin-Lattice Relaxation Times of Metallic Antimony at Low Temperatures,* J. Low Temp. Phys. **101**, 611 (1995).

[106] R. Hewitt and D. MacLaughlin, *Nuclear Spin Relaxation in the Quadrupole Spectrum of Antimony Metal,* J. Magn. Reson. **30**, 483 (1978).

[107] A. Narath, *Nuclear Magnetic Resonance in Hexagonal Lanthanum Metal: Knight Shifts, Spin Relaxation Rates, and Quadrupole Coupling Constants,* Phys. Rev. **179**, 359 (1968).

[108] G. Ashton, D. Hsu, and R. Leisure, *Direct Acoustical Measurement of Nuclear Spin-Lattice Relaxation Times: Application to Aluminum and Tantalum,* Phys. Rev. B **23**, 5681 (1981).

[109] C. Dimitropoulos, M. Maglione, and F. Borsa, *Nuclear Magnetic and Quadrupole Resonance in Metallic Powders in the Presence of Strong Quadrupole Interaction - Rhenium Metal,* Phys. Rev. B **37**, 3159 (1988).

[110] C. Dimitropoulos and J. Bucher, *Nuclear Magnetic and Quadrupole Resonance in Metallic Powders in the Presence of Strong Quadrupole Interaction - Rhenium Metal,* Phys. Rev. B **39**, 7232 (1989).

[111] P. Gregers-Hansen, M. Krusius, and G. Pickett, *Sign of the Nuclear Quadrupole Interaction in Rhenium Metal,* Phys. Rev. Lett. **27**, 38 (1971).

[112] H. Collan, M. Krusius, and G. Pickett, *Suppression of the Nuclear Heat Capacity in Bismuth Metal by very slow Spin-Lattice Relaxation and a new Value for the Electronic Specific Heat,* Phys. Rev. Lett. **23**, 11 (1969).

[113] T. Bastow and H. Whitfield, *Nuclear Quadrupole Resonance in Arsenic and Bismuth Metal,* Solid State Commun. **18**, 955 (1976).

[114] S. Satoh, Y. Kitaoka, H. Yasuoka, S. Takayanagi, and T. Sugawara, *Spin-Echo Studies of $^{141}Pr$ Nuclear Relaxation in a Singlet Ground State System $Pr_{1-x}La_xIn_3$,* J. Phys. Soc. Jpn. **50**, 351 (1980).

[115] Y. Karaki, Y. Koike, M. Kubota, H. Ishimoto, and Y. Onuki, *Nuclear Magnetism of $PrIn_3$,* Czechoslovak Journal of Physics **46**, 2209 (1996).

[116] R. Müller, C. Buchal, H. Folle, M. Kubota, and F. Pobell, *A Double-Stage Nuclear Demagnetization Refrigerator,* Cryogenics **20**, 395 (1980).

[117] H. Ishimoto, N. Nishida, T. Furubayashi, M. Shinohara, Y. Takano, Y. Miura, and K. Ono, *Two-Stage Nuclear Demagnetization Refrigerator Reaching 27 μK,* J. Low Temp. Phys. **55**, 17 (1984).

[118] K. Gloos, P. Smeibidl, C. Kennedy, A. Singsaas, P. Sekowski, R. Müller, and F. Pobell, *The Bayreuth Nuclear Demagnetization Refrigerator,* J. Low Temp. Phys. **73**, 101 (1988).

[119] S. Wiegers, T. Hata, C. Kranenburg, P. van de Haar, R. Jochemsen, and G. Frossati, *Compact $PrNi_5$ Nuclear Demagnetization Cryostat,* Cryogenics **30**, 770 (1990).

[120] W. Yao, T. Knuuttila, K. Nummila, J. Martikainen, A. Oja, and O. Lounasmaa, *A Versatile Nuclear Demagnetization Cryostat for Ultralow Temperature Research,* J. Low Temp. Phys. **120**, 121 (2000).

[121] D. Nguyen, A. Sidorenko, M. Müller, S. Paschen, A. Waard, and G. Frossati, *The Vienna Nuclear Demagnetization Refrigerator,* J. Phys.: Conf. Ser. **400**, 052024 (2012).

[122] I. Todoshchenko, J. Kaikkonen, R. Blaauwgeers, P. Hakonen, and A. Savin, *Dry Demagnetization Cryostat for Sub-Millikelvin Helium Experiments: Refrigeration and Thermometry,* Rev. Sci. Instr. **85**, 085106 (2014).

[123] J. Rowell and D. Tsui, *Hot Electron Temperature in InAs Measured by Tunneling,* Phys. Rev. B **14**, 2456 (1976).

[124] B. Karimi and J. Pekola, *Noninvasive Thermometer Based on the Zero-Bias Anomaly of a Superconducting Junction for Ultrasensitive Calorimetry,* Phys. Rev. Appl. **10**, 054048 (2018).

[125] D. Maradan, L. Casparis, T. Liu, D. Biesinger, C. Scheller, D. Zumbühl, J. Zimmermann, and A. Gossard, *GaAs Quantum Dot Thermometry Using Direct Transport and Charge Sensing,* J. Low Temp. Phys. **175**, 784 (2014).

[126] T. Ihn, *Semiconductor Nanostructures*, 1st ed. (Oxford, 2009).

[127] A. Rossi, T. Ferrus, and D. Williams, *Electron Temperature in Electrically Isolated Si Double Quantum Dots,* Appl. Phys. Lett. **100**, 133503 (2012).

[128] A. Mavalankar, S. Chorley, J. Griffiths, G. Jones, I. Farrer, D. Ritchie, and C. Smith, *A Non-Invasive Electron Thermometer Based on Charge Sensing of a Quantum Dot,* Appl. Phys. Lett. **103**, 133116 (2013).

[129] P. Torresani, M. Martinez-Perez, S. Gasparinetti, J. Renard, G. Biasiol, L. Sorba, F. Giazotto, and D. Franceschi, *Nongalvanic Primary Thermometry of a Two-Dimensional Electron Gas,* Phys. Rev. B **88**, 245304 (2013).

[130] L. Spietz, K. Lehnert, I. Siddiqi, and R. Schoelkopf, *Primary Electronic Thermometry Using the Shot Noise of a Tunnel Junction,* Science **300**, 1929 (2003).

[131] Z. Iftikhar, A. Anthore, S. Jezouin, F. D. Parmentier, Y. Jin, A. Cavanna, A. Ouerghi, U. Gennser, and F. Pierre, *Primary Thermometry Triad at 6 mK in Mesoscopic Circuits,* Nature Communications **7**, 12908 (2016).

[132] A. Feshchenko, M. Meschke, D. Gunnarsson, M. Prunnila, L. Roschier, J. Penttilá, and J. Pekola, *Primary Thermometry in the Intermediate Coulomb Blockade Regime,* Journal of Low Temperature Physics **173**, 36 (2013).

[133] M. Meschke, J. Engert, D. Heyer, and J. Pekola, *Comparison of Coulomb blockade Thermometers with the International Temperature Scale PLTS-2000,* International Journal of Thermophysics **32**, 1378 (2011).

[134] J. P. Pekola, J. Toppari, J. Kauppinen, K. Kinnunen, A. Manninen, and A. Jansen, *Coulomb Blockade-Based Nanothermometry in Strong Magnetic Fields,* Journal of Applied Physics **83**, 5582 (1998).

[135] M. Meschke, A. Kemppinen, and J. Pekola, *Accurate Coulomb Blockade Thermometry up to 60 K,* Phil. Trans. R. Soc. A **374**, 20150052 (2016).

[136] T. Bergsten, T. Claeson, and P. Delsing, *A Fast, Primary Coulomb Blockade Thermometer,* Appl. Phys. Lett. **78**, 1264 (2001).

[137] O. Hahtela, E. Mykkänen, A. Kemppinen, M. Meschke, M. Prunnila, D. Gunnarson, L. Roschier, J. Penttilä, and J. Pekola, *Traceable Coulomb Blockade Thermometry,* Metrologia **54**, 69 (2017).

[138] C. Wasshuber, *Computational Single-Electronics*, 1st ed. (Springer, 2001).

[139] K. Likharev, *Single-Electron Devices and Their Applications,* Proceedings of the IEEE **87**, 606 (1999).

[140] J. Niemeyer, *Eine einfache Methode zur Herstellung kleiner Josephson-Elemente,* PTB-Mitt. **84**, 251 (1974).

[141] M. Prunnila, M. Meschke, D. Gunnarson, S. Enouz-Vedrenne, J. Kivioja, and J. Pekola, *Ex-Situ Tunnel Junction Process Technique Characterized by Coulomb Blockade Thermometry,* J. Vac. Sci. Technol. B **28**, 1026 (2010).

[142] A. Brenner and S. Senderoff, *Calculation of Stress in Electrodeposits from the Curvature of a Plated Strip,* J. Res. Natl. Bur. Stand. **42**, 105 (1949).

[143] F. D'Heurle and J. Harper, *Note on the Origin of Intrinsic Stresses in Films Deposited via Evaporation and Sputtering,* Thin Solid Films **171**, 81 (1989).

[144] J. Thornton and D. Hoffman, *Stress-Related Effects in Thin Films,* Thin Solid Films **171**, 5 (1989).

[145] R. Koch, *The Intrinsic Stress of Polycrystalline and Epitaxial Thin Metal Films,* J. Phys.: Condens. Matter **6**, 9519 (1994).

[146] K. Gloos, P. Koppinen, and J. Pekola, *Properties of Native Ultrathin Aluminum Oxide Tunnel Barriers,* J. Phys.: Condens. Matter **15**, 1733 (2003).

[147] P. Koppinen, L. Väistö, and I. Maasilta, *Complete Stabilization and Improvement of the Characteristics of Tunnel Junctions by Thermal Annealing,* Appl. Phys. Lett. **90**, 053503 (2007).

[148] W. Rippard, A. Perella, F. Albert, and R. Buhrmann, *Ultrathin Aluminum Oxide Tunnel Barriers,* Phys. Rev. Lett. **88**, 046805 (2002).

[149] A. Toxen, *Size Effects in Thin Superconducting In Films,* Phys. Rev. **133**, 442 (1961).

[150] J. Puippe and N. Ibl, *Influence of Charge and Discharge of Electric Double Layer in Pulse Plating,* Journal of Applied Electrochemistry **10**, 775 (1980).

[151] R. M. Mueller, C. Buchal, T. Oversluizen, and F. Pobell, *Superconducting Aluminum Heat Switch and Plated Press-Contacts for Use at Ultralow Temperatures,* Review of Scientific Instruments **49**, 515 (1978).

[152] D. Glattli, P. Jacques, A. Kumar, P. Pari, and L. Saminadayar, *A Noise Detection Scheme with 10 mK Noise Temperature Resolution for Semiconductor Single Electron Tunneling Devices,* Journal of Applied Physics **81**, 7350 (1997).

[153] M. Thalmann, H.-F. Pernau, C. Strunk, E. Scheer, and T. Pietsch, *Comparison of Cryogenic Low-Pass Filters,* Review of Scientific Instruments **88**, 114703 (2017).

[154] D. Matsumoto, C. Reynolds, and A. Anderson, *Thermal Boundary Resistance at Metal-Epoxy Interfaces,* Phys. Rev. B **16**, 3303 (1977).

[155] V. Deshpande, M. Bockrath, L. Glazman, and A. Yacoby, *Electron Liquids and Solids in One Dimension,* Nature **464**, 209 (2010).

[156] B. Braunecker, P. Simon, and D. Loss, *Nuclear Magnetism and Electron Order in One-Dimensional Conductors,* Phys. Rev. B **80**, 165119 (2009).

[157] E. Chekhovich, M. Makhonin, A. Tartakovskii, A. Yacoby, H. Bluhm, K. Nowack, and L. Vandersypen, *Nuclear Spin Effects in Semiconductor Quantum Dots,* Nature materials **12**, 494 (2013).

[158] M. Hasan and C. Kane, *Colloquium: Topological Insulators,* Rev. Mod. Phys. **82**, 3045 (2010).

[159] A. Mackenzie and Y. Maeno, *The Superconductivity of* $Sr_2RuO_4$ *and the Physics of Spin-Triplet Pairing,* Rev. Mod. Phys. **75**, 657 (2003).

[160] M. Vojta, *Quantum Phase Transitions,* Rep. Prog. Phys. **66**, 2069 (2003).

[161] J. Klinovaja, P. Stano, A. Yazdani, and D. Loss, *Topological Superconductivity and Majorana Fermions in RKKY Systems,* Phys. Rev. Lett. **111**, 186805 (2013).

[162] O. Saira, A. Kemppinen, V. Maisi, and J. Pekola, *Vanishing Quasiparticle Density in a Hybrid Al/Cu/Al Single-Electron Transistor,* Phys. Rev. B **85**, 012504 (2012).

[163] N. Samkharadze, A. Kumar, M. Manfra, L. N. Pfeiffer, K. West, and G. Csáthy, *Integrated Electronic Transport and Thermometry at Millikelvin Temperatures and in Strong Magnetic Fields,* Review of Scientific Instruments **82**, 053902 (2011).

[164] T. A. Knuuttila, J. T. Tuoriniemi, and K. Lefmann, *Relaxation of Polarized Nuclei in Superconducting Rhodium,* Phys. Rev. Lett. **85**, 2573 (2000).

[165] C. Enss and S. Hunklinger, *Low-Temperature Physics*, Vol. 1 (Springer, 2005).

[166] O. Symko, *Nuclear Cooling Using Copper and Indium,* Journal of Low Temperature Physics **1**, 451 (1969).

[167] J. Xu, O. Avenel, J. S. Xia, M.-F. Xu, T. Lang, P. L. Moyland, W. Ni, E. D. Adams, G. G. Ihas, M. W. Meisel, N. S. Sullivan, and Y. Takano, *Nuclear Demagnetization Cryostat at University of Florida Microkelvin Laboratory,* Journal of Low Temperature Physics **89**, 719 (1992).

[168] M. Tinkham, *Introduction to Superconductivity* (Courier Corporation, 1996).

[169] K. Gloos, R. S. Poikolainen, and J. P. Pekola, *Wide-Range Thermometer Based on the Temperature-Dependent Conductance of Planar Tunnel Junctions,* Applied Physics Letters **77**, 2915 (2000).

[170] F. Mueller, R. Schouten, M. Brauns, T. Gang, W. Lim, N. Lai, A. Dzurak, W. van der Wiel, and F. Zwanenburg, *Printed Circuit Board Metal Powder Filters for Low Electron Temperatures,* Review of Scientific Instruments **84**, 044706 (2013).

[171] J. Reynard, C. Verove, E. Sabouret, B. Motte, B. Descouts, C. Chaton, J. Michailos, and K. Barla, *Integration of Fluorine-Doped Silicon Oxide in Copper Pilot Line for 0.12 µm Technology,* Microelectronic Engineering **60**, 113 (2002).

[172] D. Freude and J. Haase, *NMR Basic Principles and Progress*, Vol. 29 (Springer, 1993).

[173] M. Sarsby, N. Yurttagül, and A. Geresdi, *500 Microkelvin Nanoelectronics,* Nature Communications **11**, 1492 (2019).

[174] J. Johansson and D. Haviland, *Random Background Charges and Coulomb Blockade in One-Dimensional Tunnel Junction Arrays,* Phys. Rev. B **63**, 014201 (2000).

[175] K. Yano, T. Ishii, T. Sano, T. Mine, F. Murai, T. Hashimoto, T. Kobayashi, T. Kure, and K. Seki, *Single-Electron Memory for Giga-to-Tera Bit Storage,* Proceedings of the IEEE **87**, 633 (1997).

[176] N. Bakhvalov, G. Kazacha, K. Likharev, and S. Serdyukova, *Single-Electron Solitons in One-Dimensional Tunnel Structures,* Sov. Phys. JETP **68**, 581 (1989).

[177] M. Amman, E. Ben-Jacob, and K. Mullen, *Charge Solitons in 1D Array of Mesoscopic Tunnel Junctions,* Phys. Lett. A **142**, 431 (1989).

[178] K. Hirvi, M. Paalanen, and J. Pekola, *Numerical Investigation of One-Dimensional Tunnel Junction Arrays at Temperatures above the Coulomb Blockade Regime,* J. Appl. Phys. **80**, 256 (1996).

[179] P. Gray and D. Brown, *Density of $SiO_2$-Si Interface States,* Appl Phys. Lett **8**, 31 (1966).

[180] Y. Cheng, *Electronic States at the Silicon-Silicon Dioxide Interface,* Progress in Surface Science **8**, 181 (1977).

[181] H. Deuling, E. Klausmann, and A. Goetzberger, *Interface States in Si-SiO2 Interfaces,* Solid-State Electronics **15**, 559 (1972).

[182] G. Ehnholm, J. Ekström, J. Jacquinot, M. Loponen, O. Lounasmaa, and J. Soini, *Evidence for Nuclear Antiferromagnetism in Copper,* Phys. Rev. Lett. **42**, 1702 (1979).

[183] H. R. Folle, M. Kubota, C. Buchal, R. M. Mueller, and F. Pobell, *Nuclear Refrigeration Properties of $PrNi_5$,* Zeitschrift für Physik B Condensed Matter **41**, 223 (1981).

[184] Y. Tang, E. Adams, K. Uhlig, and D. Bittner, *Nuclear Cooling and the Quadrupole Interaction of Indium,* J. Low Temp. Phys. **60**, 351 (1985).

[185] D. Schmoranzer, R. Gazizulin, S. Triqueneaux, E. Collin, and A. Fefferman, *Development of a sub-mK Continuous Nuclear Demagnetization Refrigerator,* J. Low Temp. Phys. **196**, 261 (2019).

[186] R. Toda, S. Murakawa, and H. Fukuyama, *Design and Expected Performance of a Compact and Continuous Nulcear Demagnetization Refrigerator for Sub-1 mK Application,* J. Phys.: Conf. Ser. **969**, 012093 (2018).

[187] B. Bleaney, *Enhanced Nuclear Magnetic Cooling - A New Perspective,* J. Phys.: Condens. Matter **2**, 7265 (1990).

[188] W. Anderson, F. Thatcher, and R. Hewitt, *Nuclear Magnetic Resonance in Dilute Alloys of Indium-Lead and Indium-Tin,* Phys. Rev. **171**, 541 (1968).

[189] F. Thatcher and R. Hewitt, $^{115}$*In NMR in the Indium-Rich Alloys In-Cd, In-Hg, and In-Tl at 4.2 K,* Phys. Rev. B **1**, 454 (1970).

[190] R. Hewitt and T. Taylor, *Nuclear Quadrupole Resonance and the Electric Field Gradient in Metallic Indium,* Phys. Rev. **125**, 524 (1962).

[191] W. Brewer and G. Kaindl, *Nuclear Quadrupole Alignment of Lu, In, and Zn,* Hyperfine Interactions **4**, 576 (1978).

[192] Y. Karaki, M. Kubota, and H. Ishimoto, *Specific Heat Below 1 mK and the Electric-Field Gradient in Indium,* Phys. Rev. B **54**, 427 (1996).

[193] H. Haug, K. Weiss, and M. Van Hove, *Heat Exchange in Liquid Helium by Phonon Tunneling Through Very Thin Plates,* J. Low Temp. Phys. **4**, 263 (1971).

[194] Q. Zhu, A. Toda, Y. Zhang, T. Itoh, and R. Maeda, *Void-Free Copper Filling of Through Silicon Vias by Periodic Pulse Reverse Electrodeposition,* J. Electrochem. Soc. **161**, 263 (2014).

[195] Y. Castrillejo, P. Hernandez, J. Rodriguez, and M. Vega, *Electrochemistry of Scandium in the Eutectic LiCl-KCl,* Electrochemica Acta **71**, 166 (2012).

[196] Q. Zhang, Z. Duan, Y. Hua, and Y. Li, *Electrodeposition of Lanthanum from a Dicyanamide Anion Based Ionic Liquid,* Journal of Rare Earths **32**, 114 (2014).

[197] N. Yurttagül, M. Sarsby, and A. Geresdi, *Indium as a High-Cooling-Power Nuclear Refrigerant for Quantum Nanoelectronics,* Phys. Rev. Applied **12**, 011005 (2019).

[198] Y. Tian, C. Liu, D. Hutt, and B. Stevens, *Electrodeposition of Indium Bumps for Ultrafine Pitch Interconnection,* Journal of Electronic Materials **43**, 594 (2014).

[199] Y. Sadana, J. Singh, and R. Kumar, *Electrodeposition of Antimony and Antimony Alloys - A Review,* Surf. Tech. **24**, 319 (1985).

[200] S. El Rehim and A. El Sayed, *Electroplating of Antimony and Antimony-Tin Alloys,* J. Appl. Electrochem. **17**, 156 (1987).

[201] W. Parker, H. Bildstein, N. Getoff, H. Fischer-Colbrie, and H. Regal, *Molecular Plating II - A Rapid and Quantitative Method for the Electrodeposition of the Rare-Earth Elements,* Nuclear Instruments and Methods **26**, 61 (1964).

[202] A. Baca, F. Ren, J. Zolper, R. Briggs, and S. Pearton, *A Survey of Ohmic Contacts to III-V Compound Semiconductors,* Thin Solid Films **308**, 599 (1997).

[203] V. Rideout, *A Review of the Theory and Technology for Ohmic Contacts to Group III-V Compound Semiconductors,* Solid-State Electronics **18**, 541 (1975).

[204] M. Iqbal, D. Reuter, A. Wieck, and C. van der Wal, *Robust Recipe for Low-Resistance Ohmic Contacts to a Two-Dimensional Electron Gas in GaAs/AlGaAs Heterostructure,* Solid-State Electronics **1407.4781** (2014).

[205] H. Pothier, S. Gueron, N. Birge, D. Esteve, and M. Devoret, *Energy Distribution Function of Quasiparticles in Mesoscopic Wires,* Phys. Rev. Lett. **79**, 3490 (1997).

[206] A. Kitaev, *Fault-Tolerant Quantum Computation by Anyons,* Annals of Physics **303**, 2 (2003).

[207] V. Lahtinen and J. Pachos, *A Short Introduction to Topological Quantum Computation,* SciPost Phys. **12** (2017).

[208] D. Tsui, H. Stormer, and A. Gossard, *Two-Dimensional Magnetotransport in the Extreme Quantum Limit,* Phys. Rev. Lett. **48**, 1559 (1982).

[209] W. Pan, H. L. Stormer, D. C. Tsui, L. N. Pfeiffer, K. W. Baldwin, and K. W. West, *Transition from an Electron Solid to the Sequence of Fractional Quantum Hall States at Very Low Landau Level Filling Factor,* Phys. Rev. Lett. **88**, 176802 (2002).

[210] G. Moore and N. Read, *Nonabelions in the Fractional Quantum Hall Effect,* Nucl. Phys. B **360**, 362 (1991).

[211] W. Pan, J.-S. Xia, V. Shvarts, D. E. Adams, H. L. Stormer, D. C. Tsui, L. N. Pfeiffer, K. W. Baldwin, and K. W. West, *Exact Quantization of the Even-Denominator Fractional Quantum Hall State at $\nu = 5/2$ Landau Level Filling Factor,* Phys. Rev. Lett. **83**, 3530 (1999).

[212] R. Willett, L. Pfeiffer, and K. West, *Measurement of Filling Factor 5/2 Quasiparticle Interference with Observation of Charge $e/4$ and $e/2$ Period Oscillations,* Proc. Nat. Acad. Sci. **106**, 8853 (2009).

[213] P. Gammel, D. Bishop, J. Eisenstein, J. English, A. Gossard, R. Ruel, and S. H.L., *Ultralow Temperature Behaviour of the 52 Fractional Quantum Hall Effect,* Phys. Rev. B **38**, 10128 (1988).

[214] J. Eisenstein, K. Cooper, L. Pfeiffer, and K. West, *Insulating and Fractional Quantum Hall States in the First Excited Landau Level,* Phys. Rev. Lett. **88**, 076801 (2002).

[215] J. Xia, W. Pan, C. Vicente, E. Adams, N. Sullivan, H. Stormer, D. Tsui, L. Pfeiffer, K. Baldwin, and K. West, *Electron Correlation in the Second Landau Level: A Competition Between Many Nearly Degenerate Quantum Phases,* Phys. Rev. Lett. **93**, 176809 (2010).

[216] A. Kumar, G. Csathy, M. Manfra, L. Pfeiffer, and K. West, *Nonconventional Odd-Denominator Fractional Quantum Hall States in the Second Landau Level,* Phys. Rev. Lett. **105**, 246808 (2010).

[217] P. Simon and D. Loss, *Nuclear Spin Ferromagnetic Phase Transition in an Interacting Two Dimensional Electron Gas,* Phys. Rev. Lett. **98**, 156401 (2007).

[218] N. Samkharadze, R. Dohyung, L. Pfeiffer, K. West, and G. Csathy, *Observation of an Anomalous Density-Dependent Energy Gap of the $\nu = 5/2$ Fractional Quantum Hall State in the Low-Density Regime,* Phys. Rev. B **96**, 085105 (2017).

[219] V. Mourik, K. Zuo, S. Frolov, S. Plissard, E. Bakkers, and L. Kouwenhoven, *Signatures of Majorana Fermions in Hybrid Superconductor-Semiconductor Nanowire Devices,* Science **336**, 1003 (2012).

[220] M. Lejinse and K. Flensberg, *Introduction to Topological Superconductivity and Majorana Fermions,* Semicond. Sci. Technol. **27**, 124003 (2012).

[221] M. Kjaergaard, K. Wölms, and K. Flensberg, *Majorana Fermions in Superconducting Nanowires without Spin-Orbit Interaction,* Phys. Rev. B. **85**, 020503 (2014).

[222] B. Braunecker, G. Japaridze, J. Klinovaja, and D. Loss, *Spin-Selective Peierls Transition in Interacting One-Dimensional Conductors with Spin-Orbit Interaction,* Phys. Rev. B. **82**, 045127 (2010).

[223] B. Braunecker, P. Simon, and D. Loss, *Nuclear Magnetism and Electronic Order in Carbon Nanotubes,* Phys. Rev. Lett. **102**, 116403 (2009).

[224] B. Braunecker and P. Simon, *Interplay Between Classical Magnetic Moments and Superconductivity in Quantum One-Dimensional Conductors - Toward a Self Sustained Topological Majorana Phase,* Phys. Rev. Lett. **111**, 147202 (2013).

[225] V. Kornich, P. Stano, A. Zyuzin, and D. Loss, *Voltage-Induced Conversion of Helical to Uniform Nuclear Spin Polarization in a Quantum Wire,* Phys. Rev. B. **91**, 195423 (2015).

[226] T. Meng and D. Loss, *Helical Nuclear Spin Order in Two-Subband Quantum Wires,* Phys. Rev. B. **87**, 235427 (2013).

[227] C. P. Scheller, T.-M. Liu, G. Barak, A. Yacoby, L. N. Pfeiffer, K. W. West, and D. M. Zumbühl, *Possible Evidence for Helical Nuclear Spin Order in GaAs Quantum Wires,* Phys. Rev. Lett. **112**, 066801 (2014).

[228] B. Braunecker and P. Simon, *Self Stabilizing Crossover Between Topological and Non-Topological Ordered Phases in One-Dimensional Conductors,* Phys. Rev. B. **92**, 241410 (2015).

[229] M. Wimmer, A. Akhmerov, J. Dahlhaus, and C. Beenakker, *Quantum Point Contact as a Probe of a Topological Superconductor,* New. J. Phys. **13**, 053016 (2011).

[230] W. Coish and J. Baugh, *Nuclear Spins in Nanostructures,* Phys. Stat. Sol. B **10**, 2203 (2009).

[231] W. Chang, S. Albrecht, T. Jespersen, F. Kuemmeth, P. Krogstrup, J. Nygard, and C. Marcus, *Hard Gap in Epitaxial Semiconductor-Superconductor Nanowires,* Nature Nanotechnology **10**, 232 (2015).

[232] D. Rainis and D. Loss, *Conductance Behavior in Nanowires with Spin-Orbit Interaction - A Numerical Study,* Phys. Rev. B **90**, 235415 (2014).

[233] S. Giblin, S. Wright, J. Fletcher, M. Kataoka, M. Pepper, T. Janssen, D. Ritchie, C. Nicoll, D. Anderson, and G. Jones, *An Accurate High-Speed Single-Electron Quantum Dot Pump,* New. J. Phys. **12**, 073013 (2010).

[234] J. Pekola, O. Saira, V. Maisi, A. Kemppinen, M. Möttönen, Y. Pashkin, and D. Averin, *Single-Electron Current Sources - Toward a Refined Definition of the Ampere,* Rev. Mod. Phys. **85**, 1421 (2013).

[235] M. Devoret and R. Schoelkopf, *Superconducting Circuits for Quantum Information - An Outlook,* Science **339**, 1169 (2013).

[236] F. Fröwis, P. Sekatski, W. Dür, N. Gisin, and N. Sangouard, *Macroscopic Quantum States: Measures, Fragility, and Implementations,* Rev. Mod. Phys. **90**, 025004 (2018).

# ACKNOWLEDGEMENTS

In the first place, I would like to express my gratitude to Prof. dr. Leo Kouwenhoven and dr. Attila Geresdi for giving me the possibility to do my PhD research at Qutech and to give me guidance and support on the way.

A huge thanks goes to dr. Matthew Sarsby, who is representing the other integral part of the microkelvin team. This work profited significantly from his cryogenics skills.

I would like to thank the Nederlandse Organisatie voor Wetenschappelijk Onderzoek (NWO) and Microsoft Corp. for funding this project, as well as the Technical University of Delft and QuTech for providing the research infrastructure.

Many thanks to all people of QuTech, and especially the topological quantum computation group, for friendly group athmosphere and enlighting discussions.

A special thanks goes to the Kavli Nanolab team, without their support this work would not have been possible. Special thanks here to Marco van der Krogt, Marc Zuiddam, Anja van Langen-Suurling, Charles de Boer, Ewan Hendriks, and Eugene Straver.

Great thanks to Ruud Schmits and dr. Alexandra Fursina for the great times in cleanroom 0750 and many successful troubleshooting sessions with various Raith tools.

I want to specifically thank Nico Alberts for his decisive contributions to the work, Mark Ammerlaan for the technical support, Raymond Schouten and Raymond Vermeulen for helping input regarding electronics, as well as Jason Mensingh, dr. Olaf Benningshof, and Remco Roeleveld for technical support and advice regarding cryogenics.

I also want to thank Marcel Ridder and Kenichiro Nagayoshi from SRON for the great collaboration on electrodeposition and for kindly hosting me in Utrecht.

Big thanks to Jenny Boks-Zondervan, Simone Berkouwer, and Csilla Buiting-Csikós for their great support and their open and friendly attitude.

I would like to thank the thesis committee: Prof. dr. Jukka Pekola, Prof. dr. Dominik Zumbühl, Prof. dr. Gary Steele, dr. Sonia Conesa-Boj, and Prof. dr. Yaroslav Blanter for their commitment.

Last but not the least, I would like to thank Christine Nebel for also supporting me during difficult times and always standing by my side.

# Curriculum Vitæ

## Nikolai Yurttagül

| | |
|---|---|
| 10-01-1987 | Born in Berlin, Germany. |
| 2005–2008 | High School<br>Bröndby Oberschule, Berlin Steglitz-Zehlendorf, Germany |
| 2008–2009 | Military Service<br>3./Feldjägerbataillon 151, Germany |
| 2009–2012 | B.Sc. in Molecular Life Science<br>Medizinische Universität zu Lübeck<br>*Thesis:* Quantifizierung der Katalytischen Aktivität der Galaktosyltransferase B mittels NMR<br>*Promotor:* Prof. dr. T. Peters |
| 2012–2015 | M.Sc. in Nanostructure Science<br>Universität Kassel<br>*Thesis:* Kontrolle der Mechanischen Spannung in PECVD Siliziumnitrid/Siliziumoxid Multischichtsystemen<br>*Promotor:* Prof. dr. H. Hillmer |

# List of Publications

4. **N. Yurttagül**, M. Sarsby, A. Geresdi, *Indium as a High-Cooling-Power Nuclear Refrigerant for Quantum Nanoelectronics*, Physical Review Applied **12**, 011005 (2019).

3. M. Sarsby, **N. Yurttagül**, A. Geresdi, *500 Microkelvin Nanoelectronics*, Nature Communications **11**, 1492 (2020).

2. **N. Yurttagül**, M. Sarsby, A. Geresdi, *Coulomb Blockade Thermometry Beyond the Universal Regime* (in preparation).

1. **N. Yurttagül**, M. Sarsby, A. Geresdi, *Microkelvin Nuclear Nanocalorimetry* (in preparation).